Information Propagation in the Cortex Across the Sleep–Wake Cycle

A Computational Study

Farhad Razi

TESI DOCTORAL UPF / year 2023

THESIS SUPERVISOR
Dr. Belén Sancristóbal
Barcelona School of Design and Engineering (ELISAVA)

THESIS TUTOR
Dr. Rubén Moreno-Bote
Department of Information and Communication Technologies

"The knowledge of anything, since all things have causes, is not acquired or complete unless it is known by its causes."

–Ibn Sina (Avicenna) (973-1037 A.D.), Persian polymath.
From: Charles F. Horne, ed., The Sacred Books and Early Literature of the East, (New York: Parke, Austin, & Lipscomb, 1917), Vol. VI: Medieval Arabia, pp. 90-91.

"For let Philosopher and Doctor preach
Of what they will, and what they will not – each
Is but one Link in an eternal Chain
That none can slip, nor break, nor over-reach.

–Omar Khayyam (1048-1131 A.D.), Persian polymath.
Translated by Edward Fitzgerald

I dedicate this dissertation to Atossa, the light of my life, and to my parents.
For your constant love and support.

Acknowledgment

I would like to thank Dr. Belén Sancristóbal and Dr. Rubén Moreno-Bote for offering me the PhD position. I am extremely grateful to Prof.Dr. Belén Sancristóbal for her continuous support, invaluable supervision and patience during my doctoral studies. Her knowledge and experience, as well as her confidence in me, have encouraged me in my doctoral studies.

You have to be lucky to have great colleagues. I would like to thank all my friends and colleagues at the Center for Brain and Cognition (CBC), Barcelona. My special thanks to my friends Indre and Ruben who have welcomed me so warmly and are such great people. I cannot thank you enough for your support.

If you get off on the wrong foot on a new journey, all you need is the help of good people. There are many people who have helped me and to whom I am very grateful. Special thanks to Arezou Rezazadeh and Rasoul Nikbakht for their help when I arrived in Barcelona. People like you revive the hope for a better future.

Living abroad can be difficult, especially if you are not able to communicate, but having great friends alleviates it. I cannot thank my friends enough: Adrian, Ruben, Alba, Alejandro, Luis, Laura, Luke, Pablo and my other friends at Law & Philosophy research group at Universitat Pompeu Fabra, Barcelona. Thanks for including me even when I was unable to communicate in English or Spanish. Thanks for inviting me to every private and public meeting and embracing the challenge of speaking in English instead of Spanish. Thanks for creating such great memories.

There are two things that become more valuable as they age: Wine and friendship. I would like to thank my friend Adib, who has always been there for me. Sometimes, you should stop writing pages and leave it at one word: "One friend does what a hundred people cannot do." I would also like to thank my friends Milad and Mojde for supporting me. I hope to see you somewhere soon.

Somethings are beyond words, yet they speak for themselves. "Mam"and "Dad" are probably the most self-explanatory. Mom and Dad, I am extremely grateful to you for your constant love and support and for all your hard efforts to make ends meet. Mom and Dad, I never told you how much I regret what I made you go through when I was imprisoned for my beliefs.

My sister Atossa, you cannot imagine how much I love you. I can not help laughing when I remember your attempts in childhood to trick me into getting you a glass of water. I have seen how mature you think, analyze and behave even when you were a child. Atossa, remember "*if you're going to try, go all the way. Otherwise, don't even start*" (Charles Bukowski). You may feel the urge to give up. But remember that everyone has felt and experienced that urge. See the glimmer of light at the end of the tunnel. I know, more than all the stars, that the bright future is yours.

Whether positive or negative, our environment shapes our personality. I would like to thank everyone who influenced my life, including my teachers, friends, relatives, and "*the stranger who greeted me with the hat tip and plastic smile*" (Forough Farrokhzad).

Abstract

During the deep phases of sleep we do not normally wake up by a thunder, but we nevertheless notice it when awake. The exact same sound gets to our ears and cortex through the thalamus and still, it triggers two very different responses. There is growing experimental evidence that these two states of the brain—sleep and wakefulness—distribute sensory information in different ways across the cortex. In particular, during sleep, neural responses remain local and do not spread out across distant synaptically connected regions. On the contrary, during wakefulness, stimuli are able to elicit a wider spatial response. We have used a computational model of coupled cortical columns to study how these two propagation modes arise. Moreover, the transition from sleep-like to waking-like dynamics occurs in agreement with the synaptic homeostasis hypothesis and only requires upscaling of excitatory synapses. We have found that, in order to reproduce the aforementioned observations, synaptic upscaling has to be selectively applied: synaptic connections between distinct cortical columns have to be upscaled over local ones.

Resum

Durant les fases profundes del son normalment no ens despertem amb un tro, però, tanmateix, ho notem quan estem desperts. El mateix so arriba exactament igual a les nostres orelles i còrtex a través del tàlem i, tot i així, desencadena dues respostes molt diferents. Hi ha una creixent evidència experimental que aquests dos estats del cervell—son i vigília—distribueixen la informació sensorial de diferents maneres a través de l'escorça. En particular, durant el son, les respostes neuronals romanen locals i no s'estenen per regions distants connectades sinàpticament. Per contra, durant la vigília, els estímuls són capaços de provocar una resposta espacial més àmplia. Hem utilitzat un model computacional de columnes corticals acoblades per estudiar com sorgeixen aquests dos modes de propagació. A més, la transició de la dinàmica del son a la de la vigília es produeix d'acord amb la hipòtesi de l'homeòstasi sinàptica i només requereix un reescalament de les sinapsis excitadores. Hem trobat que, per reproduir les observacions esmentades anteriorment, s'ha d'aplicar selectivament el reforç sinàptic: les connexions sinàptiques entre columnes corticals diferents s'han d'augmentar sobre les locals.

Preface

This dissertation is an original intellectual product by the author, Farhad Razi. All the Python codes needed in this Thesis are developed by Farhad Razi. The main contribution of this Thesis is the proposal of a synaptic mechanism that accounts for different propagation patterns of information in the cerebral cortex during sleep and wakefulness.

A version of the hypothesis in this Thesis has been published in the following paper: Razi, F.; Moreno-Bote, R.; Sancristóbal, B. Computational Modeling of Information Propagation during the Sleep–Waking Cycle. Biology 2021, 10, 945. doi:10.3390/biology1010094.

A working paper is currently under preparation with the title: Neural Correlates of Different Information Propagation Patterns during the Sleep–Waking Cycle.

Table of Contents

List of Figures

List of Tables

Chapter 1

INTRODUCTION

All humans and most animals sleep. Sleep is a global state of the body and the mind. Sleep reduces the energy demand of the brain by slowing the metabolic rate [1], which, in turn, affects sensory perception. For instance, a thunderstorm can go unnoticed while we are asleep, whereas we normally notice it when we are awake. In this study, we seek to investigate the neural substrate of such a different behavioral response during deep sleep stages (aka NREM sleep) and wakefulness.

Here, we present the state of the art in sleep research along three sections. In the first section, the electrophysiology and neurobiology of sleep-wake states are discussed. First, the neural origins underlying the electrophysiological characteristics of these states are presented. Finally, the subcortical structures involved in the development of sleep-wake states and their neuromodulatory milieu that might control the electrophysiological characteristics are presented.

The second section is devoted to the electrophysiological recordings during auditory stimulation in NREM sleep and wakefulness. In this section, we provide an overview of brain responses to auditory stimuli measured by electroencephalography (EEG) and extracellular single-unit recordings. We then present a human study on brain responses to non-sensory

stimuli, supporting the findings of above studies.

The Third section addresses the mechanisms underlying different propagation patterns of neural firing responses in NREM sleep and wakefulness. The current scientific consensus is that differences in propagation patterns in the cerebral cortex between NREM sleep and wakefulness are not due to altered strength of cortico-cortical synaptic pathways, but to altered dynamics of the thalamocortical network [2, 3]. However, as far as our own research is concerned, there is insufficient evidence to support this view.

To assess the role of the cortico-cortical synaptic pathways in tuning propagation patterns of neural firing responses in the cerebral cortex during NREM sleep and wakefulness, we first provide an overview of a thalamocortical model that describes the neural groups and synaptic pathways involved in propagation of neural firing responses in the cerebral cortex. Then, we review the literature on the dynamics of the thalamocortical network and we argue that experimental evidence challenges these mechanisms as a sufficient mechanism for attenuating propagation of neural firing responses in the cerebral cortex. Finally, we provide support for the missing piece of the puzzle, namely the role of cortico-cortical synapses as a mechanistic explanation.

In the final section, we discuss whether experimental studies in the second section supports the view that propagation of information about external stimuli attenuates along a hierarchical cortical processing chain during NREM sleep compared with wakefulness. To this end, we present a framework to define information and methods for its quantification. Then we asses whether evidence in experimental observations in the second section supports this view. Finally, the reader will also find a reflection on the mechanisms accounting for attenuation of information propagation given experimental observations in the third section.

It is also important to note that the studies reviewed include both human and animal models. Given the great similarities between mammalian and human brains (see [4] for rodents and humans), the analysis of ani-

mal models has improved the understanding of the electrophysiology and neuromodulatory milieu of sleep–wake states.

1.1 Characteristics of Sleep–Wake States

Sleep is a vital brain state that enhances memory and learning functions [5, 6, 7, 8, 9, 10, 11]. It is often accompanied by loss of interaction with the external environment. Behaviorally, this can be clearly observed in the cessation of actions, as sleep affects reproduction, exploration, protection, and rearing of offspring. In the laboratory, the states of wakefulness and sleep are distinguished using techniques that record the electrical activity of the brain and body.

1.1.1 Electrophysiology of Sleep–Wake States

Since the invention of electroencephalography (EEG) in 1924 by German psychiatrist Hans Berger, researchers have used EEG techniques to record the electrical activity of the brain during wakefulness and sleep. Since then, electrophysiological recordings have been used to distinguish between waking and sleeping states. Early EEG recordings showed that characteristics of the electrophysiology of brain activity change between wakefulness and sleep [12, 13, 14] (see Figure 1.1A).

Wakefulness is characterized by low-amplitude–high-frequency EEG activity [15, 1] (see Figure 1.1B). In contrast, during sleep ,the brain alternates between two distinct states, rapid eye movement (REM) and non-rapid eye movement (NREM) sleep [15, 1]. During REM sleep, also called paradoxical sleep, EEG activities are similar to those during wakefulness, hence the name paradoxical sleep [15, 1] (see Figure 1.1B). However, in NREM sleep, the frequency and amplitude of EEG activities begins to slow down and increase, respectively, with increasing depth of NREM sleep [14, 15, 1] (see Figure 1.1B).

NREM sleep is further divided into three distinct stages [15, 1]. Each NREM stage (N1, N2, and N3) corresponds to a deeper sleep level. Arousal thresholds, a measure of sleep depth, increase with increasing sleep depth, with N3 being the deepest sleep stage and having the highest arousal threshold [15]. The first stage of NREM sleep (N1) resembles drowsy wakefulness and is the stage at which the transition from wakefulness to sleep occurs [15, 1].

The N2 stage, also referred to as light NREM sleep, is characterized by the appearance of waveforms including K-complexes (<1 Hz) and sleep spindles (10-16 Hz) in the EEG signals [1]. K-complexes are waveforms that last about one second and precede sleep spindles. They are characterized by a brief positive high-voltage excursion followed by a slower negative deflection around 350-550 ms and a final positive peak at 900 ms [16]. Spindles last 1-3 s and are transient oscillations at 10-16 Hz generated by thalamic neurons during NREM sleep [17, 18, 19].

In contrast, the EEG signals in the N3 stage, also referred to as deep NREM sleep, exhibit high-amplitude–low-frequency (0.1-4 Hz) waves, also referred to as sleep slow wave [1]. Sleep slow waves are divided into two distinct oscillatory rhythms in the brain: delta oscillations (1-4 Hz) and slow oscillations (0.1-1 Hz) [20, 18, 1]. Note that throughout this study, we will use the term NREM sleep to refer to both N2 and N3 stages of NREM sleep.

Studies using *in vivo* and *in vitro* techniques suggest that the generation of NREM-related brain rhythms is due to intrinsic properties of thalamic and cortical neurons during NREM sleep. In the following, we review the neural origin of brain rhythms during NREM sleep.

Neural origin of the K-complex (N2)

The neural origin underlying the generation of K-complexes in EEG signals is thought to be the same as that underlying slow oscillations [21]. Briefly, cortical neurons fall into periods of prolonged hyperpolarization

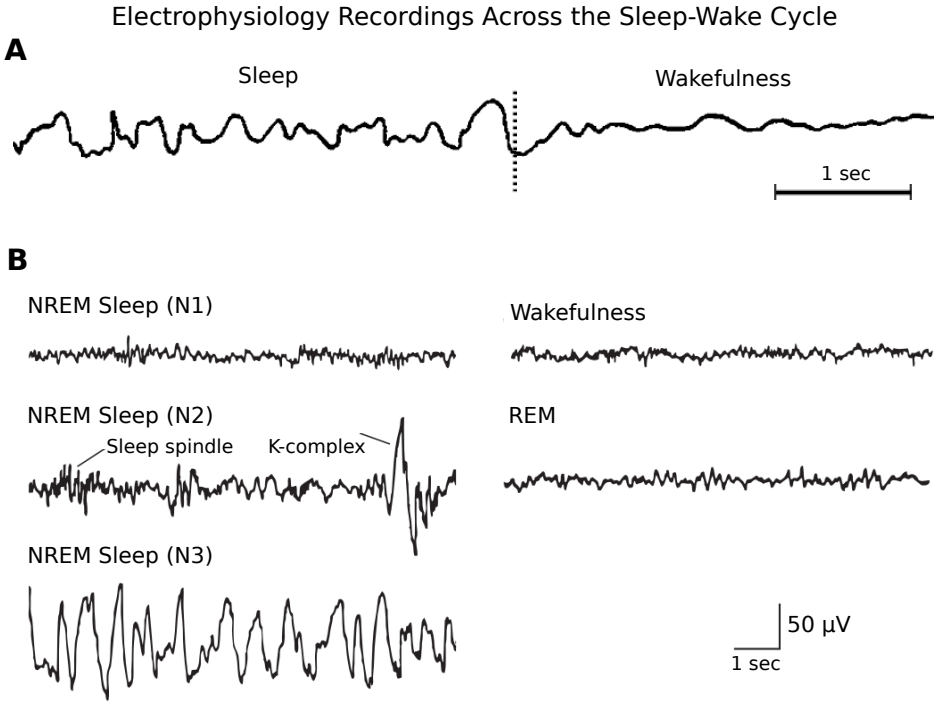

Figure 1.1: Electrophysiology recordings across the sleep–wake cycle in humans. (**A**). The amplitude and frequency of the EEG signals decrease and increase, respectively, from sleep to wakefulness in vertex of human brain. The dashed vertical line represent s the presentation of a loud sound that led to awakening of the sleeping subject. Figure taken from [14]. (**B**). *Left*. EEG recording in humans during NREM sleep. Amplitude and frequency of EEG signals increase and decrease, respectively, with increasing depth of NREM sleep. During light NREM sleep (stage N2), spindles and K-complexes occur. During deep NREM sleep (stage N3), sleep slow waves (0.5-4 Hz) are observed. *Right*. EEG recordings in humans during wakefulness (top) and REM sleep (bottom). Figure taken from [1].

following periods of intense firing. Synchronization of such activity by a group of neurons results in the appearance of K-complexes in the EEG signals.

Microelectrode recordings in epilepsy patients have also shown that spontaneous and evoked K-complexes in widespread cortical areas are associated with reduced neural firing, probably an isolated Down-state [22]. This evidence may suggest that the occurrence of K-complexes increases with increasing depth of NREM sleep and forms slow oscillations during deep NREM sleep.

Neural origin of the sleep spindle (N2)

Thalamic neurons include relay neurons (thalamic neurons that project to the cerebral cortex, also called thalamocortical neurons), local inhibitory interneurons, and the thalamic reticular nucleus (TRN) [17, 19, 23].

Thalamc neurons are hyperpolarized during NREM sleep. As a result, the firing profile of thalamic neurons shifts from tonic firings during wakefulness to burst firings during NREM sleep [17, 19, 23]. In particular, TRN burst activity triggers spindle activity by mediating synaptic inhibition at various thalamic relay neurons that is larger and slower than the TRN-tonic-mediated inhibition [19, 1, 24]. Accordingly, thalamic relay neurons generate a rebound of burst firings that are monosynaptically projected to cortical areas. Feedback of cortical activity to thalamic neurons, as well as thalamic burst firings to TRN neurons, maintains spindle activity. Widespread connections from the TRN complex to other thalamic relay neurons can result in a local spindle synchrony. Finally, spindle activity can be terminated by a combination of intrathalamic, cortical, and brainstem mechanisms (see for review [1, 24]).

Neural origin of delta oscillation (N3)

Studies in cats using *in vivo* techniques suggest that delta oscillations (1-4 Hz) are generated in the thalamus [18, 25]. Thalamic neurons are further hyperpolarized from N2 to N3 stage, which activates low-threshold calcium channels [18]. As a result, a calcium spike occurs following burst firings in thalamic relay neurons. The thalamic burst firings result in bursts in a large number of cortical neurons. Widespread connections from the TRN complex to other thalamic relay neurons can result in a local delta synchronization in thalamic relay neurons, which, in turn, is transferred to the cortex. Feedback from corticothalamic neurons can further enhance delta synchronization in thalamic relay neurons [18] (see for review [18, 1]).

Neural origin of slow oscillation (N3)

Intracellular recordings from cortical neurons in cats have shown that cortical neurons alternate between two distinct periods during slow oscillations: long-lasting depolarized periods periodically interrupted by long periods of hyperpolarization [20, 26] (see Figure 1.2A). Neural firing rates during depolarized periods were characterized with persistent firing activity as high as in wakefulness, and thus are referred to as Up states. During hyperpolarized periods, referred to as Down states, firing activity vanished. Furthermore, fluctuations in membrane potential during NREM sleep showed a bimodal distribution, due to the alternation between Up and Down states [26] (see Figure 1.2B left). On the other hand, wakefulness was associated with stable neural firing rates, and fluctuations in membrane potential showed a Guassian-like distribution (see Figure 1.2B right). REM sleep, like wakefulness, was associated with stable neural firing rates and a Guassian-like distribution of membrane potential.

Experimental studies suggest that the generation of slow oscillations has a cortical origin, as removal of the cortex terminates slow oscillations in thalamic neurons [27]. Studies using *in vitro* cortical slices from ferrets

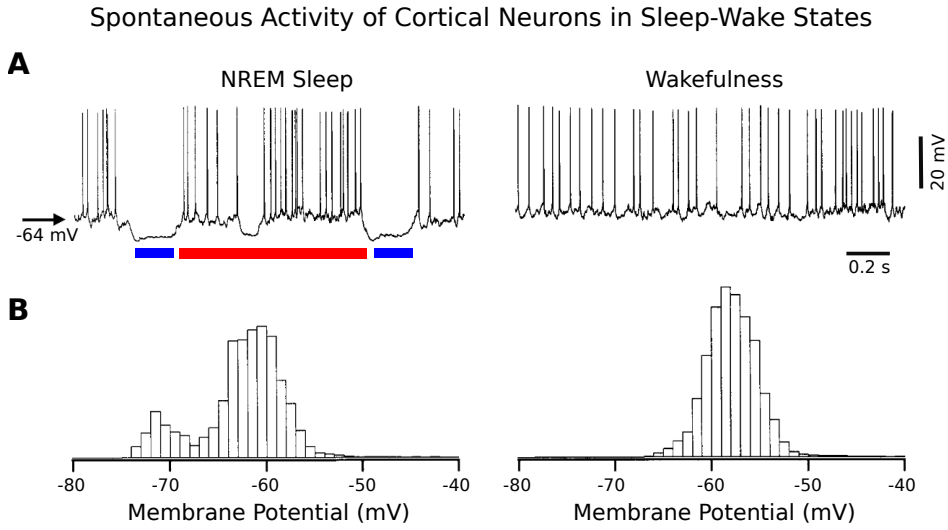

Figure 1.2: Spontaneous activity of cortical neurons in sleep–wake states. (**A**). Intracellular activity in a representative neuron from the cat posterior association suprasylvian area during slow wave sleep (left) and wakefulness (right). Horizontal blue and red bars indicate hyperpolarized and polarized periods associated with Down and Up states, respectively. (**B**). Histograms of membrane potential in slow wave sleep and wakefulness show that the distribution of membrane potential shifts from a bimodal to a Gaussian-like distribution. Figure taken from [26].

have also shown that cortical neurons in slices can generate slow oscillations in the absence of the thalamus by alternating between periods of depolarized Up and hyperpolarized Down states [28]. This pattern of activity is often referred to as *cortical bistability* [29, 30, 31].

Studies in rats have shown that cortical bistability during NREM sleep is associated with the phase of sleep slow waves. Extracellular recordings from rat barrel cortex showed that the negative phase of the sleep slow waves occurs almost simultaneously with periods when all recorded neurons are silent [32] (see Figure 1.3). These periods in which cortical neurons in the same electrode contact are silent and simultaneously spend their time in the Down-state are referred to as OFF periods. Alternatively, periods in which at least a subset of cortical neurons are active and spend their time in the Up-state are referred to as ON periods. OFF periods account for a small fraction of neural activities [33] during slow wave sleep. In fact, cortical neurons spend most of their time in ON periods, which are similar in dynamics to wakefulness [34], and are only occasionally interrupted by spontaneous OFF periods [32].

The mechanism underlying cortical bistability is attributed to activity-dependent potassium currents (e.g., current through KCa and KNa, calcium- and sodium-activated channels, respectively.) [35, 18, 28, 36, 37, 31]. Neuromodulators released in the cortex from the subcortical ascending arousal network affect the strength of these potassium currents. These neuromodulators block the activity-dependent potassium channels [17]. As a result, the reduction in the neuromodulators in the cerebral cortex during NREM sleep increases activity-dependent potassium currents following trains of action potentials in Up-state. This mechanisms result in prolonged afterhyperpolarization periods of neural silence [17], Down-state. Finally, stochastic release of presynaptic vesicles results in activation of postsynaptic cortical neurons and terminates Down-state [31].

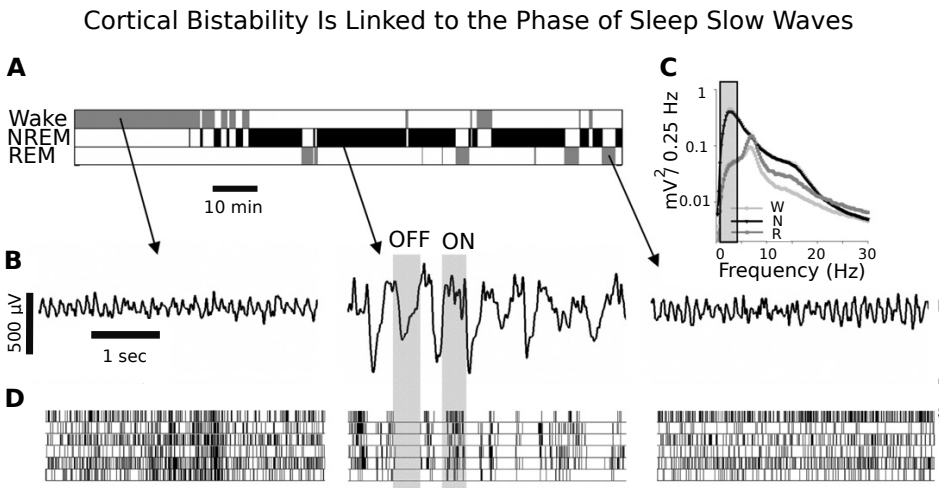

Figure 1.3: Cortical bistability is linked to the phase of sleep slow waves. Hypnogram (**A**) and EEG traces (**B**) from the right barrel cortex of a representative rat during a 2-hour interval starting at light onset. Note that the EEG signals exhibit low-amplitude–high-frequency fluctuations during wakefulness and REM sleep, whereas during NREM sleep they exhibit large amplitude–low-frequency component. (**C**). Average EEG power spectra in NREM sleep, REM sleep, and wakefulness. Note the high values of spectral power in the slow frequency range in NREM sleep. (**D**). Raster plots of spike activity for the 6 channels from a microwire array placed in the left barrel cortex recorded simultaneously in the same rat. Note that OFF periods correspond to times when nearby neuron activity is silent. Horizontal lines below the spike activity during NREM sleep delineates OFF (on bottom) and ON periods (on top). Figure taken from [32].

1.1.2 Neurochemistry of Sleep–Wake States

Changes in electrophysiological features of brain activity across sleep–wake cycle might be reflection of changes in neuromodulatory input synthesized in subcortical areas. In a seminal study in 1949, Moruzzi and Magoun showed that stimulation of the brainstem of anesthetized cats converts slow wave activity, the electrophysiological hallmark of NREM sleep, into wakefulness-like dynamics, low-amplitude and high-frequency activity [38] (see Figure 1.4A). This suggests the possible role of subcortical areas and their neurochemical synthesis in the generation of sleep–wake states.

There are several subcortical areas, such as the brainstem, posterior hypothalamus, and basal forebrain, that have been implicated as networks for the generation of sleep–wake states. Neural groups in subcortical regions can be classified into wake-, NREM- or REM-promoting neural system based on their firing patterns in each vigilance state [39]. Changes in the firing pattern of these subcortical areas in the sleep–wake states change the concentration of synthesized neurochemicals in several brain regions and thus can control sleep–wake states.

Neurochemicals are the molecules of the nervous system involved in the chemical transmission of messages. The two main types of neurochemicals are neurotransmitters and neuromodulators. The functions of neurotransmitters differ from those of neuromodulators. A neurotransmitter is a chemical that is used to transmit a message from one neuron to another neuron; this process is called neurotransmission. A neuromodulator, on the other hand, modulates neurotransmission between two neurons.

Wake-promoting neural system

Following the observations of Moruzzi and Magoun in 1949 [38], it has been proposed that the brainstem encompasses neural nuclei that forms the wake-promoting neural system in the brain, also known as the ascend-

ing arousal network. The ascending arousal network in the brainstem is composed of various groups of neurons that differ in their neurochemical synthesis. The main groups involved in arousal are monoaminergic (MAergic) and cholinergic nuclei that synthesize monoamines (MAs) and acetylcholine (ACh), respectively (see for review [40, 1, 39]).

Firing rate of the ascending arousal network are high during wakefulness and decrease during sleep [41]. For instance, single- and multi-unit recordings in rats have shown that firings in LC neurons (a nuclei in ascending arousal network) are high during wakefulness and decrease during sleep [42]. The higher firing rate of MAergic and cholinergic nuclei during wakefulness increases the concentration of MAs and ACh in several brain regions in the cerebral cortex, thalamus and other subcortical structures (see red and green dots in Figure 1.4B left column). Monoamines (MAs) act as neuromodulators that affect neurotransmission between groups of neurons, whereas ACh acts as both a neurotransmitter and a neuromodulator. Although MAs and ACh can increase excitability in cortical neurons by increasing the signal-to-noise ratio, the functional roles of MAs and ACh in the cerebral cortex are not homogeneous [17]. For instance, when receptive field of a neuron is stimulated, presence of ACh can further increases evoked firing rates without changing the spontaneous firing rates [17].

NREM-promoting neural system

Several groups of GABAergic neurons in subcortical areas regulate sleep (see for review [40, 1, 39]). During NREM sleep, the higher firing rate of the NREM-promoting neural system increases the concentration of GABAergic input in several regions of the cerebral cortex and in subcortical structures (see Figure 1.4B). During wakefulness, higher firing rates of MAergic and cholinergic nuclei inhibit NREM-promoting neurons [44]. The reciprocal inhibitory interaction between NREM-promoting neurons and the ascending arousal network is a key factor in triggering the sleep–wake flip-flop.

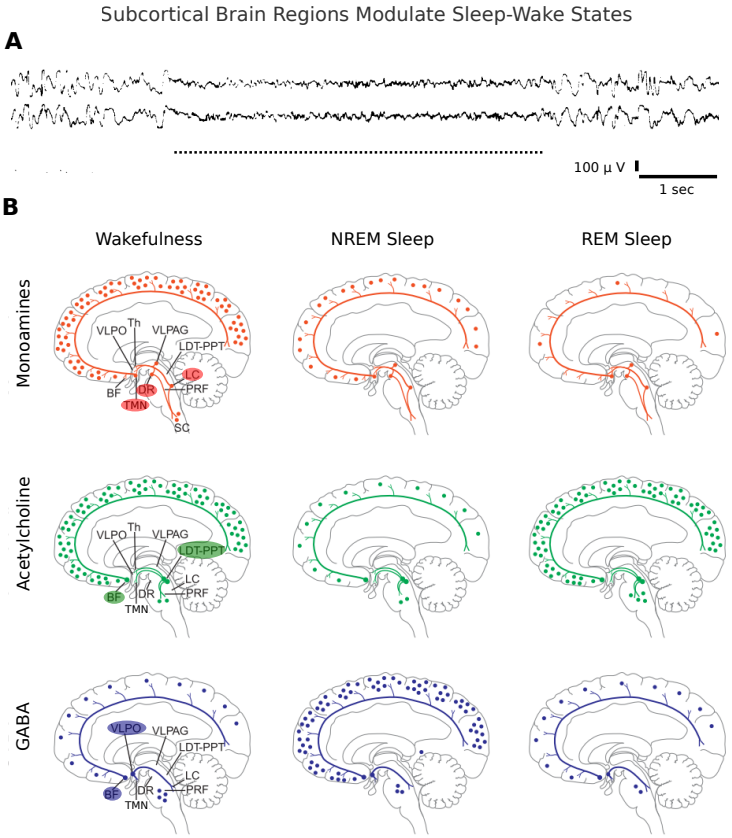

Figure 1.4: Subcortical brain regions modulate sleep–wake states. (**A**). Stimulation of the left reticular formation in an anesthetized cat converts high-amplitude–low-frequency voltage fluctuations in slow wave activities into low-amplitude–high-frequency components in left and right sensorimotor cortex (from top to bottom). The black horizontal dash line represents the stimulation period. Figure taken from [38]. (**B**). Schematic representation of the concentration of neural chemicals and brain nuclei controlling the sleep–wake cycle in a sagittal view of the human brain. The colored lines represent chemically encoded projections of MAergic (red), cholinergic (green), and GABAergic (blue) neurons for wakefulness, NREM sleep and REM sleep (from left to right column). LC, DR, TMN nuclei (red patches) constitute the ascending arousal network promoting (next page)

Figure 1.4 *(previous page)*: wakefulness. Neurons in LDT-PPT and BF nuclei (green patches) promote REM sleep. Neurons in VLPO and BF nuclei (blue patches) promote NREM sleep. Abbreviations: LC, locus coeruleus, DR, DR, dorsal raphe; TMN, tuberomammillary nucleus; BF, basal forebrain; LDT/PPT, laterodorsal and pedunculopontine tegmental nuclei; VLPO, ventrolateral preoptic area of the hypothalamus; PRF, pontine reticular formation; SC, spinal cord; Th, thalamus. Schematic taken from [43].

REM-promoting neural system

The cholinergic neurons play an important role in generating REM sleep as they do for wakefulness (see for review [40, 1, 39]). The firing pattern of the cholinergic neurons is heterogeneous and can be divided into three groups. The largest subpopulation fires both in wakefulness and REM. The second largest subpopulation promote REM sleep by firing during REM and the smallest subpopulation fires only during wakefulness [45]. During REM sleep, the higher firing rate of the REM-promoting neural system increases ACh concentration in several regions of the cerebral cortex, thalamus and subcortical structures (see Figure 1.4B). The projections of MAergic neurons to the cholinergic REM-promoting system are inhibitory. Alternatively, the reciprocal projections from the REM-promoting to MAergic neurons are excitatory. These reciprocal interactions between ascending arousal network with REM and NREM-promoting system have been proposed as the basis of REM-NREM ultradian rhythms [46].

1.1.3 Summary

Electrophysiological recordings have provided unprecedented methods for distinguishing sleep from wakefulness. EEG signals in wakefulness exhibit low-amplitude–high-frequency fluctuations [15, 1]. Based on electrophysiological recordings, sleep is divided into rapid eye movement (REM) and non-rapid eye movement (NREM) sleep [15, 1]. EEG signals in REM

sleep are similar to those in wakefulness, particularly so when compared to NREM sleep, when the frequency and amplitude of EEG activities slow down and increase, respectively, with increasing sleep depth [15, 1]. In particular, NREM sleep is characterized by the occurrence of spindles and K-complexes (<1 Hz) in light NREM sleep (10-16 Hz) and delta (1-4 Hz) and slow oscillation (0.1-1 Hz) in deep NREM sleep [20, 18, 15, 1].

Studies using *in vitro* and *in vivo* techniques suggest that spindles and delta oscillations are generated in thalamic neurons [18] and projected to the cerebral cortex via thalamocortical pathways. Due to a progressive decrease in the neuromodulatory input from the ascending arousal network as NREM sleep progresses [17, 18], thalamic neurons become more hyperpolarized. As a result, thalamic neurons often generate sleep spindles in light NREM sleep [19, 18] and delta oscillations in deep NREM sleep [18]. Alternatively, K-complexes and slow oscillations are generated during NREM sleep due to an intrinsic property of cortical neurons, namely cortical bistability. Cortical neurons fall into a silent period, the Down-state, following trains of action potentials during Up states in NREM sleep [20, 26]. The occurrence of Down-state increases progressively with increasing depth of NREM sleep. As a result, isolated K-complexes in light NREM sleep transition to slow oscillations in deep NREM sleep.

There is ample experimental evidence for the control of subcortical structures over the rhythmic electrical activity of the brain, as stimulation of the brainstem of anesthetized cats converts slow wave activity, the electrophysiological hallmark of NREM sleep, to wakefulness-like activity [38]. Neural groups in subcortical regions can be classified into the wake-, NREM- or REM-promoting neural system based on the firing patterns in each vigilance state [39]. Changes in the firing pattern of these subcortical areas in sleep–wake states change the concentration of synthesized neurochemicals in several brain regions.

During wakefulness, the higher firing pattern of MAergic and cholinergic nuclei in wake-promoting neural system, also referred to as the ascending arousal network, results in higher extracellular concentrations of

monoamines and acetylcholine in several cortical and subcortical areas [42, 40, 43, 41, 39]. During NREM sleep, the NREM-promoting neural system inhibits the ascending arousal network [47], resulting in low extracellular concentrations of monoamines and acetylcholine [43, 39]. Alternatively, during REM sleep, the extracellular concentration of acetylcholine increases due to activation of the REM-promoting neural system, while the concentration of monoamines remains low [40, 43, 39].

Monoamines and acetylcholine act as neuromodulators in the cerebral cortex, i.e. neurochemicals that modulate membrane channels. Changes in these neuromodulators impact the cerebral cortex. For instance, silent neuromodulators from ascending arousal network during NREM sleep changes dynamics of the thalamic and cortical neurons resulting in the brain-rhythms captured by EEG signals across sleep–wake cycles. For instance, decreased neuromodulatory input from the ascending arousal network to the cortical neurons during NREM sleep results in cortical bistability, which manifests as slow oscillations in the EEG signal [20, 26]. Changes in the level of neuromodulators not only shift the dynamics, but also neurotransmission between neural groups. Although MAs and ACh can increase excitability in cortical neurons by increasing the signal-to-noise ratio (SNR), the functional roles of MAs and ACh in the cerebral cortex are not homogeneous [17]. For instance, when receptive field of a neuron is stimulated, presence of ACh can further increases evoked firing rates without changing the spontaneous firing rates [17].

1.2 Electrophysiological Recordings During Auditory Stimulation Across Sleep–Wake States

Sleep is associated with sensory disconnection from the external environment. However, there are numerous life experiences that show that loss of behavioral responsiveness during sleep does not indicate loss of sensory

processing. For instance, sleeping parents awaken to the sounds of their baby. Not only the presence but also the absence of a sensory stimulus with subjective significance can awaken a sleeping individual, just as the miller awakens when the mill stops [48]. Nevertheless, there is a general consensus that sleep affects cognitive functions.

Here we will only examine the literature addressing brain responses to auditory stimuli and exclude studies of olfactory and visual stimuli. Because nasal breathing is slower and shallower [49] and eyelids are closed during sleep, olfactory and visual stimuli may be partially intercepted in the periphery, making it difficult to tease out differences in brain responses to sensory stimuli during sleep compared to wakefulness.

In addition, we exclude REM sleep. First, because this study is a computational study in which neural activity is modeled such that it is possible to distinguish between NREM-like dynamics and wakefulness-like dynamics. Distinguishing REM sleep from other states requires other signals, such as electromyography (EMG) and electrooculography (EOG), which are not modeled in this study. Second, motor neurons in the spinal cord are inhibited in REM sleep [39]. Therefore, it remains difficult to attribute the loss of behavioral responses during REM sleep to inhibition of motor neurons in the spinal cord or to attenuated propagation of neural responses among distinct cortical areas.

Brain activity in response to auditory stimuli can be measured using noninvasive methods such as electroencephalography (EEG) and neuroimaging techniques (such as positron emission tomography of the brain and functional magnetic resonance imaging) or by invasive methods such as local field potential (LFP) and single unit (SU) recordings.

In this section, we will first discuss EEG studies suggesting that auditory stimuli reach the cortex, but that neural markers for cognitive functions associated with the stimuli decrease during NREM sleep [48, 50, 51, 52, 53, 54, 55, 56]. Neuroimaging techniques provide high spatial resolution at the expense of temporal resolution, which is advantageous for demonstrating the functional organization of cognitive processes, such as the lan-

guage system in the human brain [57, 58, 59]. However, because brain activation in neuroimaging techniques reflects average activation over time intervals of seconds, it may mask different temporal responses of the brain to auditory stimuli during NREM sleep and wakefulness (for neuroimaging studies during sleep and wakefulness, see [60, 61, 59, 62, 63, 64]).

Next, we will review SU recording studies to clarify the extent to which neural responses to auditory stimuli are modulated during NREM sleep. These studies suggest that auditory-evoked neural responses are attenuated in higher cortical areas, although responses in primary areas are preserved during NREM sleep compared with wakefulness [65, 66, 67, 68]. LFP signals, on the other hand, provide a remarkable method for monitoring neural activity. However, because local and non-local sources contribute to LFP signals via volume conduction [69], it is difficult to determine the local modulation of neural responses at each recording site. In addition, the spatial extent of volume conduction is different in NREM sleep and wakefulness because of the different frequency arrangement, making it difficult to determine changes in neural responses in NREM sleep and wakefulness.

Finally, we present a human study reporting brain responses to transcranial magnetic stimulation (TMS) [70], supporting the view that evoked responses are attenuated along a hierarchical cortical processing chain.

1.2.1 EEG Recordings During Auditory Stimulation

EEG recordings track electrical brain activity from the scalp with a high temporal resolution ($\approx$1 ms)[71]. Although the poor spatial resolution of EEG recordings makes it difficult to assign a topographic origin to neural responses along sensory pathways, the high temporal resolution allows tracking of different brain responses to different stimuli.

EEG studies have shown that loss of behavioral responsiveness is not indicative of loss of sensory processing during NREM sleep. There are numerous studies suggesting that auditory stimuli reach the cortex and subjective significance and semantics are extracted from auditory stimuli

during NREM sleep [48, 50, 51, 52, 53, 54, 55, 56]. Nevertheless, neural markers of cognitive functions associated with auditory stimuli decrease during NREM sleep compared with wakefulness.

Subjective significance is extracted from auditory stimuli during NREM sleep

Early EEG studies in humans have measured brain responses to auditory stimuli during NREM sleep [16] (see Figure 1.5A). The auditory evoked EEG response develops gradually and increases in amplitude and duration from wakefulness to NREM sleep, forming the K-complex during light and deep NREM sleep-state [72, 73, 74]. The auditory evoked K-complex might represents a stimulus-specific neural activation followed by a neural suppression, the Down state. Experimental studies have shown that the evoked K-complex habituates with stimulus repetition and dishabituates with a deviant stimulus [48, 75, 76], similar to auditory evoked responses during wakefulness [77, 78].

In a brilliant 1960 study, Oswald et al. developed a paradigm that exploited the habituation and dishabituation properties of the auditory evoked K-complex to examine the ability of the sleeping brain to capture the significance of auditory stimuli [48]. In the experiment, participants were asked to clench their fists when they heard their own name (auditory stimuli with subjective significance) or a control name (e.g., other names representing auditory stimuli without subjective significance) during sleep. Galvanic skin responses (GSR) and EEG recordings showed significantly stronger occurrence of hand movements and evoked K-complexes, respectively, to own's name than to control names during light NREM sleep (see Figure 1.5B). The stronger evoked K-complex responses to own name than to control names indicate stronger habituation to the control stimuli, suggesting that the cerebral cortex is involved in the genuine discriminative analysis of the subjective significance of auditory stimuli during NREM sleep. Moreover, GSR recordings showed decreased hand movements to

own name in deep NREM sleep, suggesting that discriminative ability can be maintained in deep NREM sleep but associated behavioral markers decrease compared with light NREM sleep.

Semantics are extracted from auditory stimuli during NREM sleep

In addition to extracting subjective significance, there is compelling experimental evidence that semantics of auditory stimuli, the correct meaning of a word in a given context, are extracted during NREM sleep [50, 52, 53, 54]. Studies suggest that extracting semantic in classification tasks can occur up to the preparation of a motor response during NREM sleep [53, 54]. In these studies, awake participants were instructed to classify words as animals or objects based on their semantic category by pressing a button through lateralized hand responses, and they were asked to perform the categorization also during sleep (see Figure 1.6A). As an indicator of responsiveness to extracting semantics, the motor preparation response was examined during wakefulness and NREM sleep. The motor preparation response was calculated as the subtraction of contralateral from ipsilateral EEG activation at central electrodes. It was found that the motor preparation response associated with semantic categorization persisted during NREM sleep but decreased with increasing depth of NREM sleep (see Figure 1.6B,C).

Amplification of neural responses of relevant versus irrelevant auditory stimuli persists during NREM sleep

Recently, amplification of neural responses of relevant versus irrelevant auditory stimuli, i.e., the ability to selectively attend relevant stimuli in a cocktail party paradigm, was shown to persist during NREM sleep [55]. The experimental design in this study consisted of two phases, the training phase and the testing phase. In the training phase, participants were presented with two isolated speech streams (real speech such as a narrative and

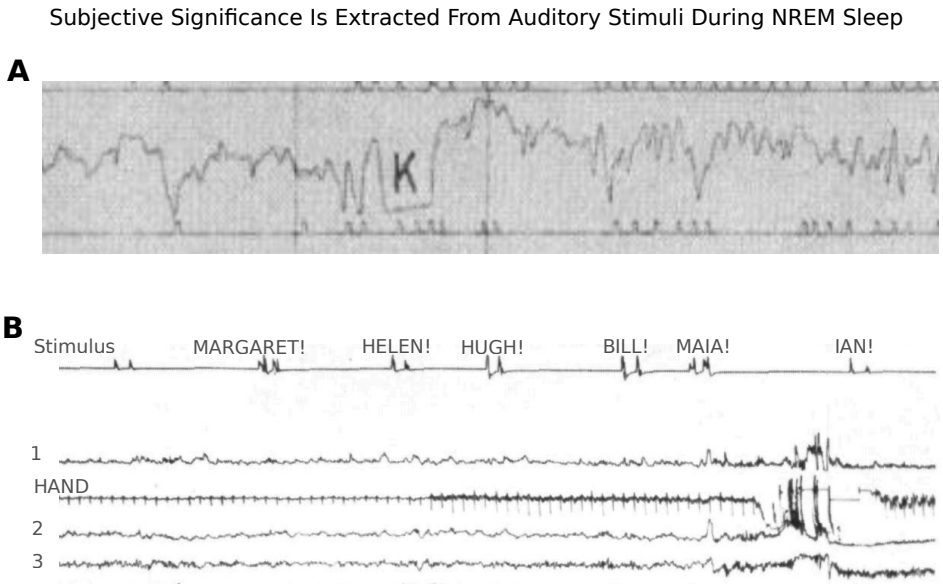

Figure 1.5: Subjective significance is extracted from auditory stimuli during NREM sleep. (**A**). Discovery of K-complex to an auditory stimulus during light NREM sleep. Human EEG recording (bipolar montage) from the left central electrode showing the evoked K complex to an auditory stimulus. a tone, during light NREM sleep. The vertical bars mark the beginning and end of the stimulus. Figure taken from [16]. (**B**). Subjective significance of auditory stimuli is processed during NREM sleep. EEG and GSR signals from a subject named MAIA during light NREM sleep. Note the drastic changes in EEG and GSR signals when her name is played. The first trace represents the timing of the stimuli played. Figure taken from [48].

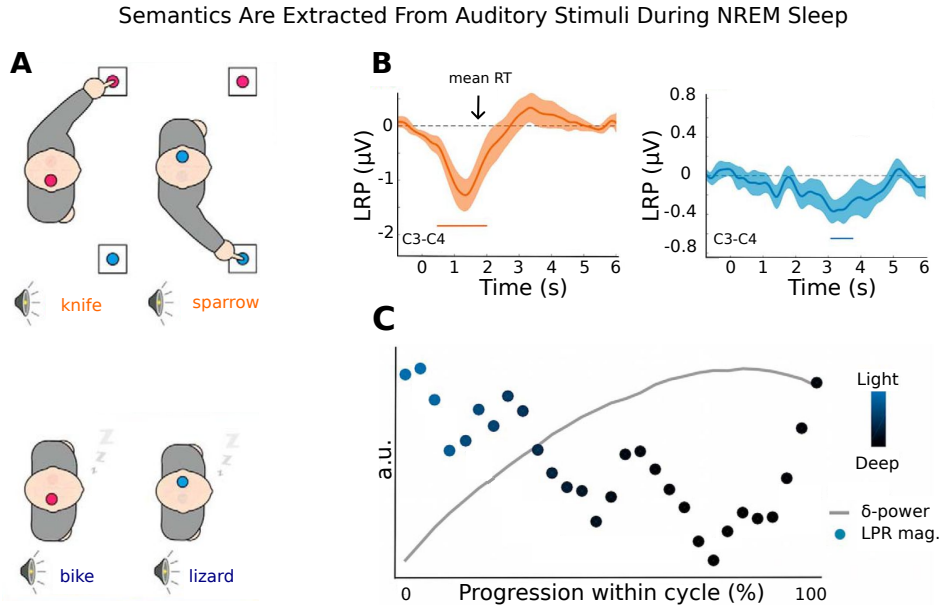

Figure 1.6: Semantics are extracted from auditory stimuli during NREM sleep. Motor preparation response associated with semantic categorization persists during NREM sleep. (**A**). Experimental paradigm. Participants classify words as animals or objects based on their semantic category by pressing a button in wakefulness (*top*) through lateralized hand responses. Participants are reminded to categorize the semantic category as they fall asleep, with new words in NREM sleep unbeknown to them (*bottom*). (**B**). Motor preparation response. The lateralized readiness potential (LRP) represents the motor preparation response and is calculated as the subtraction of contralateral from ipsilateral EEG signal at the central electrodes. It is an index of the motor preparation response associated with semantic categorization. The LRP signals show that auditory stimuli are processed at the semantic level during wakefulness (left) and light NREM sleep (right). Shaded areas represent standard error of the mean (SEM) computed for all participants. Horizontal bars represent significant deviations in LRPs. Note that the arrow bar in the left panel indicates the response time that overlaps with the significant LRP interval. The delayed significant interval in the right panel could then indicate delayed extracting of auditory semantics during NREM (next page)

Figure 1.6 *(previous page)*: sleep compared with wakefulness. (**C**). Modulation of LRP size during NREM sleep. Motor preparation responses associated with semantic categorization persisted during NREM sleep but decreased with increasing depth of NREM sleep. The unit on y-axis represents arbitrary units (a.u.) to better visualize the dynamics of the LRP and delta power with increasing depth of NREM sleep. Figures taken from [54].

nonsense speech such as the Jabberwocky story), and a model was trained to associate the recorded EEG signals to the envelopes of the corresponding speech streams. In the test phase, participants were presented with the two speech streams simultaneously in a cocktail party paradigm (i.e., different speech streams in each ear) and were asked to attend only to one of the streams. The model was then used to reconstruct the envelope of the stream from the EEG signals recorded both during awake and NREM sleep. The Pearson correlation coefficient between the reconstructed envelope and the original envelope of the stream (either real or nonsense speech) was used to determine which speech stream had the predominant neural representation in the EEG signals (see Figure 1.7A). In the awake condition, the Pearson correlation was higher for the relevant speech stream, indicating an amplification of the neural representation of the relevant speech stream compared with the irrelevant speech stream. The amplification of the relevant speech stream compared with the irrelevant speech stream persisted during NREM sleep but decreased with increasing depth of NREM sleep (see Figure 1.7B).

Cognitive functions depend on the interaction of multiple functionally specialized groups of cortical neurons. Therefore, although cognitive functions associated with auditory stimuli decrease during NREM sleep, it remains unclear at which sites along the sensory pathways evoked neural responses to auditory stimuli are modulated across the sleep–wake cycle.

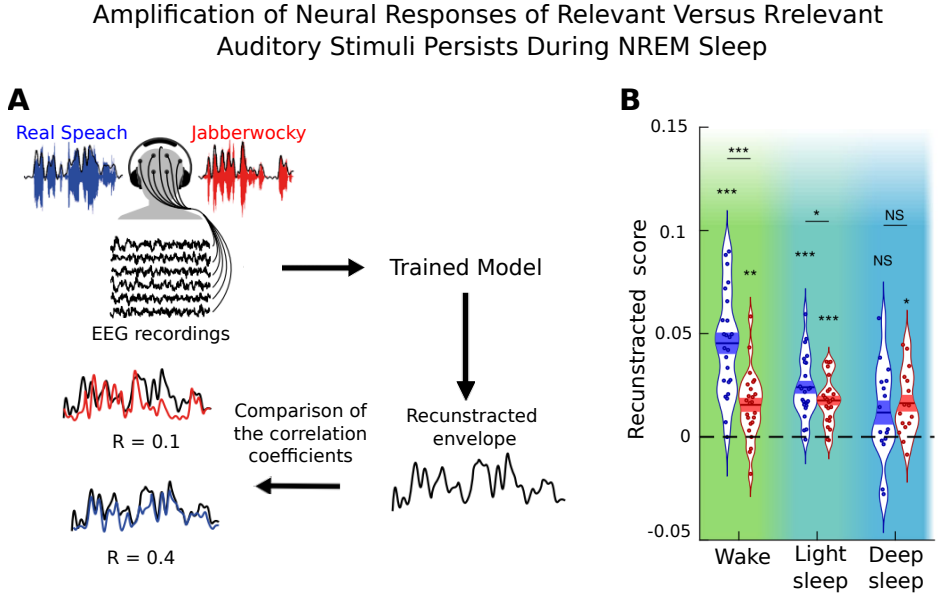

Figure 1.7: Amplification of neural responses of relevant versus irrelevant auditory stimuli persists during NREM sleep. (**A**). Experimental paradigm. In the test phase, participants were simultaneously exposed to two speech streams in a cocktail party paradigm (i.e., different speech streams in each ear) and were asked to attend the relevant speech stream (here, real speech). The EEG signals were used to reconstruct the envelope of the speech stream using a model obtained in the training phase. The Pearson correlation coefficient, R, between the reconstructed envelope and the original envelope of the speech stream was used to determine which speech stream had the predominant neural representation in the EEG signals. (**B**). Reconstruction scores for the real and nonsense stories in wakefulness, light sleep, and deep sleep. Note that these results correspond to the scenarios in which participants were asked to attend the real speech. The results were confirmed when participants were asked to attend the nonsense speech. Figures taken from [55].

1.2.2 Single-Unit Studies

Invasive recording techniques enable measurements from specific brain areas. Single-unit (SU) extracellular recordings monitor action potentials in neurons in target areas. Although this technique cannot record simultaneously from the entire brain, SU recordings allow assessment of neural responses to external stimuli in specific sensory areas.

SU recordings in nonhuman animals and humans have shown that evoked neural responses to auditory stimuli are heterogeneously modulated along the hierarchical cortical processing chain. These studies show that evoked neural responses are preserved in primary auditory cortex (A1), whereas they are attenuated in higher cortical areas during NREM sleep compared with wakefulness.

Neural firing responses are preserved in primary auditory cortex during NREM sleep

Microelectrode recordings in sleeping marmoset monkeys have shown that neural firing responses to auditory stimuli (e.g., tones, clicks, and vocalizations) in primary auditory cortex (A1) are not systematically attenuated during NREM sleep compared with wakefulness [65]. Although neural firing responses either increased or decreased in response to individual auditory stimuli, they were not significantly attenuated on average during deep NREM sleep compared with wakefulness. Moreover, the peristimulus time histogram (PSTH) of evoked responses during NREM sleep correlated highly with those during wakefulness, indicating a highly preserved temporal code of evoked responses during deep NREM sleep. Furthermore, neural tuning curves, i.e., neural firing responses as a function of stimuli, during NREM sleep were strongly correlated with those during wakefulness, indicating preserved neural sensitivity to auditory stimuli. These observations suggest that evoked neural responses to auditory stimuli in A1 of marmoset monkeys are preserved during deep NREM sleep

compared to wakefulness.

Single- and multi-unit studies in rodents have also confirmed the observations that evoked neural responses in A1 to auditory stimuli are preserved during NREM sleep compared to wakefulness [66, 67]. Microwire array recordings from the auditory cortex in rats have shown that neural firing responses to auditory stimuli (e.g., tones, clicks, and rat vocalizations) during NREM sleep are comparable to those during wakefulness [66] (see Figure 1.8A). Moreover, quantitative analysis of evoked responses revealed that neural response profiles (i.e., the selectivity of a neuron to trigger an onset, sustained, or offset response to stimuli) were preserved during NREM sleep (see Figure 1.8B). Neural firing responses for each response profile were also not significantly attenuated during deep NREM sleep compared to wakefulness (see Figure 1.8B,C). These observations suggest that evoked neural responses in A1 of rats to auditory stimuli are preserved across the sleep–wake cycle.

The above observations were recently replicated in humans. In an unprecedented study, evoked neural responses to a wide range of auditory stimuli (including clicks, tones, music, words, and sentences) were recorded in a passive paradigm in cortical areas—comprising the superior temporal gyrus, superior temporal plane, middle temporal gyrus, and orbitofrontal cortex—from epilepsy patients who had depth electrodes implanted for clinical monitoring [68]. The magnitudes of neural firing responses recorded in A1 (within the superior temporal gyrus) were not significantly attenuated during NREM sleep compared to wakefulness (see Figure 1.9). In addition to the magnitudes, the mutual information between the auditory stimuli and the spike responses in A1 was also preserved during NREM sleep compared to wakefulness. These observations suggest that auditory evoked responses in A1 are preserved in humans during NREM sleep and are as informative as in the awake state.

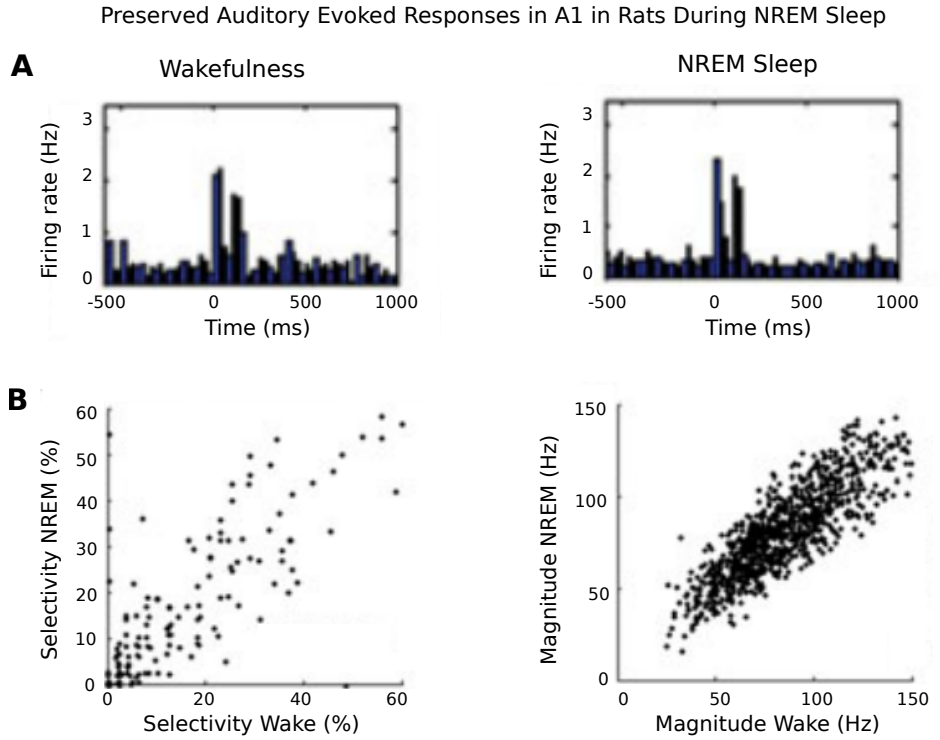

Figure 1.8: Preserved auditory evoked responses in A1 in rats during NREM sleep. (**A**). Peristimulus time histogram (PSTH) of a representative auditory response (with respect to baseline firing during wakefulness) to a 6 kHz tone with a duration of 100 ms in an A1 neuron during wakefulness (left) and NREM sleep (right). Note that this neuron triggers onset and offset responses, barely visually distinguishable visually between vigilant states. (**B**). *Left*. Scatter plot of response selectivity profile (for onset response profile) in NREM sleep (y-axis) compared with wakefulness (x-axis). The response selectivity profile of A1 neurons is comparable between NREM sleep and wakefulness. Each dot indicates the percentage of stimuli that triggered an increased onset response for each A1 neuron. Note that the firing rate selectivity profiles are preserved during NREM sleep compared with wakefulness. *Right*. Scatter plot of the response magnitudes for neurons showing onset profile during NREM sleep (y-axis) compared with (next page)

Figure 1.8 *(previous page)*: wakefulness (x-axis). The response magnitude of A1 neurons is comparable between NREM sleep and wakefulness. Each dot denotes the magnitude of the response of an A1 neuron to a particular stimulus that triggered onset response. Note that the neural selectivity are preserved during NREM sleep. These results are confirmed for the sustained and offset response types. Figures taken from [66].

Neural firing responses are heterogeneously modulated in areas downstream to the primary auditory cortex during NREM sleep

Despite the experimental evidence reviewed above, showing that neural firing responses to auditory stimuli are preserved in A1 in nonhuman animals and humans across vigilance states, heterogeneous modulation of neural firing responses emerges in cortical areas downstream to A1.

In marmoset monkeys, regions within the microelectrode recordings in the lateral belt, the secondary auditory cortex downstream to A1, have shown that neural firing responses to auditory stimuli are not significantly decreased during deep NREM sleep [65]. However, simultaneous recordings in rats from A1 and the perirhinal cortex (PRC), a higher-order cortical area also downstream to A1, have shown that neural firing responses to auditory stimuli (e.g., tones, clicks, and rat vocalizations) in the PRC decrease during NREM sleep compared with wakefulness, whereas neural firing responses in A1 are preserved (see Figure 1.10).

Studies in humans have also shown that not only the magnitude of neural firing responses but also the mutual information between auditory stimuli and spike responses decreased in areas outside A1, although they were preserved in A1 during NREM sleep compared to wakefulness (see Figure 1.11A) [68]. Moreover, the extent of attenuation increased with increasing depth of NREM sleep. Of note, neural firing responses in different cortical areas were attenuated in a heterogeneous manner during NREM sleep (see Figure 1.11C).B

It is important to note that there is compelling experimental evidence

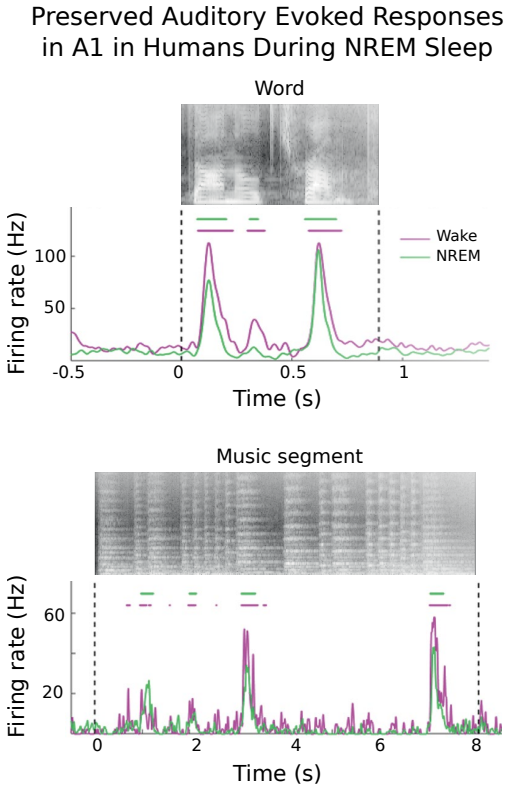

Figure 1.9: Preserved auditory evoked responses in A1 in humans during NREM sleep. Peristimulus time histogram (PSTH) of representative auditory responses in a neuron in A1 in response to a word (*top*) and a music segment (*bottom*) in a human subject during NREM sleep (in green) and wakefulness (in pink). Horizontal bars above PSTH time-courses indicate significant response intervals compared to peristimulus intervals. The grayscale soundwave spectrograms are shown above the PSTH. Vertical dotted black lines represent the stimulus onset and offset. Note that neural firing responses during NREM sleep mimic those during wakefulness in amplitude and temporal variation. Figure taken from [68].

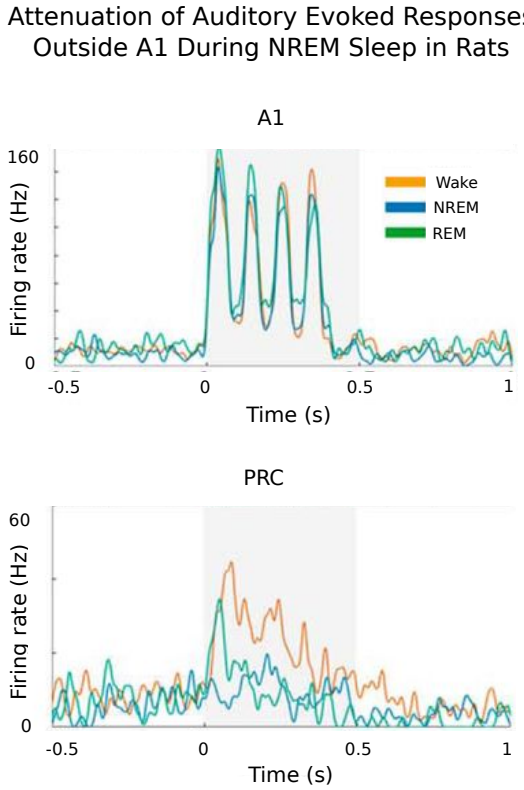

Figure 1.10: Attenuation of auditory evoked responses outside A1 during NREM sleep in rats. (**A**). Peristimulus time histogram (PSTH) of a representative auditory response in an A1 neuron (upper panel) and a PRC neuron (lower panel) recorded simultaneously in a rat during NREM sleep (in blue) and wakefulness (in orange). Neural firing responses are attenuated in the PRC, a higher-order cortical region downstream to A1, although neural firing responses are preserved in A1 during NREM sleep compared with wakefulness. Stimulus duration is marked by the gray shaded area. Figure taken from [67].

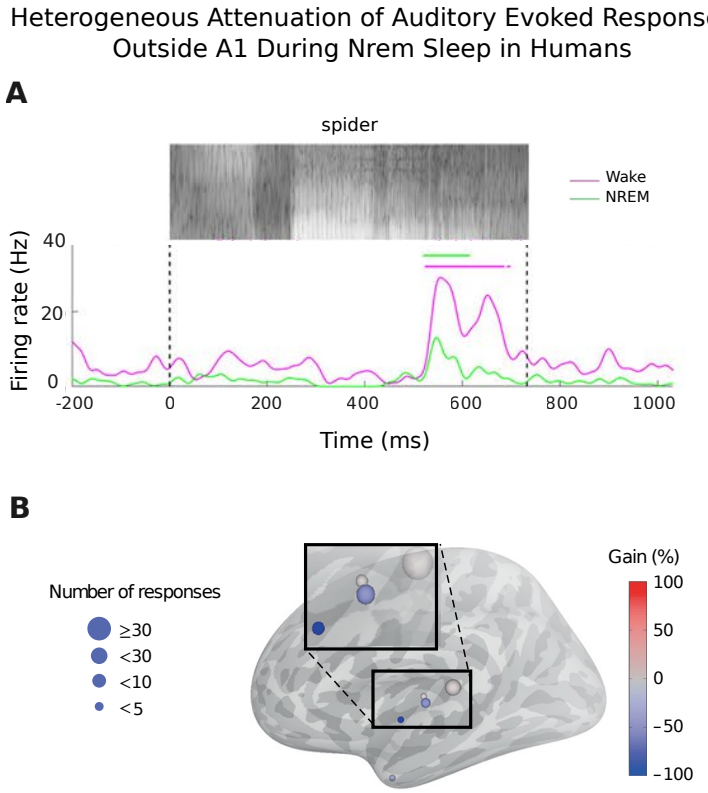

Figure 1.11: Heterogeneous attenuation of auditory evoked responses outside A1 during NREM sleep in humans. (**A**). PSTH of a representative auditory response in a neuron outside A1 in response to the word *spider* in a human subject during NREM sleep (in green) and wakefulness (in pink). Horizontal bars above PSTH time-courses indicate significant response intervals compared with spontaneous activity in prestimulus intervals. Stimulus duration is marked by the vertical dotted black lines. The grayscale soundwave spectrograms is shown above the PSTH. (**B**). Relative change in magnitude of neural firing responses (NREM versus wakefulness) in each region that showed auditory responses. Each circle shows the anatomical location of the recording region on a standard left hemisphere template. The size of the circle (left) shows the number of responses detected in that region. The color of the circle (right) shows the value of the neural (next page)

Figure 1.11 *(previous page)*: gain in this region. Neural gain is defined as the average of the relative change (NREM compared to awake) of the magnitude of evoked responses in each region. Note the heterogeneous modulation of auditory evoked responses during NREM sleep in regions outside A1, despite the preserved responses in A1. Note the heterogeneous modulation of auditory evoked responses outside A1 during NREM sleep. Figures in panels B and C taken from [68].

that attention to external stimuli [79] and higher sensory processing demands during wakefulness [80] increase brain activation to external stimuli. Therefore, it remains unclear whether or not the reduced evoked neural responses to auditory stimuli in cortical areas downstream to A1 during NREM sleep merely reflect lack of attention.

1.2.3 TMS Stimulation: A Non-sensory Approach to Response Propagation

Transcranial magnetic stimulation (TMS) is a noninvasive stimulation technique that eliminates the confounding effects of attention to external stimuli on evoked responses in the brain. The experimental setup consists of a procedure that eliminates sensory perception of stimuli during wakefulness and NREM sleep [81]. The TMS clicks associated with the coil discharge are masked by a noise that corresponds to the waveform of the noise generated by the coil.

Spatiotemporal extent of cortical activation to TMS stimulation decreases during NREM sleep compared to wakefulness

In a brilliant human study, brain responses to TMS perturbation of a selected cortical area (e.g., either right premotor or parietal cortex) were recorded with high-density electroencephalography (HD-EEG) during wake-

fulness and NREM sleep [70]. Cortical activation in response to TMS pulses was measured by current source density (CSD) analysis. CSD analysis by estimated the cortical current sources that generate the evoked EEG potentials. As expected, initial cortical activation was centered below the stimulation site in both wakefulness and NREM sleep. However, the perturbation propagated in the cerebral cortex in two different ways depending on the brain state. Perturbation propagated from the stimulated area along its anatomical connections in contralateral and ipsilateral areas during wakefulness (see Figure 1.12). On the contrary, the perturbation remained local, propagated only to areas in the vicinity of the stimulation site and dissipated rapidly during NREM sleep (see Figure 1.12). These results were reproduced when different cortical areas were stimulated [70, 81, 2].

These observations suggest that the spatiotemporal extent to which the cortex is activated in response to TMS stimuli is lower during NREM sleep than during wakefulness. These observations refute the possibility that the attenuated evoked neural responses to auditory stimuli during NREM sleep are a consequence of the lack of attention to the external stimuli.

1.2.4 Summary

Changes in the level of neuromodulators not only shift the dynamics and neurotransmission, but also might affect behavior. Behaviorally, sleep is associated with sensory disconnection from the external environment. In contrast to the extreme view of sensory disconnection from the external environment, there is compelling experimental evidence that some level of sensory processing persists during NREM sleep [48, 50, 51, 52, 53, 54, 55, 56]. This is so, even if, neural markers of cognitive functions associated with auditory stimuli, such as motor preparatory signals [53, 54] and the amplification of relevant signals [55], are attenuated during NREM sleep compared with wakefulness [48, 53, 54, 55, 56]. Given that cognitive functions depend on the interaction of multiple functionally specialized groups of cortical neurons, it is important to determine where auditory stimuli are

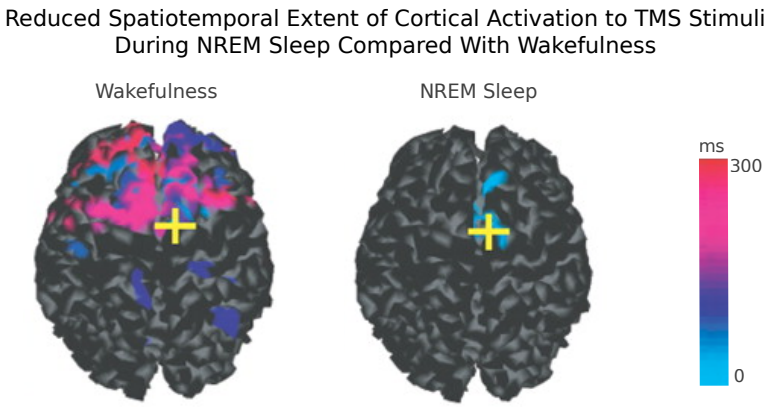

Figure 1.12: Reduced spatiotemporal extent of cortical activation to TMS stimuli during NREM sleep compared with wakefulness. Cortical activation, color-coded by the latency of region activation, to TMS stimuli during wakefulness (left) and NREM sleep (right) in one subject. The yellow cross marks the TMS target on the cortical surface. Note that in wakefulness, the perturbation propagates to a larger spatial area, whereas in NREM sleep it is confined to the stimulated area. Figure taken from [70].

modulated along the sensory pathway that differs between NREM sleep and wakefulness.

Consistent with EEG studies, extracellular SU responses in A1 recorded during a rich ensemble of auditory stimulation are preserved during NREM sleep, as compared to wakefulness, in nonhuman animals and humans [65, 66, 67, 68]. However, responses in higher cortical areas downstream to A1 are heterogeneously attenuated [65, 66, 67, 68]. Accordingly, studies show that cortical activation to TMS stimuli, which abolishes subjects' perception of the stimuli during wakefulness, remains local during NREM sleep compared with the broader spatiotemporal extent of propagation during wakefulness [70, 81]. This suggests that attenuated evoked neural responses in higher cortical areas to auditory stimuli during NREM sleep are not simply a consequence of lack of attention to the external stimuli.

1.3 Mechanisms Underling Different Propagation Patterns of Neural Firing Responses Across the Sleep–Wake States

The underlying mechanisms leading to different propagation patterns of neural firing responses in the cerebral cortex during NREM sleep and wakefulness remain largely unknown.

In a communication system, the mechanisms by which propagation of responses among system elements attenuates can be divided into two broad classes: the transducers (communication nodes) change to a less excitable state and/or the strength of the physical transmission medium (communication channels) weakens. The brain is composed of neural groups and synaptic pathways that resemble a communication system. Similarly, the attenuated propagation of neural firing responses during NREM sleep compared with wakefulness can be attributed to the altered dynamics of the neural groups and/or the strength of the synaptic pathways involved in

propagation patterns.

The current scientific consensus is that the different propagation patterns of neural firing responses in the cerebral cortex during NREM sleep and wakefulness are due to the altered dynamics of the thalamocortical network. However, as far as we know, there is not a clear evidence to support this view and changes in the cortico-cortical synaptic strength has not yet been studies. In the first part of this section we provide an overview of a thalamocortical model that describes the neural groups and synaptic pathways involved in propagation of neural firing responses in the cerebral cortex. In the following two parts, we review experimental evidence, first, supporting changes in the dynamics of the thalamocortical network as a mechanism for attenuating propagation of neural firing responses in the cerebral cortex, and second, challenging these mechanisms as a sufficient explanation. Finally, the missing piece of the puzzle, namely the role of cortico-cortical synapses is presented.

1.3.1 Model of Propagation of Neural Firing Responses in Cortical Hierarchy

The cortex and the thalamus innervate each other through massive direct excitatory projections involving cortico-thalamic (CT) and thalamocortical (TC) pathways forming the cortico-thalamo-cortical (CTC) network [82]. The CTC pathways, in addition to the cortico-cortical (CC) pathways, may serve to transmit neural firing responses between cortical areas. The first experimental evidence for CTC pathways was obtained in mouse brain slices. It was shown that a substantial proportion of evoked responses in the secondary somatosensory cortex depended on thalamic circuits when layer 5 of the primary somatosensory cortex was electrically stimulated [83].

A CTC model that proposes a hierarchical organization in the cortex for propagation of neural firing responses was developed by Sherman and

Guillery [23, 84] (see Figure 1.13). In the following, this model is briefly presented.

Motifs of the CTC model

Thalamic and cortical neurons are at the heart of the CTC model. CTC model describes that neural firing responses to an external event propagate in a hierarchical organization in the cortex along the two parallel pathways: CTC and CC pathways. Via glutamatergic pathways, thalamic neurons and cortical neurons receive two distinct classes of inputs: driver and modulatory [23, 84, 85]. Driver inputs relay neural firing responses about an external event to target neurons. Modulatory inputs modulate the response of target neurons to driver inputs [84, 85].

Thalamic neurons include relay neurons, local inhibitory interneurons, and the thalamic reticular nucleus (TRN) [17, 19, 23]. Based on the source of driver inputs, thalamic relay neurons are divided into two classes, namely first-order (FO) relay neurons and higher-order (HO) relay neurons [23, 85]. First-order relay neurons receive driver inputs mainly from the periphery and subcortical areas, whereas driver inputs to higher-order relay neurons come from layer 5 of different cortical areas (and in some cases also from subcortical areas) [84, 85] (see Figure 1.13). First-order thalamic relay neurons project the driver inputs predominantly to layer 4 of primary cortical areas. Higher-order thalamic relay neurons project primarily to cortical layer 4 of higher cortical areas (and in some cases to primary cortical areas too) [84, 85].

Modulatory inputs to first- and higher-order relay neurons are generally similarly arranged [23]. Modulatory inputs are dominant with respect to driver inputs in thalamic relay neurons and are proposed as a mechanism that controls propagation of neural firing responses through thalamic pathways without altering the properties of the receptive field [23]. Modulatory inputs consist of inputs from local GABAergic areas (including local GABAergic interneurons and TRN neurons), cortical feedback

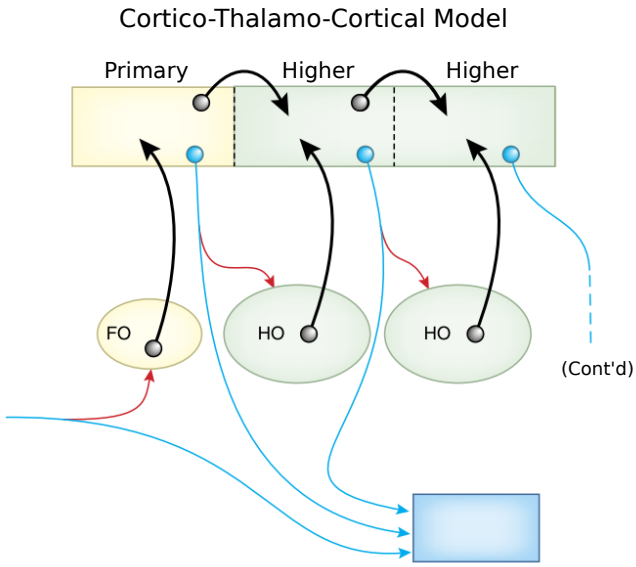

Figure 1.13: Cortico-Thalamo-Cortical model. Lower motor centers receive neural firing responses from periphery and cortical areas (blue arrows), where a copy of neural firing responses is sent directly to the thalamic relay neurons (red arrows). First-order thalamic neurons (FO) transmit a copy of neural firing responses from the periphery sent directly to lower motor centers to primary cortical areas (black arrow). Neural firing responses in the cortex propagate through two pathways, CC and CTC. The higher order thalamic neurons (HO) transmit neural firing responses via the CTC pathways. They transmit a copy of the cortical neural firing responses sent directly to the lower motor centers to the higher cortical areas. Here, the motor messages originate from layer 5 of the cortical areas in the cortical hierarchy. Figure taken from [84].

inputs from layer 6, and neuromodulatory inputs from subcortical structures, such as cholinergic, noradrenergic, serotonergic, and histaminergic inputs [17, 19, 23].

1.3.2 Dynamics of the Thalamus Are Insufficient

The thalamus is an important node in the brain that relays neural signals to the cortex by innervating almost all cortical areas via TC pathways [82]. A change in the dynamics of thalamic neurons due to decreased neuromodulatory inputs during NREM sleep could be a mechanism that attenuates propagation of neural firing responses between cortical areas.

Thalamic neurons can control propagation of neural firing responses via three types of dynamics. There is no experimental evidence for the effectiveness of the three thalamic mechanisms in attenuating propagation of neural firing responses between cortical areas via higher-order thalamic relay neurons. Moreover, the ineffectiveness of these mechanisms in attenuating propagation neural firing responses from the periphery to the cortex via first-order thalamic relay neurons may challenge the view that thalamic dynamics during NREM sleep is a sufficient explanation.

Proposed mechanisms for thalamic dynamics during NREM sleep attenuating propagation of neural firing responses

One mechanism that could attenuate propagation of neural firing responses in the cortex is the burst firing mode of thalamic relay neurons during NREM sleep. Neuromodulatory projection from the ascending arousal network in subcortical areas is silent during NREM sleep. Reduced neuromodulatory inputs hyperpolarize thalamic relay neurons and shifts the firing profile from tonic firings in wakefulness to burst firings in NREM sleep [17, 19, 23]. Although burst firings from thalamic relay cells in response to external stimuli generate a high excitatory postsynaptic potential in cortical neurons that could facilitate detection of neural firing responses,

this may affect the accuracy of spike timing and thus reduce the precision of neural firing responses transmitted to cortical neurons.

Inhibition of thalamic relay neurons by the enhanced activity of local GABAergic interneurons during NREM sleep could also lead to less excitable dynamics and attenuate propagation of neural firing responses [86]. The absence of neuromodulators during NREM sleep disinhibit local GABAergic interneurons that results in inhibiting thalamic relay neurons [17, 23, 86]. This mechanims can attenuate response of thalamic relay neurons to incoming driver inputs (for a more detailed description, see [86]). Attenuated neural firing responses in thalamic relay neurons diminish propagation of neural firing responses to cortical neurons.

Another mechanism by which the thalamus might attenuate propagation of neural firing responses to the cortex is spindle-mediated inhibition of cortical neurons, which converts cortical dynamics to less excitable dynamics [24]. This mechanism is known as the thalamic gating hypothesis. The long-held thalamic gating hypothesis states that sleep spindles interrupt the transmission of sensory signals to the cerebral cortex [19]. This view has been supported by several experimental observations. For instance, human studies found a correlation between the rate of occurrence of spindles and the arousal threshold; the higher the rate of occurrence of spindles, the higher the arousal threshold [87]. Spindles may represent a mechanism that inhibits cortical neurons. As a result of the interaction between TRN and thalamic relay neurons during spindle activity, thalamic relay neurons fire bursts during NREM sleep. These burst firings are monosynaptically projected to cortical areas and could shift the balance between excitation and inhibition in cortical pyramidal neurons toward inhibition by activating local cortical inhibitory neurons during NREM sleep. (For a more detailed description of spindle activity, see [24]).

Dynamics of the thalamus during NREM sleep do not fully account for attenuated propagation of neural firing responses in the cortex

The thalamus controls the flow of neural signals not only from the periphery to the cortex but also between cortical areas [23, 84]. However, there is compelling evidence that limits the proposed thalamic mechanisms in previous part as a mechanistic account for attenuated propagation of neural firing responses. To our knowledge, the effectiveness of thalamic dynamics in attenuating propagation of neural firing responses via higher-order thalamic relay neurons during NREM sleep has not been studied. However, there is convincing experimental evidence that thalamic dynamics does not attenuate propagation of neural firing responses via first-order thalamic relay neurons during NREM sleep. For instance, neural firing responses in A1 to auditory stimuli, which is downstream to first-order thalamic relay neurons, is preserved during NREM sleep compared to wakefulness (see Section 1.2.2), challenging the view that thalamic dynamics are sufficient to attenuate propagation of neural firing responses.

The effectiveness of spindle-mediated inhibition in attenuating propagation of neural firing responses to the primary auditory cortex was systematically studied in rats during NREM sleep. Microwire array recordings from rat primary auditory cortex showed that neural firing responses to auditory stimuli (e.g., tones, clicks, and rat vocalizations) were comparable in periods with and without spindle activity during NREM sleep [88] (see Figure 1.14A). Moreover, quantitative analysis of evoked responses revealed that neural response profiles (i.e., the selectivity of a neuron to trigger an onset, sustained, or offset response to stimuli) were preserved and neural firing responses were not significantly attenuated in periods with and without spindle activity during NREM sleep for each response profile (see Figure 1.14B).

Nevertheless, the observed correlation between the occurrence of spindles and arousal threshold in humans [87] may favor the view that spindle activity generated by higher-order thalamic relays in higher cortical areas

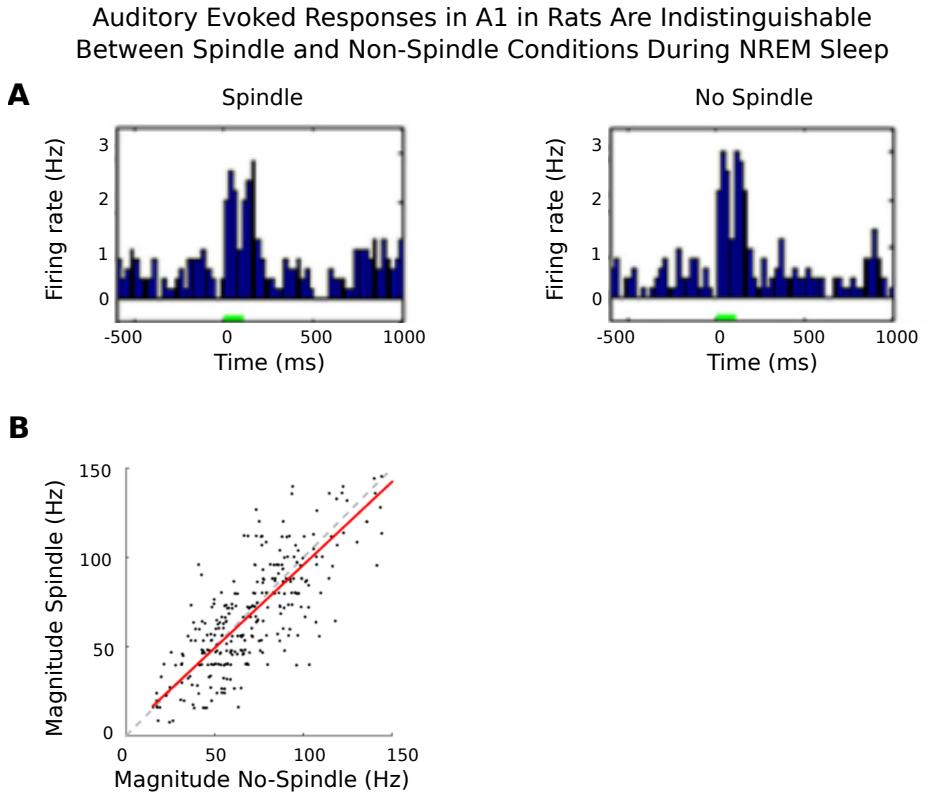

Figure 1.14: Auditory evoked responses in A1 in rats are indistinguishable between spindle and non-spindle conditions during NREM sleep. (**A**). Peristimulus time histogram (PSTH) with respect to baseline of a representative auditory response in an A1 neuron during spindle (left) and no-spindle activity (right) to an 8-kHz tone with a duration of 100 ms. Note that this neuron elicits both onset and offset responses, with both types of responses barely distinguishable visually between spindle and no-spindle activity in NREM sleep. (**B**). Scatter plot of the representative response size profile in spindle (y-axis) versus no-spindle (x-axis). The response size profile of A1 neurons is comparable between spindle and no-spindle conditions. Each dot denotes the size of an A1 neuron's response to a particular stimulus that triggered onset response. Note that the firing rate size profiles are preserved during spindle and no-spindle activity in NREM (next page)

Figure 1.14 *(previous page)*: sleep. These results are confirmed for the sustained and offset response types. Figures taken from [88].

impairs propagation of neural firing responses, in contrast to first-order relays. However, the higher arousal threshold after sleep deprivation, when spindle density is reduced (for review [24]), calls into question spindles as a sufficient mechanism for gating propagation of neural firing responses in general. It is also important to note that deep NREM sleep is associated with lower spindle density than light NREM sleep during the course of natural sleep [18, 89], whereas gating propagation of neural firing responses may correlate with sleep depth [53, 54, 55, 68]. Therefore, it seems unlikely that spindle-mediated gating by higher-order thalamic relays could be a satisfactory explanation for attenuated propagation of neural firing responses in the cerebral cortex during NREM sleep.

The other line of evidence that thalamic dynamics are insufficient comes from studies using *in vitro* cortical slices. Electrical stimulation of ferret cortical slices in the absence of the thalamus has shown that perturbations propagate in two different ways under NREM-like and wakefulness-like conditions [90].

1.3.3 Dynamics of the Cortex Are Insufficient

The high correlation between the occurrence of slow waves and attenuation of propagation of stimulus-specific neural activity during NREM sleep raises the exciting possibility that cortical dynamics during NREM sleep may explain the propagation differences between NREM sleep and wakefulness.

Decreased neuromodulatory input from subcortical areas alters the dynamics of cortical neurons. Cortical neurons tend to fall into the Down-state (an inactive state) following periods of intense firing (Up state), which is known as cortical bistability during NREM sleep. Because cortical neu-

rons are hyperpolarized during the Down-states, cortical bistability could represent a low excitable regime responsible for the attenuation of propagation of stimulus-specific neural activity during NREM sleep.

There are two types of Down-states: spontaneous and evoked. When Up state are due to nonspecific spontaneous neural firing, the following inactive states are referred to as spontaneous Down states. Down states following stimulus-specific activation are referred to as evoked Down states. Because the literature discussed below is based on extracellular rather than intracellular recordings, the terms ON and OFF periods will be used instead of Up and Down state to ensure consistent terminology [32]. Although experimental observations seem to support the view that cortical dynamics during NREM sleep attenuate propagation of stimulus-specific neural activity in the cerebral cortex, there are several considerations that suggest that cortical dynamics may be an insufficient explanation.

Spontaneous OFF periods do not fully account for attenuated propagation of neural firing responses during NREM sleep

Extracellular recordings during NREM sleep show an alternation between between OFF and ON periods that form slow waves. Because slow waves during sleep are local events [91, 30], the spontaneous OFF and ON periods during slow waves often occur out of phase in different cortical areas. This could be a mechanism that attenuates propagation of neural firing responses from a cortical region in the ON period to a cortical region in the OFF period.

Nevertheless, preserved evoked neural responses in A1 during NREM sleep and wakefulness [65, 66, 67, 68] challenges this view at least in primary areas. Moreover, microwire array recordings of A1 in rats showed that neural firing responses to tones were not systematically attenuated during OFF periods compared with ON periods during NREM sleep [88] (see Figure 1.15). Only at low intensity tones, neural firing responses during OFF periods were smaller than those during ON periods. Surprisingly,

neural firing responses during OFF periods were larger than those during ON periods to high intensity tones, with no significant difference for the middle intensity tones.

In addition, microwire array recordings suggest a complex effect of OFF periods rather than a systematic attenuation of propagation of neural firing responses between cortical areas. [67]. For instance, neurons with a late response latency profile in A1 and PRC show stronger evoked neural responses to tones in OFF periods than ON periods, whereas neurons with an early response latency profile in A1 and PRC show stronger evoked neural responses to tones in ON periods than OFF periods.

Moreover, experimental studies show that neural firing responses during NREM sleep are heterogeneously modulated in areas downstream to A1 [65, 67, 68] (see Section 1.2.2). For instance, evoked responses in perirhinal cortex (PRC) are significantly attenuated [67], whereas responses in secondary auditory cortex (A2) are preserved [65]. Therefore, it remains unclear why spontaneous OFF periods in A2 do not attenuate propagation of neural firing responses during NREM sleep, unlike their counterparts in the PRC.

Evoked OFF periods do not fully account for attenuated propagation of neural firing responses during NREM sleep

Because of cortical bistability during NREM sleep, cortical neurons can enter OFF periods following a stimulus-specific activation, which are therefore referred to as evoked OFF periods. The evoked OFF periods may limit the time window for propagation of neural firing responses by cortical areas. For instance, an evoked OFF period in a cortical area enforces a time window of neural silence that represents a less excitable neural state and thus attenuates the cortical response to stimulus-specific neural firing responses sent back from other areas, which is known as stimulus-specific cortical interactions.

This mechanism was suggested by the observation that time-locked

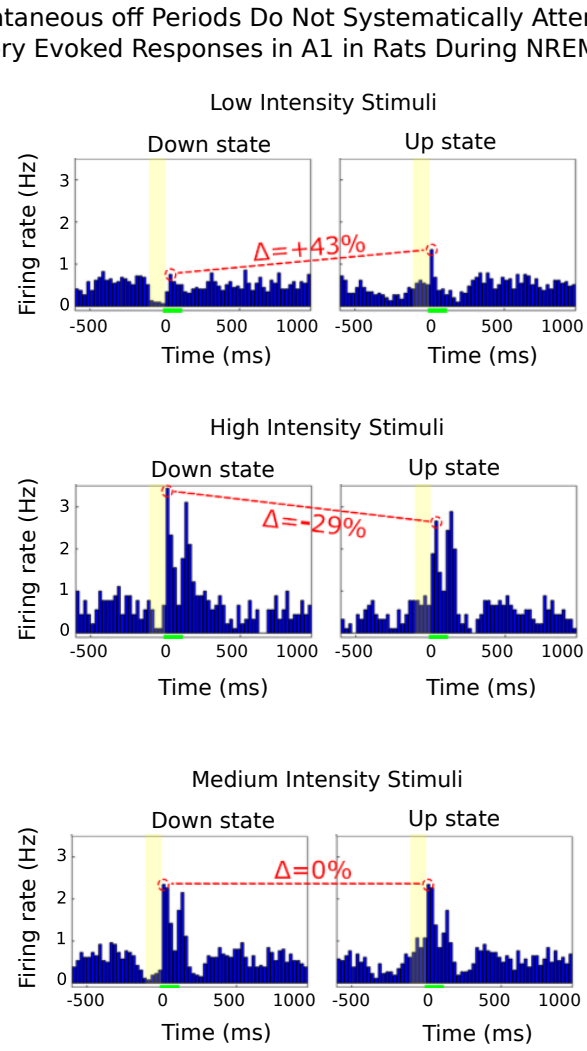

Figure 1.15: Spontaneous OFF periods do not systematically attenuate auditory evoked responses in A1 in rats during NREM sleep. Peristimulus time histogram (PSTH) with respect to baseline of a representative auditory response in an A1 neuron in Down state (left) and Up state (right) to low (30 dB), medium (55 dB), and high intensity (80 dB) tones, from top to bottom. Tones had a (next page)

Figure 1.15 *(previous page)*: duration of 100 ms and are shown as thick horizontal green bars. Note that the pre-stimulus baseline (yellow shadow) is higher for ON than for OFF periods. Δ represents the relative change in amplitude of neural firing response in Up state compare to ones in Down state. Figures taken from [88].

EEG responses to TMS stimuli during NREM sleep resemble spontaneous slow waves [81]. EEG responses to TMS stimuli in humans have been shown to switch from evoked slow waves occurring in a limited area under the stimulating site to different activation patterns characterized by low-amplitude–high-frequency components during wakefulness [70, 81]. The anthers even go beyond and claim that these findings suggest that the intrinsic tendency of cortical neurons during NREM sleep to fall into the OFF period following stimulus-specific activation may constrain long-range patterns of causal interaction between cortical areas [2].

Following this view, local field potentials (LFP) from single-pulse intracortical electrical stimulation (SPES) were analyzed in epileptic patients implanted with depth electrodes for clinical assessment [3]. Because the recording technique was not ideal for identifying spike activity, suppression of high-frequency power (20-100 Hz) was used as a proxy for the occurrence of OFF periods [92, 22]. In addition, stimulus-specific cortical interactions across recording sites were quantified by the phase-locking factor (PLF) in frequency ranges of 8-100 Hz at each recording site (PLF assesses the consistency of the phase of ongoing cortical oscillations across trials). Evoked LFP responses were found to be characterized at the network level by a larger evoked slow wave, a larger evoked OFF period, and short-lasting phase-locked activity during NREM sleep than during wakefulness (see Figure 1.16A,B). In addition, larger evoked slow waves correlated with larger evoked OFF periods, and the timing of evoked OFF periods correlated with the timing of attenuation of PLF (see Figure 1.16C). The authors claim that these observed correlations may support the view

that evoked OFF periods during NREM sleep attenuate propagation of neural firing responses in the cortex during NREM sleep.

However, there are several considerations that might limit the interpretation of these results. First, the above conclusions were based on a correlation analysis, i.e., the timing of the high-frequency power suppression in slow waves correlated with the timing of the decline of PLF [3]. Correlation does not imply a causality and may still reflect a hidden underlying mechanism. For instance, evoked OFF periods are absent during REM sleep, however, the spatiotemporal extent of propagation of TMS perturbation is smaller than wakefulness and larger than NREM sleep [93]. On the other hand, evoked OFF periods are present during ketamine-induced unresponsiveness state [94], whereas the spatiotemporal extent of propagation of TMS perturbation is smaller than wakefulness and larger than NREM sleep [95].

Second, PLF lasted longer in electrodes near the stimulation site during wakefulness than during NREM sleep, despite comparable evoked OFF periods (see Figure 1.16A). The authors proposed the phase-locked feedback activity from the rest of the network as an explanation for the persistence of PLF in wakefulness. However, this interpretation does not seem to support the original claim regarding evoked OFF periods. Evoked OFF periods in electrodes near the stimulation site have the largest amplitude which is comparable between NREM sleep and wakefulness. Therefore, it remains unclear why the evoked OFF period in the stimulated site can not attenuate stimulus-specific neural firing responses transmitted back from other areas, as opposed to NREM sleep.

It is also important to note that LFP signals are generally difficult to interpret because they reflect potentials generated at local and nonlocal sources [69]. For instance, PLF, which is calculated from the LFP signals at a particular electrode site, should not be interpreted simply as an expression of the dynamics at the recording site, because the oscillations may be the result of volume conduction of potentials generated by two dipoles located far from the recording site [69].

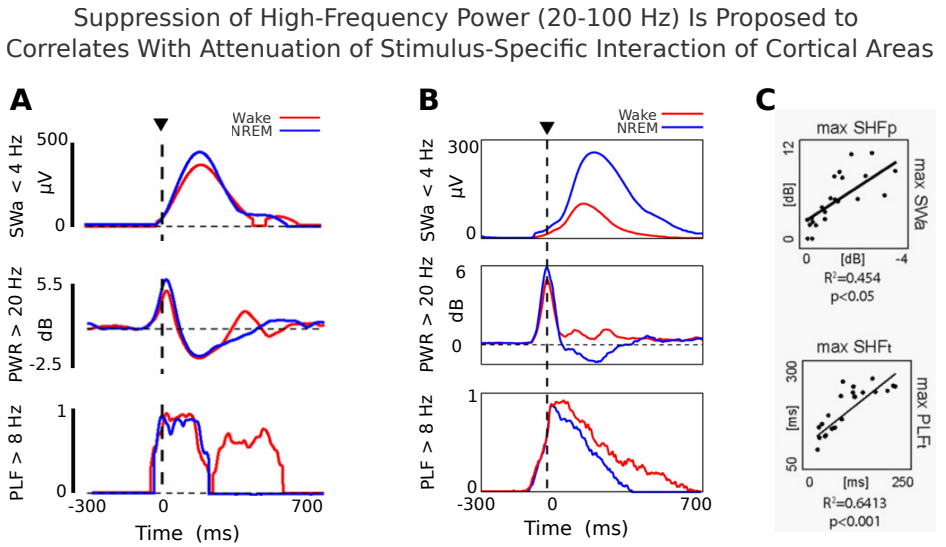

Figure 1.16: Suppression of high-frequency power (20-100 Hz) is proposed to correlates with attenuation of stimulus-specific interaction of cortical areas. (**A**). Three measurements: the amplitude of evoked slow waves, high-frequency power (20-100 Hz), and phase-locking factor (PLF), from top to bottom, in response to SPES pulses in a contact near the stimulation site for wakefulness (in red) and NREM sleep (in blue) in a human subject. (**B**). Same three measurements as in panel A, averaged across all contacts. Note that the amplitude of evoked slow waves in wakefulness is comparable to that in NREM sleep. The suppression of high-frequency power is nearly identical in awake and NREM sleep; the PLF lasts longer in awake than in NREM sleep. (**C**). *Top*. Correlation between the maximum amplitude (converted to dB) of the evoked slow wave (max SWa, y-axis) and the maximum level of high-frequency power suppression with respect to baseline (max SHFp, x-axis) across all contacts during NREM sleep for a representative subject. *Bottom*. Correlation between the timing of maximum high frequency suppression (max SHFt) and the latency at which PLF fell below the threshold for significance (max PLFt). The coefficient of determination R2 and significance level p of the correlation are given below each graph. Note that larger evoked slow waves correlate with stronger suppression of high-frequency power and earlier suppression correlates with earlier attenuation of PLF. Figures taken from [3].

Moreover, LFP signals (filtered at 0.5-300 Hz) contain little information about spike activity. Therefore, conclusions about the presence of evoked OFF periods (a state with suppressed spike activity) based on LFP signals should be made with caution in the absence of spike data. For instance, careful examination of extracellular recordings in rats and mice shows that evoked LFP signals near the stimulation site reflect evoked spike activity. However, significant evoked LFP signals are elicited at sites far from the stimulation site even though there is no evoked spike activity [66, 96] (see Figure 1.17A,B), presumably due to volume conduction and/or presynaptic activity [69].

Therefore, it remains unclear to what extent the amplitude of evoked slow waves or the suppression of high-frequency powers in the LFP represents a genuine evoked neural OFF period (neural silence mode) and whether the dropping of PLF during NREM sleep at recording sites are local events mediated by "evoked OFF periods".

Studies using *in vitro* cortical slices have also attempted to investigate cortical bistability as a mechanism for attenuated propagation of neural evoked responses. Electrical stimulation of ferret cortical slices has shown that perturbations during NREM-like and wakefulness-like states propagate in two distinct ways [90]. Spontaneous multi-unit activity (MUA) of cortical slices in the NREM-like state showed alternation between ON and OFF periods. After administration of noradrenergic and cholinergic agonists (NE+CCh), spontaneous neural signals showed wakefulness-like features (see Figure 1.18A). MUA activation in response to electrical stimulation in the NREM-like state was followed by cessation of firing, presumably an OFF period, after which MUAs returned to prestimulus levels. In contrast, activation in the awake-like state was followed by a brief decrease in firing rates, after which the MUAs rebounded at different latencies (see Figure 1.18B,C). However these observations do not seem to support cortical bistability as a mechanism that attenuates propagation of neural firing responses. That is so, because administration of kainate (an ionotropic glutamatergic receptor agonist) in that study did not enhanced

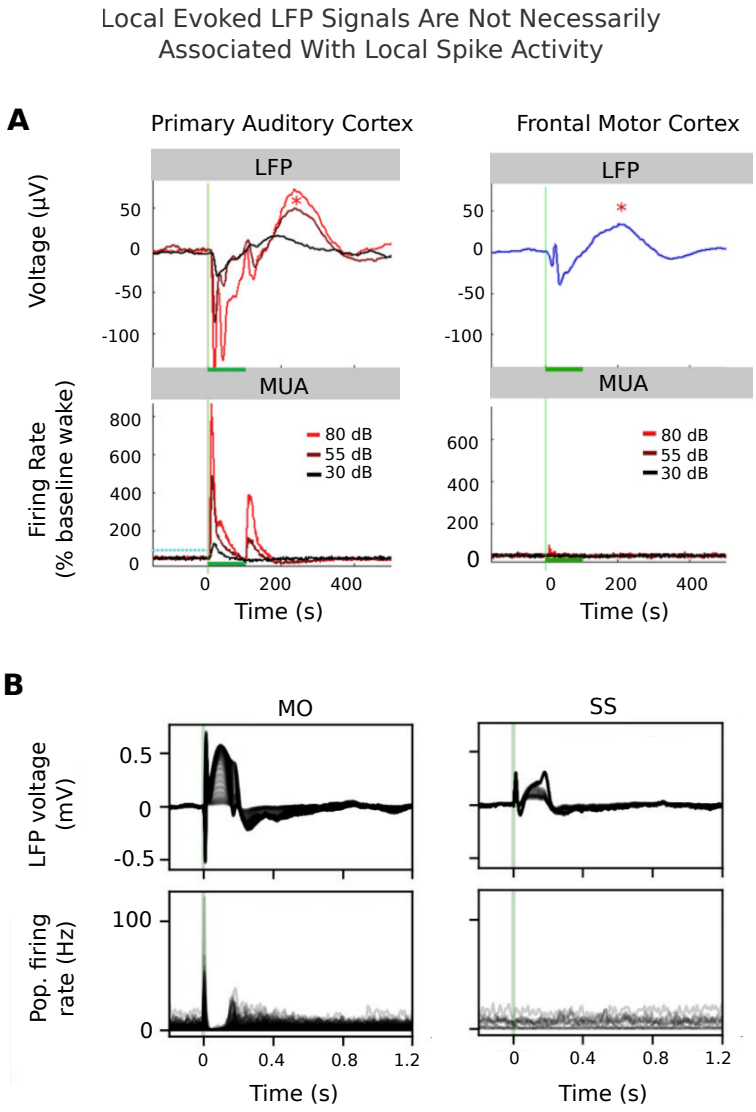

Figure 1.17: Local evoked LFP signals are not necessarily associated with local spike activity. (**A**). Average event-related LFP (top row) and multi-unit activity (bottom row) in response to 100-ms tones during NREM sleep in (next page)

Figure 1.17 *(previous page)*: auditory cortex (first column) and motor cortex (second column). Horizontal green bars mark the duration of the stimulus. Vertical green lines mark the onset of the sound. In contrast to the robust responses observed in auditory cortex, the evoked LFP responses in motor cortex are not associated with an evoked MUA. Note that the positive peak (red asterisk) corresponds to poststimulus suppression of neural activity in auditory cortex but not in motor cortex. Figures taken from [66]. (**B**). Superimposed event-related LFP (top row) and firing rates (bottom row) in motor cortex (first column) and somatosensory cortex (second column) in response to electrical stimulation of motor cortex with biphasic 400-μs current pulses during wakefulness. Vertical green lines mark the onset of the tone. Each LFP trace comes from a recorded LFP along the electrode shaft. Each firing rate trace represents a single regular spiking neuron from the same electrode. Note that the evoked LFP signals correspond to evoked local spike responses in motor cortex but not in somatosensory cortex. Figures taken from [96].

propagation of neural firing responses although it abolished the neural alternations between OFF and ON [90] (see Figure 1.18D). This evidence amplifies that the coincidence of cortical bistability and attenuated propagation of neural firing responses does not imply cortical bistability as the mechanistic account fo attenuation. This is another example of correlative evidence that does not indicate a causal relationship and may still reflect a hidden underlying mechanism.

Furthermore, experiments in rat motor cortex during wakefulness have shown that neural firing responses to electrical stimuli included rebound firing following a period of silence activity, presumably an evoked OFF period [96] (see Figure 1.19A). These observations may also challenge the view that OFF periods are a sufficient mechanisms to impair causal interaction between cortical neurons. Moreover, evoked OFF periods appear to be an insufficient explanation for the heterogeneity of modulation of neural firing responses to auditory stimuli in downstream areas to A1 during NREM sleep [65, 67, 68] (see Section 1.2.2). For instance, it remains

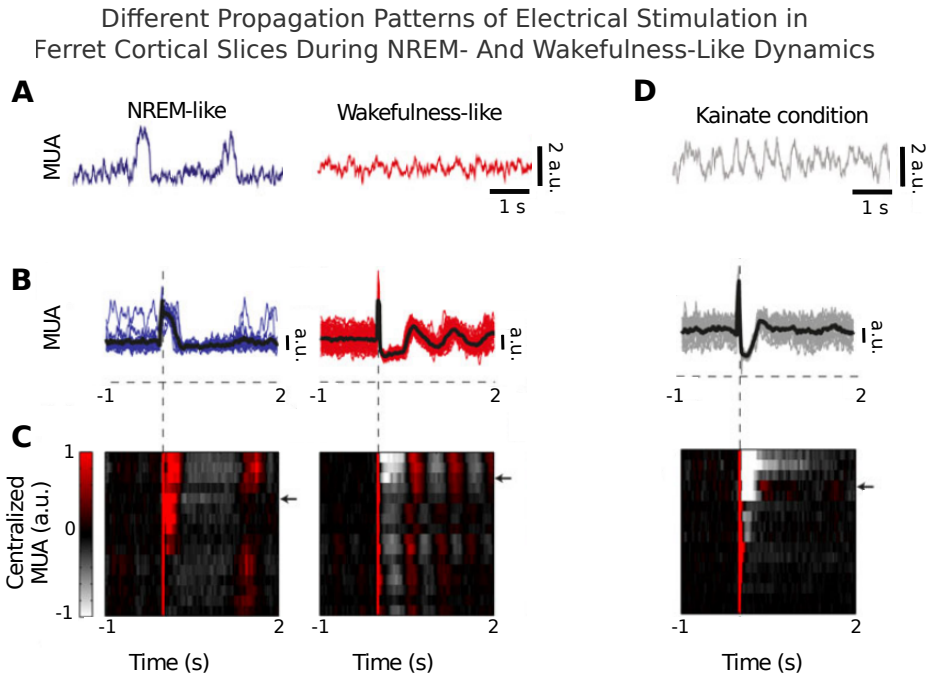

Figure 1.18: Different propagation patterns of electrical stimulation in ferret cortical slices during NREM- and wakefulness-like dynamics. (**A**). Spontaneous multi-unit activity (MUA) of cortical slices without pharmacological treatment shows NREM-like dynamics (blue), whereas wakefulness-like dynamics (red) occur after administration of noradrenergic and cholinergic agonists. To compensate for large fluctuations, MUAs were logarithmically scaled, hence the arbitrary unit (a.u.) in the vertical axis. (**B**). Superimposed evoked MUAs to electrical stimulation in a channel during NREM-like (blue) and wakefulness-like (red) states. Note that the black curve is the average over 15 trials. (**C**). For all channels of the same slice (the black arrow on the right represents the channel on panel B), the centralized (A-scored with respect to peristimulus activity) averaged MUA are shown. Note that the channels are sorted by the total amount of activity significantly different from zero. (**D**). Same as panel **A**-**C**, but for the kainate condition. Note that the slow neural oscillation is abolished (first row), but the propagation pattern is not comparable to the wakefulness-like condition. Figures taken from [90].

unclear why the evoked OFF periods in A2 do not attenuate propagation of neural firing responses during NREM sleep, unlike their counterparts in PRC. Finally, given the identical mechanism underlying evoked and spontaneous OFF periods—i.e., a neural inactive state due to activation of activity-dependent potassium currents during neural active states—it remains unclear how evoked OFF periods can attenuate incoming neural signals, whereas spontaneous OFF periods do not systematically attenuate incoming neural signals. Given these considerations, it appears that evoked OFF periods are an insufficient explanation for attenuated propagation of neural firing responses in the cerebral cortex during NREM sleep.

Moreover, auditory stimulation studies suggest that sleeping individuals can perform some degree of sensory processing during NREM sleep [48, 50, 51, 60, 63, 52, 53, 54, 55]. Processing of speech stimuli requires the integration of low-level acoustic features to extract higher-level linguistic units, which does not seem to fit with a disruption of stimulus-specific interaction between cortical areas due to cortical bistability. Another observation that challenges cortical bistability as an explanation to attenuated propagation of stimulus-evoked activities during NREM sleep is that experimental observations suggest that neural markers for the amplification of relevant auditory signals are weaker in the second half of the night than in the first half [55]. In contrast, fewer sleep slow waves occur in the second half of the night [97] and the tendency for cortical bistability should decreases in the second half of the night given that bistability tendency decreases with decreasing sleep pressure [29].

1.3.4 The Missing Piece of the Puzzle: Strength of Cortico-cortical Synapses

Although, to our knowledge, there is no study investigating the role of synaptic pathways in different propagation patterns of neural firing responses in the cortex during NREM sleep and wakefulness, several studies

suggest that it is not due to changes in synaptic pathways but to changes in thalamocortical dynamics [81, 2, 3]. The authors in [3] claimed that the comparable percentage of contacts with significant evoked LFP signals during NREM sleep and wakefulness in response to single-pulse electrical stimulation argue against disruption of synaptic pathways in NREM sleep. However, it is important to note that these observations were based on evoked LFP signals (filtered at 0.5-300 Hz), which contain little information about spike activity. A careful review of extracellular recordings in rats shows that significant evoked LFP signals are elicited at sites far from the stimulation site, presumably due to volume conduction and/or presynaptic activity [69], although there is no evoked spike activity at these same sites [66, 96] (see Figure 1.17A,B). Another consideration is that neural firing responses during NREM sleep may be significantly different from baseline but still contain less information than awake responses (see Section 1.4). Overall, it remains unclear to what extent the same percentage of significant evoked LFP signals during NREM sleep and wakefulness [3] argues against disruption of synaptic pathways during NREM sleep compared with wakefulness.

It is important to acknowledge that there is a lack of experimental studies examining the role of synapses. However, the arguments put forward so far suggest that changes in thalamocortical dynamics (including thalamic and cortical dynamics) during NREM sleep are an insufficient explanation for the attenuated propagation of neural firing responses in the cerebral cortex during NREM sleep compared with wakefulness. These arguments suggest the existing role of synaptic pathways in different propagation patterns of neural firing responses in the cortex during wakefulness and NREM sleep. Synapses in the transthalamic model can be divided into two classes: those involved in the cortico-thalamo-cortical (CTC) and those involved in the cortico-cortical (CC) pathways.

A recent study in mice examined the role of the CTC pathways and suggested that burst firings from thalamic neurons to the cerebral cortex via the CTC pathways are critical for generating different propagation patterns of

evoked neural responses during wakefulness and anesthesia [96]. Single-unit recordings from the motor cortex (MO) and somatomotor-related thalamic areas (SM-TH) in mice showed that evoked neural firing responses to electrical stimulation from MO during wakefulness consisted of an initial response followed by cessation of firing, presumably OFF period, after which the evoked responses rebounded (see Figure 1.19A). Cortical rebound responses were shown to correlate with the preceding evoked SM-TH burst firings during wakefulness (see Figure 1.19B,C). However, during anesthesia, after administration of isflorane, the cortical rebound responses disappeared, although the initial responses were preserved (see Figure 1.19A). In addition, the probability of burst firings and the relative timing between thalamic evoked activity and cortical rebound responses decreased (see Figure 1.19B,C). The authors claimed that these observations indicate the importance of CTC pathways and dynamics of thalamic relay neurons for cortical rebound responses.

Nevertheless, it remains unclear how these patterns of evoked activity in the cerebral cortex may disappear during NREM sleep, in which thalamic neurons switch to the burst firing model and have a higher tendency to fire bursts [17, 19, 23]. Moreover, perturbations in cortical slices of ferrets, lacking the thalamus, have shown that rebound spike activity follows initial activation under wakefulness-like condition [90]. Although these arguments are not sufficient to rule out the possible role of CTC synapses and thalamic dynamics, these considerations suggest that CC synapses play a role in different propagation patterns of neural firing responses in the cerebral cortex during NREM sleep and wakefulness.

Altered strength of CC synapses during NREM sleep compared with wakefulness could explain the different propagation patterns of neural firing responses. The change in CC synaptic strength is consistent with the view that neuromodulators from the ascending arousal network increase neurotransmission in cortical neurons during wakefulness by increasing the signal-to-noise ratio [17]. Another possible explanation for the weakened CC synapses during NREM sleep could be the downscal-

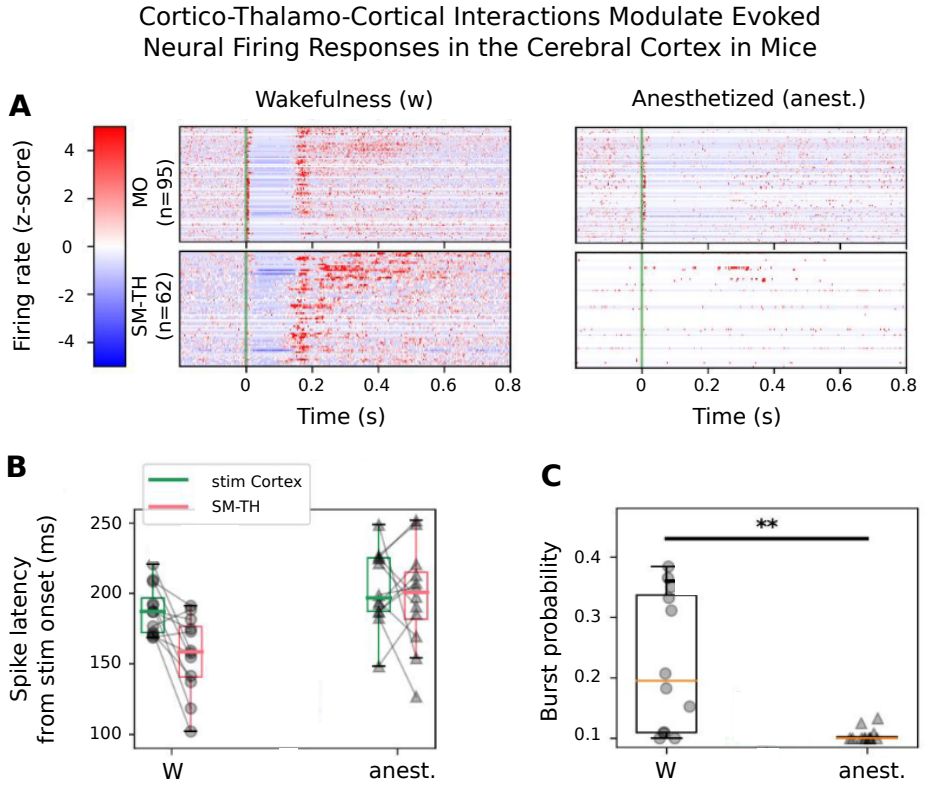

Figure 1.19: Cortico-thalamo-cortical interactions modulate evoked neural firing responses in the cerebral cortex in mice. (**A**). Average evoked neural firing responses in MO (top row) and SM-TH (bottom row) to electrical stimulation of MO in the awake state (left) and under anesthesia (right). Vertical green lines mark electrical stimulation onset. Firing rates are z-scored using average pre-stimulus firing rate of all regular spiking (RS) neurons recorded from the Neuropixels probes (n is the number of neurons). Note that cortical rebound responses decrease during anesthesia. (**B**). Spike latency in the 100-300 ms time window (around cortical rebound responses) for responsive RS neurons in stimulated cortex (green) and in the SM-TH (pink) under all conditions. (**C**). The probability of burst firings (proportion of total trials) in SM-TH within 75-300 ms (next page)

Figure 1.19 *(previous page)*: (around cortical rebound responses) after stimulus onset for the two conditions (N=12 mice). Boxplots show median, 25th, and 75th percentiles; whiskers extend from the box by 1.5 IQR. $p < 0.01$. Figures taken from [96].

ing of the conductance of excitatory synapses, a hypothesis established by researchers Giulio Tononi and Chiara Cirelli as synaptic homeostasis hypothesis (SHY).

Synaptic homeostasis hypothesis (SHY)

SHY suggests that sleep is the price the brain pays to renormalize synaptic weight [98, 99, 100, 101]. SHY predicts that synaptic strength in several cortical circuits decreases during NREM sleep due to net synaptic upscaling during wakefulness (see Figure 1.20A).

Briefly, SHY explains that the neuromodulatory milieu during wakefulness (see Section 1.1.2) results in the expression of cellular correlates of synaptic upscaling in many brain regions. As a result, the synaptic pathways that are activated in response to stimuli coming from external environment are upscaled during wakefulness, resulting in learning and memory functions of the brain. On this basis, even spontaneous neural activity during wakefulness can result in synaptic upscaling in several cortical circuits. Alternatively, changes in the neuromodulatory milieu during NREM sleep decrease expression of the cellular correlates of synaptic upscaling but increase expression of the cellular correlates of synaptic depotentiation/depression. In this view, spontaneous neural activity during NREM sleep does not results in synaptic upscaling, and synapses may downregulate via mechanisms of depotentiation/depression (see for more details [98, 99, 100, 101]).

There is ample molecular, electrophysiological, structural, and ultrastructural evidence supporting SHY (see for review [98, 99, 100, 101]).

Synaptic strength can be defined by several markers. For instance, one molecular measure of synaptic strength could be the expression of excitatory glutamatergic AMPA (Alpha-Amino-3-Hydroxy-5-Methyl-4-Isoxazole Propionic Acid) receptors at excitatory synapses [102]. Experiments in rats have shown that the expression of AMPA receptors at the synaptic level in the rat cerebral cortex was higher during wakefulness than during sleep [103].

Axon-spine interface (ASI) at excitatory synapses is a morphological measure for synaptic strength at the ultrastructural level [104]. Serial electron microscopy studies in mice have shown that the size of the ASI was larger on average during wakefulness than during sleep (see Figure 1.20B). It is important to note that these observations did not distinguish between NREM sleep and REM sleep. Nonetheless, these observations may broadly suggest that synaptic strength at excitatory synapses is greater during wakefulness than during NREM sleep.

Distance–selective synaptic homeostasis

An increase in the strength of CC synapses (upscaling of excitatory connections in SHY terminology) seems to be a plausible mechanism that enhances propagation of neural firing responses in wakefulness compared with NREM sleep. Upscaling of excitatory connections in wakefulness may result in stronger driver inputs, which could explain the larger spatiotemporal extent of response propagation in TMS studies (see Section 1.2.3) or greater evoked neural responses in higher cortical areas to auditory stimuli (see Section 1.2.2). However, it is possible that synaptic upscaling in the awake state does not guarantee enhanced propagation of neural firing responses.

Studies using *in vitro* techniques have shown that spontaneous synaptic activities modulates the gain of neural responses [105]. The higher the spontaneous synaptic activity, the less responsive neural populations are to driver inputs (injected currents). Evoked firing rates to constant driver

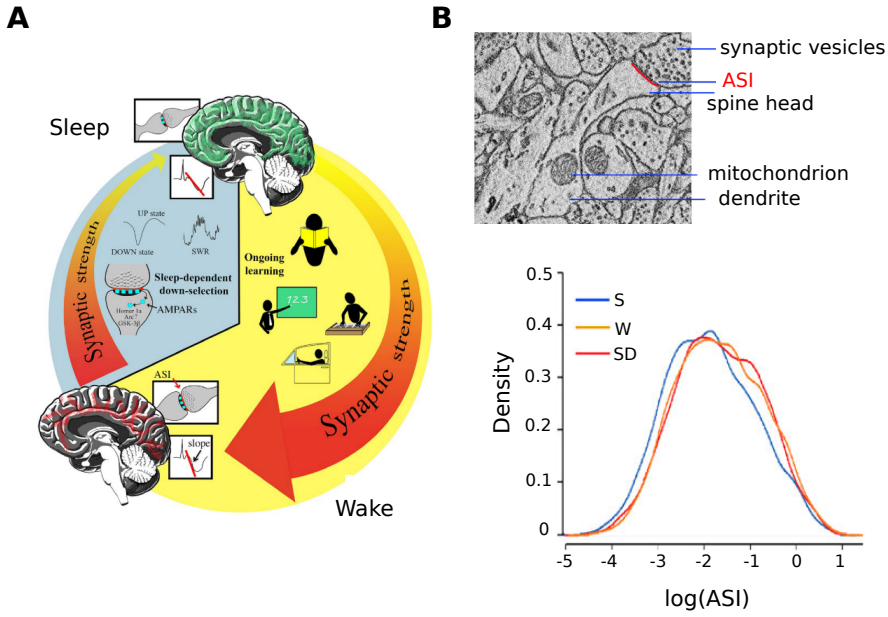

Figure 1.20: Schematic diagram describing the synaptic homeostasis hypothesis (SHY). (**A**). Renormalization of synaptic weight in the sleep-wake cycle. Due to ongoing learning and memory processes, synaptic strength increases during wakefulness in many brain circuits (red lines in the bottom sagittal view of human brain). During sleep, synaptic strength decreases in most, if not all, circuits to compensate for the net increase during wakefulness. ASI, axon-spine interface; AMPARs, AMPA receptors. Figure taken from [101]. (**B**). Electron microscopy of cortical synapses in mice. *Top*. Examples of presynaptic and postsynaptic elements in layer 2 of the primary motor cortex of a mouse, postnatal day 30. The contact area between the presynapse (synaptic vesicle) and postsynapse (spiny head) is referred to as the ASI and is highlighted in red. *Bottom*. Probability density of ASI size (log-transformed) in mice at postnatal day 30 for sleep (in blue), wakefulness (in yellow), and sleep deprivation (in red). Note that the ASI for the awake and sleep-deprived groups of animals overlap, likely indicating synaptic saturation and the need for sleep to renormalize synapses. Figures taken from [104].

currents were found to decrease when spontaneous synaptic activity was increased for pyramidal neurons in slices in a balanced configuration (i.e., increasing inhibition to regulate overexcitation) without excessive excitatory or inhibitory factors.

Therefore, upscaling of excitatory synapses (synaptic upscaling) in a balanced configuration in the waking state appears to be a phenomenon that needs fine tuning between two opposing effects on cortical neural firing responses: driving and pulling effects. Although synaptic upscaling in wakefulness may produce stronger driving forces from one cortical area to another, the higher spontaneous synaptic activities in wakefulness may attenuate neural evoked responses. One way to overcome the pulling effect of spontaneous synaptic activities in wakefulness is that synaptic upscaling occurs preferentially between distinct neural networks rather than within local and recurrent connections. We have coined this hypothesis as distance–selective synaptic homeostasis.

Distance-selective synaptic homeostasis states that upscaling of inter-synapse (intercortical excitatory synapses formed between different cortical columns) should be stronger than upscaling of intra-synapse (intracortical excitatory synapses formed within a cortical column). This hypothesis predicts that synaptic upscaling in wakefulness favors driver inputs over spontaneous synaptic activities, enhancing propagation of neural firing responses along a hierarchical cortical processing chain in wakefulness compared with NREM sleep.

To get a clear idea of our hypothesis, imagine a neural system with two distinct cortical columns that are interconnected and can represent different cortical columns, one from the primary auditory cortex (A1) and the other from perirhinal cortex (PRC). We know from experiments that the evoked neural responses in A1 during NREM sleep and wakefulness to auditory stimuli are comparable. However, the evoked neural responses in the PRC are larger during wakefulness than during NREM sleep.

Imagine that, accepting SHY, excitatory synapses are upscaled in wakefulness in a balanced configuration. Note that the increase in inhibition is

just to cancel out overexcitation due to upscaling of excitatory synapses. Given the intracortical and intercortical excitatory connections, there are three synaptic upscaling scenarios in wakefulness: local–selective, homogeneous, and distance–selective. Note that both intra- and inter-synapses are upscaled in the waking state, but the relative strength of upscaling results in three scenarios. A local–selective synaptic upscaling scenario corresponds to stronger intra-synaptic upscaling over inter-synaptic upscaling; homogeneous synaptic upscaling scenario corresponds to equal intra-synaptic upscaling and inter-synaptic upscaling; and, finally, distance–selective synaptic upscaling scenario corresponds to stronger inter-synaptic upscaling over intra-synaptic upscaling, hence the names.

We hypothesize that only spatial-selective synaptic upscaling can explain an enhanced neural firing responses in the PRC during wakefulness compared with NREM sleep. In the following we will develop such choice. Synaptic upscaling in a balanced configuration from NREM sleep to wakefulness results in higher spontaneous synaptic activities in the PRC during wakefulness compared with NREM sleep. This is true even if we assume that spontaneous presynaptic firing to the PRC (including spontaneous A1 and recurrent PRC firing) is comparable in NREM sleep and wakefulness, which is an upper bound because firing rate in NREM sleep should be smaller than wakefulness due to the Up and Down states in NREM sleep. Synaptic upscaling in wakefulness increases the driving input from A1 to PRC compared with NREM sleep for all three synaptic upscaling scenarios. Note that this is due to the synaptic upscalings in the awake state, even though the evoked neural responses in A1 are comparable in NREM sleep and the awake state. From a PRC perspective, however, only the signal-to-noise ratio (SNR) is important. The higher the SNR, the higher the evoked responses.

It is important to point out that the following part is not an analytical derivation, but a very intuitive way to understand the necessity of distance–selective synaptic upscaling in the waking state. Later, in the Result chapter, we will provide ample numerical evidence for it. Let us define SNR

as the ratio between the driver input, i.e., the signal, and the spontaneous synaptic activities, i.e, the noise. This definition of SNR has been used elsewhere as well [17]. Therefore, the driver input to PRC, in a simplistic view, is the postsynaptic excitatory currents in PRC due to presynaptic evoked firing responses in A1. The spontaneous synaptic activities in PRC consist of two contributions: postsynaptic excitatory currents due to spontaneous presynaptic firing activities in A1 and postsynaptic excitatory currents due to spontaneous recurrent firing activities in PRC. Let us denote intra-synaptic upscaling by β_{intra} and inter-synaptic upscaling by β_{inter}. Then, SNR is proportional to the ratio between driver and spontaneous synaptic activities: SNR $\propto \frac{\beta_{inter}}{\beta_{intra}+\beta_{inter}}$. Note that $\beta_{intra},\ \beta_{inter} > 1$ in wakefulness and $\beta_{intra} = \beta_{inter} = 1$ in NREM sleep. The three synaptic upscaling scenarios in the awake state are as follows: local–selective ($\beta_{intra} > \beta_{inter}$), homogeneous ($\beta_{intra} = \beta_{inter}$) and distance–selective ($\beta_{intra} < \beta_{inter}$). Therefore, the SNR for local–selective synaptic upscaling is lower in wakefulness than in NREM sleep; the SNR for homogeneous synaptic upscaling is comparable in wakefulness and NREM sleep; the SNR for distance–selective synaptic upscaling is greater in wakefulness than in NREM sleep.

It is important to emphasize that neural systems are nonlinear systems, which makes the explanation in the previous paragraph simplistic. One source of nonlinearity not considered in the above explanation is feedback loops. Feedback from PRC to A1 may affect the response of A1, which in turn may affect the response in PRC.

1.3.5 Summary

There is much evidence for attenuation of propagation of neural firing responses in the cerebral cortex during NREM sleep compared to wakefulness. However, the underlying mechanisms are unknown. However, the underlying mechanisms are unknown. The attenuated propagation can be attributed to the altered dynamics of the neural populations and/or the

strength of the synaptic pathways involved in propagation patterns. The current scientific consensus is that the altered dynamics of the thalamocortical network is the major cause of this change. However, as far as we know, there is insufficient evidence to support this view and changes in strength of the cortico-cortical synaptic pathways has not been yet studied.

The cortex and thalamus innervate each other by forming massive excitatory projections that form cortico-cortical (CC) and cortico-thalamocortical (CTC) pathways [82]. The transthalamic model describes that thalamic and cortical neurons and CTC and CC pathways are at the heart of propagation of neural firing responses in a hierarchical cortical organization [23, 84].

Thalamic neurons include thalamic relay neurons, local inhibitory interneurons, and Thalamic reticular nucleus (TRN). First-order thalamic relay neurons transmit information from the periphery to the cortex, whereas higher-order thalamic relay neurons transmit information between cortical areas via CTC pathways [84, 85]. Silent neuromodulatory projections during NREM sleep from the ascending arousal network in subcortical areas (see subsection 1.1.2) alters the dynamics of thalamic and cortical neurons, which is proposed to represent a mechanism that attenuates propagation of neural firing responses in the cerebral cortex.

Although direct experimental evidence is lacking, the fact that different propagation patterns of electrical stimulation in cortical slices appear even in the absence of thalamic neurons under NREM- and wakefulness-like conditions [90] suggests that thalamic dynamics during NREM sleep and CTC pathways are insufficient explanation for attenuated propagation of neural firing responses in the cortex during NREM sleep compared to wakefulness.

Moreover, there are ample considerations that challenges the view that dynamics of the cortex, the tendency to fall into an OFF period following periods of intense firing, is a sufficient mechanism attenuating propagation of neural firing responses. For instance, preserved evoked neural responses in A1 during NREM sleep and wakefulness [65, 66, 67, 68] challenges

effectiveness of spontaneous OFF periods in attenuating propagation patterns.

There are several considerations that also challenge the view [81, 2, 3] that evoked OFF periods following external stimuli attenuate propagation patterns in the cerebral cortex. For instance, studies supporting this view are based on LFP recording signals. Given that LFP signal has no information about spiking data, and volume conduction of potential signals and/or presynaptic activity [69] in LFP signals, it remains unclear to what extent LFP signals can be informative regarding local evoked OFF periods in which local neural spike activity is suppressed. Moreover, given the identical neural mechanisms underlying spontaneous and evoked OFF periods, it remains unclear how evoked OFF periods, unlike spontaneous OFF periods, can systematically attenuate propagation patterns.

Although, to our knowledge, there is no study investigating the role of synaptic pathways several studies suggested that the different propagation patterns in the cerebral cortex in NREM sleep compared to wakefulness is not due to changes in synaptic pathways but to changes in thalamocortical dynamics [81, 2, 3]. Authors [3] showed that the percentage of contacts with significant evoked LFP signals in response to single-pulse electrical stimulation was similar in epilepsy patients in NREM sleep and awake, arguing against disruption of synaptic pathways in NREM sleep [3]. However, it is important to note that these conclusions are based on evoked LFP signals (filtered at 0.5-300 Hz), which contain little information about spike activity. For instance, extracellular recordings in rats and mice shows that significant evoked LFP signals are elicited at sites far from the stimulation site, even though there is no evoked spike activity [66, 96], presumably due to volume conduction and/or presynaptic activity [69]. Another consideration is that evoked responses during NREM sleep may be significant compared with peristimulus activities, but still contain less information (see subsection 1.4) than in awake state.

It is important to acknowledge that there is a lack of experimental studies examining the role of synapses. However, the arguments put forward

so far suggest that changes in thalamocortical dynamics (including both thalamic and cortical dynamics) during NREM sleep are an insufficient explanation for the attenuated information propagation in the cerebral cortex during NREM sleep compared with wakefulness. Moreover, perturbations in cortical slices from ferrets lacking the thalamus have shown graded propagation of perturbation in wakefulness-like than NREM-like condition [90]. These considerations suggest that CC synapses play a role in different propagation patterns of neural firing responses in the cerebral cortex during NREM sleep and wakefulness.

In agreement with synaptic homeostasis hypothesis (SHY) [98, 99, 100, 101], upscaling of excitatory CC synapses in wakefulness may result in stronger driver inputs, which could enhance propagation of neural firing responses in wakefulness compared to NREM sleep. However, it is possible that synaptic upscaling in a balanced configuration in the awake state does not ensure enhanced propagation patterns. For instance, studies using *in vitro* techniques have shown that spontaneous synaptic activities modulate the gain of neural responses [105]. The higher the spontaneous synaptic activity, the less responsive neural populations are to driver inputs (a constant injected current).

We propose that synaptic upscaling in the waking state is a phenomenon with two opposing effects on neural firing responses: driving and pulling effects. Although synaptic upscaling in a balanced configuration in wakefulness may produce stronger driving forces from one cortical area to another, the higher spontaneous synaptic activities in wakefulness may attenuate neural evoked responses. One way to overcome the pulling effect of increased spontaneous synaptic activities in wakefulness is that synaptic upscaling occurs preferentially between distinct neural networks rather than within local and recurrent connections. We have coined this hypothesis as distance–selective synaptic homeostasis.

Distance-selective synaptic homeostasis states that inter-synaptic upscaling should be stronger than intra-synaptic upscaling in wakefulness. This way, synaptic upscaling in wakefulness favors driver inputs over spon-

taneous synaptic activities, enhancing propagation of neural firing responses along a hierarchical cortical processing chain in wakefulness compared with NREM sleep.

1.4 Information Propagation

One of the most common ways that neurons use to interact is by triggering action potentials (spikes). Action potentials are fast and high amplitude changes in the membrane potential that are transmitted between neurons. Neural spikes can be spontaneously triggered or evoked by an external stimulus. The evoked neural spikes can be unveiled by repeating the stimulus many times to obtain average neural firing responses (the peristimulus time histogram (PSTH) in spike-based theories or the average firing rate in rate-based theories) under the same stimulus conditions.

In a simplified view of a hierarchical neural processing chain, the neural spikes elicited by a group of neurons (or by a single neuron) vary in response to an external stimulus. The neural firing responses in this group cause changes in the neural spike train of a postsynaptically connected group of neurons (or in a single neuron), and so on [106, 107]. Neural spikes in the postsynaptic group carry information about the neural firing responses of the presynaptic group. But, what is information?

We refer to information from the neuron's point of view: *"a difference that makes a difference"* [108]. We propose two measures to quantify information in neural firing responses: *information detection* and *information differentiation*. Information detection measures whether neural firing responses to an stimulus differ significantly from spontaneous neural firing. In other words, information detection determines whether neural firing responses can be statistically attributed to presentation of a stimulus or not.

Although information detection is necessary for perception, it does not necessarily guarantee a high level of information about external stimuli coded in neural firing responses. For instance, imagine that neural firing

responses to two different stimuli, each, differ significantly from spontaneous neural firing activities. However, neural firing responses to these two stimuli may not differ significantly from one another. This reveals that neural firing responses do not contain information to distinguish between stimuli. Note that this case does not indicate a lack of information content in neural firing responses, but attenuated information content, because it is still able to distinguish neural firing responses from spontaneous neural firing activities.

Information differentiation measures whether neural firing responses to different stimuli differ significantly from one another. In other words, information differentiation measures whether neural firing responses can be attributed to different stimuli or not. Information differentiation is limited to the ensemble of stimuli. For instance, information content in neural firing responses can be high for the set of stimuli tested, but may decrease with respect to a new stimulus. Information detection and differentiation are sufficient to determine information content in neural firing responses of a neural system. A decrease in information detection and/or differentiation implies attenuated information content in neural firing responses.

Changes in propagation of information between two neural groups in a hierarchical neural processing chain under two different conditions can be quantified by measuring information content in each neural group in each condition. For instance, imagine that information content (information detection and differentiation) in a presynaptic neural group is preserved under two different conditions. Moreover, in the postsynaptic neural group, information detection is preserved under both conditions, whereas information differentiation is not. This implies that information content in the postsynaptic group is attenuated despite preserved information content in the presynaptic group. Accordingly, it can be claimed that propagation of information from the presynaptic to the postsynaptic neural group is attenuated from one condition to the other one. Note that this argument holds true for both spike-based and rate-based theories.

To quantify information detection and differentiation in a neural group,

supervised or unsupervised machine learning algorithms can be employed. In this study we focus on supervised techniques, but it is also important to extend the scope to unsupervised techniques in future works. In a supervised framework, information detection can be measured as the accuracy of an ideal observer to distinguish between neural firing responses to an stimulus in poststimulus intervals and spontaneous neural firing activities in peristimulus intervals. A high level of accuracy shows a high level of information detection in neural firing responses. Furthermore, information differentiation can be measured as the accuracy of an ideal observer to distinguish among neural firing responses in poststimulus intervals to different stimuli in the neural system. A high level of accuracy shows a high level of information differentiation in neural firing responses. Note that high levels of information detection and differentiation can also guarantee high accuracy of an ideal observer with priori knowledge about stimuli to decode the stimuli features.

The experimental design required to assess information content relies on a high number of trials in which neural firing responses to various stimuli are recorded. It is also important to note that the two measures of information detection and differentiation are not mutually exclusive events. For instance, both information detection and differentiation can be high in one condition but low in another condition.

Does the literature reviewed in Section 1.2 suggest that information content along a hierarchical cortical processing chain decreases during NREM sleep compared with wakefulness?

It is important to highlight that the literature reviewed in Section 1.2 lacks a systematic and direct quantification of information content along a neural pathway. However, there are compelling observations indicating that information content in A1 is preserved during NREM sleep compared to wakefulness and that it attenuates in higher cortical areas downstream to A1.

For instance, single-unit studies in monkeys showed that averaged amplitudes and variability of neural firing responses, temporal encoding and neural tuning curves in A1 are preserved in NREM sleep compared to wakefulness [65]. Moreover, single-unit studies in rats showed that amplitude and selectivity of neural firing responses in A1 are preserved in NREM sleep compared to wakefulness [66]. Furthermore, a recent human study also reported that amplitude of neural firing responses along with mutual information between the ensemble of auditory stimuli and neural firing responses are preserved in A1 [68]. This evidence might suggest that the information content in A1 is preserved during NREM sleep compared to wakefulness. For instance, preserved amplitude and standard deviation of neural firing responses might indicate preserved information detection. On the other hand, preserved tuning curves, or response selectivity for stimuli, or mutual information might indicate preserved information differentiation.

Alternatively, it seems plausible to conclude that information content in cortical areas downstream to A1 attenuates heterogeneously. Studies in monkeys [65] suggest that auditory information is preserved in the secondary auditory cortex, whereas studies in rats [67] suggest that auditory information is attenuated in perirhinal cortex. Moreover, a recent human study reported that amplitude of neural firing responses along with mutual information between the ensemble of auditory stimuli and neural firing responses attenuate heterogeneously in cortical areas downstream to A1 during NREM sleep compared to wakefulness [68].

This evidence might suggest that information propagation attenuates along a hierarchical cortical processing chain in NREM sleep compared to wakefulness. The other line of evidence for attenuation of information content comes from TMS studies reporting decreased spatiotemporal extent of cortical activation to TMS stimulation during NREM sleep compared to wakefulness [70]. These observations were based on current source density of evoked EEG signals rather than spike activity. Nevertheless, recent experimental observations show that the amplitude of current source den-

sity correlates with local spike activity [96]. Therefore, the shorter-lasting significant current source densities in NREM sleep could be due to a more rapid attenuation of neural firing responses in NREM sleep compared with wakefulness. Nevertheless, it is important to note that further data analysis is needed to draw more robust conclusions about the attenuation of information propagation along a hierarchical cortical processing chain during NREM sleep compared to wakefulness.

Does the literature reviewed in Section 1.3 disclose the mechanisms accounting for attenuated information propagation along a hierarchical cortical processing chain during NREM sleep compared with wakefulness?

It is important to highlight that nearly all studies reviewed in Section 1.3 have not evaluated information content and are based on amplitude of neural firing responses. This also applies to the CTC model. The CTC model proposes a hierarchical organization of the cortex for the propagation of neural firing responses. Further studies are required to evaluate its validity when reproducing propagation of information content within the cortex.

To the best of our knowledge, a solid proof of the role of the dynamics of the thalamus in attenuating propagation of information in the cortex during NREM sleep compared to wakefulness is missing and few studies are limited to evaluation of amplitude of neural firing responses. Nevertheless, preserved amplitude and selectivity of neural firing responses in A1 during spindle and no-spindle moments in NREM sleep in rats [88] might suggest that spindle mediated inhibition through first-order thalamic relay neurons in NREM sleep is an insufficient mechanism. Although further experiments and data analysis are required to evaluate the effectiveness of the dynamics of the thalamus on attenuation of information propagation in the cortex, current scientific evidence suggests that the thalamus might not be the only element at play.

The same arguments for evaluation of information applies to the role

of the dynamics of the cortex in attenuation of information propagation during NREM sleep and the strength of CTC and CC synaptic pathways. Although further experiments are required to assess the effects of the OFF periods on the information content rather than the amplitude of evoked responses, these observations and the fact that the spontaneous OFF periods account for only a small fraction of neural activity during NREM sleep [33] suggest that the spontaneous OFF periods may not effectively attenuate the transmission of auditory information in the cerebral cortex.

By and large, we believe that literature reviewed in Section 1.3 suggests that dynamics of the thalamus and the cortex and the strength of CTC synaptic pathways do not fully account for attenuation of information propagation along a hierarchical cortical processing chain during NREM sleep compared with wakefulness. Therefore, we investigate the possible role of the strength of CC synaptic pathways.

It is important to note that this claim depends on the fact that the information content about an external stimulus is preserved at the first cortical population processing the stimuli. Otherwise, the attenuated information content along a hierarchical cortical processing chain could be an epiphenomenon of the decreased information content at this first station population. Thus, more empirical data are needed to draw robust conclusions.

Chapter 2

METHODS

In this chapter, we describe the methods that is used in this study to evaluate our hypothesis. In particular, how synaptic upscaling modulate information propagation from one cortical column to another in wakefulness compared to NREM sleep. To do so, this chapter is devoted into two sections. In the first section, we provide the computational model used in this study. Next, we describe the tools we have used to analyze simulated data by the computational model.

2.1 Computational Model

Computational modeling is a technique using mathematical models to simulate and study complex systems, especially when analytical solutions are not available. Computational models rely on several specific conceptual and mathematical assumptions and use a set of quantitative variables that characterize the under study system. In computational neuroscience, computational models of neurons are mathematical descriptions of biological properties of neurons that generate neural activities recorded in laboratories, e.g., electrical membrane potentials, firing rate activities, etc.

In this section, we describe the computational model and the computational pipeline used in this study. In the first part, we introduce the neural-mass model that describes average neural activity of a single cortical column. In the second part, we extend the model to two cortical columns coupled bidirectionally with excitatory synapses. Finally, we present the computational pipeline used to evaluate responses of models to transient excitatory inputs.

2.1.1 One-Cortical-Column Model

Recordings of the extracellular neural field are thought to capture the superposition of all transmembrane currents, such as the synaptic and ionic currents [69]. To reproduce the dynamic features of these signals, we used a neural mass model representing average membrane potential of a neural cortical column that results in generation of characteristics of NREM sleep and wakefulness [109, 110]. A single cortical column consists of pyramidal, *p*, and inhibitory, *i*, populations that are interconnected (see Figure 2.1A for schematic).

Neural Mass Model

The dynamics of average membrane potential of each cortical population, $V_{p/i}$, is determined by the mathematical formalism of the classical conductance-based model [111] with one leak, two synaptic currents and an activity-dependent potassium current as follows:

$$\tau_p \dot{V}_p = -I^p_{\mathrm{L}} - I^p_{\mathrm{AMPA}} - I^p_{\mathrm{GABA}} - \tau_p C_m^{-1} I_{\mathrm{KNa}}, \tag{2.1}$$

$$\tau_i \dot{V}_i = -I^i_{\mathrm{L}} - I^i_{\mathrm{AMPA}} - I^i_{\mathrm{GABA}}, \tag{2.2}$$

where $\tau_{p/i}$, $I^{p/i}_{\mathrm{L}}$, $I^{p/i}_{AMPA}$ and $I^{p/i}_{GABA}$ are, respectively, the membrane time constant and the leak, AMPAergic and GABAergic currents of population

p or i. I_{KNa} is the activity-dependent potassium current of the pyramidal population (see Section 2.1.1). C_m is the membrane capacitance in the Hodgkin–Huxley model.

Average firing rate of each population is modeled as an instantaneous function of average membrane potential $V_{p/i}$ according to a sigmoid function [112, 113]:

$$Q_{p/i}(V_{p/i}) = Q_{p/i}^{max} \frac{(1 + \tanh(C(V_{p/i} - \theta_{p/i})/\sigma_{p/i}))}{2}, \qquad (2.3)$$

where $Q_{p/i}^{max}$, $\theta_{p/i}$ and $\sigma_{p/i}$ represent the maximum firing rate, firing rate threshold and inverse neural gain of population p or i, respectively (see Tables 2.1 and 2.2 for symbol description and parameter value, respectively). Here, $C = \frac{\pi}{2\sqrt{3}}$ is a constant linking the neural gain to the slope of the sigmoid function [109]. The nonlinear function is consistent with experimental observations that firing rate and membrane potential of cortical neurons *in vivo* follows a nonlinear increasing curve [26].

Model Synapses

Synapses are the structure that permit signal transmission between and within populations. They are modeled by presynaptic and postsynaptic elements. The presynaptic element is the presynaptic activities which have an intrinsic and an extrinsic origin. The intrinsic or recurrent activity is the input that each population receives from local pyramidal and inhibitory populations. The extrinsic element comes from non-explicitly modeled nearby cortical columns that impinges on population p and i only through excitatory synapses. This is consistent with the morphology of cortical neurons, in which pyramidal neurons have larger projecting axons than the more localized inhibitory axons [114, 115, 116]. This has also been reflected in numerous computational studies [117, 118, 119, 120, 121].

The model incorporates Dale's principle: an excitatory (inhibitory) population performs excitation (inhibition) at all of its synaptic connec-

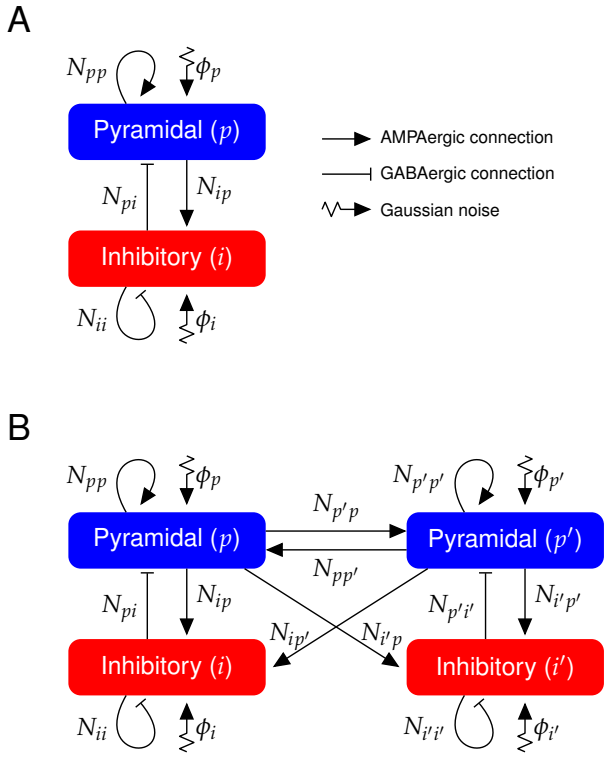

Figure 2.1: Diagram of the neural mass model. (**A**) A cortical column containing one pyramidal and one inhibitory population. The couplings between pyramidal and inhibitory populations are mediated through AMPAergic and GABAergic connections (see Tables 2.1 and 2.2 for symbol description and parameter values). (**B**) Neural mass model describing two mutually coupled cortical columns. The connections between two cortical columns are only AMPAergic, i.e., only the pyramidal populations target both pyramidal and inhibitory populations from the other cortical column (see Tables 2.1 and 2.4 for symbol description and parameter values).

tions to other populations, regardless of the identity of the target population. Given a presynaptic population k' and a postsynaptic population k, the time course of synaptic activity, $s_{kk'}$, at time t, depends on the pyramidal or inhibitory nature of the presynaptic population k'.

The postsynaptic element is modeled by ionotropic receptors including AMPA and GABA receptors. Synapses are considered AMPAergic for excitation, i.e., when the population k' is the pyramidal one, and GABAergic for inhibition, i.e., when the population k' is the inhibitory one. The mathematical formalism adopted is the convolution of the presynaptic firing, $Q_{k'}$, with average synaptic response to a single spike $\alpha_{k'}$ which has an exponential decay time course [122]:

$$s_{kk'} = N_{kk'} Q_{k'}(V_{k'}) \circledast \alpha_{k'}, \tag{2.4}$$

$$\alpha_{k'} = \gamma_{k'}^2 \, t \, \exp(-\gamma_{k'} t), \tag{2.5}$$

where $N_{kk'}$ is the mean number of synaptic connections from the presynaptic population k' to the postsynaptic population k. $\gamma_{k'}$ describes the time constant of the dynamics of a synapse activated by the presynaptic firing of the population k'. The set of Equations (2.4) and (2.5) lead to the second-order differential equation (derived in detail in Appendix A.1):

$$\ddot{s}_{kk'} = \gamma_{k'}^2 \, (N_{kk'} \, Q_{k'}(V_{k'}) + \phi_k - s_{kk'}) \, - 2\gamma_{k'} \, \dot{s}_{kk'}, \tag{2.6}$$

where Equation (2.6) describes dynamics of synaptic currents due to firing of the presynaptic population k' onto the postsynaptic population k. Moreover, the noise ϕ_k is simulated independently for each cortical population as a Gaussian process with zero autocorrelation time constant, with zero mean and standard deviation of 1.8 ms^{-1}. Note that the Gaussian noise is applied only on excitatory synapses. The AMPAergic and GABAergic synaptic currents are defined as:

$$I^k_{\text{AMPA}} = \bar{g}_{\text{AMPA}} \, s_{kp} \, (V_k - E_{\text{AMPA}}), \tag{2.7}$$

$$I^k_{\text{GABA}} = \bar{g}_{\text{GABA}}\, s_{ki}\, (V_k - E_{\text{GABA}}), \tag{2.8}$$

where $\bar{g}_{\text{AMPA}}$ and $\bar{g}_{\text{GABA}}$ are, respectively, the average AMPAergic and GABAergic conductance. E_{AMPA} and E_{GABA} are the reversal potentials of the AMPAergic and GABAergic currents.

Activity-Dependent Potassium Current

Slow oscillation is the hallmark of neuronal cortical activity during NREM sleep and anesthesia. It consists of silent (Down) and persistent (Up) firing patterns of activity that alternate. Activation of the slow activity-dependent K^+ current has been suggested as a possible mechanism for triggering the Down state initiation [28, 36, 37, 31]. The sodium-dependent potassium current I_{KNa} and sodium concentration [Na] are implemented in the model as follows:

$$I_{\text{KNa}} = \bar{g}_{\text{KNa}}\, \frac{0.37}{1 + (\frac{38.7}{[\text{Na}]})^{3.5}}\, (V_p - E_{\text{K}}), \tag{2.9}$$

$$\tau_{\text{Na}}\, \dot{[\text{Na}]} = \alpha_{\text{Na}} Q_p(V_p) - \text{Na}_{\text{pump}}([\text{Na}]), \tag{2.10}$$

where $\bar{g}_{\text{KNa}}$, E_{K}, τ_{Na} and α_{Na} correspond to average conductance of I_{KNa}, the Nernst reversal potential of the I_{KNa} current, the time constant of the extrusion of sodium concentration and average influx of sodium concentration per firing. Na_{pump} is a function representing the sodium pumps that determines the extrusion of sodium concentration through sodium pumps (see Appendix A.1 for details).

Upscaling Excitatory Synapses

The neural mass model proposed by [109, 110] is able to generate the physiological characteristics of the sleeping cortex for particular values of the parameters. There, the authors showed that by reducing σ_p and $\bar{g}_{\text{KNa}}$,

Symbol	Description
$Q_k^{\max}$	Maximal firing rate of population k
θ_k	Firing rate threshold of population k (sigmoid function half activation)
σ_k	Inverse neural gain of the sigmoid function of population k
τ_k	Membrane time constant of population k
C_m	Membrane capacitance in the HH model
ϕ_k	Gaussian noise on population k
$N_{kk'}$	Mean number of synaptic connections from presynaptic population k' to postsynaptic population k
γ_m	Time constant of the postsynaptic response of synapse type m
$\bar{g}_{\mathrm{X}}$	Average X-ergic conductance
E_{X}	Reversal potential of the X-ergic current
$\bar{g}_{\mathrm{KNa}}$	Average conductance of sodium-dependent potassium channel
E_{K}	Nernst reversal potential of potassium channel
τ_{Na}	Time constant of sodium extrusion
α_{Na}	sodium influx through population firing rate
R_{pump}	Strength of the sodium pump
$\mathrm{Na}_{\mathrm{eq}}$	Resting state sodium concentration equilibrium

Table 2.1: Parameter description for the neural mass model.

Symbol	Value	Unit
$Q_p^{\max}$	0.03	ms^{-1}
$Q_i^{\max}$	0.06	ms^{-1}
θ_p, θ_i	-58.5	mV
σ_p	6.7	mV
σ_i	6	mV
τ_p, τ_i	30	ms
C_m	1	$\mu\mathrm{F}/\mathrm{cm}^2$
$\phi_{p/i}$	1.8	ms^{-1}
N_{pp}	144	–
N_{ip}	36	–
N_{pi}	160	–
N_{ii}	40	–
γ_p	$70 \cdot 10^{-3}$	ms^{-1}
γ_i	$58.6 \cdot 10^{-3}$	ms^{-1}
$\bar{g}_{\mathrm{AMPA}}$	1	ms
$\bar{g}_{\mathrm{GABA}}$	1	ms
E_{AMPA}	0	mV
E_{GABA}	-70	mV
E_{L}^p	-66	mV
E_{L}^i	-64	mV
$\bar{g}_{\mathrm{KNa}}$	1.9	$\mathrm{mS}/\mathrm{cm}^2$
E_{K}	-100	mV
τ_{Na}	1.7	ms
α_{Na}	2	$\mathrm{mM} \cdot \mathrm{ms}$
R_{pump}	0.09	mM
$\mathrm{Na}_{\mathrm{eq}}$	9.5	mM

Table 2.2: Parameter values in one-cortical-column model.

the model generates the low-amplitude–high-frequency fluctuations in average membrane potential characteristic of wakefulness. However, with their proposed set of parameter values, firing rate of the pyramidal population is saturated at its maximum, given by $Q_p^{\max}$ of the sigmoid function $Q_p(V_p)$. This can limit evaluation of the model's responses to inputs due to response saturation. Therefore, we propose a different set of bifurcation parameters to place the model in the wakefulness regime.

We choose to upscale average conductance of excitatory synapses to transition from NREM sleep to wakefulness, consistent with SHY and active neuromodulatory inputs of synaptic upscaling from subcortical regions. Excitatory synapses within a cortical column, here now on, are referred to as intra synapses. In wakefulness, intra synapses are upscaled by a factor β_{intra}, in a balanced configuration, i.e., increasing inhibition to regulate overexcitation of each population. Thus, average conductance of inhibitory synapses is upregulated on pyramidal and inhibitory populations by a factor β^p_{GABA} and β^i_{GABA}, respectively. This procedure guarantee that intra-synaptic upscalings are in a balanced configuration by keeping the steady state value of average membrane potential of the pyramidal V_p and inhibitory V_i populations equal to their values in the Up state during NREM sleep (see Table 2.2 to compare parameter values between brain states), in agreement with experimental studies [26, 34]. To avoid, repetition, we factor the term *in a balanced configuration* whenever we use *synaptic upscaling in wakefulness*.

Values of V_p and V_i are determined by simulating 500 trials (4 s long in duration) of NREM dynamics. Distribution of firing rate signals in NREM sleep is bimodal and the polarized peak of distribution is associated with Up states. The peak value of distribution of firing rate signals during Up states is used to compute the steady state value of V_p and V_i in wakefulness. β^p_{GABA} and β^i_{GABA} on pyramidal and inhibitory populations, respectively, is upregulated until these V_p and V_i values are obtained for the corresponding intra-synaptic upscaling, β_{intra}, in wakefulness (see Appendix A.2 for dynamical constraints on β^p_{GABA} and β^i_{GABA} on pyramidal and inhibitory

	$\boldsymbol{\beta_{intra} = 2}$	$\boldsymbol{\beta_{intra} = 3}$	$\boldsymbol{\beta_{intra} = 4}$
$\boldsymbol{\beta^{p}_{\text{GABA}}}$	1.961	3.343	4.724
$\boldsymbol{\beta^{i}_{\text{GABA}}}$	2.165	3.407	4.65

Table 2.3: Values of β^{k}_{GABA} for intra-synaptic upscalings in wakefulness in one-cortical-column model.

populations in one-cortical-column model).

Given above description, the Equations 2.7 and 2.8 transform to :

$$I^{k}_{\text{AMPA}} = \beta_{intra}\ \bar{g}_{\text{AMPA}}\ s^{\text{intra}}_{kp}\ (V_k - E_{\text{AMPA}}), \tag{2.11}$$

$$I^{k}_{\text{GABA}} = \beta^{k}_{\text{GABA}}\ \bar{g}_{\text{GABA}}\ s^{\text{intra}}_{ki}\ (V_k - E_{\text{GABA}}), \tag{2.12}$$

Note that in NREM sleep $\beta_{intra} = 1$ and $\beta^{k}_{\text{GABA}} = 1$ for $k \in \{p,\ i\}$. For the values in wakefulness see Tables 2.3. For full model equations see Appendix A.1.

2.1.2 Two-Cortical-Column Model

We extend the model to two bidirectionally connected cortical columns (see Figure 2.1B). Parameters for each cortical column is the same as in one-cortical-column model (see Table 2.2 and 2.1). We consider that the connectivity between the two cortical columns is symmetric and excitatory due to the longer axons of pyramidal neurons as compared to the short-range axons of inhibitory neurons [114, 115, 116, 117, 118, 119, 120]. For notation convenience, we use $p,\ i$ to refer to pyramidal and inhibitory population in the first cortical column and $p',\ i'$ for populations in the second cortical column (see Table 2.4 for the values of connectivity between two cortical columns).

Symbol	Value	Description
$N_{pp'}$, $N_{p'p}$	16	Mean number of synaptic connections from p to p' (and p' to p)
$N_{ip'}$, $N_{i'p}$	4	Mean number of synaptic connections from p to i' (and p' to i)

Table 2.4: Connectivity parameters between two cortical columns.

Excitatory synapses between two cortical columns, here now on, are referred to as inter synapses, as opposed to the intra synapses in each individual cortical column. In NREM, excitatory connections in two-cortical-column increase the excitation on both pyramidal and inhibitory populations within each cortical column. To counterbalance overexcitation in NREM, average conductance of inhibitory synapses within each cortical column is upregulated by a factor β^{k}_{GABA}, $k \in \{p,\ i,\ p',\ i'\}$. To do so, steady state values of V_p and V_i in one-cortical-column model are determined by simulating a deterministic trial (in the absence of Gaussian noise) in NREM sleep. Then, these values are used to compute β^{k}_{GABA}, $k \in \{p,\ i,\ p',\ i'\}$, in NREM sleep in two-cortical-column model (see Appendix A.2 for dynamical constraints on β^{k}_{GABA}, $k \in \{p,\ i,\ p',\ i'\}$, on pyramidal and inhibitory populations in two-cortical-column model). Please note that due to the symmetry connectivity paradigm the values for pyramidal populations in each cortical columns are equal, so is for inhibitory populations. Note that $\beta^{p/p'}_{\text{GABA}} = 1.18$ and $\beta^{i/i'}_{\text{GABA}} = 1.149$ in NREM sleep in two-cortical-column model.

Synaptic upscalings in wakefulness in two-cortical-column model occurs in two directions: intra-connections and inter-connections. Therefore, synaptic upscalings in wakefulness in two-cortical-column model introduce three synaptic upscaling classes: local-selective ($\beta_{intra} > \beta_{inter}$), homogeneous ($\beta_{intra} = \beta_{inter}$), and distance-selective synaptic upscaling

($\beta_{intra} < \beta_{inter}$). Note that any of the synaptic upscaling cases in wakefulness introduces overexcitation within each cortical columns. To counterbalance overexcitation, average conductance of inhibitory synapses within each cortical column is upregulated by a factor β^k_{GABA}, $k \in \{p,\ i,\ p',\ i'\}$. To do so, we used the values of V_p and V_i in Up states in one-cortical-column model. Then, β^k_{GABA}, $k \in \{p,\ i,\ p',\ i'\}$, is upregulated until these V_p and V_i values are obtained for the corresponding intra- and inter-synaptic upscaling in wakefulness, β_{intra} and β_{inter}, respectively (see Appendix A.2 for dynamical constraints on β^k_{GABA}, $k \in \{p,\ i,\ p',\ i'\}$, in two-cortical-column model). By doing so, we keep the steady state value of V_p and V_i in two-cortical-column model equal to the values in wakefulness and Up states of NREM sleep in one-cortical-column model (see Table 2.5 for values of β^k_{GABA} in wakefulness).

Given above description, the second-order differential equations for AMPAergic postsynaptic responses in the first cortical column due to the inter-cortical-column coupling are as follows:

$$\ddot{s}^{\text{inter}}_{pp'} = \gamma^2_{p'}\ (N_{pp'}\ Q_{p'}(V_{p'}) - s^{\text{inter}}_{pp'})\ - 2\gamma_{p'}\ \dot{s}^{\text{inter}}_{pp'}, \tag{2.13}$$

$$\ddot{s}^{\text{inter}}_{ip'} = \gamma^2_{p'}\ (N_{ip'}\ Q_{p'}(V_{p'}) - s^{\text{inter}}_{ip'})\ - 2\gamma_{p'}\ \dot{s}^{\text{inter}}_{ip'}, \tag{2.14}$$

where $N_{kp'}$ is the mean number of synaptic connections from a presynaptic pyramidal population p' in the second cortical column to postsynaptic populations k, $k \in \{p,\ i\}$, in the first cortical column. Therefore, the AMPAergic current to the postsynaptic population k in the first cortical column is as follows:

$$\begin{aligned} I^k_{\text{AMPA}} = &\ \beta_{intra}\ \bar{g}_{\text{AMPA}}\ s^{\text{intra}}_{kp'}\ (V_k - E_{\text{AMPA}}) \\ &+\ \beta_{inter}\ \bar{g}_{\text{AMPA}}\ s^{\text{inter}}_{kp'}\ (V_k - E_{\text{AMPA}}), \end{aligned} \tag{2.15}$$

$$I^k_{\text{GABA}} = \beta^k_{\text{GABA}}\ \bar{g}_{\text{GABA}}\ s^{\text{intra}}_{ki}\ (V_k - E_{\text{GABA}}), \tag{2.16}$$

where $k \in \{p,\ i\}$. Swapping indexes between the first and second cortical column results in the AMPAergic postsynaptic responses in the second cor-

	$\boldsymbol{\beta_{intra} = 2}$	$\boldsymbol{\beta_{intra} = 4}$	$\boldsymbol{\beta_{intra} = 15}$
$\boldsymbol{\beta_{inter} = 2}$	$\beta_{\text{GABA}}^{p/p'} = 2.268$ $\beta_{\text{GABA}}^{i/i'} = 2.441$	$\beta_{\text{GABA}}^{p/p'} = 3.650$ $\beta_{\text{GABA}}^{i/i'} = 3.683$	$\beta_{\text{GABA}}^{p/p'} = 5.032$ $\beta_{\text{GABA}}^{i/i'} = 4.926$
$\boldsymbol{\beta_{inter} = 4}$	$\beta_{\text{GABA}}^{p/p'} = 2.422$ $\beta_{\text{GABA}}^{i/i'} = 2.579$	$\beta_{\text{GABA}}^{p/p'} = 3.803$ $\beta_{\text{GABA}}^{i/i'} = 3.821$	$\beta_{\text{GABA}}^{p/p'} = 5.185$ $\beta_{\text{GABA}}^{i/i'} = 5.064$
$\boldsymbol{\beta_{inter} = 15}$	$\beta_{\text{GABA}}^{p/p'} = 2.575$ $\beta_{\text{GABA}}^{i/i'} = 2.717$	$\beta_{\text{GABA}}^{p/p'} = 3.957$ $\beta_{\text{GABA}}^{i/i'} = 3.960$	$\beta_{\text{GABA}}^{p/p'} = 5.339$ $\beta_{\text{GABA}}^{i/i'} = 5.202$

Table 2.5: Values of β_{GABA}^{k}, $k \in \{p,\ i,\ p',\ i'\}$, for various synaptic upscalings in wakefulness in two-cortical-column model.

tical column due to the inter-cortical-column coupling (see Appendix A.1 for the full model equations).

2.1.3 Computational pipeline

The computational pipeline consists of two stages. In the first stage, we evaluate spontaneous activity of the model under different scenarios. We also evaluate sensitivity of the model generating the dynamical features of NREM sleep for the parameter of the Gaussian noise varied by 10%. Then, we evaluate changes in the dynamical features of the one-cortical-column model upon intra-synaptic upscaling given the parameters provided in Table 2.2 and Table 2.3. We show that intra-synaptic upscaling generates wakefulness-like dynamics. Note that synaptic upscaling is always in a balanced configuration (see subsection 2.1.1) and we omit "in a balanced configuration" to avoid repetition. Finally, we evaluate the dynamical features of the two-cortical-column model in NREM sleep and intra- and

inter-synaptic upscalings in wakefulness given the parameters provided in Table 2.2, 2.4 and 2.5.

In the second stage, the models are subject to inputs with increasing amplitude. Two different types of inputs are applied: injected inputs and synaptic inputs. Injected inputs correspond to inputs that are modeled as an excitatory electrical current, I^p_{input}, to the pyramidal population and are not synaptic as:

$$\tau_p \dot{V}_p = -I^p_{\text{L}} - I^p_{\text{AMPA}} - I^p_{\text{GABA}} - \tau_p C_m^{-1} I_{\text{KNa}} + I^p_{\text{input}}, \tag{2.17}$$

This procedure resembles current injection techniques, hence the name, and guarantee that the excitatory effect of a given input amplitude is the same for NREM sleep and various intra-synaptic upscalings in wakefulness. Note that I^p_{input} is zero before input onset and after input offset.

Synaptic inputs correspond to inputs that are applied through a synapse mimicking the presynaptic firing of a pyramidal population $Q_{p^{um}}^{\text{input}}$, which is not explicitly modeled, hence the name. We consider that the unmodeled upstream cortical column forms synapses with the pyramidal and inhibitory population in the one-cortical-column model with the mean number of synaptic connections of $N_{pp^{um}}$ and $N_{ip^{um}}$ (16 and 4, respectively), where index um stands for unmodeled cortical cortical column. The AMPAergic postsynaptic response in the cortical column due to firing of unmodeled upstream cortical column follows:

$$\ddot{s}_{kp^{um}}^{\text{input}} = \gamma_{p^{um}}^2 \left(N_{kp^{um}} \, Q_{p^{um}}^{\text{input}} - s_{kp^{um}}^{\text{input}} \right) - 2\gamma_{p^{um}} \, \dot{s}_{kp^{um}}^{\text{input}}, \tag{2.18}$$

where k is either the pyramidal or the inhibitory postsynaptic population of the cortical column model. Given the synapse from unmodeled cortical column could be either inter or intra synapse, the excitatory postsynaptic current to the postsynaptic population k in one-cortical-column corresponding to the input are as follows:

$$I^{k}_{\text{input}} = \beta^{\text{input}}_{inter/intra}\ \bar{g}_{\text{AMPA}}\ s^{\text{input}}_{kp^{um}}\ (V_k - E_{\text{AMPA}}) \tag{2.19}$$

for $k \in \{p, i\}$. Taking into account the postsynaptic currents associated with the input, Equation 2.1 and 2.2 are as follows:

$$\tau_p \dot{V_p} = -I^{p}_{\text{L}} - I^{p}_{\text{AMPA}} - I^{p}_{\text{GABA}} - \tau_p C_m^{-1} I_{\text{KNa}} - I^{p}_{\text{input}}, \tag{2.20}$$

$$\tau_i \dot{V_i} = -I^{i}_{\text{L}} - I^{i}_{\text{AMPA}} - I^{i}_{\text{GABA}} - I^{i}_{\text{input}}, \tag{2.21}$$

Inputs, whether injected or synaptic, are modeled as boxcar function with a duration of 100 ms.

In the second stage of the computational pipeline, we subject the computational models to injected and synaptic inputs. First, the one-cortical-column model is subject to injected and synaptic inputs. Note that injected input to the one-cortical-column model, I^{p}_{input}, is zero before input onset and after input offset. Synaptic input to the one-cortical-column mode is applied through an inter synapse, as:

$$I^{k}_{\text{input}} = \beta^{\text{input}}_{inter}\ \bar{g}_{\text{AMPA}}\ s^{\text{input}}_{kp^{um}}\ (V_k - E_{\text{AMPA}}) \tag{2.22}$$

Given the presence of inter and intra synapses, synaptic upscalings occur in three synaptic upscaling scenarios: local-selective, homogeneous, distance-selective synaptic upscalings. Note that $Q^{\text{input}}_{p^{um}}$ is zero before input onset and after input offset.

Then, we subject the two-cortical-column model to injected and synaptic inputs. Note that in two-cortical-column model, one of the columns receives the inputs directly and, from now on, it is deferred as *perturbed cortical column*. The second cortical column that does not receive inputs directly is referred as *unperturbed cortical column*. Injected inputs to the two-cortical-column model, I_{input}, are applied to the pyramidal population of the perturbed cortical column (for instance see Equation 2.17). Note that $I^{p'}_{\text{input}}$ is zero for pyramidal population in the unperturbed cortical column.

Synaptic inputs to the two-cortical-column model are applied to the perturbed cortical column through an intra synapse, as:

$$I^k_{\text{input}} = \beta^{\text{input}}_{intra}\, \bar{g}_{\text{AMPA}}\, s^{\text{input}}_{kp^{um}}\, (V_k - E_{\text{AMPA}}) \tag{2.23}$$

The choice of intra synapse over inter synapse was due to the saturation of evoked responses in the perturbed column for inter-synaptic upscalings. Note that $Q^{\text{input}}_{p^{um}}$ is zero for the unperturbed cortical column, so is I^k_{input}, $k \in \{p',\ i'\}$.

We applied inputs (whether injected or synaptic inputs) with increasing amplitudes. Amplitude range of inputs is chosen such that the amplitude of evoked responses for the largest input amplitude does not saturate.

Numerical Integration

Simulations are implemented and run in Python, using a stochastic Heun method [123] with a step size of 0.1 ms. The code is available at github. Each simulation (trial) is run independently, with the initial conditions of all variables randomly selected from a uniform distribution. Trials are simulated with the length of 4 s (after discarding the first 4 s from the beginning of the simulation to eliminate transient dynamics towards the stable solution).

In the first stage of the computational pipeline, 500 independent trials are simulated separately to validate standard deviation of the Gaussian noise. Then, 500 trials are simulated separately for NREM sleep and various synaptic upscalings in wakefulness in one- and two-cortical-column models, given the parameters in Table 2.2 and 2.4.

Simulations in the second stage consist of two steps. In the first step, we simulate one deterministic trial (in the absence of Gaussian noise) for one- and two-cortical-column models subject to injected and synaptic inputs to evaluate deterministic responses. We also compute the excitatory-inhibition (E/I) ratio of synaptic currents on pyramidal population in peristimulus intervals for each brain state and in one- and two-cortical-column

model. The E/I ratio was defined as the ratio $|I^p_{\text{AMPA}}|/|I^p_{\text{GABA}}|$ in peristimulus intervals (see Equations 2.11 and 2.12 for two-cortical-column model and Equations 2.15 and 2.16 for two-cortical-column model) when the model is simulated in the absence of the noise (deterministic simulations). That is so, because the average of this ratio computed in the stochastic condition will approach the deterministic value for sufficiently large number of trials. Note that $|\ |$ represents the absolute value function. Note that the baseline E/I ratio is identical when the models are subjected to injected and synaptic inputs.

Next, 500 independent trials are simulated separately for NREM sleep and various synaptic upscalings in wakefulness in one- and two-cortical-column models subjected to injected and synaptic inputs to evaluate stochastic evoked responses.

2.2 Data Analysis

All data analyses were carried out offline with Python. We analyzed firing rate signals from the pyramidal populations.

2.2.1 Analysis of Spontaneous Activities

We used the 500 independent trials for each brain state in the first stage of the computational pipeline to evaluated the dynamical features of spontaneous activities. We used firing rate signals of the pyramidal populations in NREM sleep and various synaptic upscalings in wakefulness in one- and two-cortical-column models. Note that given the symmetric connectivity paradigm in two-cortical-column model, analysis of spontaneous activities were restricted to the pyramidal population in the first cortical columns.

Analysis of Amplitude-Frequency Content of Firing Rate Signals

To evaluate the spread of the spontaneous firing rate values, we computed the normalized distribution of firing rate signals for each brain state separately with a bin size of 1 mV (for instance see Figures S5.2 and S5.9).

To evaluate the degree of similarity between each time series with its lagged version, we also computed auto correlation of firing rate signals and averaged it across 500 trials for each brain state separately (for instance see Figures S5.3 and S5.4).

To quantify frequency content of firing rate signals in each brain state, we computed spectrogram. To do so, we first windowed each firing rate signal in 2 s length intervals with a 90% overlap within which the signal is considered quasi-stationary [124]. Then, each window was tapered with a Hann function to control for the spectral leakage, and we computed the discrete Short-Time Fourier Transform (STFT). Next, the power spectral density (PSD) on each time window was obtained from the amplitude of the STFT. Because each brain state were independently simulated and were not time-locked events, we averaged the PSD over all time windows separately for each brain state [125]. To better observe the wide dynamic range of the firing rate signals, we plotted the spectrogram in units of logarithmic decibels (dB), defined as:

$$\text{dB} = \log_{10}\left(\frac{P}{P_r}\right), \tag{2.24}$$

where P is averaged PSD and P_r the reference PSD, set at 1 $(\text{mV})^2$/Hz. The spectrogram of firing rate signals were averaged over 500 trials for each brain state (for instance see Figures S5.5 and S5.12).

To quantify changes in each frequency band, we computed power ratio of each frequency band with respect to the total power within each signal. Then it was averaged over 500 trials (for instance see Figures S5.6 and S5.13). Finally, distribution of log ratio between high (>30 Hz) and low (<4 Hz) frequency bands was computed to further verify the different dynamics

between NREM and synaptic upscalings in wakefulness (for instance see Figures S5.7 and S5.14)

2.2.2 Analysis of Deterministic Evoked Responses

Trials in the second stage of the computational pipeline were used to evaluated evoked responses in NREM sleep and various synaptic upscalings in wakefulness in one- and two-cortical-column model.

Evoked responses in the absence of Gaussian noise (deterministic evoked responses) were evaluated for one- and two-cortical-column models subjected to injected and synaptic inputs. Amplitude of evoked responses with respect to peristimulus intervals at input offset were extracted for NREM sleep and various synaptic upscalings in wakefulness. Deterministic evoked responses were used to show the pulling and driving effects of synaptic upscaling on amplitude of evoked responses.

In the following, we used two classes of discriminative and generative classification models in machine learning techniques to estimate information content in stochastic evoked responses.

2.2.3 Discriminative Modeling

We used the 500 independent trials for various input amplitudes of injected and synaptic inputs to evaluate information content separately in NREM sleep and various synaptic upscalings in wakefulness for one- and two-cortical-column models. To evaluate information content in stochastic evoked responses, we used discriminative modeling: binomial and multinomial logistic classification models.

Binomial Logistic classification

To measure information detection, we quantified how well firing rates at input offset for a given input amplitude are classified from spontaneous ac-

tivities (firing rates in a random time point in peristimulus intervals). To do so, a Generalized Linear Model (GLM) was derived separately for various input amplitudes in NREM sleep and various synaptic upscalings in wakefulness to model the true distribution $q(y \mid x)$ from which data (y, x) were generated. y is the response variable and takes on either 0 for absence of input (denoting distribution of spontaneous activities) or 1 presence of input (denoting distribution of evoked responses for the given input amplitude). The covariate x is the value of firing rate of pyramidal population in the corresponding distributions. Constructing the GLM proceeded with three steps of model selection, estimation of model parameters and prediction [126].

The Bernoulli distribution was selected for modeling due to the binomial–valued nature of the response variable $y \in \{0, 1\}$. Bernoulli distributions are a member of exponential family [127, 128], and the GLM for Bernoulli distributions is called binomial logistic classification model [126, 129, 128]. Independent simulations across trials satisfied the assumption of independent observations in GLM.

To estimate model parameters and evaluate performance of the classification model on making predictions, samples were split into training and test sets. Samples were composed of 1000 values that were composed of 500 values in the absence of input (class 1) and 500 values for presence of input (class 2). First, a binomial logistic classification model was fitted on training set. The Newton-Raphson iterative optimization technique was carried out to optimize model parameters that maximize the log likelihood function [127, 129, 130].

Then, model performance on making predictions was evaluated on test set. To eliminate the effect of class imbalances in training and tests sets, stratified random sampling was used. 10-fold cross-validation was carried out to partition randomly samples into 10 subsets (folds) of equal size. All samples except the first subset were used as training set to fit the binomial logistic classification model. The held-out subset was used as test set and its samples were predicted by the model to estimate model per-

formance. The procedure repeated for the all other subsets such that all subsets were used only once as test set [131]. Model performance was defined as the proportion of the correctly predicted samples in test set [131]. Classification accuracy score, representing model performance estimate, was averaged over values of 10 performance estimates produced by 10-fold cross-validation [131]. The classification accuracy score was used as the measure that quantifies information detection. The larger value of classification accuracy represents a higher information detection.

Multinomial Logistic classification

To measure information differentiation, we quantified how well firing rates at input offset for various input amplitudes are classified from one another. To do so, a Generalized Linear Model (GLM) was derived separately in NREM sleep and various synaptic upscalings in wakefulness to model the true distribution $q(y \mid x)$ from which data (y, x) were generated. y is the response variable and $y \in \{0, 1, \ldots, N\}$, where N denotes number of inputs. The covariate x is the value of firing rate of pyramidal population in distributions corresponding to each input. Constructing the GLM proceeded with three steps of model selection, estimation of model parameters and prediction [126].

The Multinomial distribution was selected for modeling due to the multinomial–valued nature of the response variable. Multinomial distributions are a member of exponential family, and the GLM for Multinomial distributions is called multinomial logistic classification model (also known as softmax classification). Independent simulations across trials for various input amplitudes satisfied the assumption of independent observations in GLM.

As in *Binomial Logistic classification*, stratified-10-fold cross-validation was used to optimize model parameters and evaluate performance of classification models on making predictions. Training sets were used to estimate model parameters. The Newton-Raphson iterative optimization technique

was implemented to optimize model parameters that maximize the log likelihood function [127, 130, 129]. Then, the model parameters were used to make predictions on test sets. Model performance was defined as the proportion of the correctly predicted samples in test set [131]. Classification accuracy score over 10 performance estimates was used as the measure that quantifies information differentiation. The larger value of classification accuracy represents a higher information differentiation.

2.2.4 Generative Modeling

As an extension, we used generative modeling to evaluate information content in stochastic evoked responses. We used Gaussian discriminant analysis (GDA), as opposed to Naive Bayes approach, since the covariate x is continuous.

Gaussian Discriminant Analysis

To measure information detection we quantified how well firing rates at input offset for a given input amplitudes are classified from spontaneous activities. Binomial GDA models the distribution $q(x \mid y)$ according to a binomial normal distribution. Then, the Bayes' rule was used to model the true distribution $q(y \mid x)$. $q(x \mid y)$ was parameterized with a mean and variance for each response variable. Given the unidimensional covariate x, mean and variance for each response variable were scalar variables.

To measure information differentiation we quantified how well firing rates at input offset for various input amplitudes are classified from one another. Multinomial GDA models the distribution $q(x \mid y)$ according to a multinomial normal distribution. As in Binomial GDA, the Bayes' rule was used to model the true distribution $q(y \mid x)$. $q(x \mid y)$ was parameterized with a mean and variance for each response variable.

As in *Binomial Logistic classification*, stratified-10-fold cross-validation was used separately for Binomial GDA and Multinomial GDA to estimate

model parameters and evaluate performance of the classification models on making predictions. Training sets were used to estimate mean and variance of covariate x for each response variable separately for Binomial GDA and Multinomial GDA. Then, the model parameters were used along with the Bayes' rule to make predictions on test sets separately for Binomial GDA and Multinomial GDA. Model performance was defined as the proportion of the correctly predicted samples in test set [131].

Classification accuracy score in Binomial GDA over 10 performance estimates was used as the measure that quantifies information detection. The larger value of classification accuracy represents a higher information detection. Accordingly, classification accuracy score in Multinomial GDA over 10 performance estimates was used as the measure that quantifies information differentiation. The larger value of classification accuracy represents a higher information differentiation.

2.2.5 Significance Tests and Information Theory

Significance Test

In a different approach from machine learning techniques, we used significance tests to evaluate how well evoked responses in poststimulus intervals are different from spontaneous activities in peristimulus intervals.

Since the number of trials was large (500 trials) for the Central Limit Theorem to hold, we computed an independent t-test value (*t*-value) at every time point as $t = (\bar{x}_1 - \bar{x}_2)/(s\sqrt{2/n})$, where $\bar{x}_1$ and $\bar{x}_2$ are averages across time-locked trials of firing rate signals in poststimulus intervals and peristimulus intervals, respectively. s is sample standard deviation, whose variance is $s^2 = ((n-1)s_1^2 + (n-1)s_2^2)/(2n-1)$. $s_{1/2}^2$ is variance of variable $x_{1/2}$ across trials. Statistical significance was set at p-values below 0.05 and Bonferroni correction was used to control for family-wise error in multiple comparisons of temporal t-tests. The consecutive time points with a significant difference were referred as t-cluster statistic [132]. The area

of t-cluster statistic was used as the measure that quantifies information detection. The larger value of the area of t-cluster statistic represents a higher information detection.

Information Theory

In a different approach from machine learning techniques, we used information theory to evaluate how well firing rates at input offset are informative about applied inputs. Mutual information measures information about an input in probability distribution of firing rates as follows [107]:

$$I(R, s_j) = \sum_i p(r_i|s_j) \log_2 \frac{p(r_i|s_j)}{p(r_i)}, \tag{2.25}$$

where $I(R, s_j)$ is the mutual information between distribution of firing rates and input s_j. $p(r_i)$ and $p(r_i|s_j)$ are, respectively, the probability that firing rates take the value r_i and the conditional probability that firing rates take the value r_i for a given input s_j. Summing values of mutual information for all inputs results in a scalar mutual information value $I(R, S)$. The scalar value of mutual information, $I(R, S)$, is a good predictive measure of information differentiation. A larger separation among distribution of evoked responses to various input amplitudes results in a larger mutual information value. Therefore, the larger value of mutual information represents a higher information differentiation. Note that to compute mutual information in Equation 2.25, we discretized firing rate signals into 0.3 Hz bins to compute the probabilities.

2.2.6 Result Validation

It is important to note that evoked neural responses are temporally dynamic. Unlike significance test, other methods to quantify information content were restricted to the evoked responses at input offset. Moreover,

to quantify information detection, distribution of evoked responses at input offset were evaluated against distribution of spontaneous activities at a random time point in peristimulus intervals.

To evaluate validity of our result for the choice of time points different than used, we first quantified information detection. The distribution of evoked responses at input offset were evaluated against the distribution of spontaneous activities at a another random time point in peristimulus intervals. Then, we quantified information detection and differentiation at different time points than at input offset. We evaluated distribution of evoked responses at 20 ms prior and post input offset to compute information content in the temporal evoked responses. The reason that we avoided temporal classification across the time series of evoked responses was due to the long-lasting and heavy computational jobs for optimization of model parameters.

Above procedure was carried out for discriminative models, generative models and mutual information. In addition, we used two different discretization parameters (0.2 Hz bins and 0.6 Hz bins) for mutual information to test validity of our results for different bin size used in mutual information.

Chapter 3

RESULTS

In the following chapter, we present results of the computational pipeline described in Section 2.1.3. Briefly, the computational pipeline consists of two stages. In the first section we present results of the first stage of the computational pipeline: evaluation of the spontaneous activity of the model under different scenarios. We also evaluate sensitivity of the model generating the dynamical features of NREM sleep for the parameter of the Gaussian noise varied by 10%. Then, we evaluate changes in the dynamical features of the one-cortical-column model upon intra-synaptic upscaling. We show that intra-synaptic upscaling generates wakefulness-like dynamics. Note that synaptic upscaling is always in a balanced configuration (see Section 2.1.1) and we omit "in a balanced configuration" to avoid repetition. Finally, we evaluate the dynamical features of the two-cortical-column model in NREM sleep and intra- and inter-synaptic upscalings in wakefulness.

Next, we present results for the second stage of the computational pipeline. In the second stage, the models are subject to inputs with increasing amplitude. Two different types of inputs are applied: injected inputs and synaptic inputs. Injected inputs correspond to inputs that are modeled as an excitatory electrical current to the pyramidal population and are not

synaptic (see Equation 2.17). This procedure resembles current injection techniques, hence the name. Synaptic inputs correspond to inputs that are applied through a synapse mimicking the presynaptic firing of a pyramidal population, which is not explicitly modeled, hence the name (for instance see Equation 2.18). We consider that the unmodeled upstream cortical column forms synapses with the pyramidal and inhibitory population in the one-cortical-column model with the mean number of synaptic connections of $N_{pp^{um}}$ and $N_{ip^{um}}$ (16 and 4, respectively), where index um stands for unmodeled cortical cortical column. Inputs, whether injected or synaptic, are modeled as boxcar function with a duration of 100 ms.

In the second stage of the computational pipeline, we subject the computational models to injected and synaptic inputs. First, the one-cortical-column model is subject to injected and synaptic inputs. Note that inputs are zero before input onset and after input offset. Then, we subject the two-cortical-column model to injected and synaptic inputs. Note that in two-cortical-column model, one of the columns receives the inputs directly and, from now on, it is deferred as *perturbed cortical column*. The second cortical column that does not receive inputs directly is referred as *unperturbed cortical column*.

We also compute the excitatory-inhibition (E/I) ratio of synaptic currents on pyramidal population in peristimulus intervals for each brain state and in one- and two-cortical-column model. The E/I ratio was defined as the ratio $|I^p_{\text{AMPA}}|/|I^p_{\text{GABA}}|$ in peristimulus intervals (see Equations 2.11 and 2.12 for two-cortical-column model and Equations 2.15 and 2.16 for two-cortical-column model) when the model is simulated in the absence of the noise (deterministic simulations). That is so, because the average of this ratio computed in the stochastic condition will approach the deterministic value for sufficiently large number of trials. Note that $|\ |$ represents the absolute value function. Note that the baseline E/I ratio is identical when the models are subjected to injected and synaptic inputs. Results of the computational pipeline are provided in the ascending order in section 2-5.

We applied inputs (whether injected or synaptic inputs) with increasing

amplitudes. Amplitude range of inputs is chosen such that the amplitude of evoked responses for the largest input amplitude does not saturate. It is important to note that the analysis in this chapter are restricted to the firing rate of pyramidal populations measured at input offset. Finally, we show in that our results are valid at time points different than input offset. We also use a battery of different methods and show that our results are independent of the analysis used.

3.1 Spontaneous Brain States

The one-cortical-column model contains only one cortical column and is able to generate electrophysiological signals associated with NREM sleep (Figure 3.1A). Compared to wakefulness, simulated signals in NREM sleep reproduce three well-observed features: (1) firing rate signals show large amplitude fluctuations in NREM sleep, (2) distribution of firing rate signals is bimodal and (3) they carry more spectral power within the SO (<1 Hz) and delta (1-4 Hz) frequency bands than in wakefulness. Dynamical features of NREM sleep are robust to the changes in the standard deviation of the Gaussian noise in the model (see Figure S5.1 - S5.7).

In agreement with SHY (see Section 1.3.4), intra-synaptic upscaling by a factor β_{intra} (see Equation 2.11) shifts gradually the dynamics from NREM-like to wakefulness-like dynamics (see Figure S5.8 - S5.14). Spontaneous firing rate signals show low amplitude fluctuations in wakefulness (W) compared to NREM sleep (see Figure 3.1B). Distribution of firing rate signals shifts from a bimodal distribution in NREM sleep to a unimodal distribution in wakefulness. Moreover, firing rate signals carry lower spectral power within the SO (<1 Hz) and delta (1-4 Hz) frequency bands in wakefulness than in NREM sleep.

These results are reproduced in the two-cortical-column model as well (see Figure S5.15 - S5.21). Firing rate signals in NREM sleep in the two-cortical-column model carry more power on lower frequency bands and

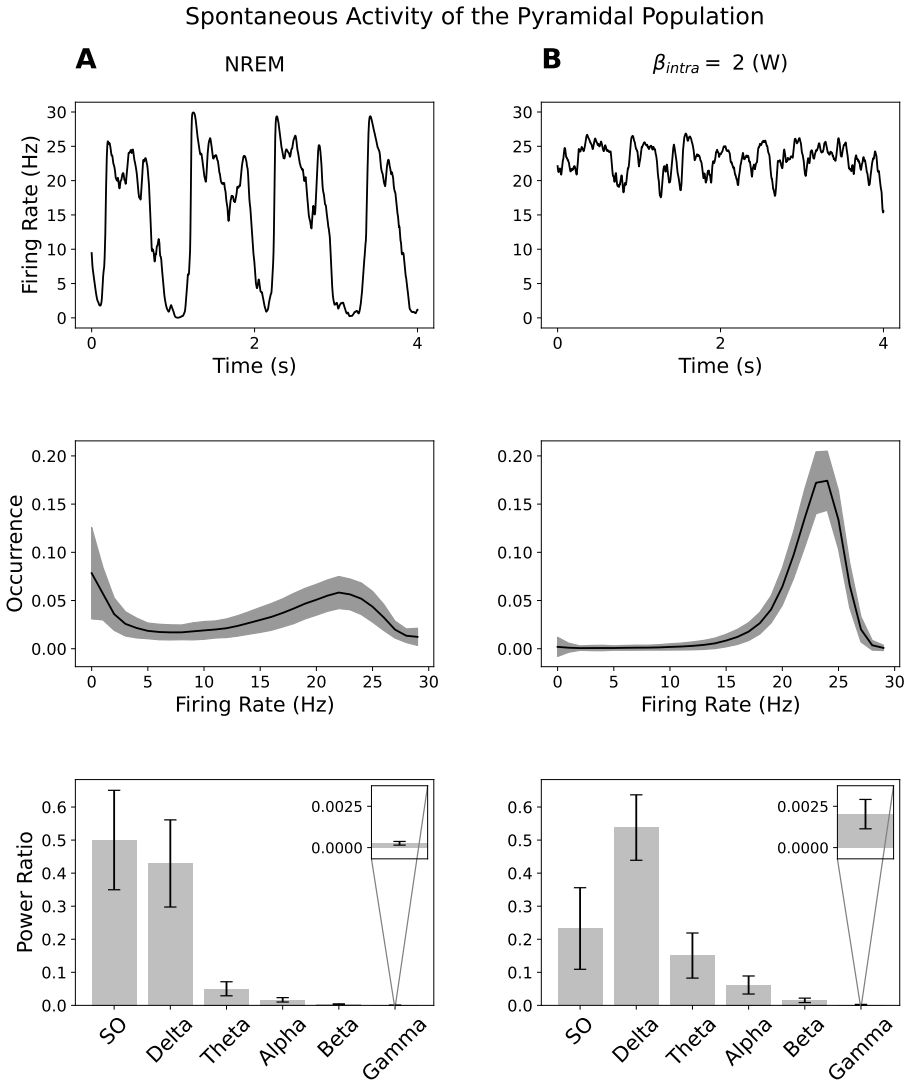

Figure 3.1: Spontaneous activity in NREM sleep and wakefulness (W) in the one-cortical-column model. (**A**) Electrophysiological features of NREM sleep. *Top*. Simulated firing rate signals showing large amplitude fluctuations in NREM sleep between periods of sustained activity (Up state) and silent (next page)

Figure 3.1 *(previous page)*: activity (Down states). *Middle*. Average of the distribution firing rate, which is a bimodal distribution in NREM sleep. Shaded area corresponds to standard deviation over 500 trials. *Bottom*. Firing rate signals carry more spectral power within the SO (<1 Hz) and delta (1-4 Hz) frequency bands in NREM sleep. Error bar shows standard deviation over 500 trials. (**B**) Results as in panel **A**, but for wakefulness (W). *Top*. Simulated signals showing low amplitude fluctuations in wakefulness. *Middle*. Distribution of firing rate signals is unimodal in wakefulness. *Bottom*. Firing rate signals in wakefulness carry less spectral power within the SO (<1 Hz) compared to the ones' in NREM sleep. Signals in wakefulness carry more spectral power within higher frequencies than in NREM sleep (see the inset).

have larger amplitude of fluctuations compared to the ones' in wakefulness. However, it is important to note that the dynamical features of NREM sleep is compromised upon connecting two cortical columns with respect to the ones for the one-cortical-column model. These results can reflect experimental observations that cortical de-afferentation boosts dynamical features of NREM sleep [2].

3.2 Perturbed Brain States

In this section we present results of subjecting the one- and two-cortical-column models to injected and synaptic inputs.

3.2.1 Injected Inputs to the One-Cortical-Column Model: Pulling Effect on Information Content

We applied injected inputs with amplitude ranging from 10 mV to 80 mV by steps of 10 mV to the pyramidal population in the one-cortical-column model. This procedure is suitable to show the pulling effect (as introduced

in Section 1.3.4) of intra-synaptic upscaling on response amplitude and information content.

Deterministic Responses

Simulations in the absence of noise (deterministic evoked responses) show that intra-synaptic upscaling (i.e.,increasing β_{intra}) generates a pulling effect on evoked responses (see Figure 3.2A and Figure S5.22A), i.e, decrease of the evoked responses. Amplitude of evoked responses (with respect to peristimulus activity) is larger in NREM sleep than in wakefulness. It is important to note that these results are in agreement with observations *in vitro* where increasing spontaneous synaptic activities in a balanced configuration attenuates amplitude of evoked responses [105]. Intra-synaptic upscaling in a balanced configuration in wakefulness attenuates the E/I ratio of the pyramidal population in peristimulus intervals (see Figure 3.2B). Interestingly, changes in the E/I ratio in prestimulus interval correlates with the pulling effect. As the E/I ratio of the pyramidal population decreases pulling effects on evoked responses to inputs are larger.

Stochastic Responses

To evaluate pulling effects on information content, 500 independent trials in the presence of Gaussian noise were simulated (see Appendix A.1 for the full model equations). Evoked responses to inputs in NREM sleep have a slow wave shape, on average, that consists of two deflections (see Figure S5.23). The first deflection reflects an increase in firing rate above peristimulus values (corresponding to a poststimulus neuronal activity in response to inputs). The second deflection reflects a decrease in firing rate that extends beyond input offset (corresponding to a poststimulus suppression of neuronal activity). Evoked responses in wakefulness consist of an increase in firing rate above peristimulus values (corresponding to a poststimulus neuronal activity in response to inputs), whereas the poststimulus

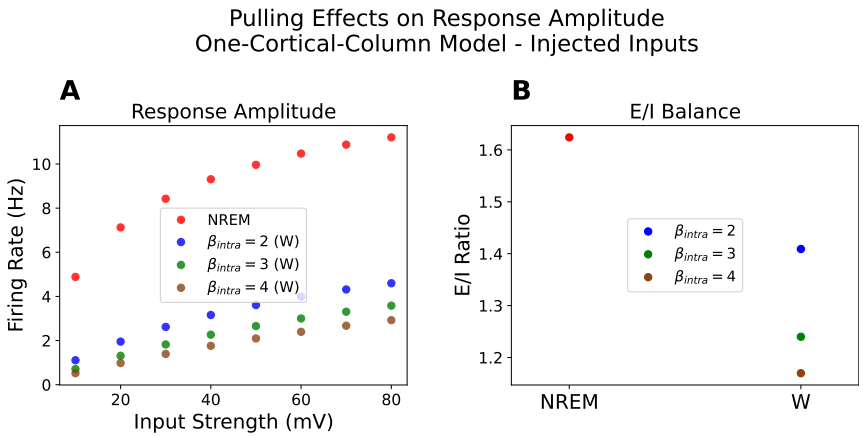

Figure 3.2: Pulling effect due to intra-synaptic upscaling on amplitude of evoked responses in the one-cortical-column model. (**A**). Amplitude of deterministic firing rate evoked responses at input offset for various input amplitudes (injected inputs) in NREM (red) and various intra-synaptic upscalings in wakefulness (color coded). Amplitude of evoked responses increases with increasing input amplitude. However, it decreases with increasing intra-synaptic upscaling in wakefulness, showing the pulling effect. (**B**). The E/I ratio in peristimulus intervals for NREM (red) and various intra-synaptic upscalings in wakefulness (color coded as in panel **A**). Intra-synaptic upscaling in a balanced configuration in wakefulness cause a decrease of the E/I ratio. Note that the decrease in the E/I ratio in peristimulus intervals correlates with the pulling effect due to intra-synaptic upscaling.

suppression of neuronal activity is either absent or not comparable to the ones in NREM sleep (see Figure S5.23 and S5.24). These results are in agreement with results obtained by Nir and colleagues [66].

Evoked responses at input offset have larger values, on average, and smaller standard deviation with increasing input amplitude in both NREM sleep and wakefulness (see Figure S5.25). Moreover, increasing the intra-synaptic upscaling in wakefulness increases the standard deviation of evoked responses (see Figure S5.25 and S5.26). The decrease in amplitude and increase in standard deviation of evoked responses as synaptic upscaling increases in wakefulness causes the distribution of evoked responses to various input amplitudes become closer to the distribution of spontaneous activities (for instance see Figure S5.27). Moreover, it causes the distribution of evoked responses for various input amplitudes to overlap. Therefore, increasing intra-synaptic upscaling in wakefulness attenuates information detection and differentiation.

To quantify changes in information detection and differentiation, discriminative models (logistic classification) are implemented (see Section 2.2.3). Information detection enhances with increasing input amplitude in both NREM sleep and wakefulness (see Figure 3.3A). Moreover, intra-synaptic upscaling attenuates information detection in wakefulness. Likewise, information differentiation is larger in NREM sleep and attenuates with increasing intra-synaptic upscaling in wakefulness (see Figure 3.3B). The E/I ratio in peristimulus intervals (see Figure 3.2B) is a good predictive of attenuation of information detection and information differentiation with increasing intra-synaptic upscaling in wakefulness. It in is interesting that the strength of E/I ratio in baseline predicts the strength of pulling effects due to synaptic upscaling.

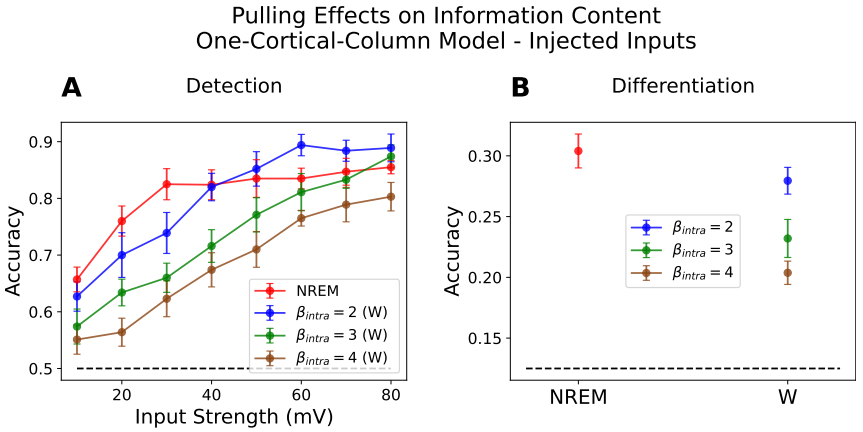

Figure 3.3: Pulling effect due to intra-synaptic upscaling on information content in the one-cortical-column model. (**A**). Information detection (see Section 2.2.3) at input offset for various input amplitudes (injected inputs) in NREM (red) and various intra-synaptic upscalings in wakefulness (color coded). Information detection increases with increasing input amplitude. However, it decreases with increasing intra-synaptic upscaling in wakefulness. (**B**). Information differentiation at input offset for NREM (red) and various intra-synaptic upscalings in wakefulness (color coded as in panel **A**). Increasing intra-synaptic upscaling in wakefulness decreases information differentiation. Error bar shows 95 percent confidence interval. Black dash line represents the chance-level accuracy $= \frac{1}{\#\text{input amplitudes}}$.

3.2.2 Synaptic Inputs to the One-Cortical-Column Model: Driving Effect on Information Content

Synaptic inputs with amplitude ranging from 0.01 ms^{-1} to 0.07 ms^{-1} by a step size of 0.01 ms^{-1} are applied through an inter-synapse. Inputs, firing rate of the unmodeled upstream cortical column, are implemented as a boxcar function with a duration of 100 ms. Given the presence of inter synapse, synaptic upscalings occur in three synaptic upscaling scenarios: local-selective, homogeneous, distance-selective synaptic upscalings (as introduced in Section 1.3.4).

Deterministic Responses

Deterministic evoked responses show that increasing the inter-synaptic upscaling when the intra-synaptic upscaling in wakefulness is kept constant generates driving effects on evoked responses (see Figure S5.22B). Amplitude of evoked responses at input offset is larger in NREM sleep compared to wakefulness (see Figure 3.4A-C). Moreover, amplitude of evoked responses increases with increasing inter-synaptic upscaling (i.e., increasing β_{inter}) when intra-synaptic upscaling (i.e., β_{intra}) in wakefulness is kept constant. It is important to note that the opposite upscaling policy, i.e., intra-synaptic upscaling when inter-synaptic upscaling is kept constant, shows the pulling effect on amplitude of evoked responses (see Figure 3.4D). These results show that synaptic upscaling in the presence of synaptic inputs introduces a competition between pulling and driving effects on evoked responses.

Stochastic Responses

Stochastic evoked responses at offset have larger values, on average, and smaller standard deviation with increasing input amplitude in both NREM sleep and wakefulness (see Figure S5.28). Increasing inter-synaptic up-

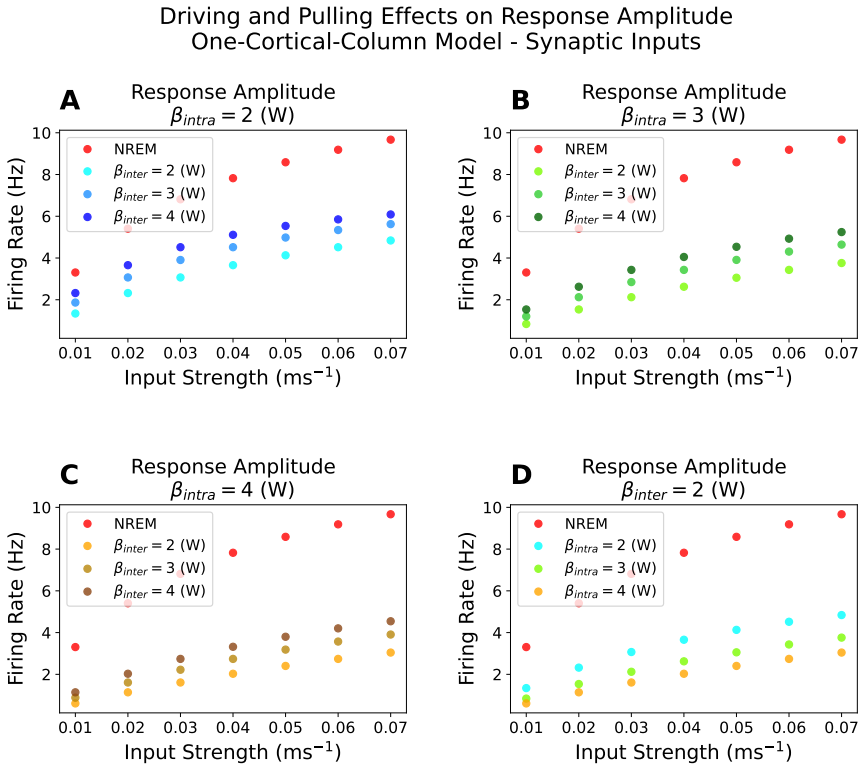

Figure 3.4: Driving and pulling effect due to synaptic upscaling on amplitude of evoked response in the one-cortical-column model. (**A**). Amplitude of deterministic evoked responses at input offset for various input amplitudes (Inter-synaptic inputs to the one-cortical-column model) in NREM (red) and various inter-synaptic upscalings when intra-synaptic upscaling in wakefulness is kept constant at $\beta_{intra} = 2$ (color coded). The driving effect is revealed in the increase of the amplitude of evoked responses with increasing inter-synaptic upscaling in wakefulness. Results as in panel **A**, but for $\beta_{intra} = 3$ (**B**) and $\beta_{intra} = 4$ (**C**). (**D**). Pulling effect due to intra-synaptic upscaling on amplitude of deterministic evoked responses when inter-synaptic upscaling in wakefulness is kept constant at $\beta_{inter} = 2$. Results in panel **D** reproduce results in Figure 3.2A.

scaling when intra-synaptic upscaling is kept constant in wakefulness decreases standard deviation of evoked responses (see Figure S5.29A-C). The increase in amplitude and decrease in standard deviation of evoked responses with increasing inter-synaptic upscaling when intra-synaptic upscaling is kept constant in wakefulness causes the distribution of evoked responses to various input amplitudes become distant to the distribution of spontaneous activities. Moreover, it cause the distribution of evoked responses for various input amplitudes to become distant to each other. Therefore, increasing inter-synaptic upscaling in wakefulness enhances information detection and differentiation. On the other hand, increasing intra-synaptic upscaling, when inter-synaptic upscaling is kept constant, decreases amplitude and increases standard deviation of evoked responses (for instance see second row in Figure S5.28, and Figure S5.29), hence resulting in attenuation of information content, as in injected inputs in the previous Section 3.2.1.

Logistic classification techniques quantified the above descriptions. Information detection enhances with increasing input amplitude both in NREM sleep and wakefulness (see Figure 3.5A-C). Increasing inter-synaptic upscaling when intra-synaptic upscaling is kept constant in wakefulness enhances information detection (for instance see Figure 3.5A). However, intra-synaptic upscaling when inter-synaptic upscaling is kept constant in wakefulness attenuates information detection. Note that amplitude of evoked responses in NREM sleep is larger than in any synaptic upscalings in wakefulness (see Figure 3.4 and S5.22B). However, larger standard deviation of evoked responses in NREM sleep (see Figure S5.29D) prevents information detection compared to wakefulness.

Likewise, information differentiation in NREM sleep is not larger than in wakefulness (see Figure 3.5D). Nevertheless, information differentiation enhances with increasing inter-synaptic upscaling when intra-synaptic upscaling is kept constant in wakefulness. On the other hand, information differentiation attenuates with increasing intra-synaptic upscaling when inter-synaptic upscaling is kept constant in wakefulness.

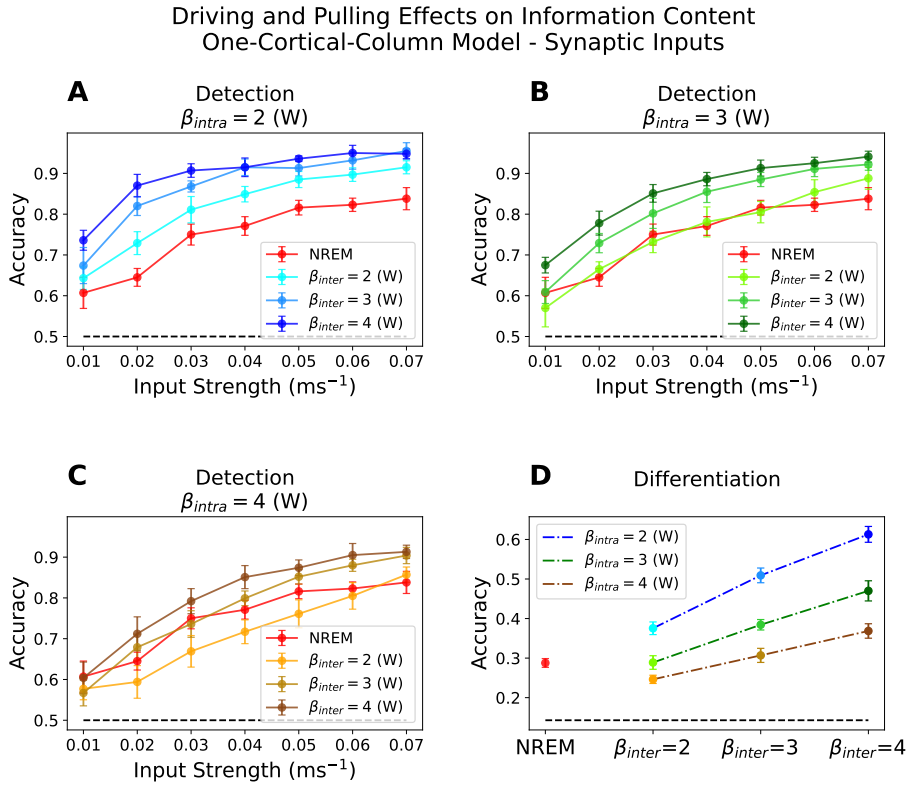

Figure 3.5: Driving and pulling effect due to synaptic upscaling on information content in the one-cortical-column model. (**A**). Information detection at input offset for various input amplitudes (Inter-synaptic inputs) in NREM (red) and various inter-synaptic upscalings when intra-synaptic upscaling in wakefulness is kept constant at $\beta_{intra} = 2$ in wakefulness (color coded). Information detection increases with increasing inter-synaptic upscaling, a hallmark of driving effect. Results as in panel **A**, but for $\beta_{intra} = 3$ (**B**) and $\beta_{intra} = 4$ (**C**). Note that information detection decreases overall with increasing intra-synaptic upscaling, which directly show the pulling effect. (**D**). Information differentiation at input offset for NREM (red) and various synaptic upscalings in wakefulness (color coded as in panel **A**, **B** and **C**). Information differentiation increases with increasing inter-synaptic upscaling, when intra-synaptic upscaling is kept constant in (next page)

Figure 3.5 *(previous page)*: wakefulness (dash lines color coded in legend). On the other hand, information differentiation decreases with increasing intra-synaptic upscaling, when inter-synaptic upscaling is kept constant in wakefulness. Error bar shows 95 percent confidence interval. Black dash line represents the chance-level accuracy $= \frac{1}{\#\text{input amplitudes}}$.

Synaptic upscaling of both intra-connections and inter-connections introduces three synaptic upscaling scenarios: local-selective ($\beta_{intra} > \beta_{inter}$), homogeneous ($\beta_{intra} = \beta_{inter}$), and distance-selective synaptic upscaling ($\beta_{intra} < \beta_{inter}$). Rearranging results according to these scenarios shows that information content in distance selective synaptic upscaling is larger than homogeneous and local-selective synaptic upscaling in wakefulness (see Figure 3.6).

3.2.3 Injected Inputs to the Two-Cortical-Column Model: Information Propagation

Injected inputs with amplitude ranging from 10 mV to 130 mV by a step size of 10 mV are applied to the pyramidal population in the two-cortical-column model. The increase in input range compared to Section 3.2.1 is the result of additional pulling effects due to the second cortical column, which allows us to explore larger input amplitudes before evoked responses in the perturbed column saturate.

Deterministic Responses

Deterministic evoked responses in the perturbed column reproduce the results in Section 3.2.1. Amplitude of evoked responses is larger in NREM sleep than at any synaptic upscalings in wakefulness. Here, both inter- and intra-synaptic upscaling generate a pulling effect on the amplitude of evoked responses in wakefulness since inputs are applied independent of

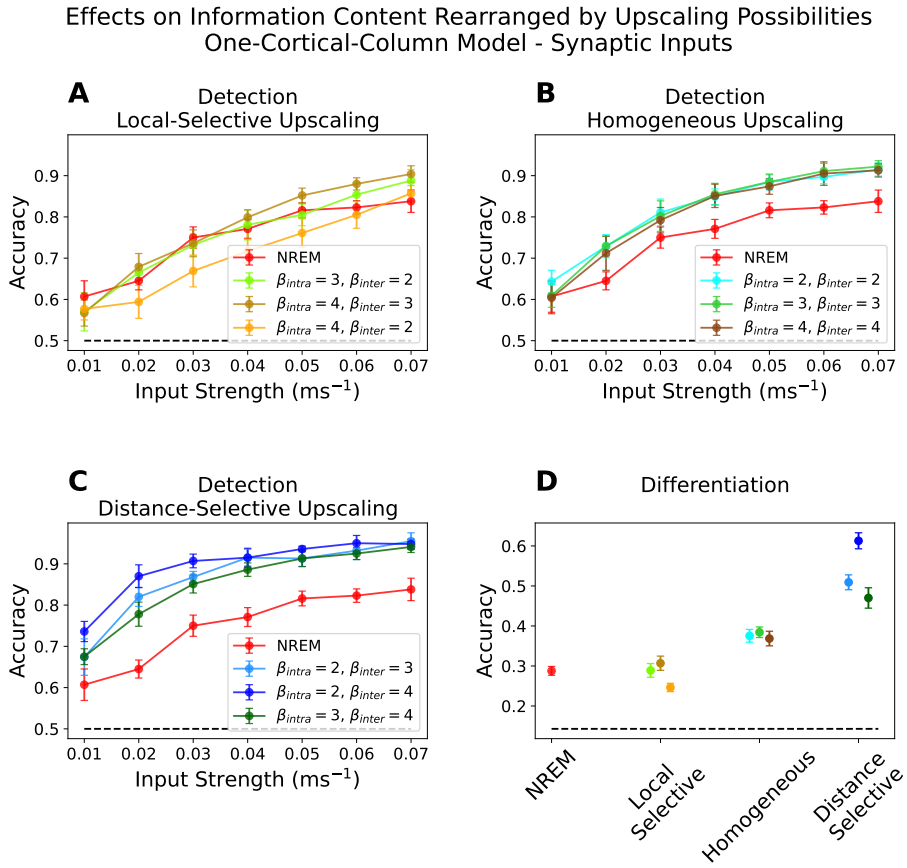

Figure 3.6: Driving and pulling effect due to synaptic upscaling on information content in the one-cortical-column model rearranged by synaptic upscaling scenarios. Figures are as in Figure 3.5, but rearranged based on synaptic upscaling scenarios in wakefulness. Information detection for local-selective (**A**), homogeneous (**B**) and distance-selective (**C**) synaptic upscaling scenarios in wakefulness. (**D**) Information differentiation (as in Figure 3.5D) for NREM and three various synaptic upscaling scenarios (color coded as in panel **A**-**C**) in wakefulness. Error bar shows 95 percent confidence interval. Black dash line represents the chance-level accuracy $= \frac{1}{\#\text{input amplitudes}}$.

synapse (see Figure 3.7A-C).

As in the one-cortical-column model, synaptic upscaling in wakefulness in a balanced configuration attenuates the E/I ratio of the pyramidal population (see Figure 3.7D). As the E/I ratio of the pyramidal population decreases, the pulling effect on evoked responses to inputs increases. It is important to note that decrease in the E/I ratio is larger for increasing intra-synaptic upscaling than inter-synaptic upscaling. This is due to the larger number of intra-connections than inter-connections in the model.

On the other hand, deterministic evoked responses in the unperturbed column reproduce driving and puling effects of synaptic upscaling. Inputs travel indirectly to the unperturbed column through inter-synapses. Therefore, increasing inter-synaptic upscaling when intra-synaptic upscaling is kept constant in wakefulness generates driving effects in the unperturbed column (see Figure 3.8A-C). On the other hand, increasing intra-synaptic upscaling when inter-synaptic upscaling is kept constant in wakefulness generates pulling effects in the unperturbed column (see Figure 3.8D).

Stochastic Responses

Stochastic evoked responses in NREM sleep have a slow wave shape, on average, consisting of a poststimulus neuronal activity followed by a poststimulus suppression of neuronal activity in response to inputs (see Figure S5.30). Evoked responses in wakefulness contain only a poststimulus neuronal activity and lacked the suppression of neuronal activity (see Figure S5.30 and S5.31)

Logistic classification on evoked responses at offset shows that information detection decreases with increasing intra-synaptic upscaling in wakefulness (see Figure 3.9A). Pulling effects of intra-synaptic upscaling on information content in the perturbed column reproduces results in Section 3.2.1.

Despite the obvious decrease in amplitude of evoked responses for increasing inter-synaptic upscaling, the pulling effect on information detec-

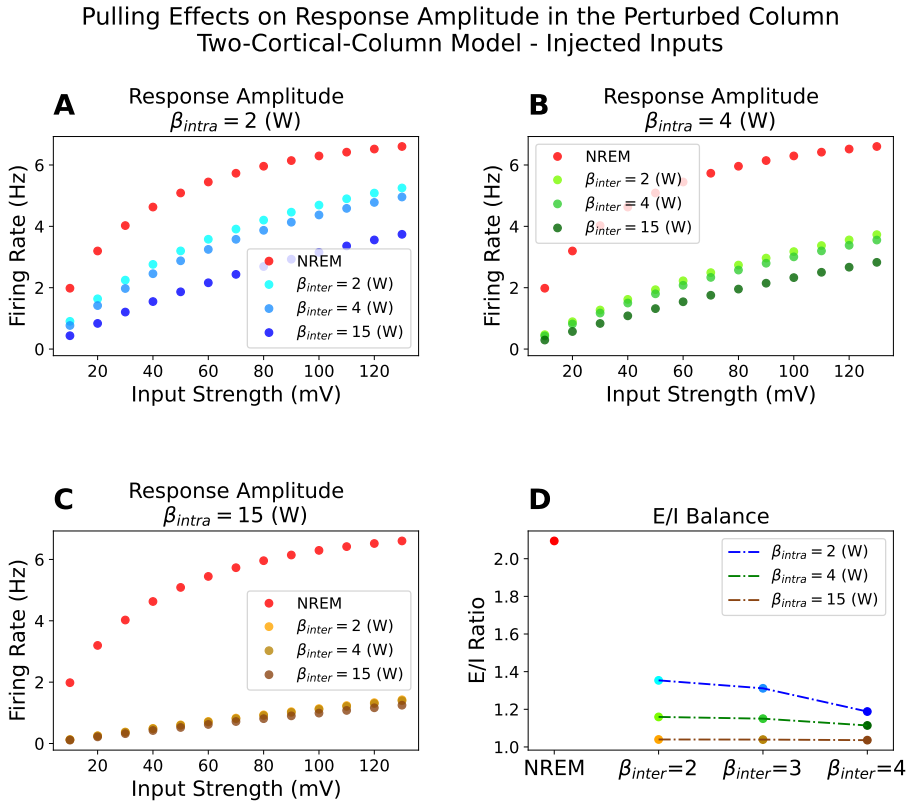

Figure 3.7: Pulling effects of synaptic upscaling on amplitude of evoked responses in the two-cortical-column model. Evoked responses corresponds to the perturbed column. (**A**). Amplitude of deterministic firing rate evoked responses at input offset for various input amplitudes (injected inputs) in NREM (red) and various inter-synaptic upscalings, when intra-synaptic upscaling in wakefulness is kept constant at $\beta_{intra} = 2$ (color coded). Amplitude of evoked responses decreases with increasing inter-synaptic upscaling, which shows the pulling effect. Results as in panel **A**, but for when intra-synaptic upscaling in wakefulness is kept constant at $\beta_{intra} = 4$ (**B**) and $\beta_{intra} = 15$ (**C**). Note that amplitude of evoked responses decreases overall with increasing intra-synaptic upscaling: pulling effect. (**D**). The E/I ratio in peristimulus intervals for NREM (red) and various synaptic upscalings in wakefulness (color coded as in panel **A**-**C**). Synaptic (next page)

Figure 3.7 *(previous page)*: upscaling in a balanced configuration in wakefulness decreases the E/I ratio in peristimulus intervals. The decrease in the E/I ratio correlates with the pulling effects of inter- and intra-synaptic upscalings on amplitude of evoked responses to inputs. Note that the decrease in the E/I ratio for increasing intra-synaptic upscaling is larger than those for increasing inter-synaptic upscaling, resulting in a larger pulling effect on amplitude of evoked responses for intra-synaptic upscaling.

tion is not obvious. It occurs due to the competition between pulling and driving effects on the distribution of spontaneous activities and distribution of evoked responses (see Figure S5.32). It is so because the standard deviation of distribution of spontaneous activities also changes as a function of synaptic upscaling. Spontaneous activity is the response of the model to the Gaussian noise. Gaussian noise is implemented through an intra-synapse. Therefore, intra-synaptic upscaling is a competition between pulling and driving effects on amplitude of spontaneous responses to the Gaussian noise. Pulling effect is due to the intra-synapse representing recurrent synapses and driving effect is due to the intra-synapse that carries Gaussian noise to cortical column. On the other hand, increase in inter-synaptic upscaling generates pulling effects and decreases standard deviation of distribution of spontaneous activities (see Figure S5.33).

Nevertheless, synaptic upscaling does not enhance information detection in the unperturbed column unless inter-synaptic upscaling is larger than intra-synaptic upscaling (see Figure 3.9B). This is due to the competition of intra- and inter-synaptic upscaling on amplitude and standard deviation of evoked responses and spontaneous activities (see Figure S5.34).

Likewise, information differentiation in the perturbed column in NREM sleep is larger than at any synaptic upscaling in wakefulness (see Figure 3.10A). Moreover, it diminishes with increasing intra-synaptic upscaling when inter-synaptic upscaling is kept constant in wakefulness. On the other hand, information differentiation in the unperturbed column in wake-

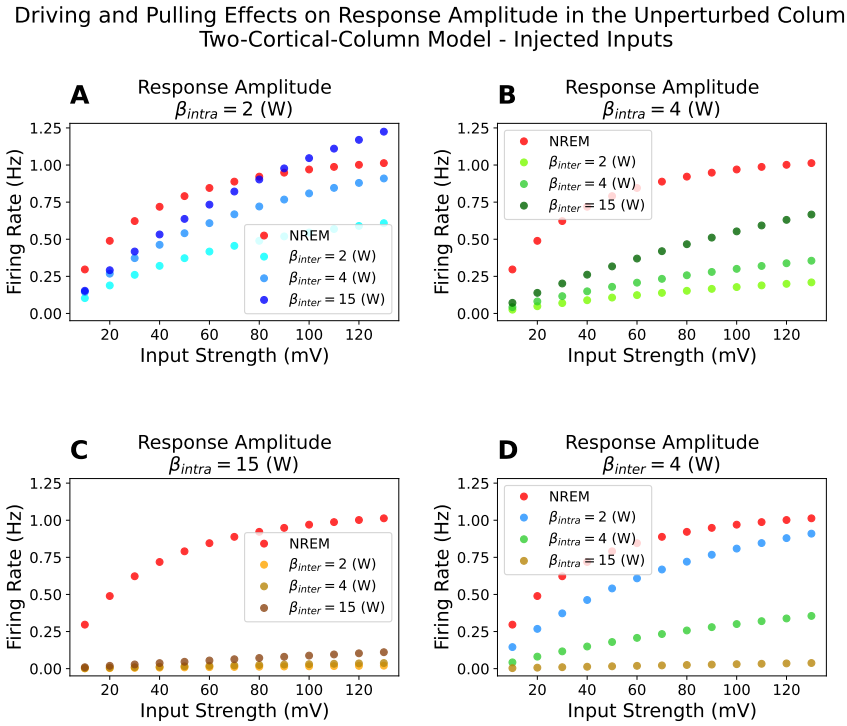

Figure 3.8: Driving and pulling effect due to synaptic upscaling on the amplitude of evoked response in the two-cortical-column model. Evoked responses corresponds to the unperturbed column. (**A**). Amplitude of deterministic firing rate evoked responses at input offset for various input amplitudes (injected inputs) in NREM (red) and various inter-synaptic upscalings, when intra-synaptic upscaling in wakefulness is kept constant at $\beta_{intra} = 2$ (color coded). Amplitude of evoked responses increases with increasing inter-synaptic upscaling, which shows the driving effect. Results as in panel **A**, but for when intra-synaptic upscaling in wakefulness is kept constant at $\beta_{intra} = 4$ (**B**) and $\beta_{intra} = 15$ (**C**). (**D**). Pulling effect due to intra-synaptic upscaling on amplitude of evoked responses when inter-synaptic upscaling in wakefulness is kept constant at $\beta_{inter} = 2$: pulling effect.

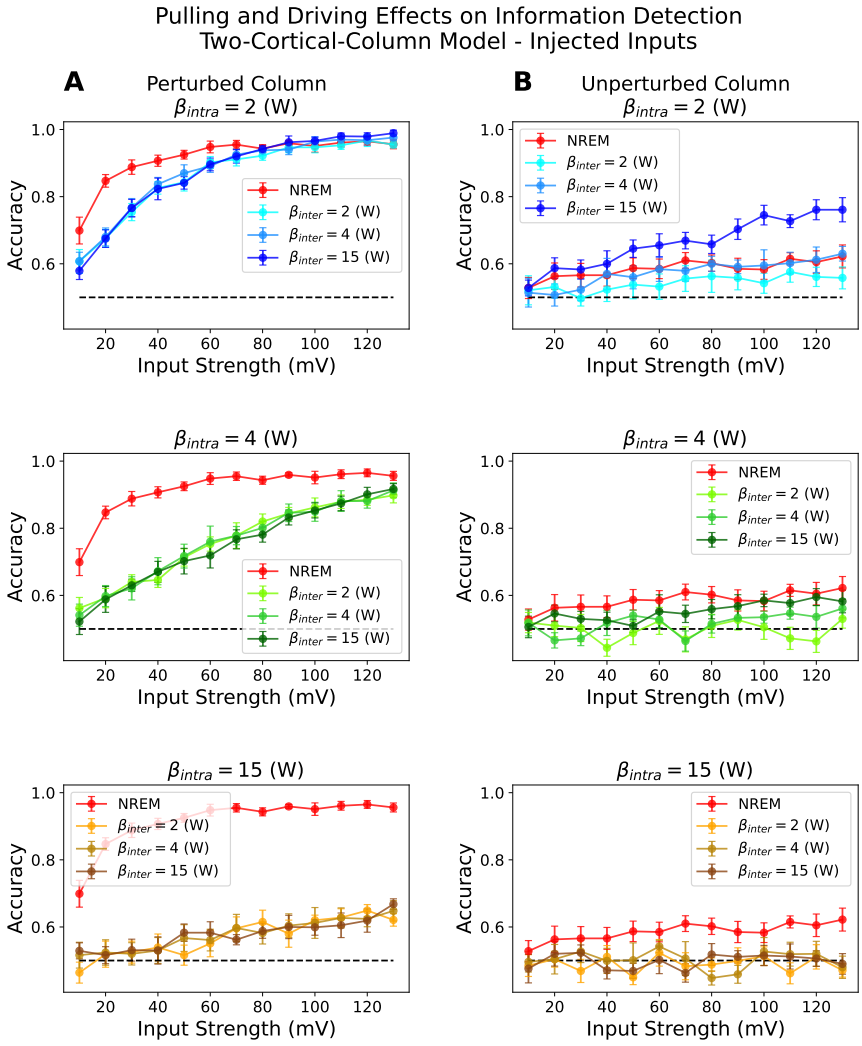

Figure 3.9: Pulling and driving effects due to synaptic upscaling on information detection in the two-cortical-column model. (**A**). Information detection at input offset in the perturbed column for various input amplitudes (injected inputs) in NREM (red) and various synaptic upscalings in wakefulness (color coded). *Top*. Information detection remains comparable when inter-synaptic (next page)

Figure 3.9 *(previous page)*: upscaling increases in wakefulness when intra-synaptic upscaling is kept constant at $\beta_{intra} = 2$. *Middle*, *Bottom*. Results as in *Top*, but for $\beta_{intra} = 4$ and $\beta_{intra} = 15$, respectively. Note that intra-synaptic upscaling decreases information detection in the perturbed column due to the pulling effect. (**B**). Results as in panel **A**, but for the unperturbed column. Intra-synaptic upscaling decreases information detection in the unperturbed column due to the pulling effect. Note that information detection when inter-synaptic upscaling increases in wakefulness for $\beta_{intra} = 2$ is comparable in the perturbed column (light blue in **A** *Top*), however, only $\beta_{inter} = 15$ enhances information detection in the unperturbed column due to the driving effect (dark blue in **B** *Top*). Error bar shows 95 percent confidence interval. Black dash line represents the chance-level accuracy $= \frac{1}{\#\text{input amplitudes}}$.

fulness is not enhanced unless inter-synaptic upscaling is larger than intra-synaptic upscaling (see Figure 3.10B). As in Section 3.2.1, the strength of E/I ratio in peristimulus intervals (see Figure 3.7D) correlates with the level of information detection and differentiation in the perturbed column. This is important from These results show that distance-selective synaptic upscaling enhances information propagation from perturbed to the unperturbed column.

It is important to note that the increase in intra-synaptic upscaling attenuates information content in the perturbed cortical column, which might lead to a corresponding decrease in information content in the unperturbed cortical column. For instance, attenuated propagation of information to the unperturbed column in the case of $\beta_{intra} = 15,\ \beta_{inter} = 15$ compared to $\beta_{intra} = 2,\ \beta_{inter} = 15$ might be due, to start with, to less information content in the perturbed column (see Figure 3.9). Therefore, it remain unclear whether information content in the unperturbed column for $\beta_{intra} = 15,\ \beta_{inter} = 15$ could have been comparable to $\beta_{intra} = 2,\ \beta_{inter} = 15$ if information content in the perturbed column was comparable. To untangle this ambiguity, in the next section, we provide a control condition where

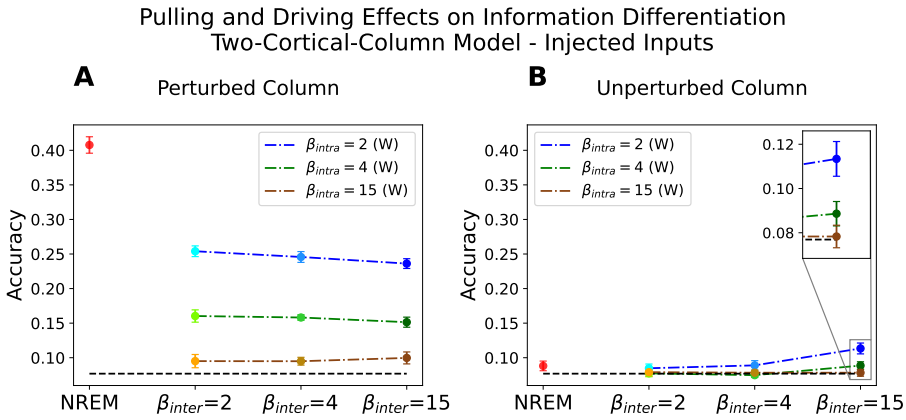

Figure 3.10: Pulling and driving effects due to synaptic upscaling on information differentiation in the two-cortical-column model. (**A**). Information differentiation at input offset in the perturbed column for various input amplitudes (injected inputs) in NREM (red) and various synaptic upscalings in wakefulness (color coded). Information differentiation decreases with increasing intra-synaptic upscaling when inter-synaptic upscaling in wakefulness is kept constant. Note that the decrease in the E/I ratio in Figure 3.7D is predictive of pulling effects of synaptic upscaling on information differentiation. (**B**). Results as in panel **A**, but for the unperturbed column. Intra-synaptic upscaling decreases information differentiation in the unperturbed column (see the inset plot), showing the pulling effect. Note that information differentiation in the unperturbed cortical column is larger at $\beta_{intra} = 2$ and $\beta_{inter} = 15$ than $\beta_{intra} = 2$ and $\beta_{inter} = 2$ even though information differentiation in the perturbed column is the largest at $\beta_{intra} = 2$ and $\beta_{inter} = 2$, which highlights the driving effect due to inter-synaptic upscaling. Error bar shows 95 percent confidence interval. Black dash line represents the chance-level accuracy $= \frac{1}{\#\text{input amplitudes}}$.

information content in the perturbed cortical column is comparable among different synaptic upscalings.

3.2.4 Synaptic Inputs to the Two-Cortical-Column Model: Information Propagation (Control Condition)

Here, we provide a control condition where information content in the perturbed column is comparable across various synaptic upscalings. Results in the previous section showed that synaptic upscaling generates a pulling effect on information content in the evoked responses of perturbed cortical column to injected inputs. However, the results from Section 3.2.2 shows that synaptic inputs can generate competing effects of pulling and driving on information content. Therefore, synaptic inputs to two-cortical-column model has potential to preserved information content in the perturbed cortical column.

Synaptic inputs with amplitude ranging from 0.01 ms^{-1} to 0.11 ms^{-1} by a step size of 0.01 ms^{-1} are applied through an intra-synapse to the perturbed column. The increase in input range compared to Section 3.2.2 is the result of additional pulling effects due to bidirectional coupling with a second cortical column which allows us to explore larger input amplitudes before evoked responses in the perturbed column saturate. Unlike Section 3.2.2, synaptic inputs are applied through an intra synapse. This is so because evoked responses in the perturbed column for inter synaptic upscaling $\beta_{inter} = 15$ saturate. To prevent saturation of evoked responses we applied the synaptic inputs through an intra synapse.

Deterministic Responses

Amplitude of deterministic evoked responses is larger in NREM sleep than at any synaptic upscalings in wakefulness (see Figure 3.11). In this control condition, amplitude of deterministic evoked responses in local-selective and homogeneous synaptic upscalings are larger than distance-selective

synaptic upscalings (see Figure 3.11A). Nevertheless, synaptic upscaling has a different effect in the unperturbed column. Amplitude of deterministic evoked responses in distance-selective synaptic upscalings is larger than homogeneous and local-selective synaptic upscalings (see Figure 3.11B).

Stochastic Responses

Logistic classification on evoked responses in the perturbed column at offset shows that information detection remain comparable between NREM sleep and the three synaptic upscaling scenarios in wakefulness (see Figure 3.12A-C). Amplitude of evoked responses is larger for local-selective synaptic upscaling in the perturbed column in wakefulness (S5.35). However, the larger standard deviation of evoked responses for local-selective synaptic upscalings makes information detection comparable among synaptic upscaling scenarios in wakefulness (see Figure S5.36A).

Despite comparable information detection in the perturbed column, information detection in the unperturbed column is not enhanced compared with NREM sleep unless inter-synaptic upscaling is larger than intra-synaptic upscaling (see Figure 3.13A-C). This is due to the competition of intra- and inter-synaptic upscalings in the regulation of the amplitude and standard deviation of evoked responses and spontaneous activities (see Figure 3.11B, and Figure S5.36B and S5.37). Arranging results according to synaptic upscaling scenarios shows that information content in the unperturbed column is larger in distance-selective synaptic upscaling scenario than homogeneous and local-selective synaptic upscaling scenarios (see Figure 3.13A-C).

Likewise, information differentiation in NREM sleep and other synaptic upscalings in wakefulness are comparable in the perturbed column (see Figure 3.12D). Nevertheless, synaptic upscaling does not enhance information differentiation in the unperturbed column in wakefulness compared to NREM sleep (and chance level) unless inter-synaptic upscaling is larger than intra-synaptic upscaling (see Figure 3.13D). These results highlight

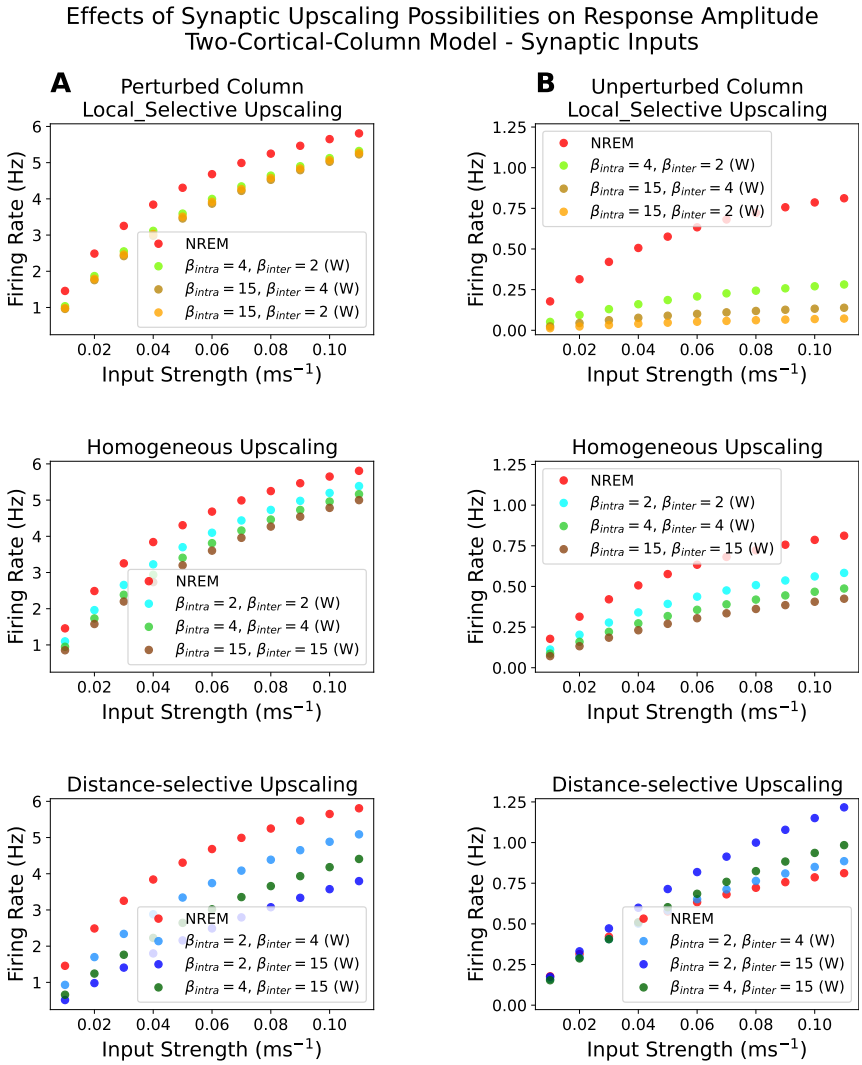

Figure 3.11: Effects of synaptic upscalings on amplitude of evoked responses in the two-cortical-column model. (**A**) Amplitude of deterministic evoked responses in firing rate signals in the perturbed column at input offset for various input amplitudes (Intra-synaptic inputs) in NREM (red) and various synaptic (next page)

Figure 3.11 *(previous page)*: upscalings in wakefulness (color coded). Amplitude of evoked responses is larger in local-selective synaptic upscalings(*Top*) in wakefulness compared to homogeneous (*Middle*) and distance-selective synaptic upscalings (*Bottom*) in wakefulness. (**B**) Results as in panel **A**, but for the unperturbed column. Amplitude of evoked responses is larger in distance-selective synaptic upscalings (*Bottom*) in wakefulness compared to homogeneous (*Middle*) and local-selective synaptic upscalings (*Top*) in wakefulness. Note that although amplitude of evoked responses in the perturbed column for local-selective synaptic upscaling is the largest in wakefulness, they trigger the smallest evoked responses in the unperturbed column. On the other hand, evoked responses in the perturbed column in wakefulness is the smallest in distance-selective synaptic upscalings. However, distance-selective synaptic upscalings enhance amplitude of evoked responses in the unperturbed column.

the hypothesis that distance-selective upscaling enhances information propagation from the perturbed to the unperturbed column.

3.2.5 Robustness of the Computational Results

In this section we check whether our results in previous sections are robust and hold to the choice of time points different than input offset and to different methods of quantification of information.

Choice of Time Point

Information detection at input offset comes from the comparison between distribution of evoked responses at offset and distribution of spontaneous activities at a time point within the peristimulus interval. Our results concerning information detection, described in previous sections, are valid for even if the selected time point in the peristimulus interval is changed (see Figure S5.38 for Section 3.2.1; Figure S5.39 for Section 3.2.2; Figure S5.40 for Section 3.2.3; Figure S5.41 and Figure S5.42 for Section 3.2.4).

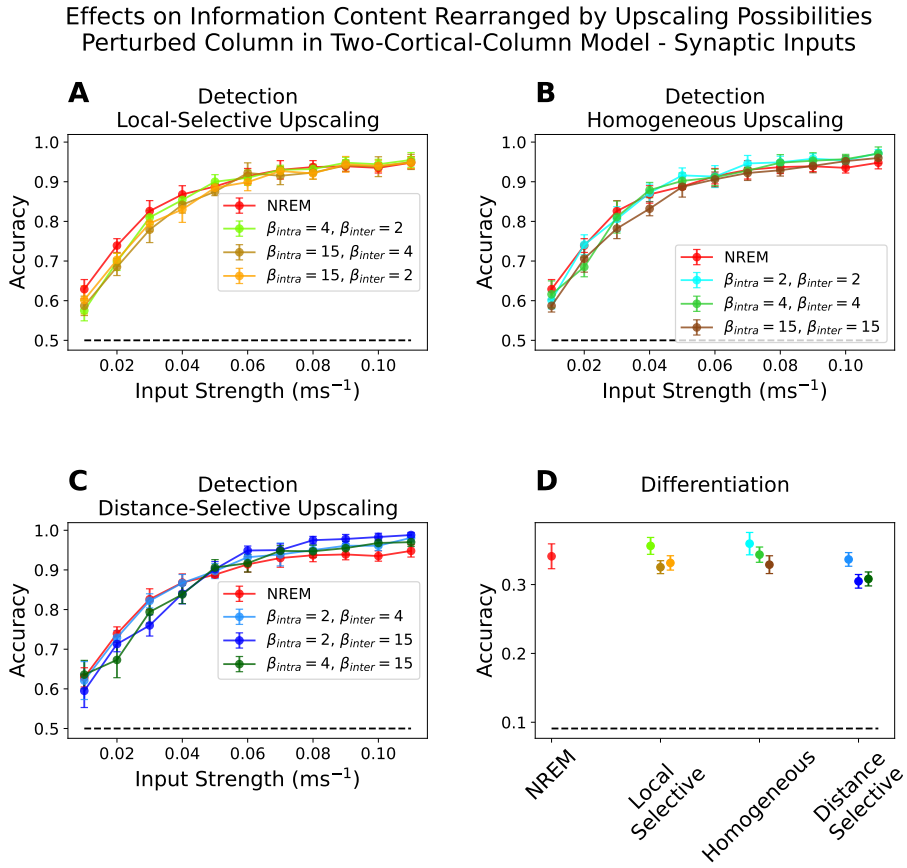

Figure 3.12: Effects of synaptic upscalings on information content in the perturbed column in the two-cortical-column model rearranged by synaptic upscaling scenarios. Results correspond to the perturbed column. (**A**). Information detection at input offset for various input amplitudes in NREM (red) and local-selective synaptic upscalings in wakefulness (color coded). As in panel **A**, but for homogeneous (**B**) and distance-selective (**C**) synaptic upscalings in wakefulness, respectively. Note that information detection in the perturbed column is comparable among the three synaptic upscaling scenarios and NREM sleep. (**D**) Information differentiation for NREM and three synaptic upscaling scenarios in wakefulness. Note that information differentiation in the perturbed column is (next page)

Figure 3.12 *(previous page)*: comparable among the three synaptic upscaling scenarios and NREM sleep. Error bar shows 95 percent confidence interval. Black dash line represents the chance-level accuracy $= \frac{1}{\#\text{input amplitudes}}$.

Then we evaluated information content at 20 ms prior to input offset. Information detection and differentiation are, to a large degree, comparable 20 ms prior to input offset with the ones at offset (see Figure S5.43 for Section 3.2.1; Figure S5.44 for Section 3.2.2; Figure S5.45 and S5.46 for Section 3.2.3; Figure S5.47, and S5.48 for Section 3.2.4).

Moreover, our results are still valid even at 20 ms post input offset (see Figure S5.49 for Section 3.2.1; Figure S5.50 for Section 3.2.2; Figure S5.51 and S5.52 for Section 3.2.3; Figure S5.53 and S5.54 for Section 3.2.4). It is important to note that information content decays at 20-ms-post-offset compared to the ones at input offset in the perturbed column when injected inputs are applied (Section 3.2.1 and Section 3.2.3). Information decay when synaptic inputs are applied (Section 3.2.2) is slower. This includes the decay of information in the perturbed column and in the unperturbed column when injected inputs are applied to the perturbed column (Section 3.2.2 and 3.2.4, respectively). This is due to difference in the way that inputs travel to a cortical column. When a cortical column receives an input through a synapse, decay of information at 20 ms post offset is smaller than when inputs are injected. Synapses introduce a form of memory due to the alpha-function activation. Nevertheless, our results are valid regarding an enhanced information propagation for distance-selective synaptic upscaling even at 20-ms-post-offset.

Generative Model

Our results also holds when using generative models (Gaussian discriminant analysis) on evoked responses at input offset (see Figure S5.55 for Section 3.2.1; Figure S5.56 for Section 3.2.2; Figure S5.57 and S5.58

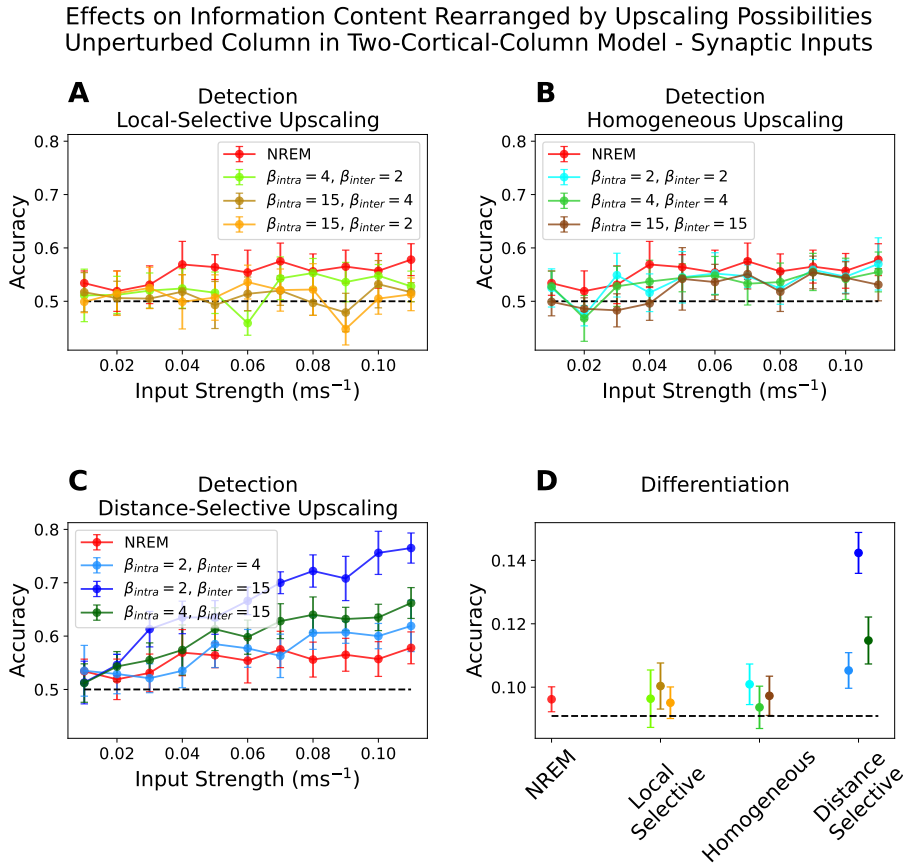

Figure 3.13: Effects of synaptic upscalings on information content in the unperturbed column in the two-cortical-column model rearranged by synaptic upscaling scenarios. As in Figure 3.12, but for the unperturbed column. (**A**). Information detection at input offset for various input amplitudes in NREM (red) and local-selective synaptic upscaling scenario in wakefulness (color coded). As in panel **A**, but for homogeneous (**B**) and distance-selective (**C**) synaptic upscaling scenarios in wakefulness, respectively. Note that information detection is comparable among the three synaptic upscaling scenarios in the perturbed column (see Figure 3.12A-C), however, only distance-selective synaptic upscaling scenario in wakefulness enhances information detection in the unperturbed (next page)

Figure 3.13 *(previous page)*: column compare to homogeneous and local-selective synaptic upscaling scenarios and NREM sleep. (**D**) Information differentiation for NREM and three various synaptic upscaling scenarios in wakefulness. Note that information differentiation is comparable among the three synaptic upscaling scenarios in the perturbed column (see Figure 3.12D), however, distance-selective synaptic upscaling scenario in wakefulness enhances information differentiation in the unperturbed column compare to homogeneous and local-selective synaptic upscaling scenarios and NREM sleep. Error bar shows 95 percent confidence interval. Black dash line represents the chance-level accuracy $= \frac{1}{\#\text{input amplitudes}}$.

for Section 3.2.3; Figure S5.59 and S5.60 for Section 3.2.4). Information detection implementing generative models is also independent of the choice of the time point in peristimulus intervals (see Figure S5.61 for Section 3.2.1; Figure S5.62 for Section 3.2.2; Figure S5.63 for Section 3.2.3; Figure S5.64 and Figure S5.65 for Section 3.2.4).

Moreover, information content implementing generative models at 20 ms prior to input offset is to a large degree comparable with the ones at offset (see Figure S5.66 for Section 3.2.1; Figure S5.67 for Section 3.2.2; Figure S5.68 and S5.69 for Section 3.2.3; Figure S5.70 and S5.71 for Section 3.2.4).

Furthermore, our results are valid even at 20 ms post input offset (see Figure S5.72 for Section 3.2.1; Figure S5.73 for Section 3.2.2; Figure S5.74 and S5.75 for Section 3.2.3; Figure S5.76 and S5.77 for Section 3.2.4). Information content decays at 20 ms post offset compared to the ones at offset for Section 3.2.1, 3.2.2 and the perturbed column in Section 3.2.3. However, information decay in Section 3.2.2 is slower due to synaptic dynamics. The decay of information in the unperturbed column in Section 3.2.3 and both perturbed and the unperturbed column in Section 3.2.4 are not prominent, as for discriminative models.

However, it is important to note that generative models have an overall

better accuracy in information detection (not information differentiation). The Gaussian Discriminant analysis models the distribution of data according to normal distributions. Thus, the difference between the discriminative and generative models on information detection could be a result of stronger modeling assumptions in the generative model.

Significance Tests and Information Theory

Our results are also valid for methods other than machine learning techniques. Performing significance tests on evoked responses in poststimulus intervals versus spontaneous activities in peristimulus intervals reproduces results regarding information detection (see Figure S5.78A for Section 3.2.1; Figure S5.79A-C for Section 3.2.2; Figure S5.80 for Section 3.2.3; Figure S5.81A-C and Figure S5.82A-C for Section 3.2.4).

Then, we used information theory to compute mutual information between the distribution of evoked responses at input offset and distribution of inputs. Interestingly, mutual information qualitatively reproduces the results obtained for information differentiation with machine learning techniques (see Figure S5.78B for Section 3.2.1; Figure S5.79D for Section 3.2.2; Figure S5.83 for Section 3.2.3; Figure S5.81D and Figure S5.82D for Section 3.2.4). The choice of number of bins for data discretization does not affect our results (see Figure S5.84). Moreover, mutual information at 20 ms prior to input offset is to a large degree comparable with the ones at input offset, whereas there is a decay in mutual information at 20 ms post input offset (see Figure S5.85A for Section 3.2.1; Figure S5.85B for Section 3.2.2; Figure S5.86 for Section 3.2.3; Figure S5.87 for Section 3.2.4). Note that only for the unperturbed column in Section 3.2.4 mutual information at 20 ms post input offset is larger than at input offset, which might reflect synaptic memory about the inputs. Nevertheless, implementing significance tests and information theory reproduces our results. In particular, synaptic upscaling in wakefulness does not enhance information propagation compared to NREM sleep un-

less inter-synaptic upscaling is larger than intra-synaptic upscaling, known as distance-selective synaptic upscaling.

Chapter 4

DISCUSSION

Sleep is a vital physiological state that, in the brain, is associated with enhances memory and learning functions [5, 6, 7, 8, 9, 10, 11]. However, sleep is often accompanied by loss of interaction with the surroundings which can be threatening in an ever-changing environment. Nevertheless, the loss of interaction might not indicate that sensory processing is absent during sleep. While innocuous sounds can go unnoticed without disrupting sleep, auditory stimuli with subjective significance can arouse a sleeping individual, as a baby's cry awakens the parents.

There is compelling experimental evidence that some level of auditory processing persists during deep phases of sleep, also known as NREM sleep [48, 50, 51, 52, 53, 54, 55, 56]. However, neural markers of cognitive functions associated with auditory stimuli are attenuated during NREM sleep compared with wakefulness [48, 53, 54, 55, 56]. Attenuated neural markers of these cognitive functions does not seem to be a consequence of lack of attention during NREM sleep since perceptual, semantic and motor processes can occur even without awareness during wakefulness [133, 134, 135].

There is compelling experimental evidence that auditory stimuli elicit neural firing responses in the primary auditory cortex that are similar in

NREM sleep and wakefulness [65, 66, 67, 68]. This poses a challenge to the conventional thalamic gating hypothesis because sounds seem to bypass the thalamus in both brain states. Nevertheless, experimental studies suggest that neural firing responses to auditory stimuli does attenuate in cortical areas downstream to the primary auditory cortex [65, 66, 67, 68]. Moreover, TMS stimulation studies in humans have shown that cortical activation remains local during NREM sleep compared with the broader spatiotemporal extent of propagation during wakefulness [70, 81].

These evidence opens the door to a different hypothesis than thalamic gating hypothesis: propagation of information about external stimuli is compromised during sleep compared to wakefulness along the cortical processing chain. This hypothesis is supported by the fact that effective connectivity [136] during sleep is reduced with respect to wakefulness, a feature that has also been explored in large-scale models [117, 137].

Nevertheless, the underlying mechanisms enhancing propagation of information in the cerebral cortex during wakefulness compared to NREM sleep remain largely unknown. One possible neural correlate of enhanced information propagation in the cortex could be the upscaling of excitatory synapses in wakefulness compared to NREM sleep, a hypothesis known as synaptic homeostasis hypothesis (SHY) [138, 102, 98, 99, 103, 139, 100, 101, 104, 140]. SHY states that synaptic strength in several cortical circuits decreases during NREM sleep due to net synaptic upscaling during wakefulness. Upscaling of excitatory synapses in wakefulness can increase the driver effects of neural firing responses of a presynaptic cortical area on its postsynaptic site, resulting in an increased signal-to-noise ratio.

However, we hypothesize that synaptic upscaling in a balanced configuration in wakefulness enhances not only signal, but also noise. This is in agreement with findings using *in vitro* techniques where increasing spontaneous synaptic activities attenuates neural firing responses [105]. We argue that synaptic upscaling in a balanced configuration in wakefulness is a phenomenon with two competing effects on neural firing responses: driving and pulling effect. The first tends to increase the amplitude of the neuronal

responses, whereas the second tend to bring them closer to baseline level of activity. One way to overcome the pulling effect of spontaneous synaptic activities in wakefulness is that synaptic upscaling occurs preferentially between distinct neural networks rather than within local and recurrent connections. We have coined this hypothesis as distance–selective synaptic homeostasis. Distance-selective synaptic homeostasis states that upscaling of inter-synapse (intercortical excitatory synapses formed between different cortical columns) should be stronger than upscaling of intra-synapse (intracortical excitatory synapses formed within a cortical column)

Here, we have used a computational approach to understand how synaptic upscaling in a balanced configuration in wakefulness modulates propagation of information compared to NREM sleep. By means of a neural mass model operating in two distinct brain dynamics, NREM sleep and wakefulness, we investigate propagation of information in a neural system composed of two cortical columns. Simulated firing rate signals have a bimodal distribution in the parametric space belonging to NREM dynamics, which is indicative of the alternation between Up and Down states and the presence of slow oscillations. The higher power at low frequencies in NREM versus the higher power at high frequencies in wakefulness of firing rate signals also validates the existence of these two different dynamical regimes.

Few models exhibiting both regimes have been published up to date [141, 109, 110, 142, 143, 144]. Despite the fact that any computational model with multiple parameters exhibits a rich variety of bifurcations, we show that the sleep–waking transition can be obtained with the minimum set of possible changes. Naturally, the simplest solution is to vary a single parameter. Here, increasing intra-synaptic upscaling suffices to move the system from NREM-like to waking-like dynamics. This is so because for the parameter space of the NREM state in the model, the membrane potential show large amplitude deflections to a perturbation, producing damped oscillations due to the presence of a stable spiral [145]. This behavior generates the slow oscillation in the presence of noise in NREM sleep.

Whereas intra-synaptic upscaling decreases the amplitude of deflections, which, in turn, reduces the time required to relax back to the steady state value. This behavior decreases the slow oscillation and increases higher frequency components in the presence of noise. This also explains why the dynamical features of NREM sleep are compromised when connecting two cortical columns.

In this study, the connectivity between the two cortical columns is excitatory and symmetric, but only one of the pyramidal populations receives transient excitatory inputs. We investigated how various synaptic upscalings in wakefulness modulate propagation of information about inputs to the other column in such a way that it is enhanced in the awake state when compared to NREM. Previous computational work [120] also aimed at reproducing the distinct propagation patterns that arise across the SWC, obtaining similar results to the ones described here. In particular, a wider propagation of the external perturbation occurs during wakefulness than during NREM sleep. In our case, this is quantified by information content in response of the unperturbed column, whereas [120] used the perturbational complexity index (PCI) [146]. However, the set of parameters' changes used by [120] focus on an adaptation current that weakens during wakefulness, which in our opinion is less experimentally justified. Moreover, the authors showed that during wakefulness the ratio between poststimulus and peristimulus firing rate can be greater in an area that is not directly stimulated than in the stimulation site, which requires further experimental verification.

We showed that when inter-synaptic upscalings (upscaling of synapses within a cortical column) are equal or less than intra-synaptic upscalings (upscaling of synapses between two cortical column) in wakefulness, information propagation is not enhanced compared to NREM sleep. Propagation of information enhances only when inter-synaptic upscalings are larger than intra-synaptic upscalings. Our results suggest that the synaptic homeostasis hypothesis should be heterogeneously applied, that is, that synaptic upscaling has to be spatially organized and distant synaptic con-

nections should be upscaled with respect to the local ones. This is so because intra-synaptic upscaling in a balanced configuration attenuates neural firing responses and information content, in agreement with *in vitro* studies [105].

Synaptic upscaling in wakefulness occurs due to long-term potentiation, a process involving persistent strengthening of synapses. This process leads to changes in signal transmission between neural populations. Our results establish that heterogeneity of synaptic upscaling in a balanced configuration is necessary from NREM sleep to wakefulness to account for different information propagation patterns in NREM sleep and wakefulness. Although our results need experimental validation, heterogeneity of synaptic upscalings have been reported for perforated and non-perforated synapses. Briefly, perforated synapses are on average large and have a discontinuous postsynaptic density (PSD). Non-perforated synapses are on average small and have a continuous PSD. Non-perforated synapses are more numerous than perforates synapses [104]. It was shown that, in the cortex, perforated synapses enlarge their axon–spine interface after waking relative to sleep, in contrast to the lack of change found in non-perforated synapses [104]. This morphological change specific to perforated synapses also speaks for their major role in synaptic plasticity and the selective implementation of synaptic homeostasis that we propose.

Limitations

Some limitations of the study should be explicitly acknowledged. First, our model cannot account for whole brain interactions and is restricted to the dialogue between two cortical columns. A more complex connectivity diagram comprising other cortical and subcortical structures could, nonetheless, provide spatial information about stimulus propagation. Subcortical structures, such as the brainstem and basal forebrain, are the substrate for the changes in the concentration of neuromodulators that occur throughout the sleep–weak cycle [38, 40, 1, 147, 39, 148, 149]. These neuromodula-

tors target vesicular release at the presynaptic site or transmitter receptors at the postsynaptic site and alter synaptic strength [150, 151]. We have phenomenologically implemented their role by tuning synaptic conductances but the precise effect of these substances (norepinephrine, acetylcholine, histamine, serotonin, etc.) on target brain areas is out of the scope of this study, partly because the exact microcircuitry of the ascending arousal system is still unknown.

In this study, the connectivity between the two cortical columns is excitatory and symmetric, which might not reflect the biological morphology in all area of the cortex. However, it is important to note that our results hold true even when we consider one cortical column, where we showed that distance-selective synaptic upscaling boosts information content in the one-cortical-column model subjected to synaptic inputs. Nevertheless, we acknowledge that future works are required to asses the effects of feedback connections on changes in propagation of information during wakefulness and NREM sleep. In addition, our model does not include the emergence of more elaborated receptive fields along the cortical hierarchy and it relies only on transferring information about basic stimuli features (input strength). Future works are required to elucidate how synaptic upscalings in wakefulness modulate propagation of information about higher-order stimuli features compared to NREM sleep in a higher-order neural network.

Moreover, neural mass models considers that neural communications are through rate coding. Although our hypothesis is independent of rate- or spike-based coding schemes, it is advantageous to use spiking-based models to test the validity of our results when neural communications are through spike timing.

In addition, neural mass models cannot consider the neural heterogeneity within one cortical column. Different types of neurons show distinct evoked neural responses during NREM sleep in non-human mammals [65] and rats [67]. These studies suggest that modulation of neural firing responses in neurons within one area might depends on their response la-

tency, with a larger response attenuation in late-latency neurons. The neural heterogeneity can be implemented and tested by spiking-based models. Nevertheless, we used neural mass models due to the computational power required by our study.

Despite comparable results implementing discriminative and generative supervised learning techniques, future work could extend the scope and check validity of our results regarding information propagation patterns by using unsupervised techniques. Although we did not evaluate delays in information propagation during NREM sleep and wakefulness, future work should also address this problem. The delays in propagation of information might also play a role in understanding sensory processing during sleep–waking cycle. For instance, studies have reported that all cortical components of averaged EEG responses are delayed during NREM sleep [76, 152, 51]. Since the generators of the ERPs are usually at multiple sites, delayed ERPs might indicate that propagation and integration of information in different cortical sites are compromised during NREM sleep.

Moreover, we have excluded REM sleep from our work, which is a short but relevant stage of sleep that follows NREM epochs. The LFP and EEG dynamics recorded during REM sleep show similar features to wakefulness. Since neural firing responses in the primary auditory cortex are preserved across the SWC, including REM sleep [66, 67], computationally, we could use the same set of parameters to model REM than wakefulness at a single cortical column level. However, tracking these responses up to the perirhinal cortex, shows that their amplitude is attenuated from wakefulness to NREM sleep, and has intermediate values in REM sleep [67]. In our model, this could be replicated by using a β_{inter} value for REM sleep smaller than for wakefulness. However, experimentally, SHY has only proven to be true when comparing wakefulness and NREM sleep [104]. Therefore, we need to be cautious before extending our conclusions to REM sleep. Moreover, motor neurons in the spinal cord are inhibited in REM sleep [39]. Therefore, it remains difficult to attribute

the loss of behavioral responses during REM sleep to either inhibition of motor neurons in the spinal cord or to attenuated information propagation among distinct cortical areas.

It is important to acknowledge that laminar dependence of changes in information propagation patterns in NREM sleep and wakefulness is not addressed in our work. Nevertheless, a recent study in rhesus monkeys has reported a laminar dependence of propagation of neural firing responses in early visual cortical areas [153]. Surprisingly, the authors reported that propagation of neural firing responses induced by optogenetic stimulation attenuates across cortical layers within a cortical column during wakefulness but not during NREM sleep. Interestingly, the decrease of E/I balance correlated with the attenuation of laminar propagation of neural firing responses.

Although further data analysis are required to extend these findings to information propagation of stimuli, these observations might suggest a dual-route model for propagation of information in the cerebral cortex. The dual-route model, as I may call it, would consist of two pathways: inter-areal and intra-areal. The brain state, whether sleep or wakefulness, would modulate the amount of information that can propagate through each routes under the constraint that the total amount of information propagating through inter-areal and intra-areal route is preserved across different brain states.

Therefore, the dual-route model of information propagation in the cortex states that what changes from wakefulness to NREM sleep is information routing in the cortex. During wakefulness inter-cortical synapses are strong, therefore, information travels among distinct cortical areas. Whereas, during NREM sleep, due to distance–selective synaptic homeostasis, synaptic downscalings are stronger for inter-cortical synapses. Therefore, the ability to propagate information is larger for intra-areal routes than for inter-areal routes. As a consequence, information propagation through intra-areal routes is increased during NREM sleep compared to wakefulness, resulting in increased laminar propagation of information.

The change in information routing in the cortex proposed by the dual-route model predicts that information integration among distant cortical areas, a prerequisite feature for cognitive functions, decreases during NREM sleep compared to wakefulness.

Despite the limitations of our model, our work opens the door to explore which rules need to be implemented to reproduce experimental data and guide computational principles. This is particularly important while we still lack a clear understanding of how inputs scattered along the wide dendritic tree of a pyramidal neuron are added to combine synaptic sources at short and long distances with respect to the soma.

Findings Supporting Our Results

Our study reproduces several experimental findings previously published [154]. Moreover, a similar mechanism to our hypothesis has been also suggested in a network model of macaque cortex [155]. Although this study [155] did not reproduced different brain states, authors suggested that signal transmission increases when inter-areal excitatory connection strengths and intra-areal inhibition is enhanced. Our hypothesis is also in agreement with the view that rare long-range connections boost information processing [156].

Furthermore, our hypothesis can explain various observations in EEG and fMRI studies. Distance-selective synaptic hypothesis predicts that cortical communications between distinct cortical areas are enhanced during wakefulness compared to NREM sleep. This can account for different signal routing in wakefulness compared to NREM sleep in EEG studies. EEG studies have shown that the cortical components of averaged EEG responses (arising after 20 ms stimulus onset [152, 157, 71]) are different across the scalp and this topographic distribution changes from this NREM sleep to wakefulness [76, 50, 52, 54, 158].

Finally, enhanced cortical communications predicted by our hypothesis can account for the decoupling of the brain's default mode network

during NREM sleep [159]. Regions with higher structural connectivity show higher functional connectivity [160, 161, 162, 163, 164, 165, 166, 167, 168]. Therefore, distance-selective synaptic upscaling in wakefulness can result in a higher functional connectivity between distinct cortical networks. This can explain the higher participation of the frontal cortex in the activity of the default mode network [169, 170, 171] in wakefulness compared to NREM sleep [159]. Lastly, our results can also account for the high arousal threshold in response to external sensory stimulation during NREM sleep compared to wakefulness.

Other Mechanisms to Explain Attenuated Propagation of Information During NREM Sleep Compared to Wakefulness

There is much evidence for attenuation of information propagation in the cerebral cortex during NREM sleep compared to wakefulness. However, the underlying mechanisms are unknown. However, the underlying mechanisms are unknown. Here, we have proposed a distance–selective synaptic homeostasis process. Are there other options?

Another option to control the flow of information among cortical areas is neural synchrony. Synchronous firing between two neural populations could increase propagation of information from sending to receiving neural populations. In light of this view, synchronous gamma activity was proposed as a possible mechanism explaining different information propagation during NREM sleep and wakefulness. However, synchronous gamma activity was found to be equally low in NREM sleep and REM sleep, and it can be high in anesthesia [172, 2]. Given comparable amount of propagation of information in NREM sleep and anesthesia, and the attenuated propagation of information in NREM sleep compared to REM sleep, it remains uncertain to what extend impairment of synchronous gamma activity during NREM sleep can fully account for the attenuation of information

propagation during NREM sleep compared to wakefulness.

Finally, cortical areas can communicate not only through synchrony, but also through coherence [173]. One prediction of communication-through-coherence hypothesis is that gamma-band (30-90 Hz) coherency can modulate excitation rapidly enough so that it escapes the following inhibition and activates postsynaptic neurons effectively [174]. However, human studies have reported high robust auditory-induced high-gamma (80-200 Hz) and low-gamma (40-80 Hz) power responses during NREM sleep and wakefulness [68]. It remains to be validated in [68] whether the phase coherence of evoked responses in gamma band did decrease or not during NREM sleep compared to wakefulness. However, the preserved inter-trial phase coherence (in 40 Hz) of responses to 40-Hz click-trains in A1 and areas outside A1, suggests that impairment of communication-through-coherence might be an insufficient explanation for attenuated information propagation during NREM sleep compared to wakefulness.

Contribution of Our Results

The brain is a collection of functionally distinct neural populations that forms an integrated whole which interacts with the external environment by processing the information it receives. The neural mechanisms underlying the interruption of complex cortical interactions in brain-injured or unconscious patients are still uncertain.

Experimental observations suggest that attenuation of propagation of evoked neural responses during states of unconsciousness mimics the ones' in NREM sleep. Despite preserved auditory evoked neural responses in A1 during anesthesia-induced loss of consciousness (LOC) and wakefulness, neural responses attenuate in higher-order cortical area downstream to A1 during anesthesia-induced LOC compared to wakefulness [175]. Moreover, studies in humans [176] and mice [177] have shown that cortical effective connectivity breaks down during anesthesia-induced LOC compared to wakefulness. Given the occurrence of slow wave activity during

states of LOC, the general scientific consensus is that cortical bistability is the mechanistic origin of attenuated propagation of neural responses along a hierarchical cortical processing chain [2]. Nevertheless, other lines of studies suggest that the presence or absence of electrical dynamics of sleep–waking cycles do not reflect the severity of LOC in patients with vegatative state [178, 179, 180].

Although the neural mechanisms underlying anesthesia-induced LOC and NREM sleep might not be identical, our results, with cautious, could be extended to attenuated propagation of neural responses in states of LOC and consciousness. Our results can shed light on the neural correlates of different patterns of causal interaction among cortical areas in healthy patients and patients with disorders of consciousness. This opens the door to further investigations on pharmaceutical and treatment investigations for patients with disorders of consciousness. Moreover, our results along with proposed future computational studies can be used in health sectors to investigate how noise pollution in urban areas affect sleep quality in individuals.

Conclusion

Sleep and wakefulness are distinguished by distinct behavioural, electrophysiological and molecular features. It is still unclear how these biological layers are causally connected. Here, we have explored one particular relationship between two experimentally observed changes that occur across the SWC: upscaling of excitatory synapses and the broad propagation of incoming information throughout the cortex that takes place during wakefulness. The former happens during learning and strengthens synaptic connections, a process that is compensated during NREM sleep to enable synaptic homeostasis. The later evidence may speak for a cortical gating mechanism by which signals coming from the external world only reach higher processing brain areas during wakefulness and could possibly ex-

plain the emergence of consciousness.

Our computational model links both phenomena by showing that upscaling of excitatory synapses not only triggers a dynamic change of the electrical activity of the neural networks, but also of the propagation pattern across them. However, we predict that, in order for a spatially wider response to occur during wakefulness, it is necessary that such upscaling occurs preferentially between distinct networks over local and recurrent connections.

Chapter 5

SUPPLEMENTARY FIGURES

This Chapter includes supplementary figures of the study.

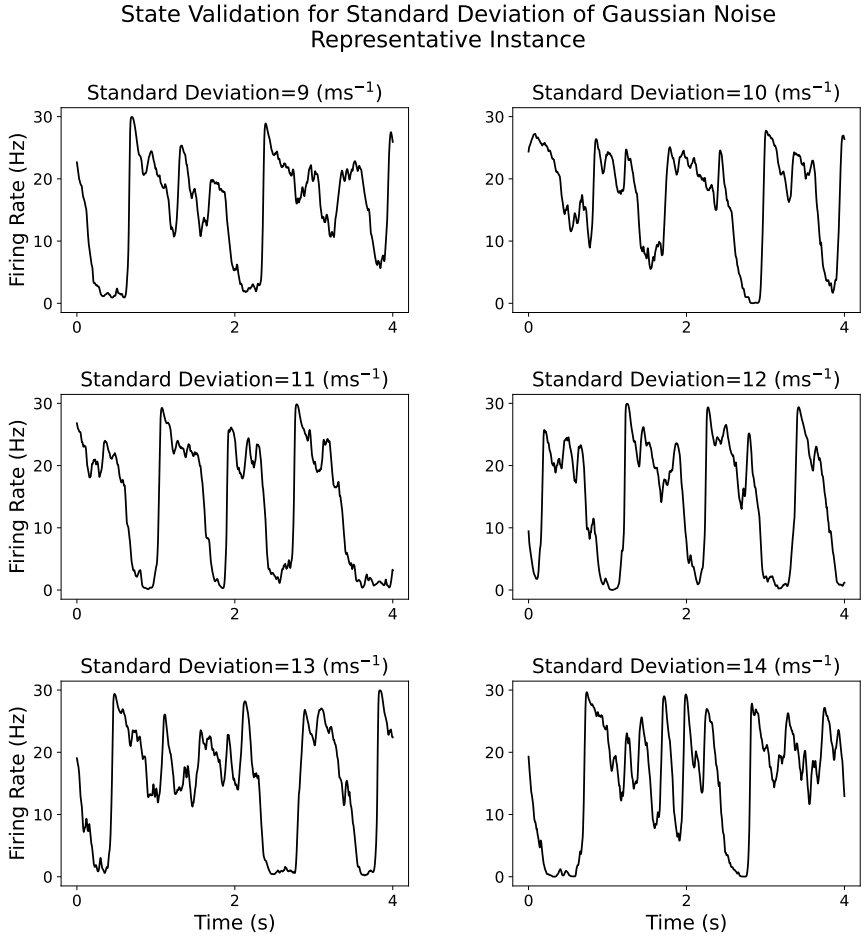

Figure S5.1: A representative instance of firing rate signals in NREM sleep for varied standard deviation of the Gaussian noise. Simulated signals shows large amplitude fluctuations in NREM sleep between periods of sustained activity (Up state) and silent activity (Down states) for various values of standard deviation of the Gaussian noise.

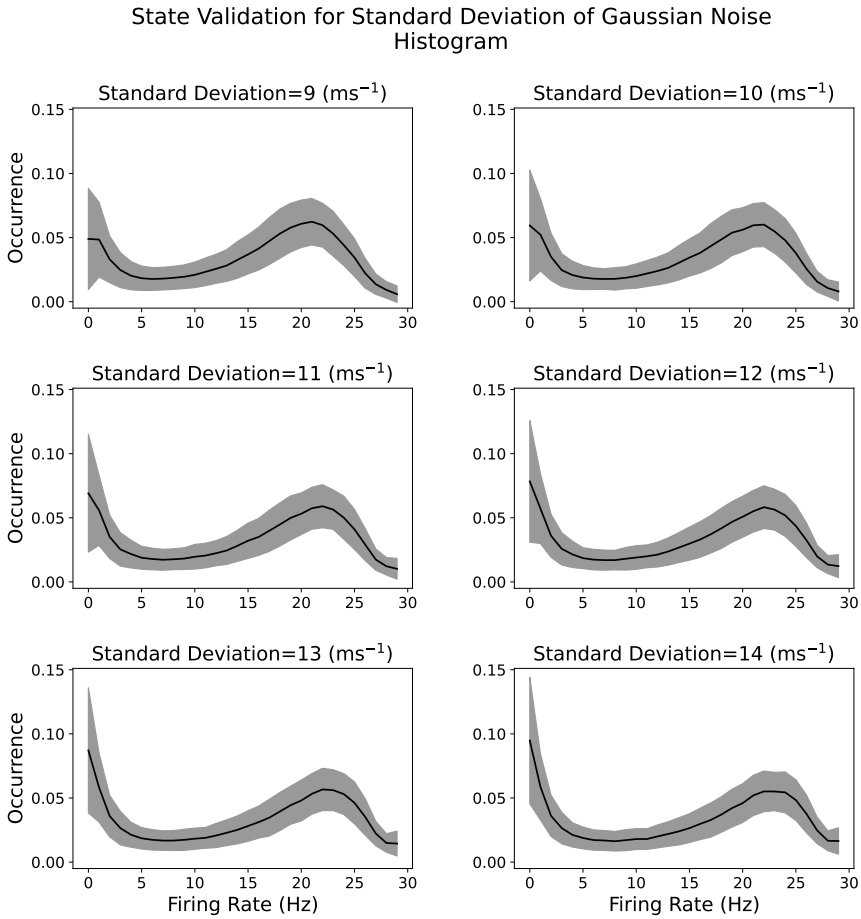

Figure S5.2: Distribution of firing rate signals in NREM sleep for varied standard deviation of the Gaussian noise. Average of the distribution firing rate, which is bimodal in NREM sleep. It is consistent across varied standard deviation of the Gaussian noise. Shaded area corresponds to standard deviation over 500 trials.

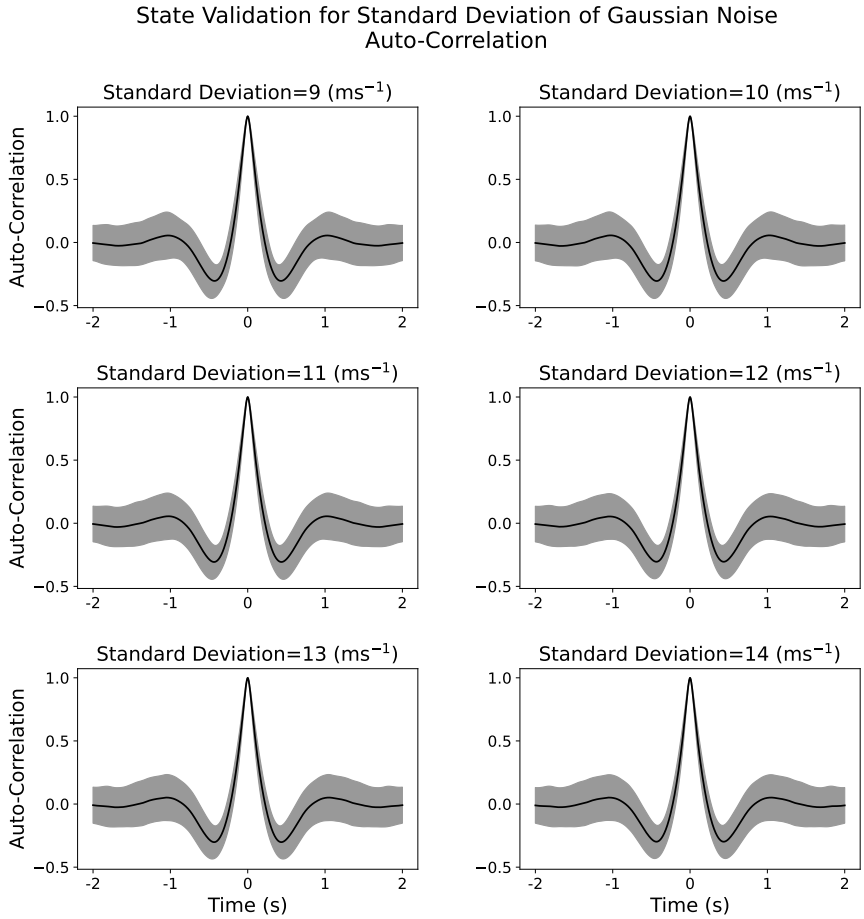

Figure S5.3: Auto-correlation of firing rate signals in NREM sleep for varied standard deviation of the Gaussian noise. Average of auto-correlation of firing rate signals shows a negative peak around 0.5 s and a subtle positive peak around 1 s, presence of slow oscillation. It is consistent across varied standard deviation of the Gaussian noise. Shaded area corresponds to standard deviation of the average of auto-correlation over 500 trials.

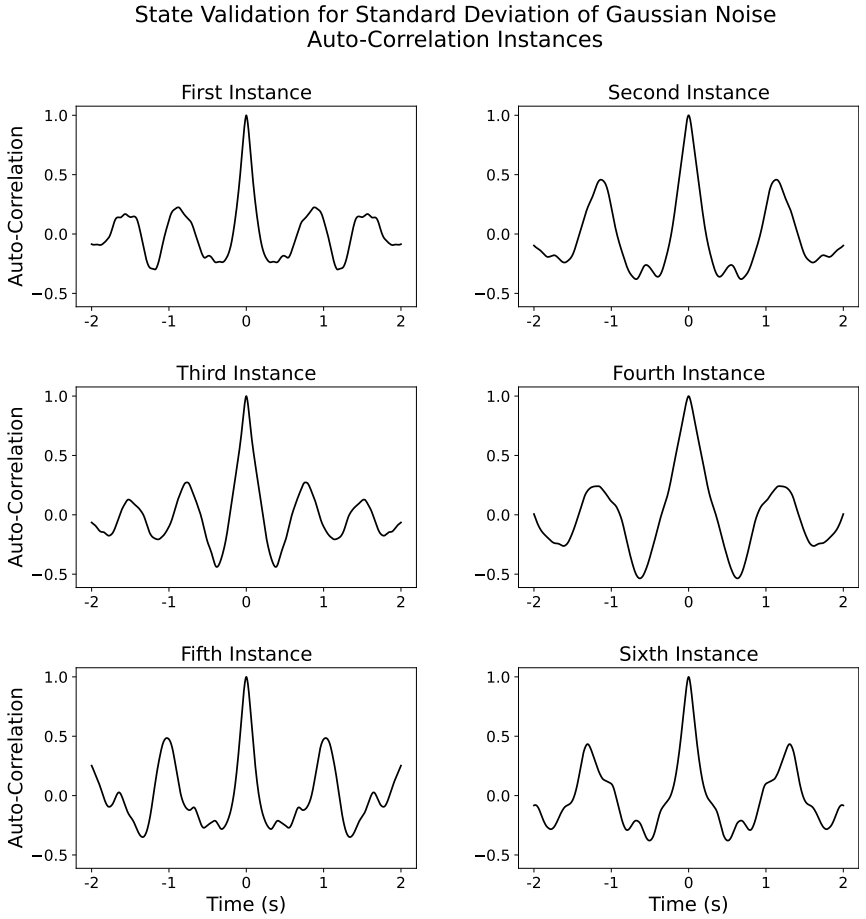

Figure S5.4: Auto-correlation of A representative instance of firing rate signals in NREM sleep for varied standard deviation of the Gaussian noise. Auto-correlation of a representative firing rate signal shows a negative peak around 0.5 s and a peak around 1 s, presence of slow oscillation. It is consistent across varied standard deviation of the Gaussian noise.

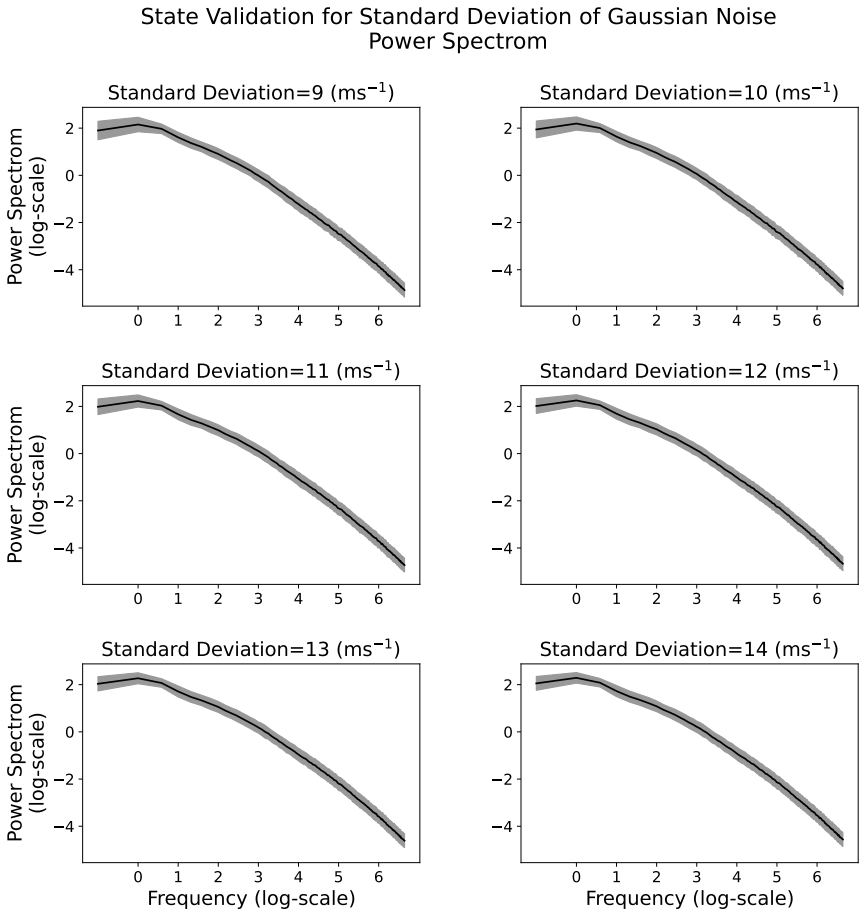

Figure S5.5: Spectral content of firing rate signals in NREM sleep for varied standard deviation of the Gaussian noise. Average power spectrum density of firing rate signals in NREM sleep is consistent across varied standard deviation of the Gaussian noise. Shaded area corresponds to standard deviation of the average of power spectrum density over 500 trials.

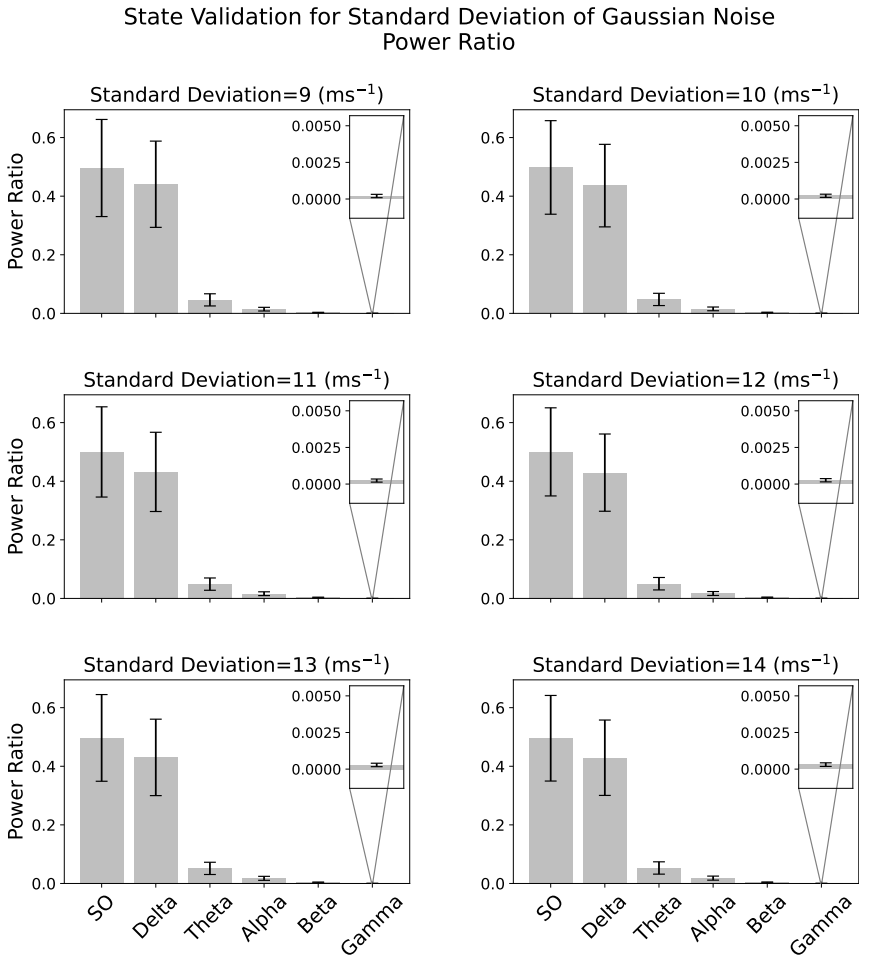

Figure S5.6: Power ratio of firing rate signals in NREM sleep for varied standard deviation of the Gaussian noise. Firing rate signals carry more spectral power within the SO (<1 Hz) and delta (1-4 Hz) frequency bands in NREM sleep. It is consistent across varied standard deviation of the Gaussian noise. Error bar shows standard deviation over 500 trials.

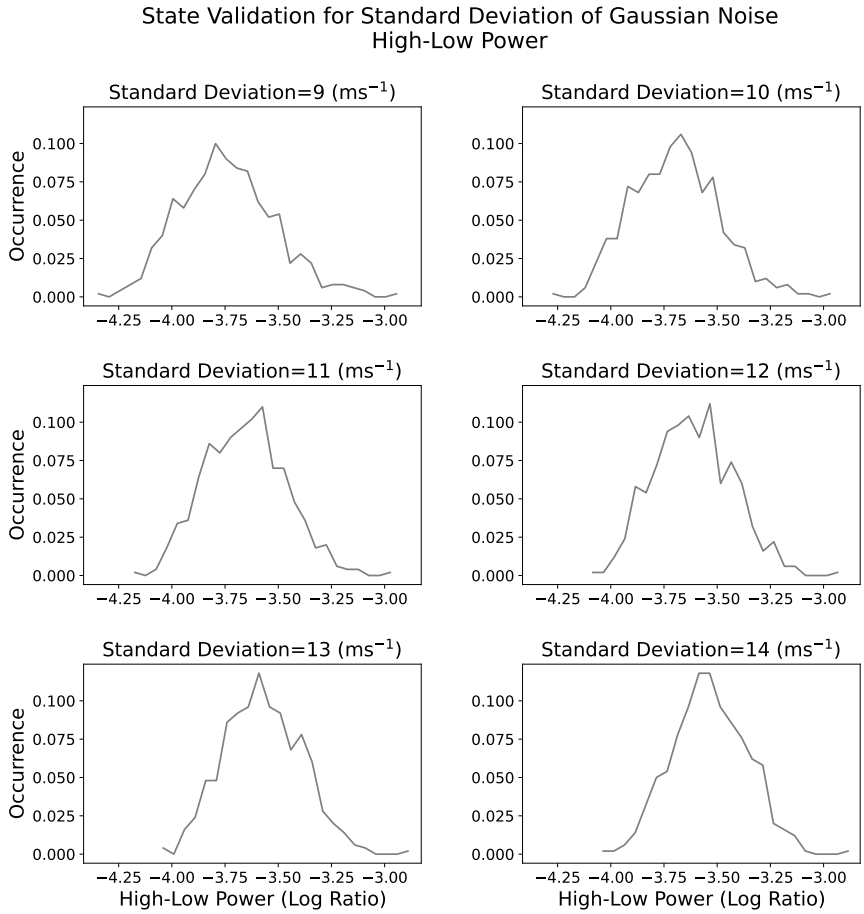

Figure S5.7: Distribution of high-/low-frequency power ratio of firing rate signals in NREM sleep for varied standard deviation of the Gaussian noise. Distribution of high-/low-frequency (where high is above 30 Hz and low is below 4 Hz) power ratio in firing rate signals in NREM sleep is consistent across varied standard deviation of the Gaussian noise.

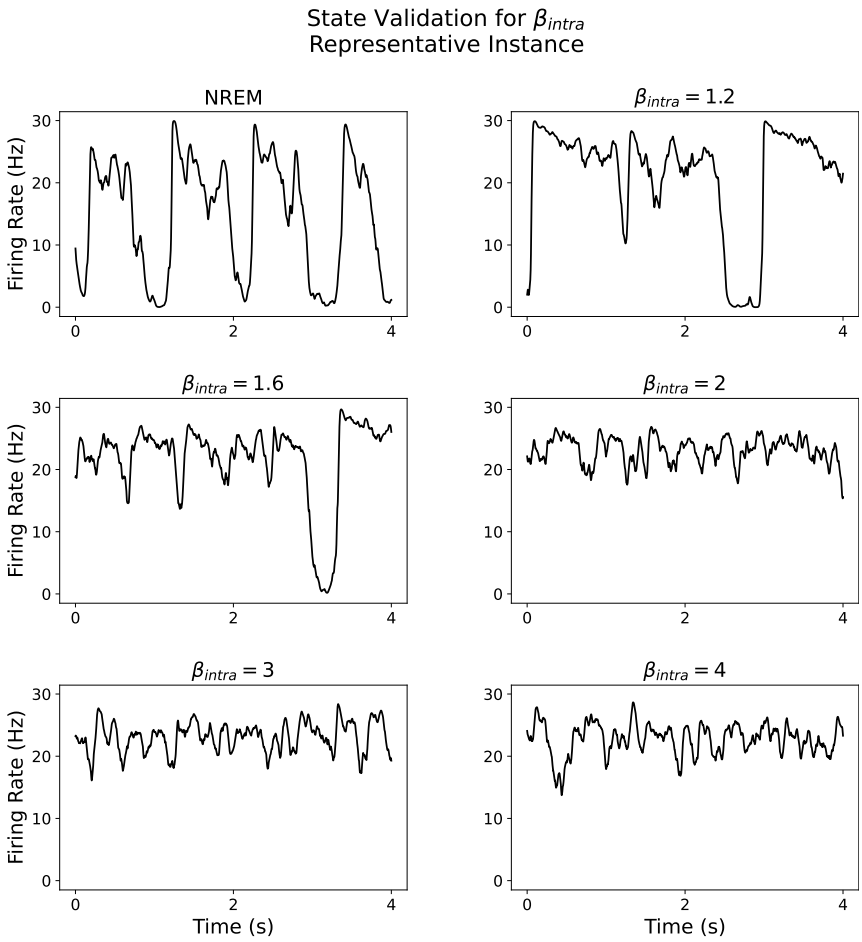

Figure S5.8: A representative instance of firing rate signals for increasing values of β_{intra}. Simulated signals shows large amplitude fluctuations in NREM sleep ($\beta_{intra} = 1$) between periods of sustained activity (Up state) and silent activity (Down states). Amplitude of fluctuations decreases with increasing β_{intra}. $\beta_{intra} \geq 2$ obliterate occurrence of Down states.

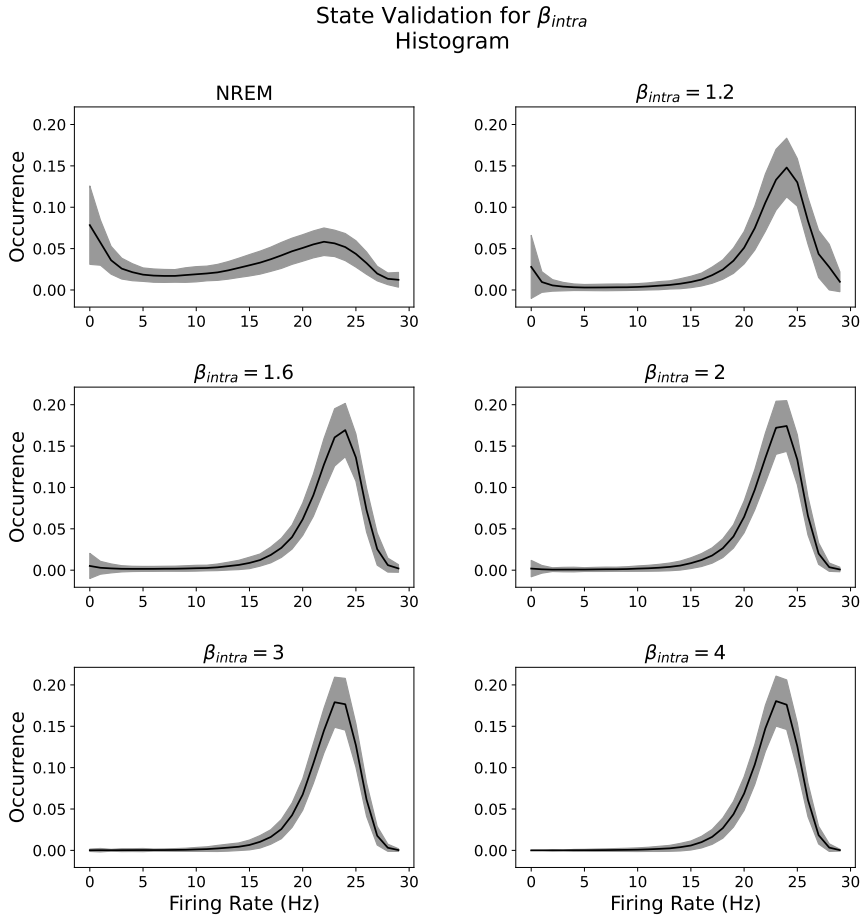

Figure S5.9: Distribution of firing rate signals for increasing β_{intra}. Average of the distribution firing rate, which is bimodal in NREM sleep ($\beta_{intra} = 1$). Bistability decreases with increasing β_{intra}. Average of distribution for $\beta_{intra} \geq 2$ is unimodal. $\beta_{intra} \geq 2$ obliterate bistability. Shaded area corresponds to standard deviation over 500 trials.

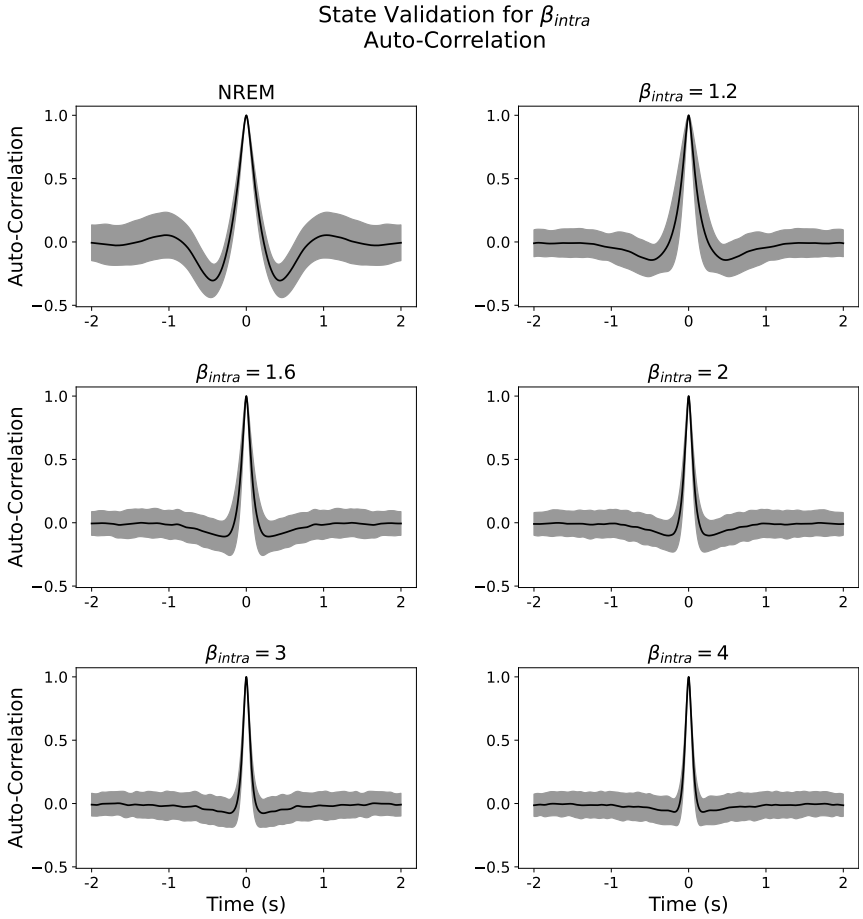

Figure S5.10: Auto-correlation of firing rate signals for increasing β_{intra}. Average of auto-correlation of firing rate signals in NREM sleep ($\beta_{intra} = 1$) shows a negative peak around 0.5 s and a subtle positive peak around 1 s, presence of slow oscillation. The peaks decrease with increasing β_{intra}. Shaded area corresponds to standard deviation of the average of auto-correlation over 500 trials.

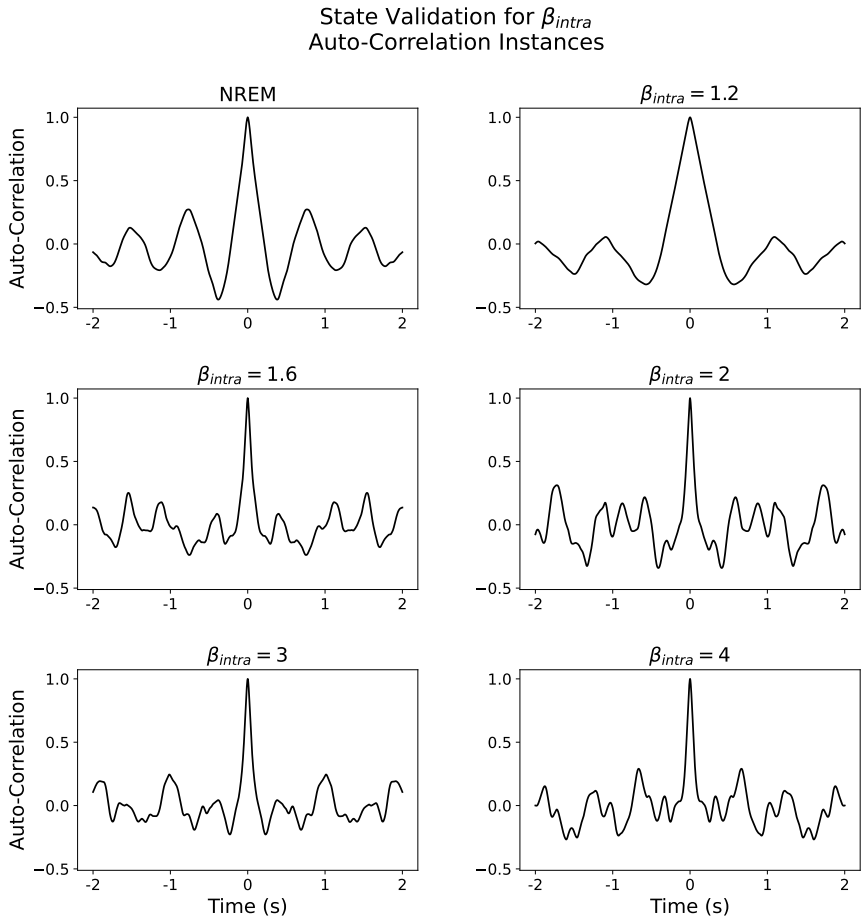

Figure S5.11: Auto-correlation of A representative instance of firing rate signals for increasing β_{intra}. Auto-correlation of a representative firing rate signal in NREM sleep ($\beta_{intra} = 1$) shows a negative peak around 0.5 s and a peak around 1 s, presence of slow oscillation. The peaks become stochastic with lower time lags (higher frequency) with increasing β_{intra}.

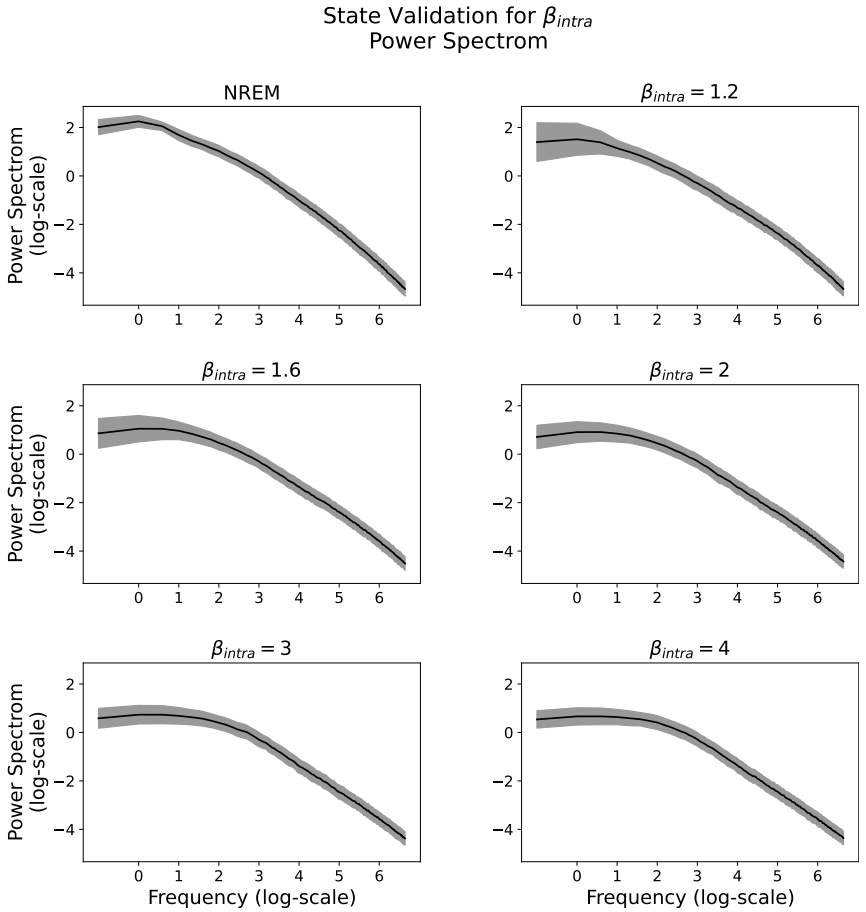

Figure S5.12: Spectral content of firing rate signals for increasing β_{intra}. Average power spectrum density of firing rate signals decreases with increasing β_{intra}. Shaded area corresponds to standard deviation of the average of power spectrum density over 500 trials.

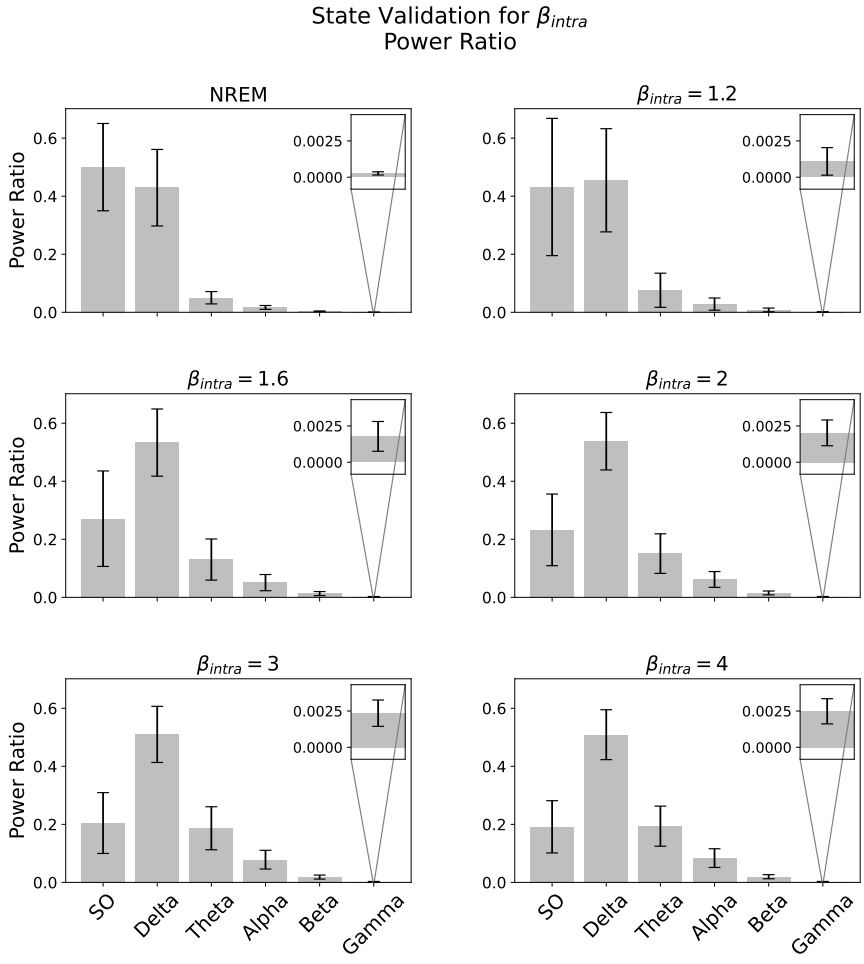

Figure S5.13: Power ratio of firing rate signals for increasing β_{intra}. Firing rate signals carry more spectral power within the SO (<1 Hz) and delta (1-4 Hz) frequency bands in NREM sleep ($\beta_{intra} = 1$). Power ratio of slow oscillation decreases with increasing β_{intra}. On the other hand, power ratio of higher frequency bands (Theta, Alpha, Beta and Gamma) increases with increasing β_{intra}. Error bar shows standard deviation over 500 trials.

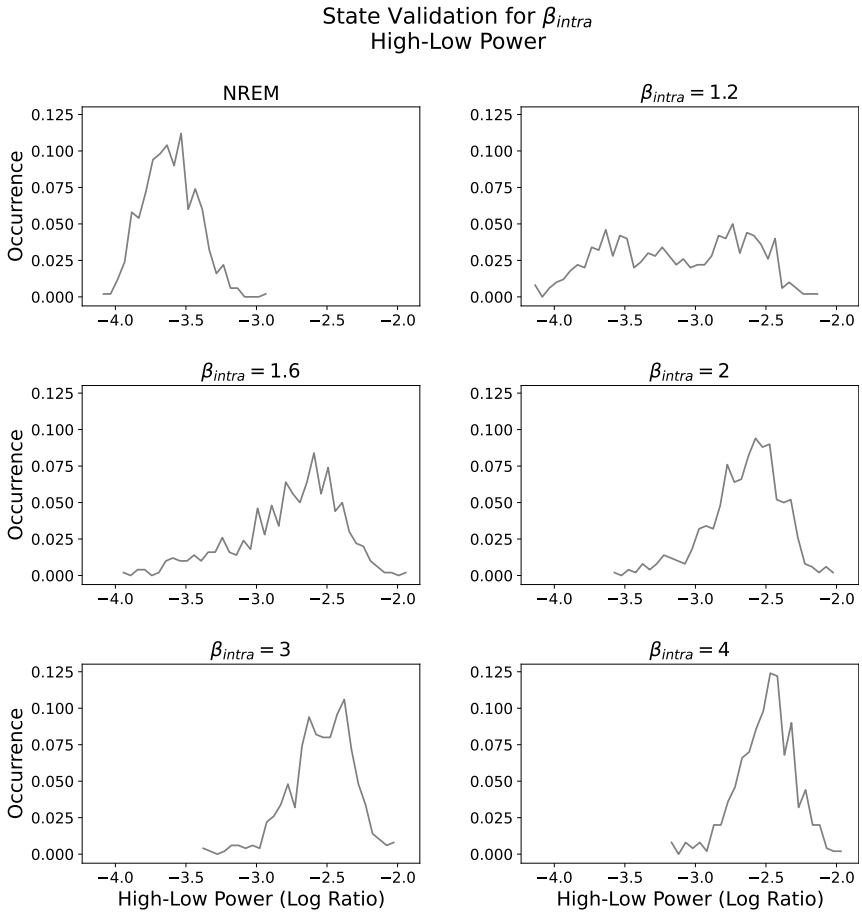

Figure S5.14: Distribution of high-/low-frequency power ratio of firing rate signals for increasing β_{intra}. Distribution of high-/low-frequency (where high is above 30 Hz and low is below 4 Hz) power ratio in firing rate signals moves to higher values with increasing β_{intra}. It confirms the spectral separation between NREM sleep ($\beta_{intra} = 1$) and $\beta_{intra} \geq 2$.

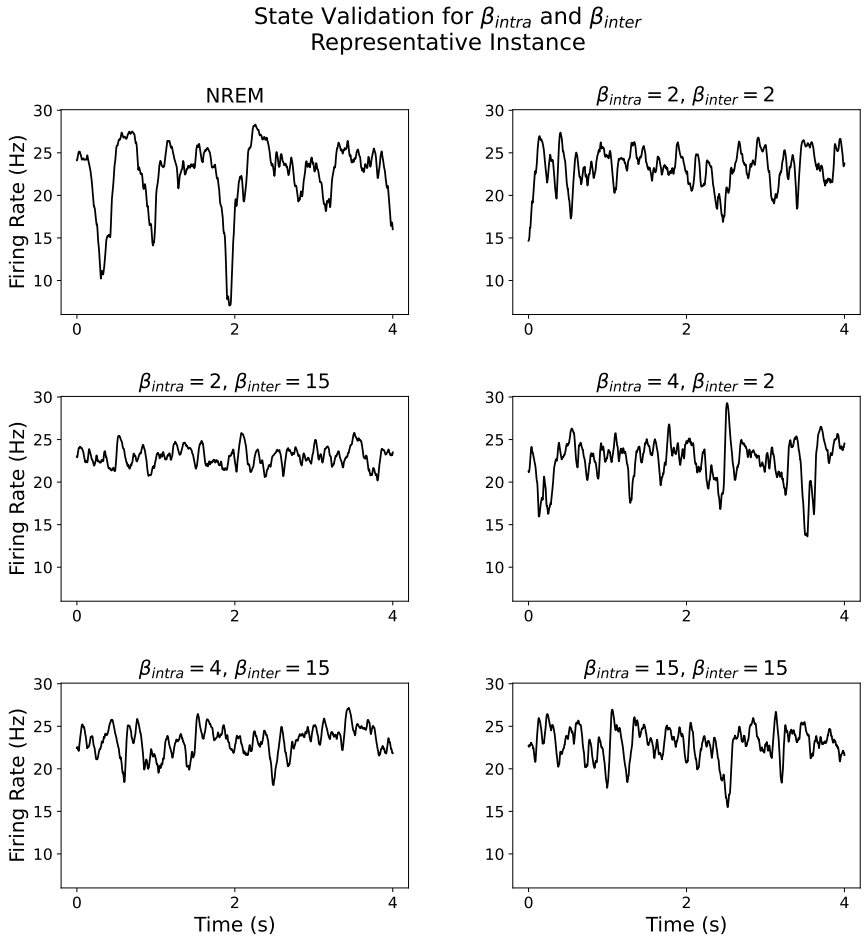

Figure S5.15: A representative instance of firing rate signals for increasing values of β_{intra} and β_{inter} in the two-cortical-column model. Simulated signals shows large amplitude fluctuations in NREM sleep ($\beta_{intra} = 1$, $\beta_{inter} = 1$) between periods of sustained activity (Up state) and silent activity (Down states). Amplitude of fluctuations decreases with increasing β_{intra} and β_{inter}.

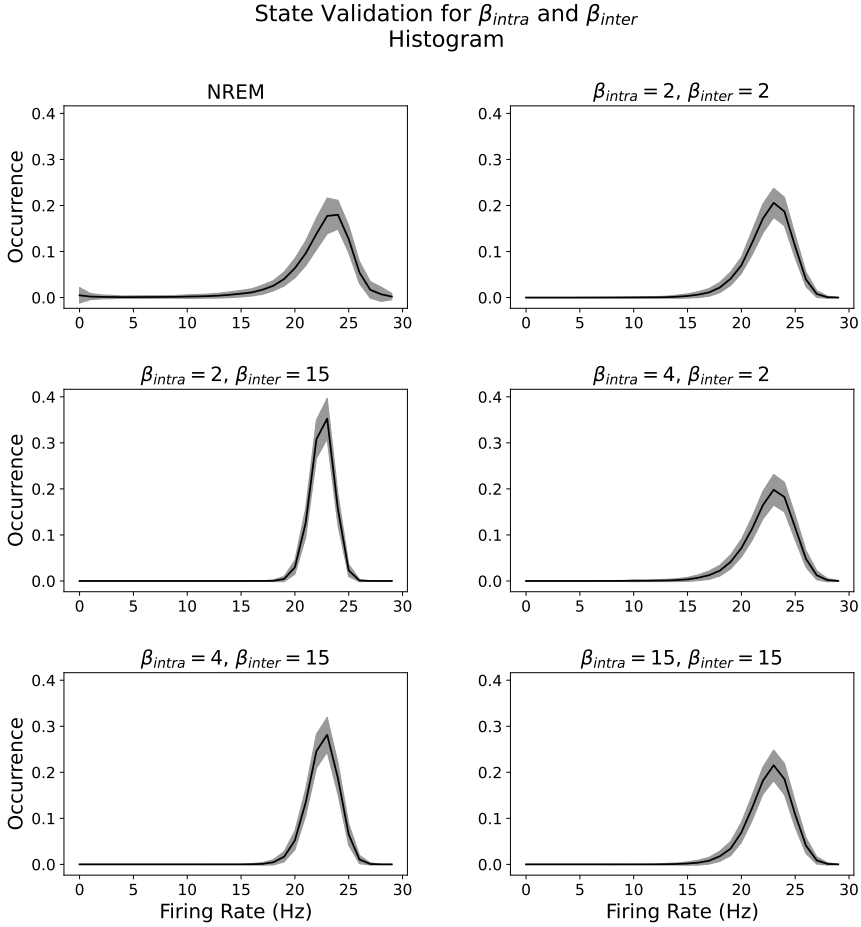

Figure S5.16: Distribution of firing rate signals for increasing β_{intra} and β_{inter} in the two-cortical-column model. Note that bistability in two cortical column model is compromised in NREM sleep compared to the one-cortical-column model. Nevertheless, bistability decreases with increasing β_{intra} and β_{inter}. Shaded area corresponds to standard deviation over 500 trials.

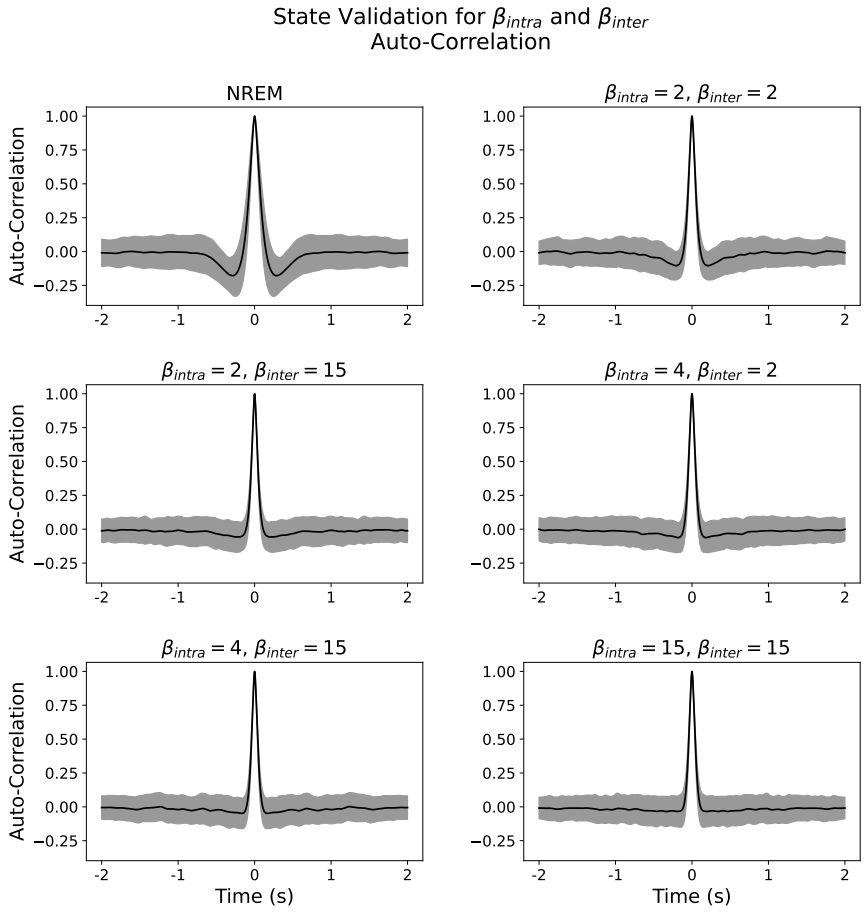

Figure S5.17: Auto-correlation of firing rate signals for increasing β_{intra} and β_{inter} in the two-cortical-column model. Average of auto-correlation of firing rate signals in NREM sleep ($\beta_{intra} = 1$, $\beta_{inter} = 1$) shows a negative peak around 0.5 s, likely presence of slow oscillation. The peaks decrease with increasing β_{intra} and β_{inter}. Shaded area corresponds to standard deviation of the average of auto-correlation over 500 trials.

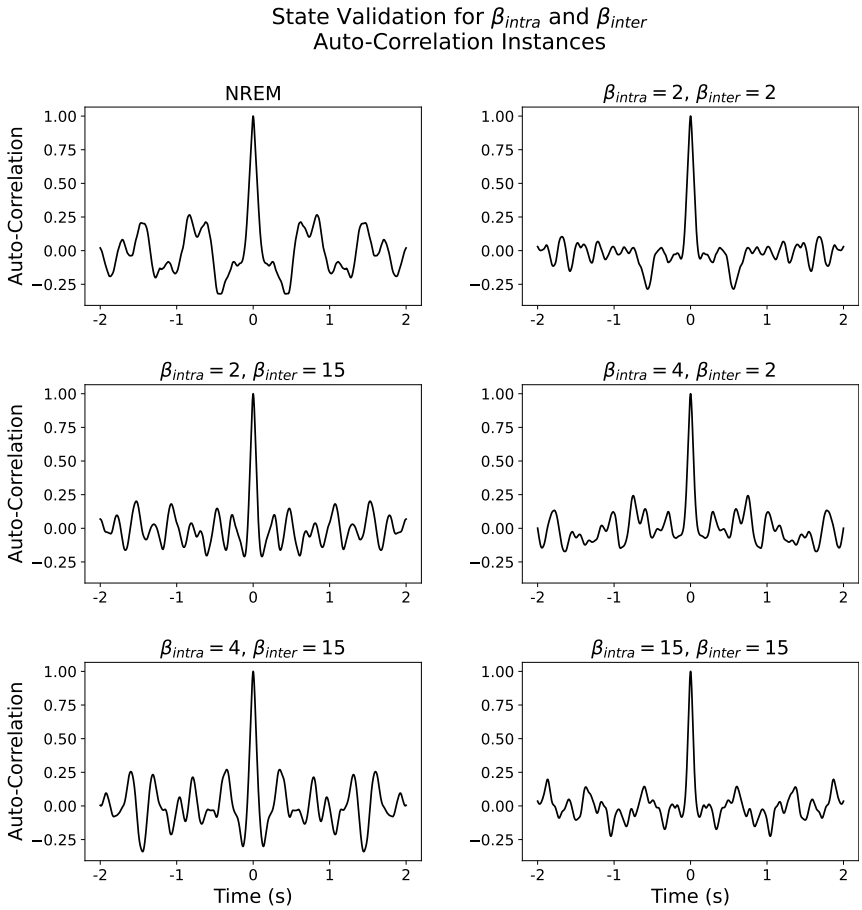

Figure S5.18: Auto-correlation of A representative instance of firing rate signals for increasing β_{intra} and β_{inter} in the two-cortical-column model. Auto-correlation of a representative firing rate signal in NREM sleep ($\beta_{intra} = 1$, $\beta_{inter} = 1$) shows a negative peak around 0.5 s and a peak around 1 s, presence of slow oscillation. The peaks become stochastic with lower time lags (higher frequency) with increasing β_{intra} and β_{inter}.

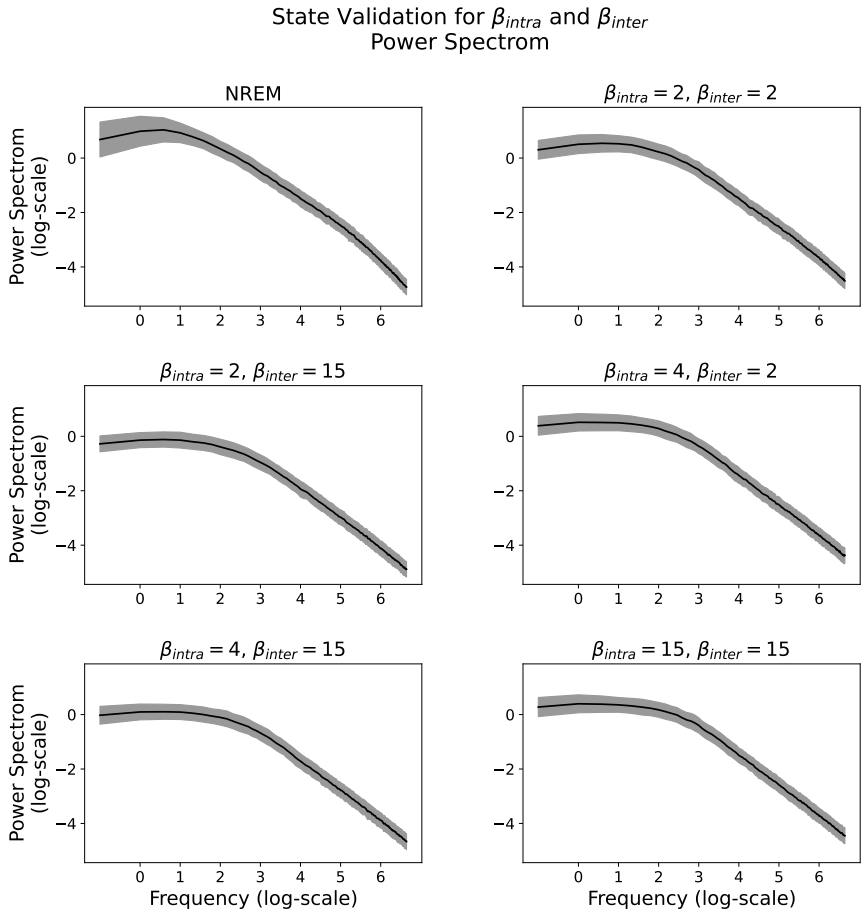

Figure S5.19: Spectral content of firing rate signals for increasing β_{intra} and β_{inter} in the two-cortical-column model. Average power spectrum density of firing rate signals decreases with increasing β_{intra} and β_{inter}. Shaded area corresponds to standard deviation of the average of power spectrum density over 500 trials.

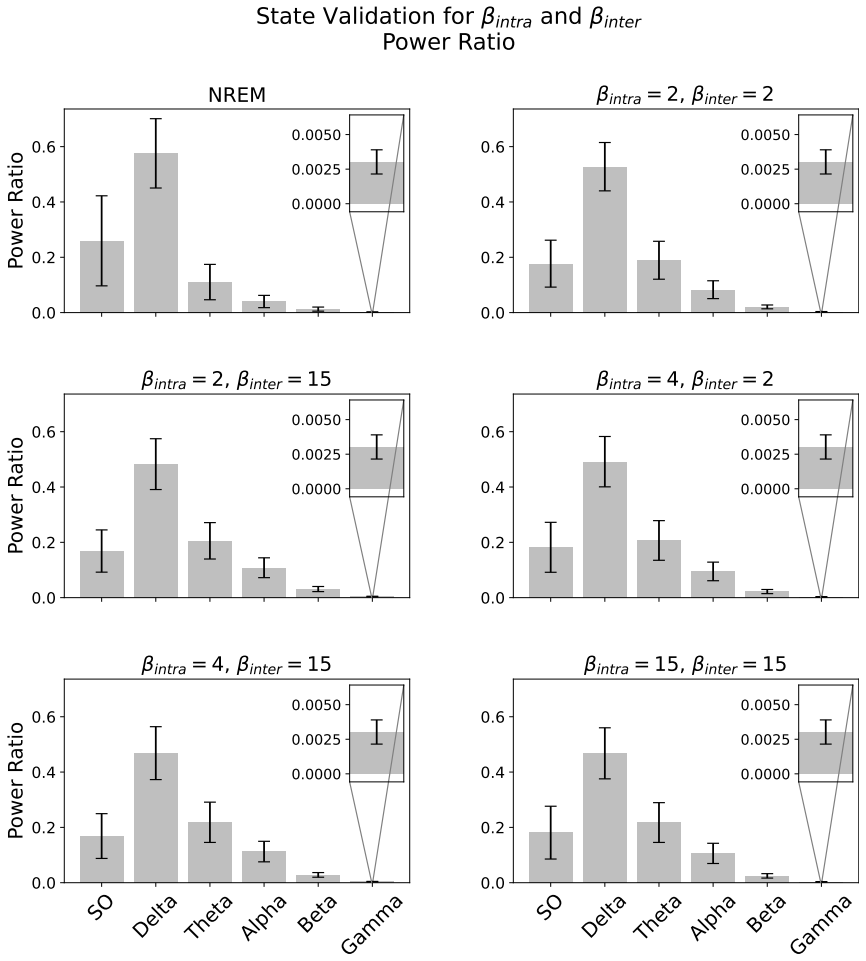

Figure S5.20: Power ratio of firing rate signals for increasing β_{intra} and β_{inter} in the two-cortical-column model. Firing rate signals carry more spectral power within the SO (<1 Hz) and delta (1-4 Hz) frequency bands in NREM sleep ($\beta_{intra} = 1$, $\beta_{inter} = 1$) than at any synaptic upscalings states. Power ratio of slow oscillation decreases with increasing β_{intra} and β_{inter}. On the other hand, power ratio of higher frequency bands (Theta, Alpha, Beta and Gamma) increases with increasing β_{intra} and β_{inter}. Error bar shows standard deviation over 500 trials.

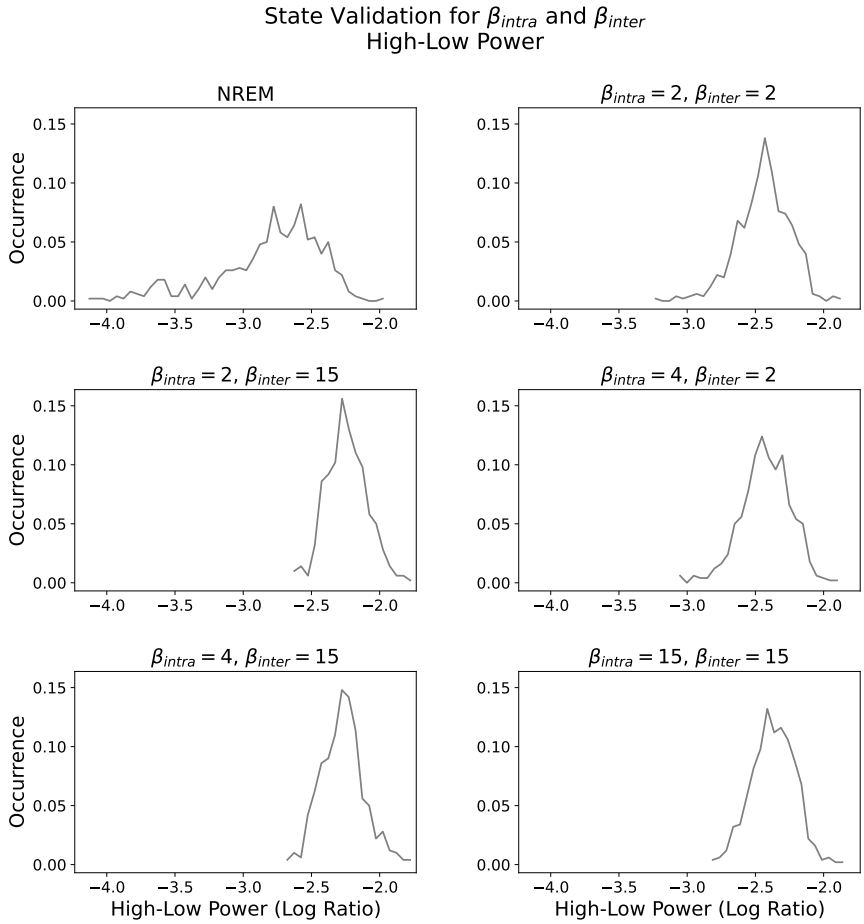

Figure S5.21: Distribution of high-/low-frequency power ratio of firing rate signals for increasing β_{intra} and β_{inter} in the two-cortical-column model. Distribution of high-/low-frequency (where high is above 30 Hz and low is below 4 Hz) power ratio in firing rate signals moves to higher values with increasing β_{intra} and β_{inter}. It confirms the spectral separation between NREM sleep ($\beta_{intra} = 1$, $\beta_{inter} = 1$) and $\beta_{intra} \geq 2$, $\beta_{inter} \geq 2$.

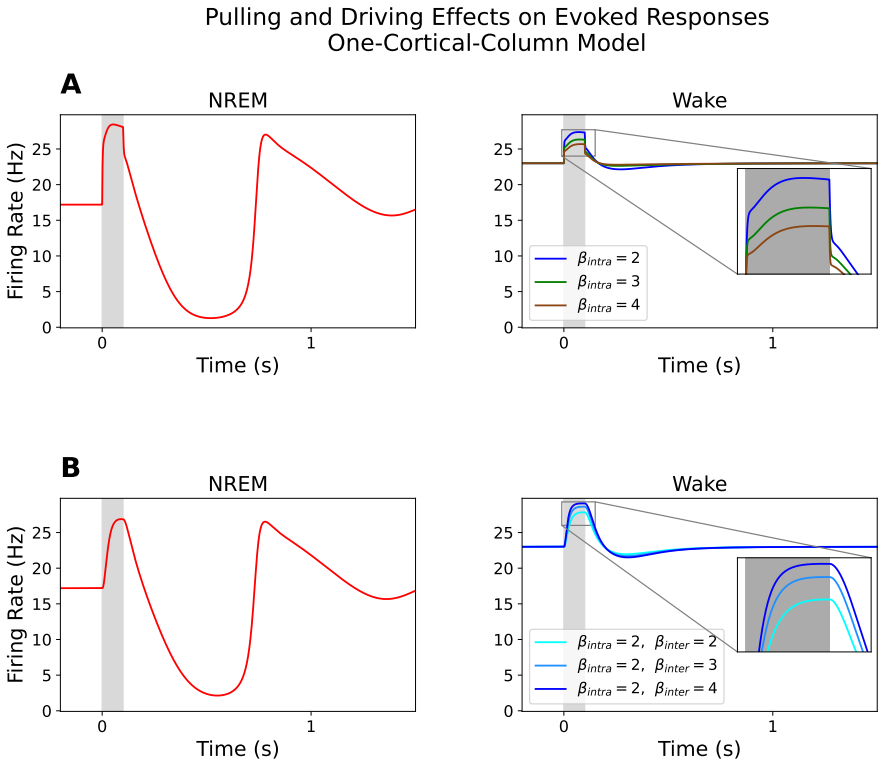

Figure S5.22: Pulling and driving effects of intra-synaptic upscaling on evoked responses in the one-cortical-column model. Deterministic firing rate signal of pyramidal population in response to an input. (**A**) The input amplitude is 70 mV (injected inputs). Figure shows the time trace of evoked response in NREM (*left*) and in wakefulness (*right*). Intra-synaptic upscaling (color coded) generates pulling effects on evoked responses in wakefulness. (**B**) As in panel **A** but for synaptic inputs when the input amplitude is 0.07 ms^{-1} and is applied through an inter-synapse. Figure shows the time trace of evoked response in NREM (*left*) and in wakefulness (*right*). Inter-synaptic upscaling (color coded) generates driving effects on evoked responses in wakefulness. Zero on x-axis represents input onset. Input duration is represented by a light gray area.

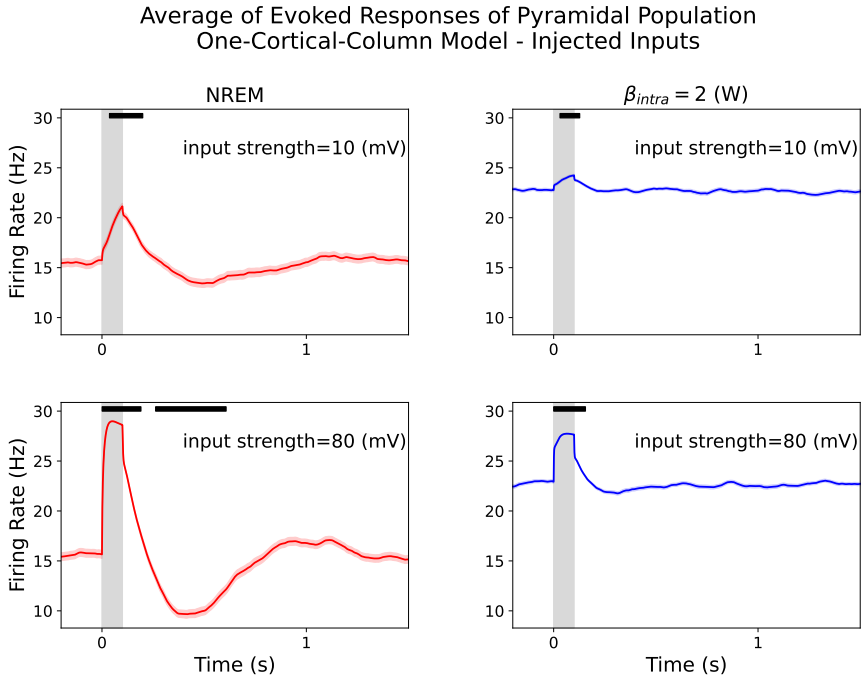

Figure S5.23: Average of evoked responses in the one-cortical-column model in the presence of Gaussian noise. Average response in NREM sleep (left column) and wakefulness (right column, $\beta_{intra} = 2$) when the amplitude of injected inputs are 10 mV (top row) and 80 mV (bottom row). Black horizontal bars show the location of significant time points (Bonferroni correction) when comparing evoked responses in poststimulus intervals with spontaneous activity in peristimulus intervals. Zero on x-axis represents input onset. Input duration is represented by a light gray area.

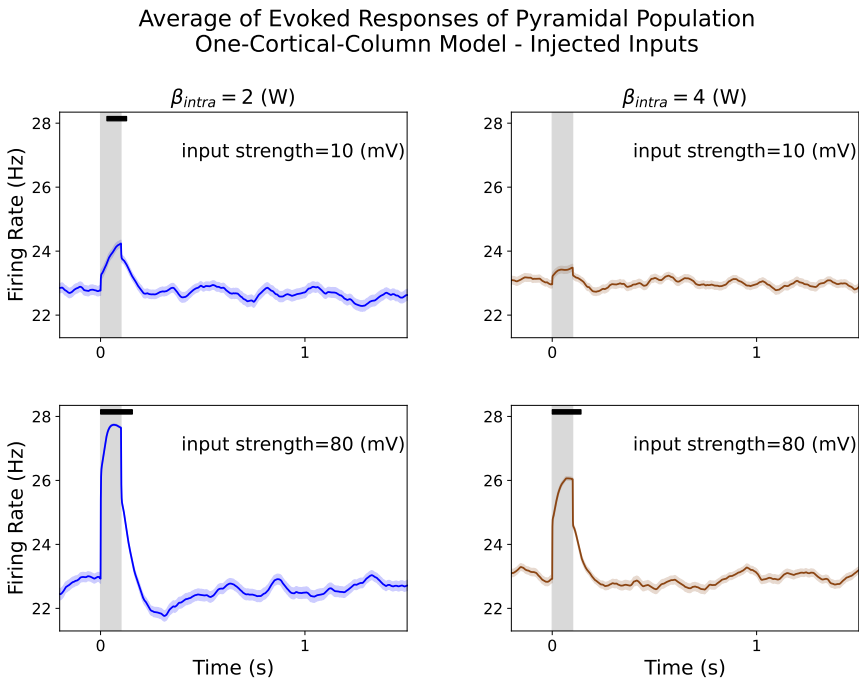

Figure S5.24: Average of evoked responses in wakefulness in the one-cortical-column model in the presence of Gaussian noise, as in Figure S5.23. Average response in wakefulness for $\beta_{intra} = 2$ (left column) and $\beta_{intra} = 4$ (right column) when the amplitude of injected inputs are 10 mV (top row) and 80 mV (bottom row). Note that the left column is identical to the right column in Figure S5.23. Black horizontal bars show the location of significant time points (Bonferroni correction) when comparing evoked responses in poststimulus intervals with spontaneous activity in peristimulus intervals. Zero on x-axis represents input onset. Input duration is represented by a light gray area.

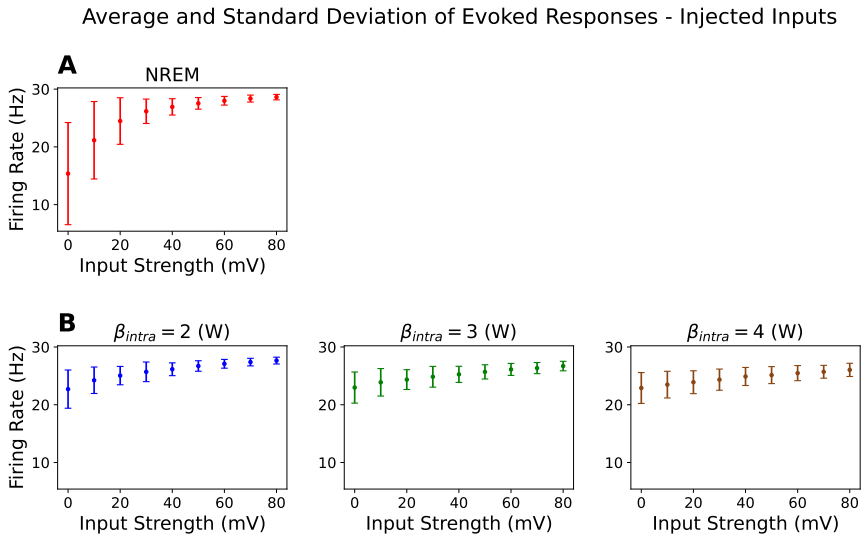

Figure S5.25: Average and standard deviation of evoked responses to injected inputs in the one-cortical-column model. Inputs are applied independent of synapse. Average and standard deviation of evoked responses in NREM sleep (panel **A**) and various intra-synaptic upscalings in wakefulness (columns in panel **B**) for various input amplitudes. input amplitude zero corresponds to spontaneous activities in peristimulus interval. Average and standard deviation of evoked responses increases and decreases, respectively, with increasing input amplitudes. Larger separation between distribution of evoked responses for a given input amplitude and distribution of spontaneous activities (input amplitude zero) determines better information detection. Larger separation among distribution of evoked responses for various input amplitudes (excluding input amplitude zero) determines better information differentiation.

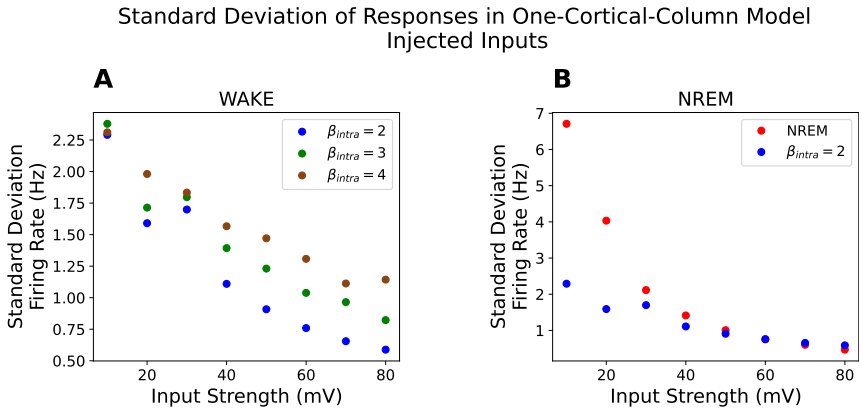

Figure S5.26: Effects of synaptic upscaling on standard deviation of evoked responses to injected inputs in the one-cortical-column model. Inputs are applied independent of synapse. Figures correspond to standard deviation of evoked responses (as in Figure S5.25). (**A**) standard deviation of evoked responses for various intra-synaptic upscalings in wakefulness for various input amplitudes. Standard deviation of evoked responses increases with increasing intra-synaptic upscaling in wakefulness. (**B**) As in panel **A**, but for NREM sleep and wakefulness ($\beta_{intra} = 2$) for various input amplitudes.

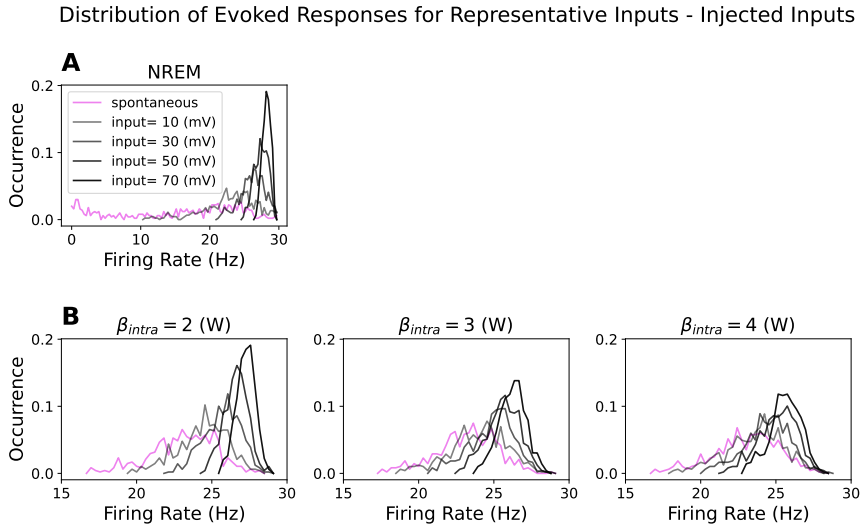

Figure S5.27: Distribution of evoked responses for representative input amplitudes. Distribution of evoked responses for representative input amplitudes (color coded) in NREM sleep (panel **A**) and various intra-synaptic upscalings in wakefulness (columns in panel **B**). Distribution of spontaneous activities in peristimulus intervals is in pink. Larger separation between distribution of evoked responses for a given input amplitude and distribution of spontaneous activities (in pink) determines better information detection. Larger separation among distribution of evoked responses for various input amplitudes determines better information differentiation.

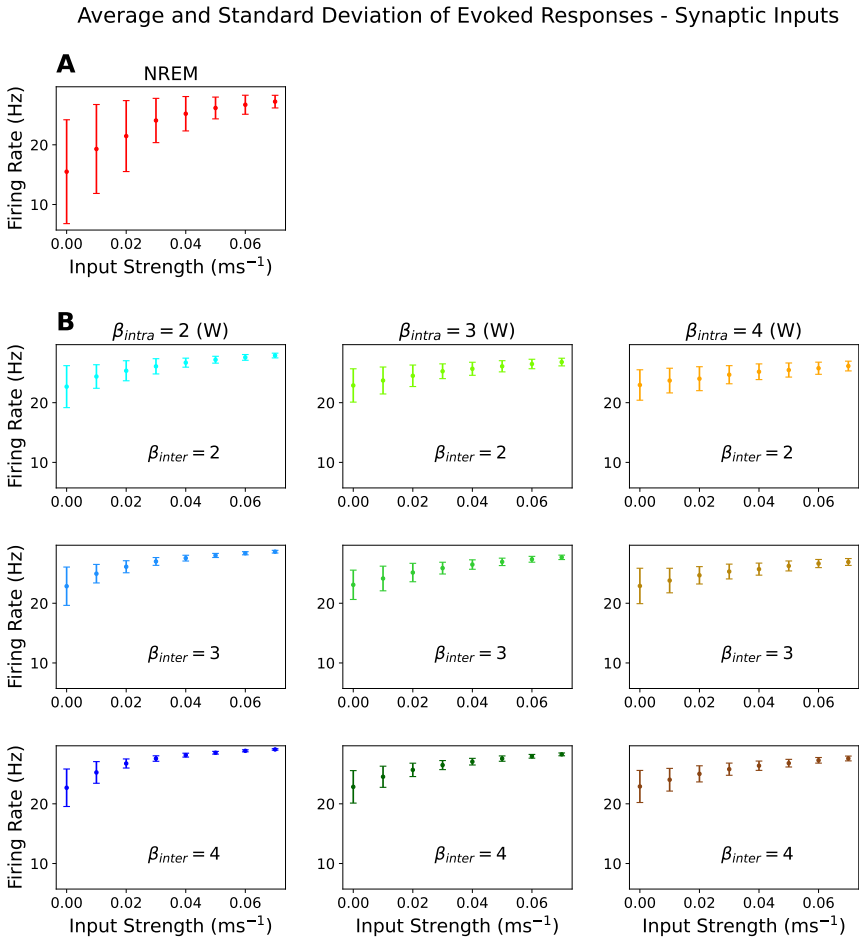

Figure S5.28: Average and standard deviation of evoked responses to synaptic inputs in the one-cortical-column model. Inputs are applied through an inter-synapse. (**A**) Average and standard deviation of evoked responses in NREM sleep for various input amplitudes. (**B**) As in panel **A**, but for various intra-synaptic upscalings (columns) and inter-synaptic upscalings (rows) in wakefulness. input amplitude zero corresponds to spontaneous activities in peristimulus intervals.

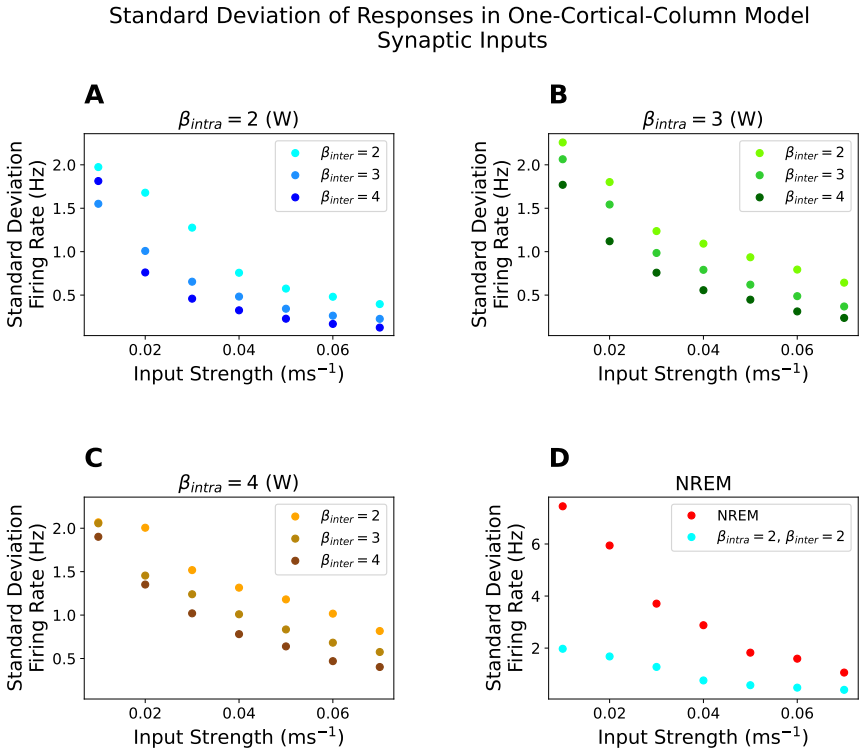

Figure S5.29: Effects of synaptic upscaling on standard deviation of evoked responses to synaptic inputs in the one-cortical-column model. Inputs are applied through an inter-synapse. Figures correspond to standard deviation of evoked responses as in Figure S5.28. (**A**) Standard deviation of evoked responses decreases with increasing inter-synaptic upscaling when intra-synaptic upscaling in wakefulness is kept constant at $\beta_{intra} = 2$. Results as in panel **A**, but for $\beta_{intra} = 3$ (**B**) and $\beta_{intra} = 4$ (**C**). Note that standard deviation of evoked responses increases with increasing intra-synaptic upscaling in wakefulness. (**D**) As in panel **A**, but for NREM sleep and $\beta_{intra} = 2$, $\beta_{inter} = 2$.

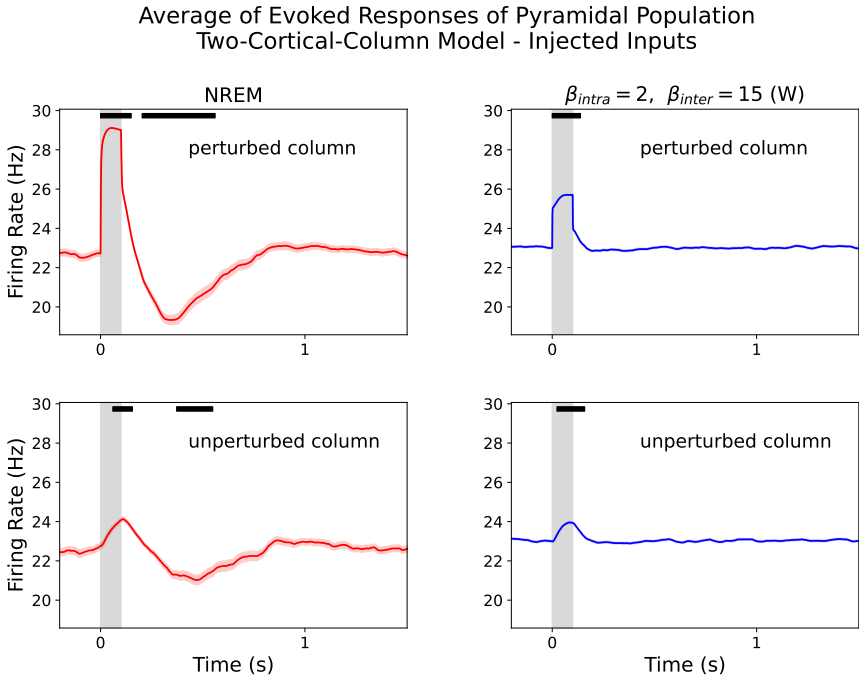

Figure S5.30: Average of evoked responses in the two-cortical-column model in the presence of Gaussian noise. Average response in NREM sleep (left column) and wakefulness (right column, $\beta_{intra} = 2$, $\beta_{inter} = 15$) for the perturbed column (top row) and the unperturbed column (bottom row). The amplitude of injected input is 80 mV. Black horizontal bars show the location of significant time points (Bonferroni correction) when comparing evoked responses in poststimulus intervals with spontaneous activity in peristimulus intervals. Zero on x-axis represents input onset. Input duration is represented by a light gray area.

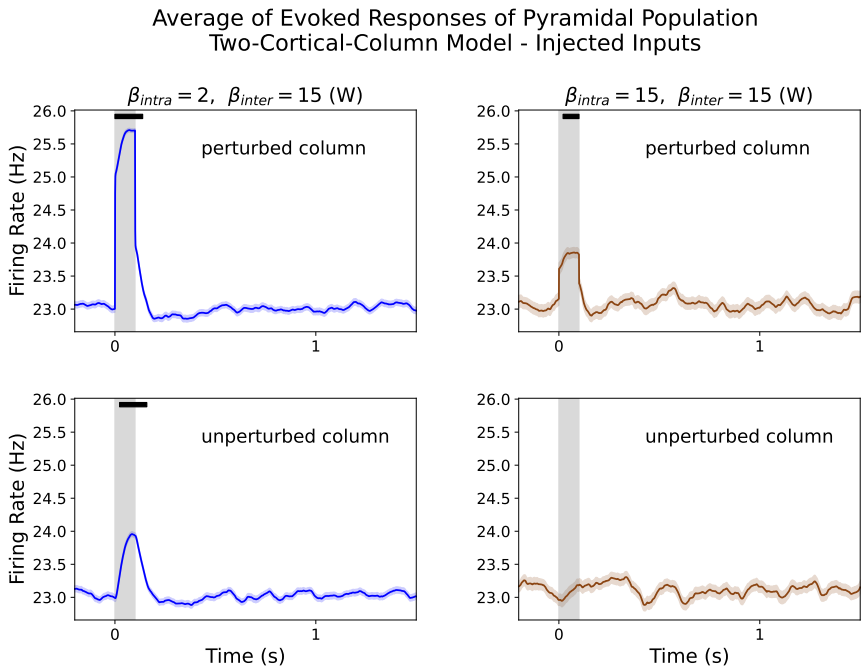

Figure S5.31: Average of evoked responses in wakefulness in the two-cortical-column model in the presence of Gaussian noise, as in Figure S5.30. Average response in wakefulness for $\beta_{intra} = 2$, $\beta_{inter} = 15$ (left column) and $\beta_{intra} = 15$, $\beta_{inter} = 15$ (right column) for the perturbed column (top row) and the unperturbed column (bottom row). The amplitude of injected input is 80 mV. Note that the left column is identical to the right column in Figure S5.30. Black horizontal bars show the location of significant time points (Bonferroni correction) when comparing evoked responses in poststimulus intervals with spontaneous activity in peristimulus intervals. Zero on x-axis represents input onset. Input duration is represented by a light gray area.

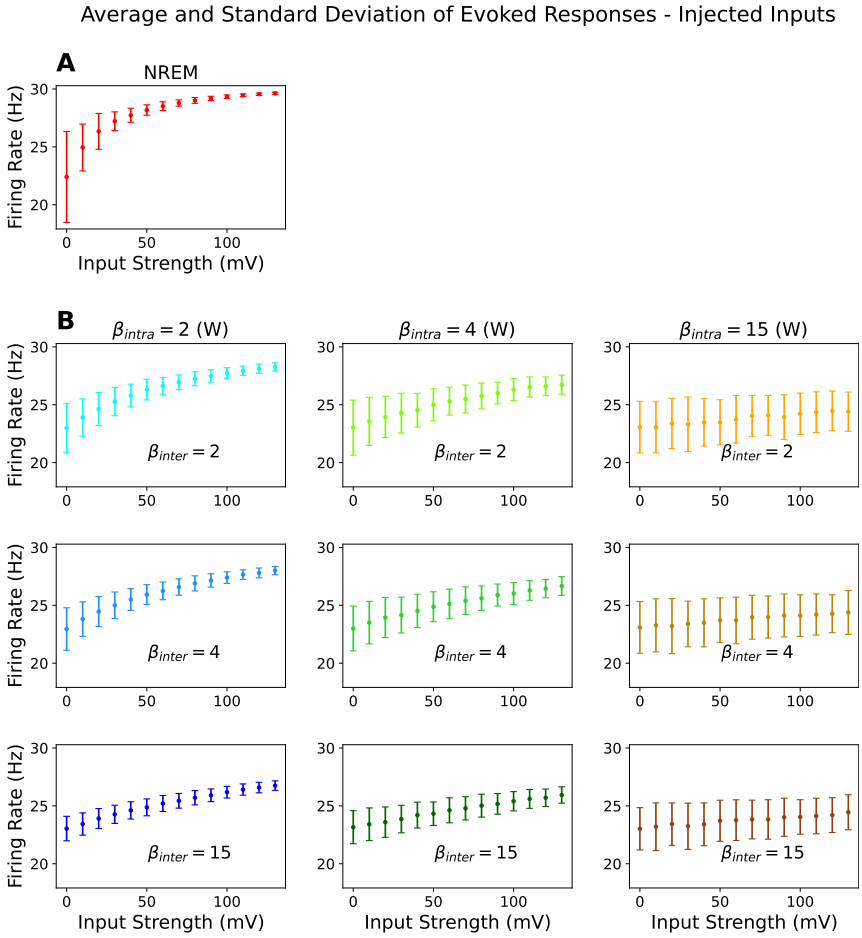

Figure S5.32: Average and standard deviation of evoked responses of the perturbed column to injected inputs in the two-cortical-column model. Inputs are applied independent of synapse. (**A**) Average and standard deviation of evoked responses in NREM sleep for various input amplitudes. (**B**) As in panel **A**, but for various intra-synaptic upscalings (columns) and inter-synaptic upscalings (rows) in wakefulness. input amplitude zero corresponds to spontaneous activities in peristimulus intervals.

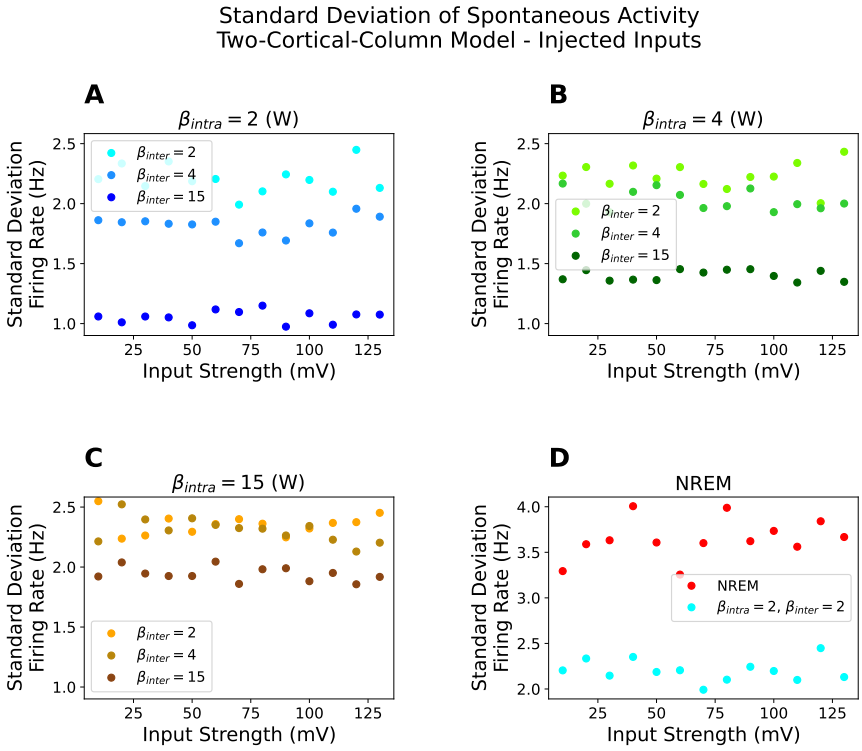

Figure S5.33: Effects of inter-synaptic upscaling on standard deviation of spontaneous activities to injected inputs in the two-cortical-column model. Figures correspond to standard deviation of spontaneous activities in peristimulus intervals of the unperturbed column for various input amplitudes (on x axis). Note that peristimulus intervals of perturbed and the unperturbed column are exchangeable due to the symmetric connections. (**A**) Standard deviation of spontaneous activities decreases with increasing inter-synaptic upscaling when intra-synaptic upscaling in wakefulness is kept constant at $\beta_{intra} = 2$. Results as in panel **A**, but for $\beta_{intra} = 3$ (**B**) and $\beta_{intra} = 4$ (**C**). Note that standard deviation of spontaneous activities increases with increasing intra-synaptic upscaling in wakefulness. (**D**) As in panel **A**, but for NREM sleep and $\beta_{intra} = 2$, $\beta_{inter} = 2$.

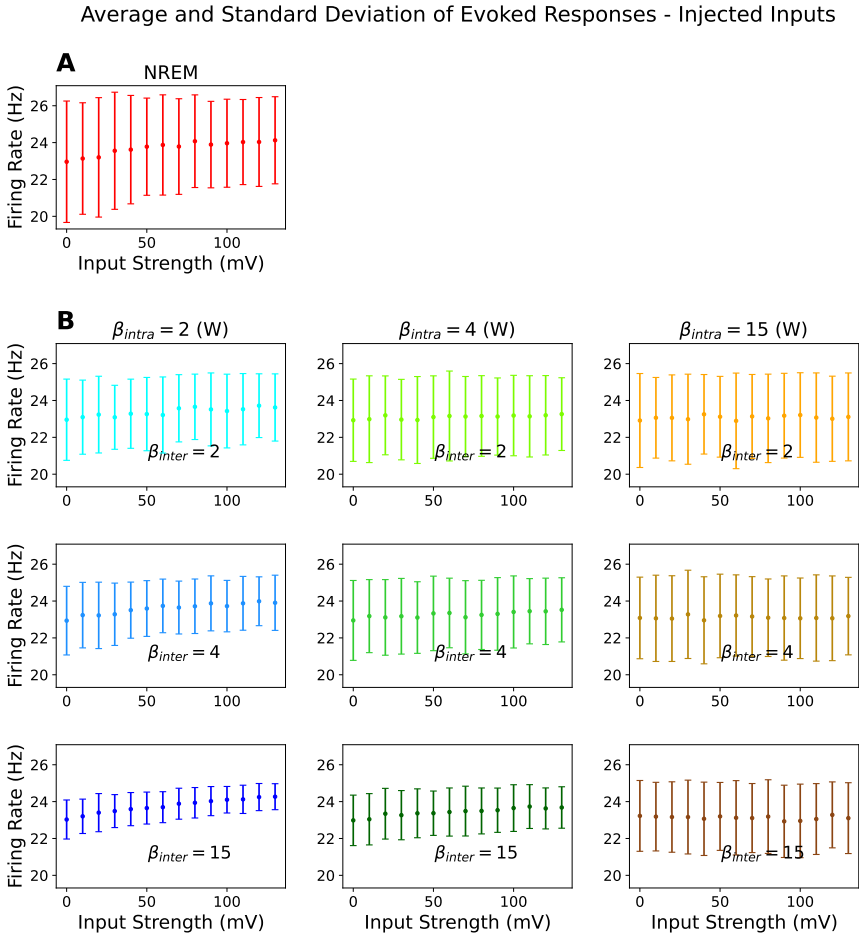

Figure S5.34: Average and standard deviation of evoked responses of the unperturbed column to injected inputs in the two-cortical-column model. Results as in Figure S5.32, but for the unperturbed column. (**A**) Average and standard deviation of evoked responses in NREM sleep for various input amplitudes. (**B**) As in panel **A**, but for various intra-synaptic upscalings (columns) and inter-synaptic upscalings (rows) in wakefulness. input amplitude zero corresponds to spontaneous activities in peristimulus intervals.

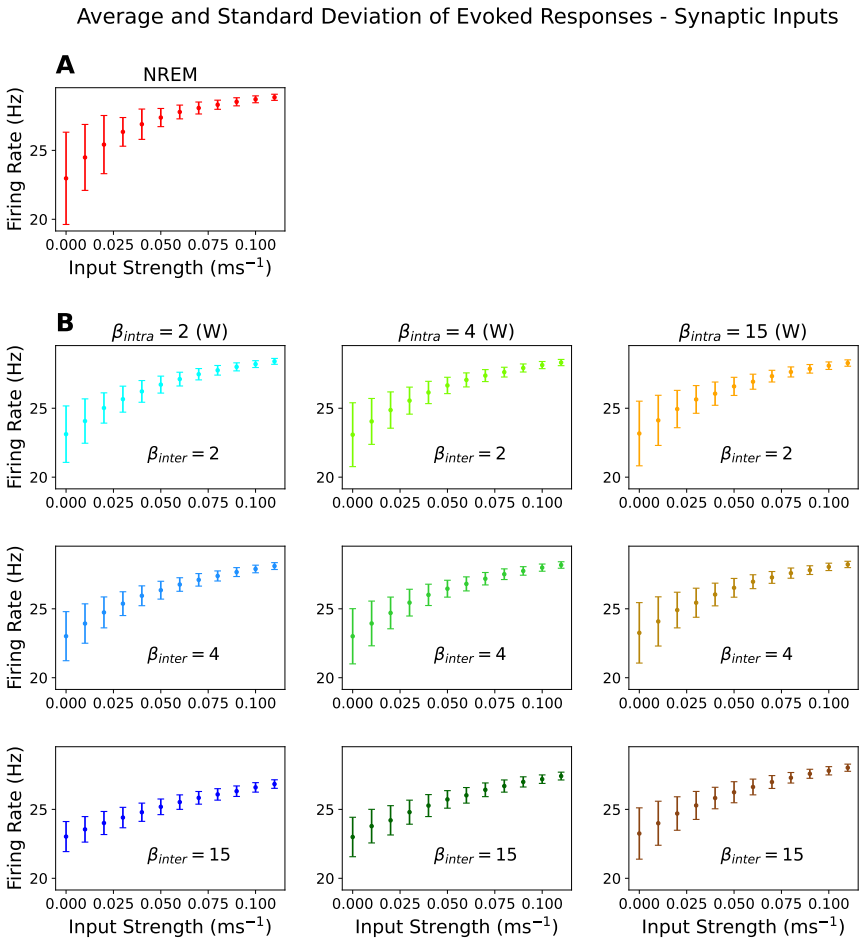

Figure S5.35: Average and standard deviation of evoked responses of the perturbed column to synaptic inputs in the two-cortical-column model. Inputs are applied through an intra-synapse. (**A**) Average and standard deviation of evoked responses in NREM sleep for various input amplitudes. (**B**) As in panel **A**, but for various intra-synaptic upscalings (columns) and inter-synaptic upscalings (rows) in wakefulness. input amplitude zero corresponds to spontaneous activities in peristimulus intervals.

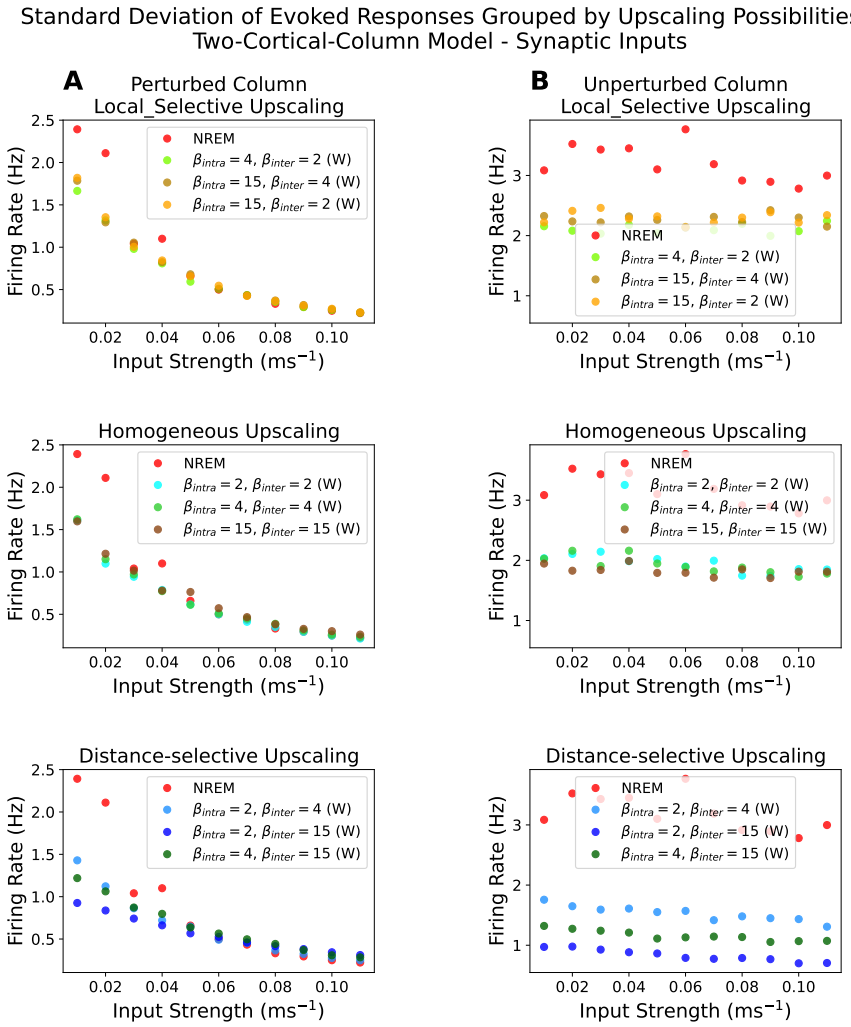

Figure S5.36: Standard deviation of evoked responses to synaptic inputs in the two-cortical-column model. Inputs are applied through an intra-synapse. (**A**) Standard deviation of evoked responses in the perturbed column in wakefulness is the largest for local-selective synaptic upscaling scenario (*Top*) and smallest for distance-selective synaptic upscaling scenario (*Bottom*). Figures (next page)

Figure S5.36 *(previous page)*: correspond to standard deviation of evoked responses in Figure S5.35 (**B**). Results as in panel **A**, but for the unperturbed column. Note that standard deviation of evoked responses in wakefulness is the largest for local-selective synaptic upscaling scenario (*Top*) and smallest for distance-selective synaptic upscaling scenario (*Bottom*).

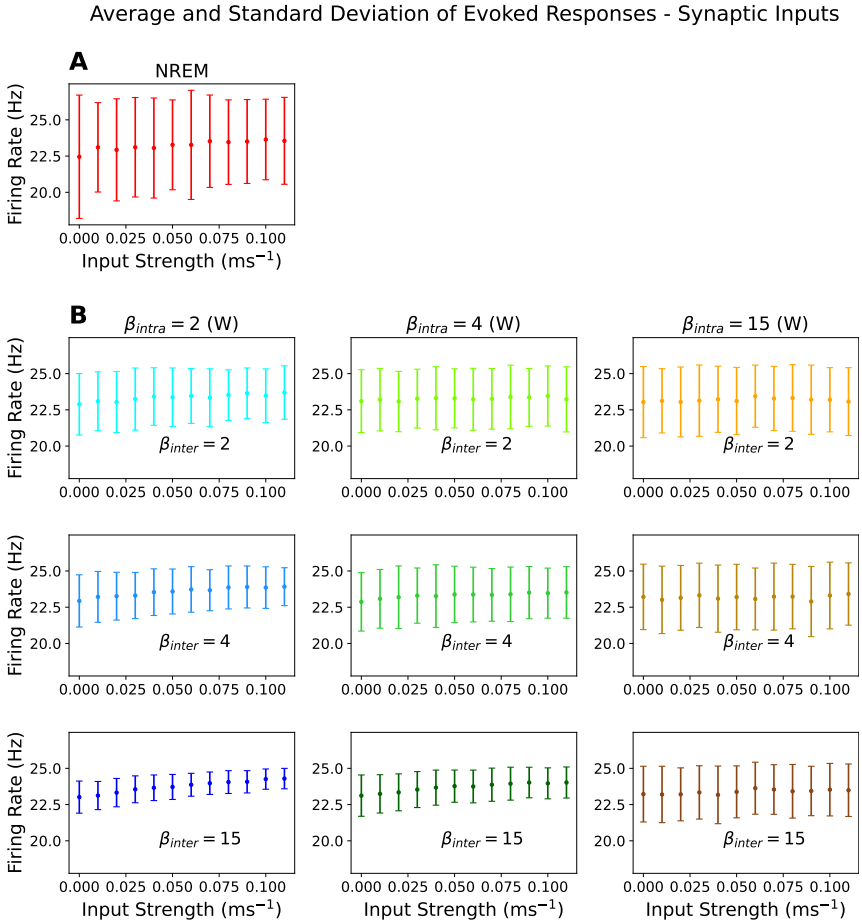

Figure S5.37: Average and standard deviation of evoked responses of the unperturbed column to synaptic inputs in the two-cortical-column model. Results as in Figure S5.35, but for the unperturbed column. (**A**) Average and standard deviation of evoked responses in NREM sleep for various input amplitudes. (**B**) As in panel **A**, but for various intra-synaptic upscalings (columns) and inter-synaptic upscalings (rows) in wakefulness. input amplitude zero corresponds to spontaneous activities in peristimulus intervals.

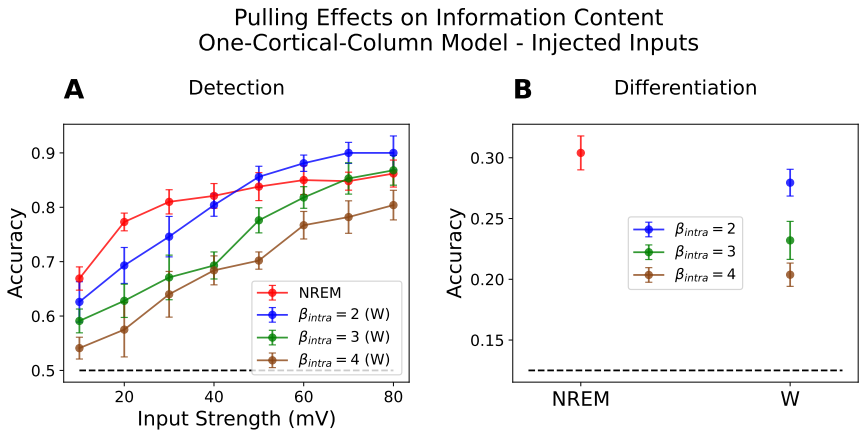

Figure S5.38: Pulling effect due to intra-synaptic upscaling on information content at offset compared to another random time point in peristimulus intervals in the one-cortical-column model. Results as in Figure 3.3. (**A**). Information detection at input offset for various input amplitudes (injected inputs) in NREM (red) and various intra-synaptic upscalings in wakefulness (color coded). (**B**). Information differentiation at input offset for NREM (red) and various intra-synaptic upscalings in wakefulness (color coded as in panel **A**). Increasing intra-synaptic upscaling in wakefulness decreases information differentiation. Note that information differentiation is independent of the choice of time point in peristimulus intervals. Error bar shows 95 percent confidence interval. Black dash line represents the chance-level accuracy $= \frac{1}{\#\text{input amplitudes}}$.

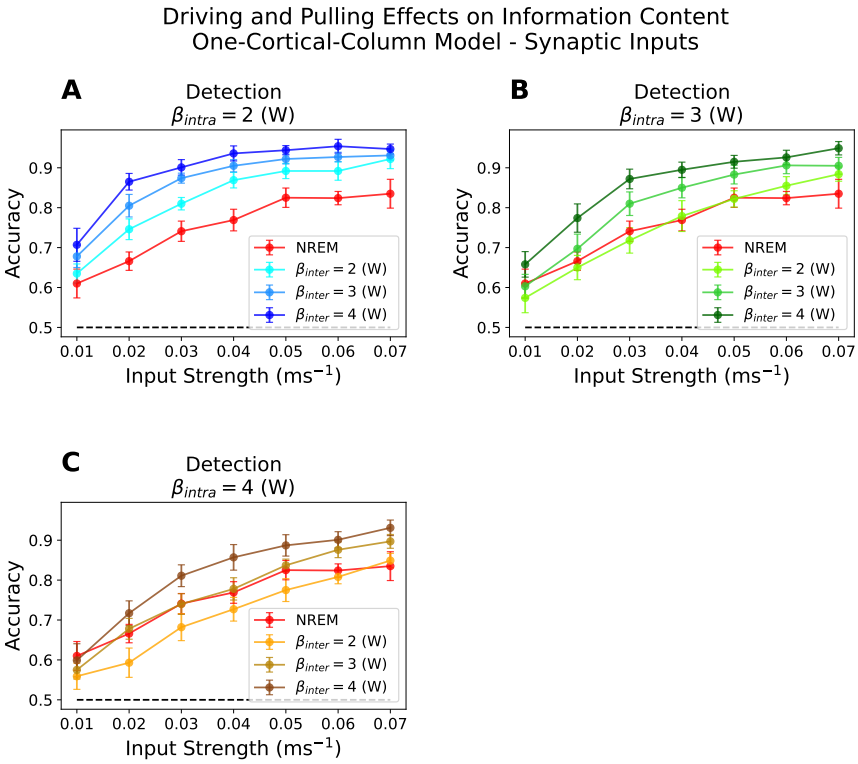

Figure S5.39: Driving and pulling effect due to synaptic upscaling on information detection at offset compared to another random time point in peristimulus intervals in the one-cortical-column model. Results as in Figure 3.5A-C. (**A**). Information detection at input offset for various input amplitudes (Inter-synaptic inputs) in NREM (red) and various inter-synaptic upscalings when intra-synaptic upscaling in wakefulness is kept constant at $\beta_{intra} = 2$ in wakefulness (color coded). Results as in panel **A**, but for $\beta_{intra} = 3$ (**B**) and $\beta_{intra} = 4$ (**C**). Error bar shows 95 percent confidence interval. Black dash line represents the chance-level accuracy $= \frac{1}{\#\text{input amplitudes}}$.

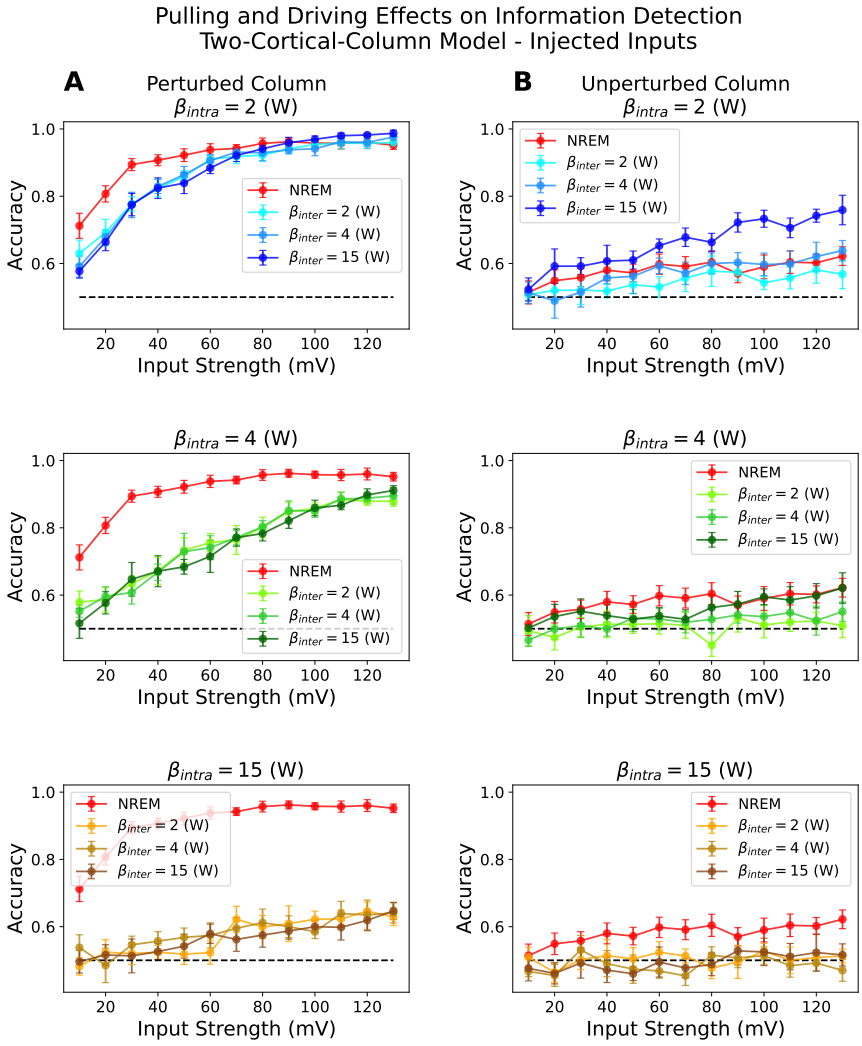

Figure S5.40: Pulling and driving effects due to synaptic upscaling on information detection at offset compared to another random time point in pristimulus interval in the two-cortical-column model. Results as in Figure 3.9. (**A**). Information detection at input offset in the perturbed column for various input amplitudes (injected inputs) in NREM (red) and various synaptic upscalings in (next page)

Figure S5.40 *(previous page)*: wakefulness when intra-synaptic upscaling is kept constant at $\beta_{intra} = 2$ (*Top*), $\beta_{intra} = 4$ (*Middle*) and $\beta_{intra} = 15$ (*Bottom*). (**B**). As in panel **A**, but for the unperturbed column. Error bar shows 95 percent confidence interval. Black dash line represents the chance-level accuracy $= \frac{1}{\#\text{input amplitudes}}$.

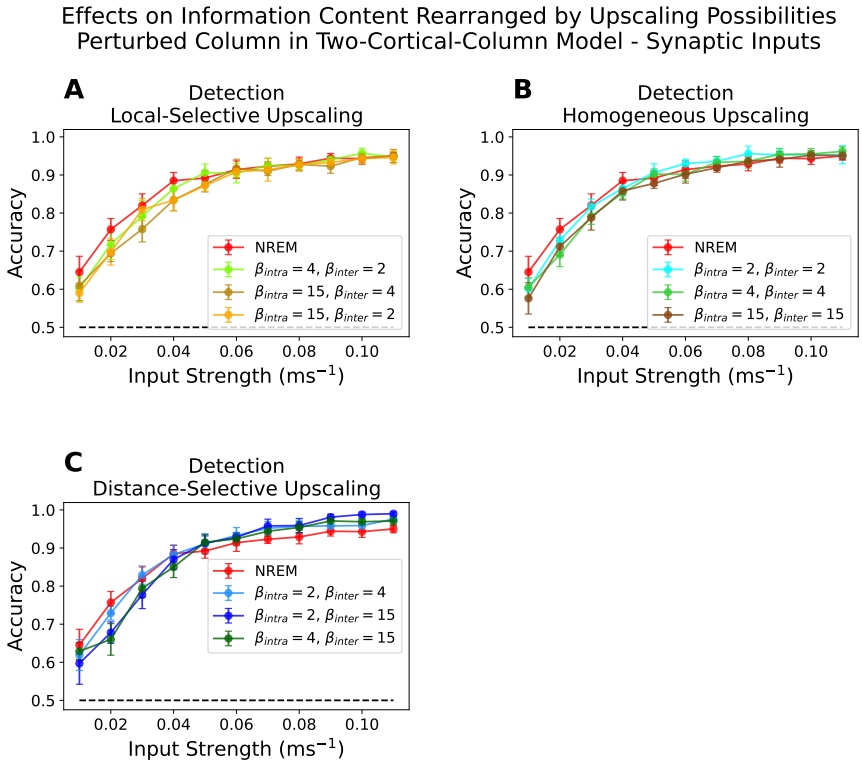

Figure S5.41: Effects of synaptic upscaling on information detection at offset compared to another random time point in pristimulus interval in the perturbed column in the two-cortical-column model rearranged by synaptic upscaling scenarios. Results as in Figure 3.12. (**A**). Information detection at input offset for various input amplitudes in NREM (red) and local-selective synaptic upscaling scenario in wakefulness (color coded). (**B**), (**C**). As in panel **A**, but for homogeneous and distance-selective synaptic upscaling scenarios in wakefulness, respectively. Error bar shows 95 percent confidence interval. Black dash line represents the chance-level accuracy $= \frac{1}{\#\text{input amplitudes}}$.

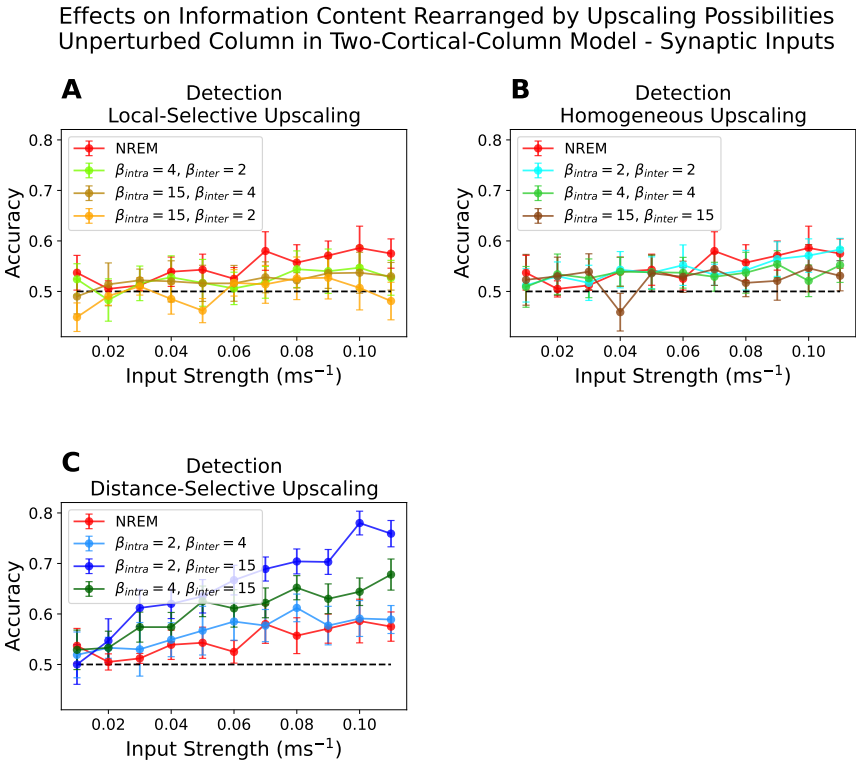

Figure S5.42: Effects of synaptic upscaling on information detection at offset compared to another random time point in pristimulus interval in the unperturbed column in the two-cortical-column model rearranged by synaptic upscaling scenarios. Results as in Figure 3.13. (**A**). Information detection at input offset for various input amplitudes in NREM (red) and local-selective synaptic upscaling scenario in wakefulness (color coded). (**B**), (**C**). As in panel **A**, but for homogeneous and distance-selective synaptic upscaling scenarios in wakefulness, respectively. Error bar shows 95 percent confidence interval. Black dash line represents the chance-level accuracy $= \frac{1}{\#\text{input amplitudes}}$.

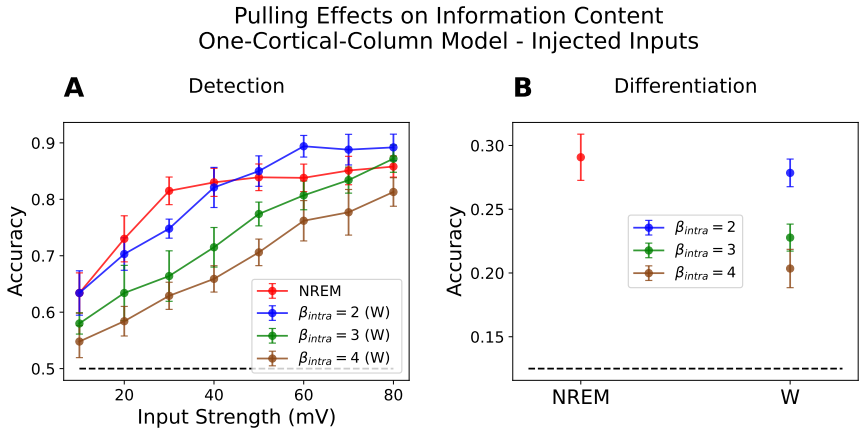

Figure S5.43: Pulling effects of synaptic upscaling on information content at 20 ms prior offset in the one-cortical-column model. Results as in Figure 3.3. (**A**). Information detection at 20 ms prior offset for various input amplitudes (injected inputs) in NREM (red) and various synaptic upscalings in wakefulness (color coded). (**B**). Information differentiation at input offset for NREM (red) and various synaptic upscalings in wakefulness (color coded as in panel **A**). Error bar shows 95 percent confidence interval. Black dash line represents the chance-level accuracy $= \frac{1}{\#\text{input amplitudes}}$.

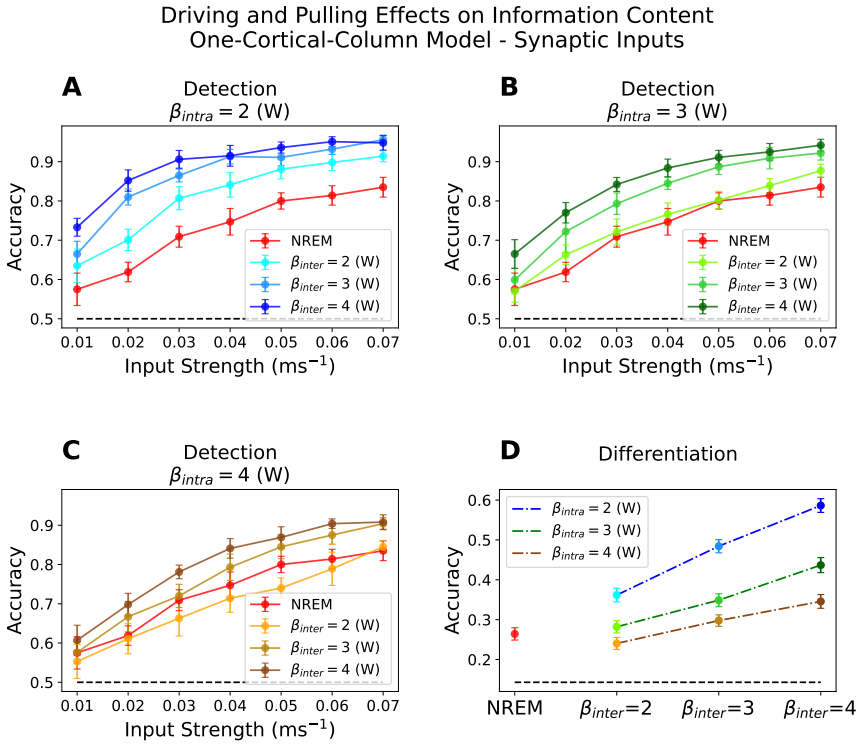

Figure S5.44: Driving and pulling effect due to synaptic upscaling on information content at 20 ms prior offset in the one-cortical-column model. Results as in Figure 3.5. (**A**). Information detection at 20 ms prior offset for various input amplitudes (Inter-synaptic inputs) in NREM (red) and various synaptic upscalings in wakefulness (color coded). Results as in panel **A**, but for $\beta_{intra} = 3$ (**B**) and $\beta_{intra} = 4$ (**C**). (**D**). Information differentiation at 20 ms prior input offset for NREM (red) and various synaptic upscalings in wakefulness (color coded). Error bar shows 95 percent confidence interval. Black dash line represents the chance-level accuracy $= \frac{1}{\#\text{input amplitudes}}$.

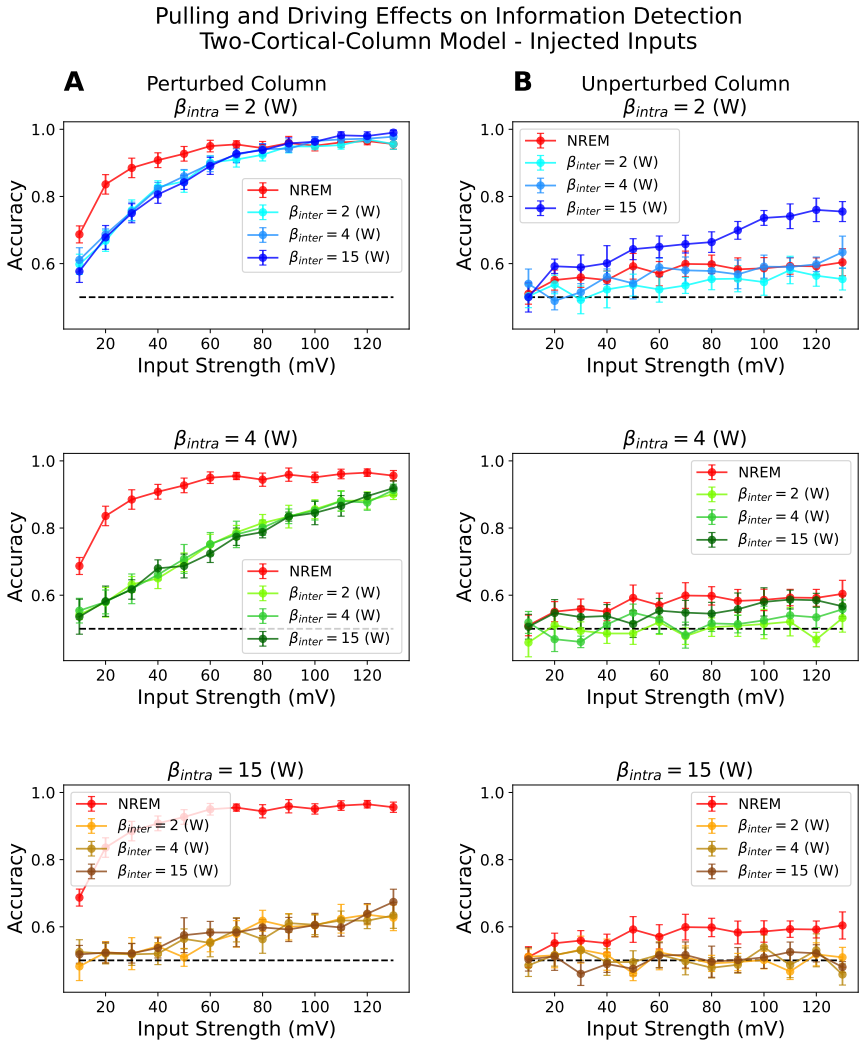

Figure S5.45: Pulling and driving effects due to synaptic upscaling on information detection at 20 ms prior offset in the two-cortical-column model. Results as in Figure 3.9. (**A**). Information detection at 20 ms prior offset in the perturbed column for various input amplitudes (injected inputs) in NREM (red) and various synaptic upscalings in wakefulness when intra-synaptic upscaling is (next page)

Figure S5.45 *(previous page)*: kept constant at $\beta_{intra} = 2$ (*Top*), $\beta_{intra} = 4$ (*Middle*) and $\beta_{intra} = 15$ (*Bottom*). (**B**). As in panel **A**, but for the unperturbed column. Error bar shows 95 percent confidence interval. Black dash line represents the chance-level accuracy $= \frac{1}{\#\text{input amplitudes}}$.

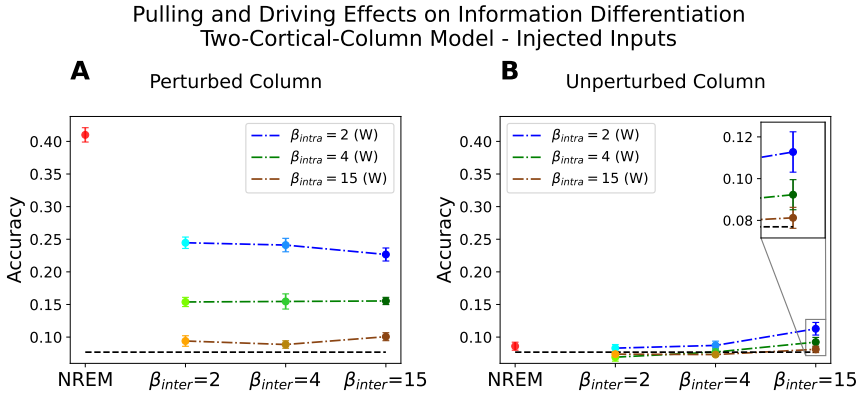

Figure S5.46: Pulling and driving effects due to synaptic upscaling on information differentiation at 20 ms prior offset in the two-cortical-column model. Results as in Figure 3.10. (**A**). Information differentiation at 20 ms prior offset in the perturbed column for various input amplitudes (injected inputs) in NREM (red) and various synaptic upscalings in wakefulness (color coded). (**B**). As in panel **A**, but for the unperturbed column. Error bar shows 95 percent confidence interval. Black dash line represents the chance-level accuracy $= \frac{1}{\#\text{input amplitudes}}$.

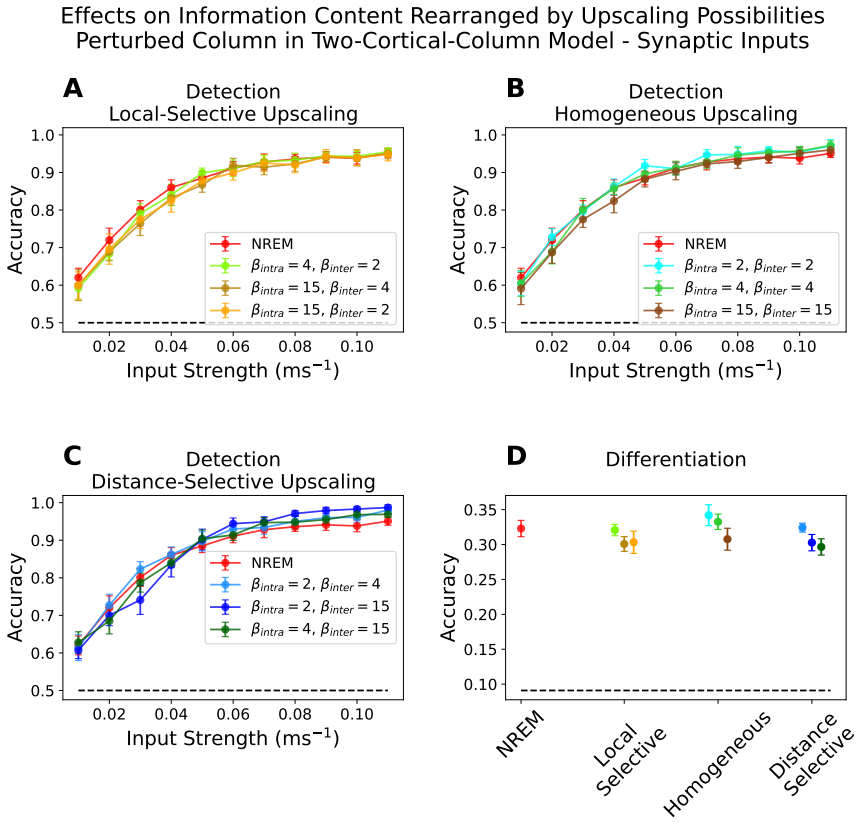

Figure S5.47: Effects of synaptic upscaling on information content at 20 ms prior offset in the perturbed column in the two-cortical-column model rearranged by synaptic upscaling scenarios. Results as in Figure 3.12. (**A**). Information detection at input offset for various input amplitudes in NREM (red) and local-selective synaptic upscaling scenario in wakefulness (color coded). (**B**), (**C**). As in panel **A**, but for homogeneous and distance-selective synaptic upscaling scenarios in wakefulness, respectively. (**D**) Information differentiation for NREM and three synaptic upscaling scenarios in wakefulness. Error bar shows 95 percent confidence interval. Black dash line represents the chance-level accuracy $= \frac{1}{\#\text{input amplitudes}}$.

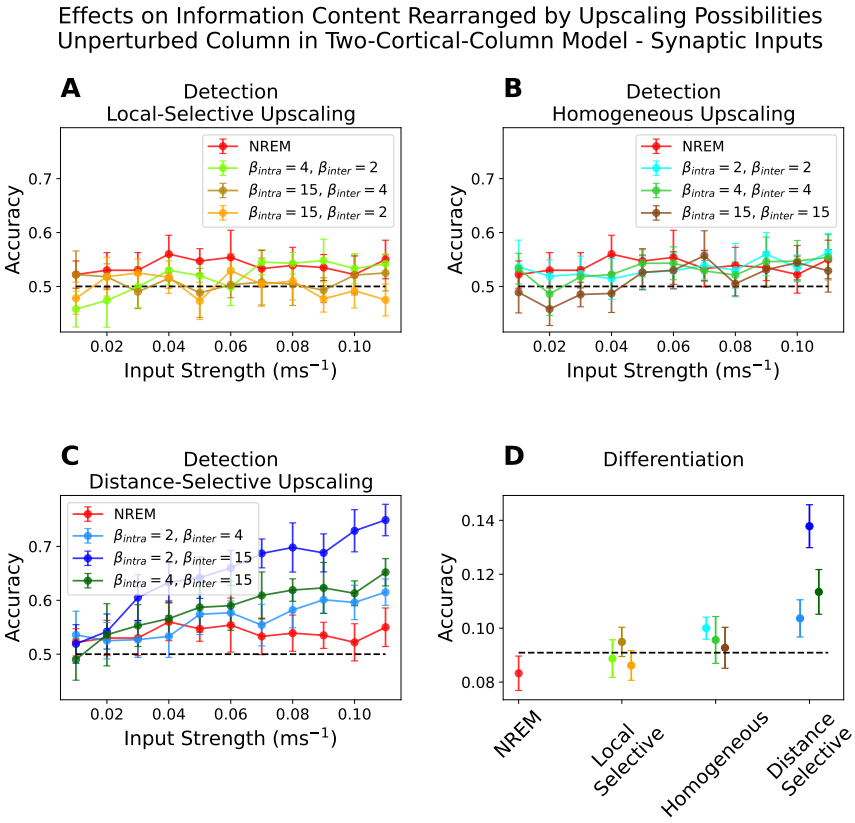

Figure S5.48: Effects of synaptic upscaling on information content at 20 ms prior offset in the unperturbed column in the two-cortical-column model rearranged by synaptic upscaling scenarios. Results as in Figure 3.13. (**A**). Information detection at input offset for various input amplitudes in NREM (red) and local-selective synaptic upscaling scenario in wakefulness (color coded). (**B**), (**C**). As in panel **A**, but for homogeneous and distance-selective synaptic upscaling scenarios in wakefulness, respectively. (**D**) Information differentiation for NREM and three synaptic upscaling scenarios in wakefulness. Error bar shows 95 percent confidence interval. Black dash line represents the chance-level accuracy $= \frac{1}{\#\text{input amplitudes}}$.

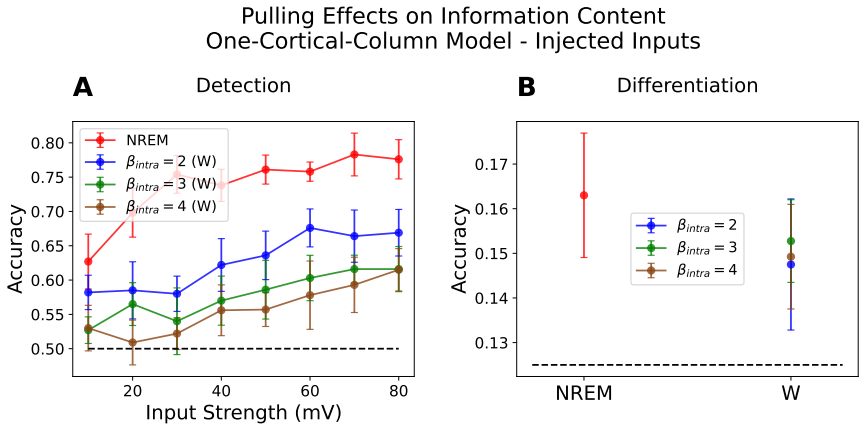

Figure S5.49: Pulling effects of synaptic upscaling on information content at 20 ms post offset in the one-cortical-column model. Results as in Figure 3.3. (**A**). Information detection at 20 ms post offset for various input amplitudes (injected inputs) in NREM (red) and various synaptic upscalings in wakefulness (color coded). (**B**). Information differentiation at input offset for NREM (red) and various synaptic upscalings in wakefulness (color coded as in panel **A**). Error bar shows 95 percent confidence interval. Black dash line represents the chance-level accuracy $= \frac{1}{\#\text{input amplitudes}}$.

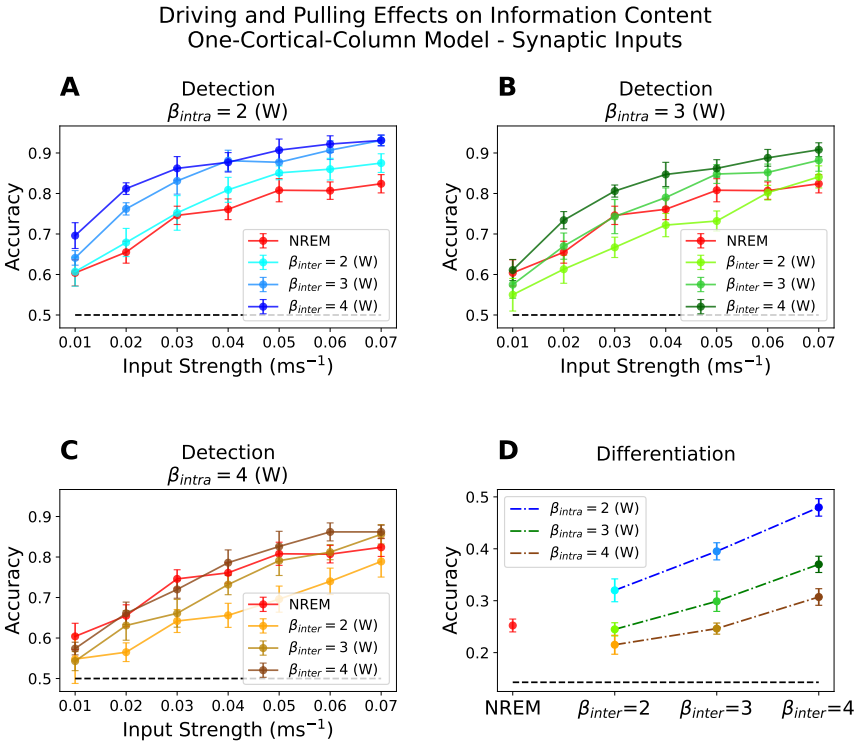

Figure S5.50: Driving and pulling effect due to synaptic upscaling on information content at 20 ms post offset in the one-cortical-column model. Results as in Figure 3.5. (**A**). Information detection at 20 ms post offset for various input amplitudes (Inter-synaptic inputs) in NREM (red) and various synaptic upscalings in wakefulness (color coded). Results as in panel **A**, but for $\beta_{intra} = 3$ (**B**) and $\beta_{intra} = 4$ (**C**). (**D**). Information differentiation at 20 ms post to input offset for NREM (red) and various synaptic upscalings in wakefulness (color coded). Error bar shows 95 percent confidence interval. Black dash line represents the chance-level accuracy $= \frac{1}{\#\text{input amplitudes}}$.

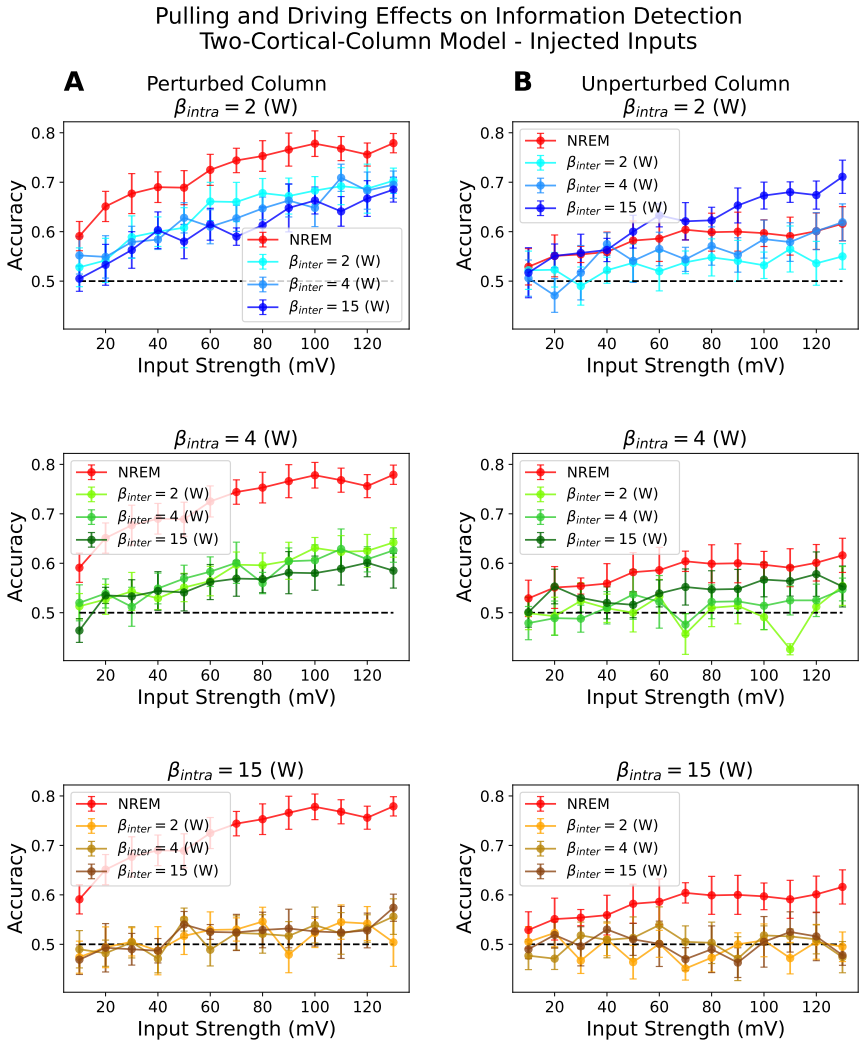

Figure S5.51: Pulling and driving effects due to synaptic upscaling on information detection at 20 ms post offset in the two-cortical-column model. Results as in Figure 3.9. (**A**). Information detection at 20 ms post offset in the perturbed column for various input amplitudes (injected inputs) in NREM (red) and various synaptic upscalings in wakefulness when intra-synaptic upscaling is (next page)

Figure S5.51 *(previous page)*: kept constant at $\beta_{intra} = 2$ (*Top*), $\beta_{intra} = 4$ (*Middle*) and $\beta_{intra} = 15$ (*Bottom*). (**B**). As in panel **A**, but for the unperturbed column. Error bar shows 95 percent confidence interval. Black dash line represents the chance-level accuracy $= \frac{1}{\#\text{input amplitudes}}$.

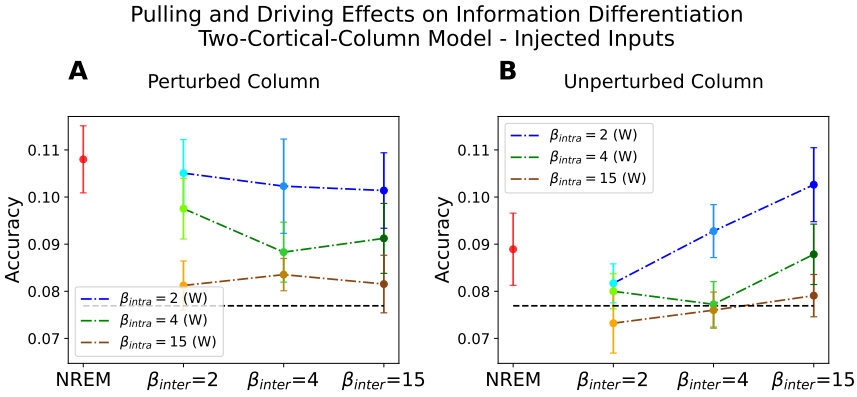

Figure S5.52: Pulling and driving effects due to synaptic upscaling on information differentiation at 20 ms post offset in the two-cortical-column model. Results as in Figure 3.10. (**A**). Information differentiation at 20 ms post offset in the perturbed column for various input amplitudes (injected inputs) in NREM (red) and various synaptic upscalings in wakefulness (color coded). (**B**). As in panel **A**, but for the unperturbed column. Error bar shows 95 percent confidence interval. Black dash line represents the chance-level accuracy $= \frac{1}{\#\text{input amplitudes}}$.

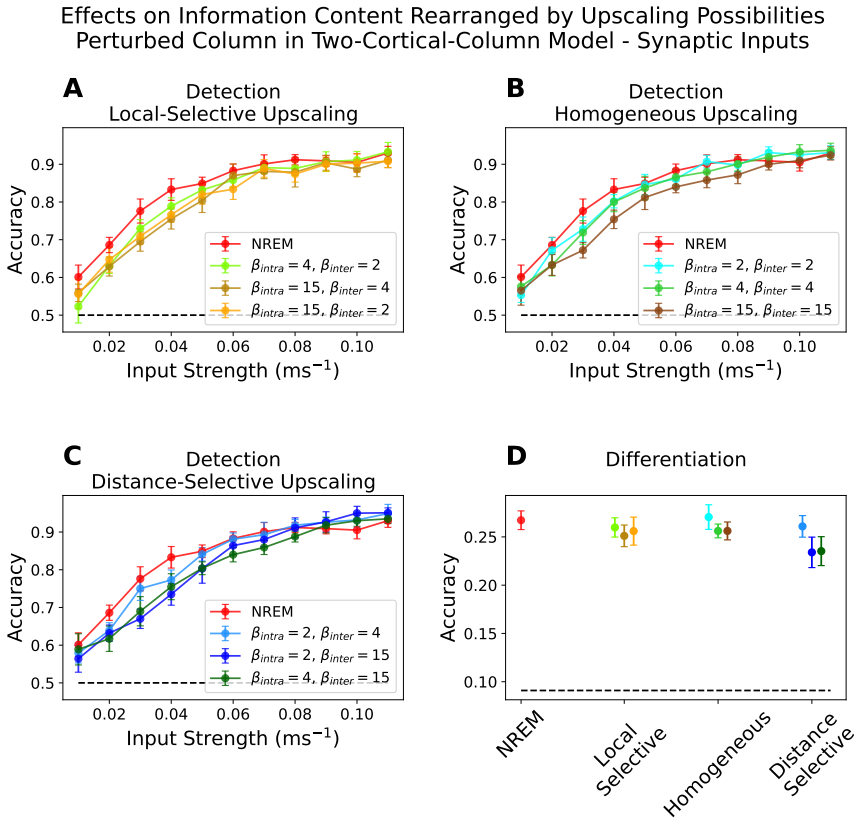

Figure S5.53: Effects of synaptic upscaling on information content at 20 ms post offset in the perturbed column in the two-cortical-column model rearranged by synaptic upscaling scenarios. Results as in Figure 3.12. (**A**). Information detection at input offset for various input amplitudes in NREM (red) and local-selective synaptic upscaling scenario in wakefulness (color coded). (**B**), (**C**). As in panel **A**, but for homogeneous and distance-selective synaptic upscaling scenarios in wakefulness, respectively. (**D**) Information differentiation for NREM and three synaptic upscaling scenarios in wakefulness. Error bar shows 95 percent confidence interval. Black dash line represents the chance-level accuracy $= \frac{1}{\#\text{input amplitudes}}$.

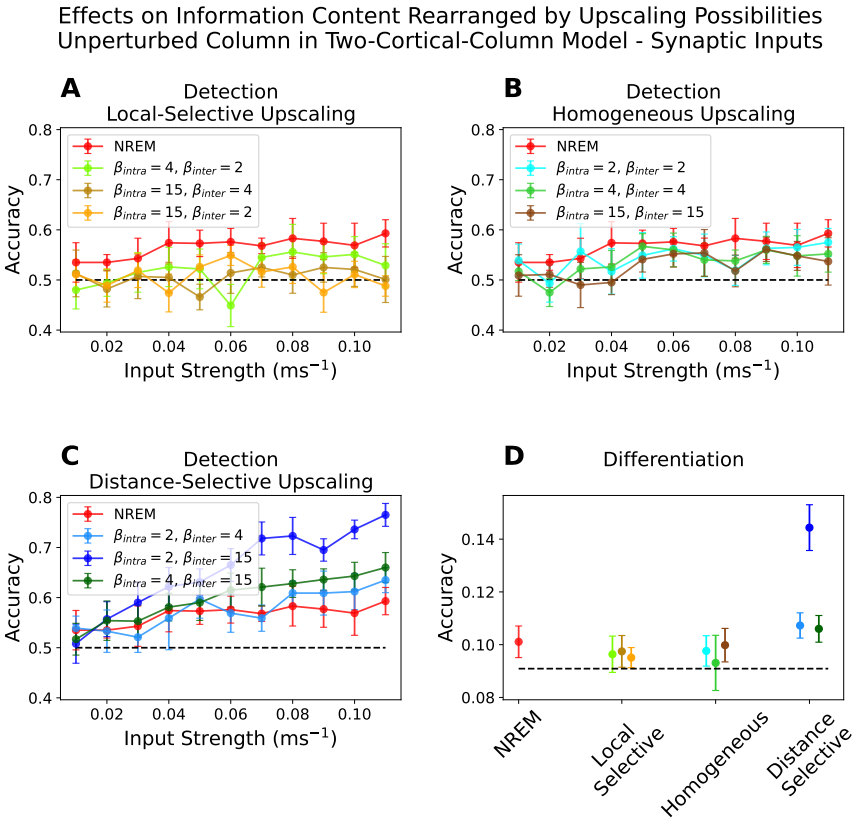

Figure S5.54: Effects of synaptic upscaling on information content at 20 ms post offset in the unperturbed column in the two-cortical-column model rearranged by synaptic upscaling scenarios. Results as in Figure 3.13. (**A**). Information detection at input offset for various input amplitudes in NREM (red) and local-selective synaptic upscaling scenario in wakefulness (color coded). (**B**), (**C**). As in panel **A**, but for homogeneous and distance-selective synaptic upscaling scenarios in wakefulness, respectively. (**D**) Information differentiation for NREM and three synaptic upscaling scenarios in wakefulness. Error bar shows 95 percent confidence interval. Black dash line represents the chance-level accuracy $= \frac{1}{\#\text{input amplitudes}}$.

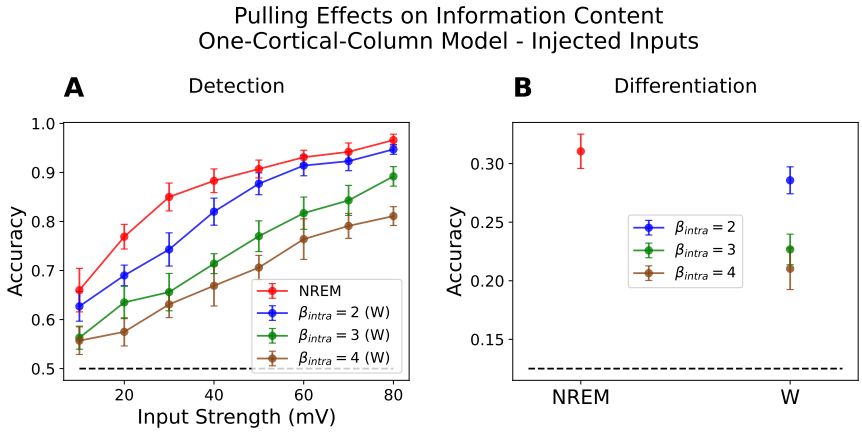

Figure S5.55: Pulling effects of synaptic upscaling on information content implementing Generative model at offset in the one-cortical-column model. Results as in Figure 3.3. (**A**). Information detection at offset for various input amplitudes (injected inputs) in NREM (red) and various synaptic upscalings in wakefulness (color coded). (**B**). Information differentiation at input offset for NREM (red) and various synaptic upscalings in wakefulness (color coded as in panel **A**). Error bar shows 95 percent confidence interval. Black dash line represents the chance-level accuracy $= \frac{1}{\#\text{input amplitudes}}$.

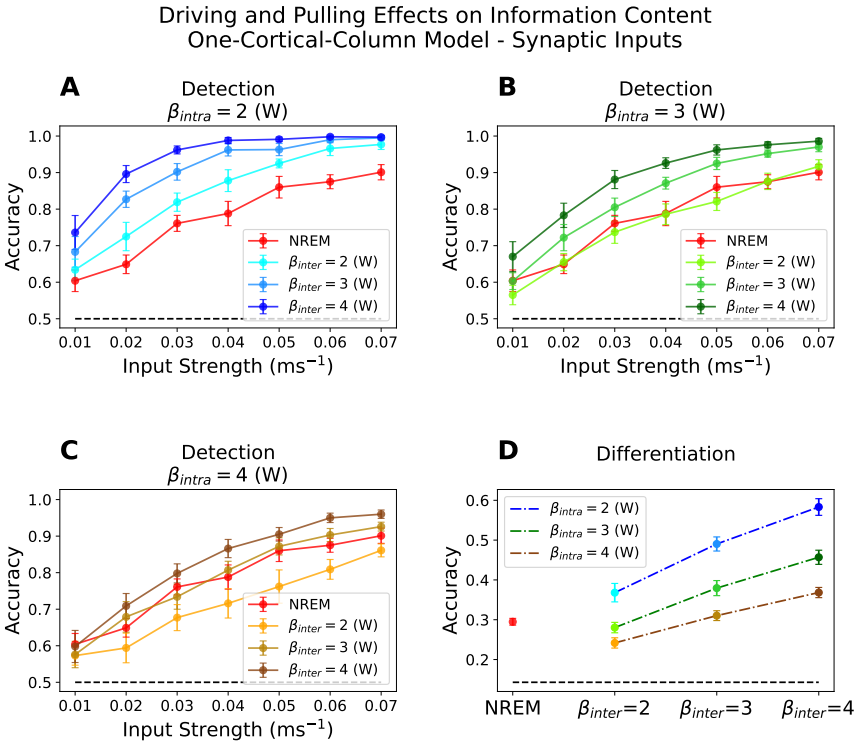

Figure S5.56: Driving and pulling effect due to synaptic upscaling on information detection implementing Generative model at offset in the one-cortical-column model. Results as in Figure 3.5. (**A**). Information detection at offset for various input amplitudes (Inter-synaptic inputs) in NREM (red) and various synaptic upscalings in wakefulness (color coded). Results as in panel **A**, but for $\beta_{intra} = 3$ (**B**) and $\beta_{intra} = 4$ (**C**). (**D**). Information differentiation at 20 ms prior input offset for NREM (red) and various synaptic upscalings in wakefulness (color coded). Error bar shows 95 percent confidence interval. Black dash line represents the chance-level accuracy $= \frac{1}{\#\text{input amplitudes}}$.

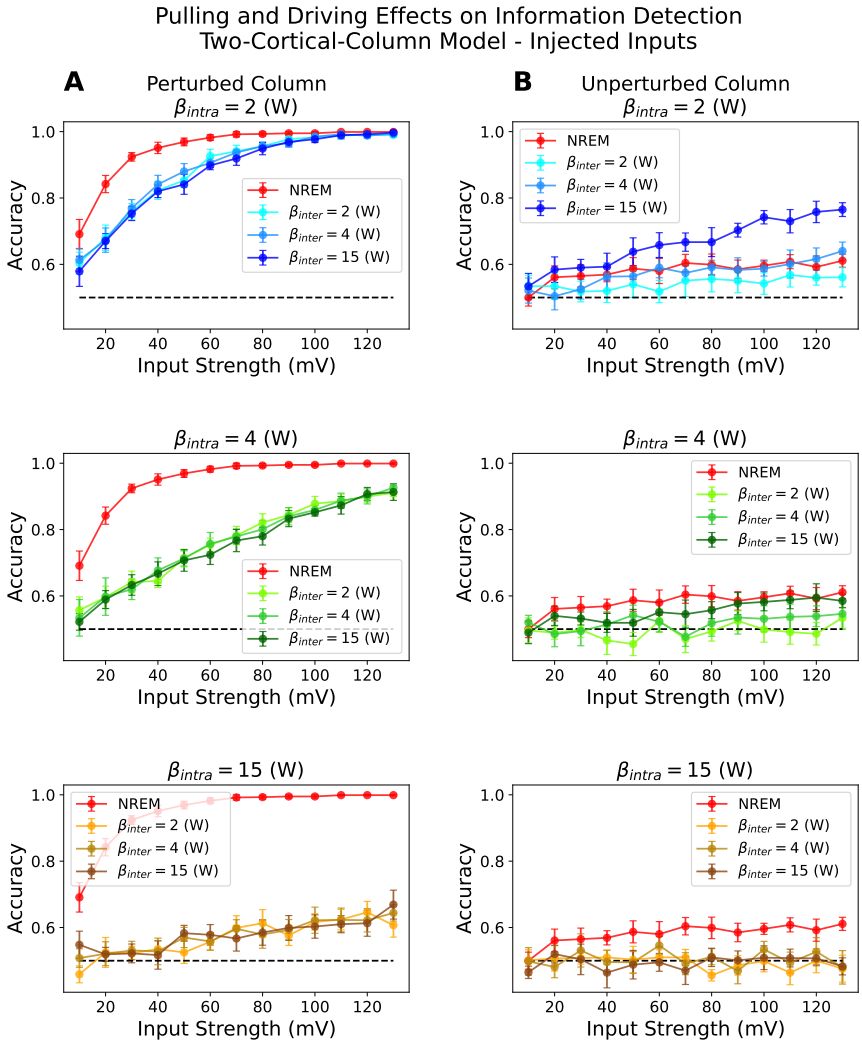

Figure S5.57: Pulling and driving effects due to synaptic upscaling on information detection implementing Generative model at offset in the two-cortical-column model. Results as in Figure 3.9. (**A**). Information detection at offset in the perturbed column for various input amplitudes (injected inputs) in NREM (red) and various synaptic upscalings in wakefulness when intra-synaptic (next page)

Figure S5.57 *(previous page)*: upscaling is kept constant at $\beta_{intra} = 2$ (*Top*), $\beta_{intra} = 4$ (*Middle*) and $\beta_{intra} = 15$ (*Bottom*). (**B**). As in panel **A**, but for the unperturbed column. Error bar shows 95 percent confidence interval. Black dash line represents the chance-level accuracy $= \frac{1}{\#\text{input amplitudes}}$.

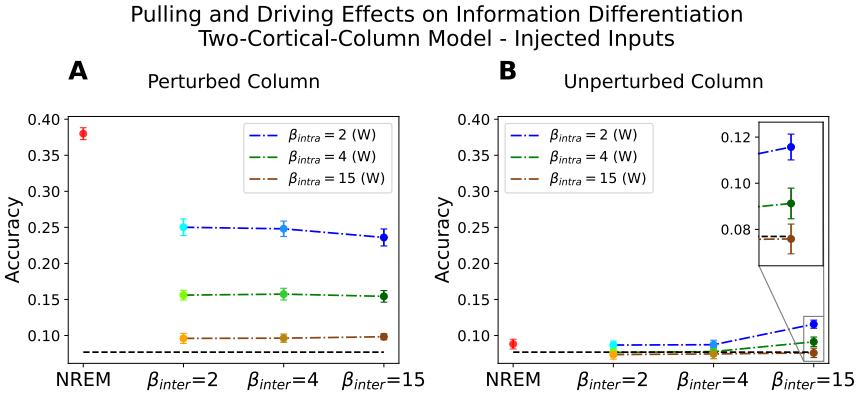

Figure S5.58: Pulling and driving effects due to synaptic upscaling on information differentiation implementing Generative model at offset in the two-cortical-column model. Results as in Figure 3.10. (**A**). Information differentiation at offset in the perturbed column for various input amplitudes (injected inputs) in NREM (red) and various synaptic upscalings in wakefulness (color coded). (**B**). As in panel **A**, but for the unperturbed column. Error bar shows 95 percent confidence interval. Black dash line represents the chance-level accuracy $= \frac{1}{\#\text{input amplitudes}}$.

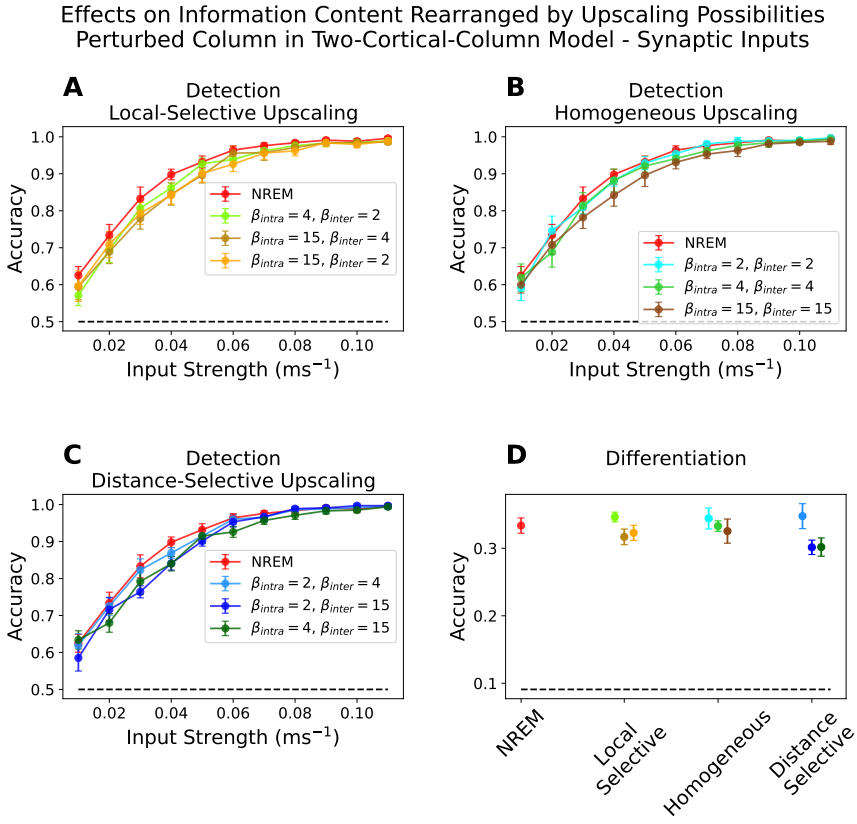

Figure S5.59: Effects of synaptic upscaling on information content implementing Generative model at offset in the perturbed column in the two-cortical-column model rearranged by synaptic upscaling scenarios. Results as in Figure 3.12. (**A**). Information detection at input offset for various input amplitudes in NREM (red) and local-selective synaptic upscaling scenario in wakefulness (color coded). (**B**), (**C**). As in panel **A**, but for homogeneous and distance-selective synaptic upscaling scenarios in wakefulness, respectively. (**D**) Information differentiation for NREM and three synaptic upscaling scenarios in wakefulness. Error bar shows 95 percent confidence interval. Black dash line represents the chance-level accuracy $= \frac{1}{\#\text{input amplitudes}}$.

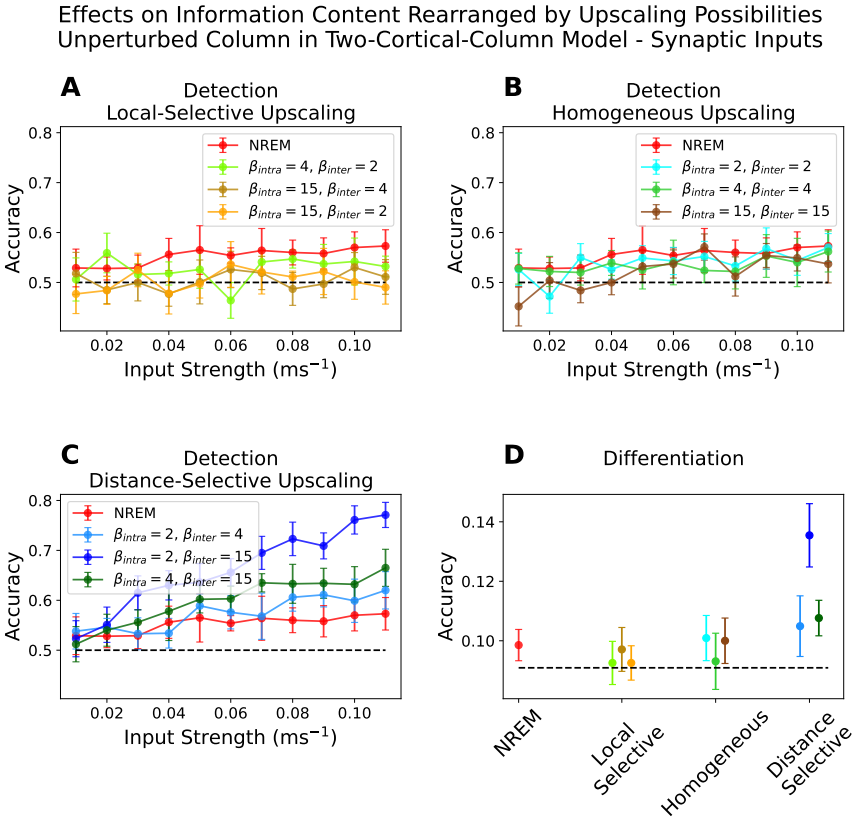

Figure S5.60: Effects of synaptic upscaling on information content implementing Generative model at offset in the unperturbed column in the two-cortical-column model rearranged by synaptic upscaling scenarios. Results as in Figure 3.12. (**A**). Information detection at input offset for various input amplitudes in NREM (red) and local-selective synaptic upscaling scenario in wakefulness (color coded). (**B**), (**C**). As in panel **A**, but for homogeneous and distance-selective synaptic upscaling scenarios in wakefulness, respectively. (**D**) Information differentiation for NREM and three synaptic upscaling scenarios in wakefulness. Error bar shows 95 percent confidence interval. Black dash line represents the chance-level accuracy $= \frac{1}{\#\text{input amplitudes}}$.

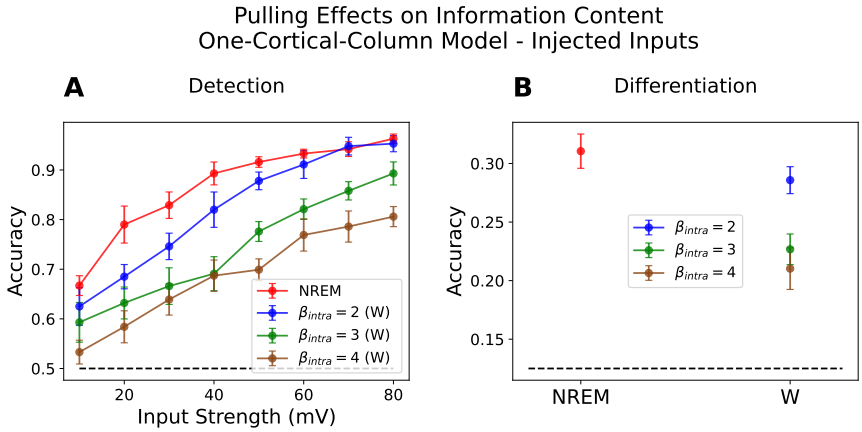

Figure S5.61: Pulling effects of synaptic upscaling on information content implementing Generative model at offset compared to another random time point in pristimulus interval in the one-cortical-column model. Results as in Figure 3.3. (**A**). Information detection at offset for various input amplitudes (injected inputs) in NREM (red) and various synaptic upscalings in wakefulness (color coded). (**B**). Information differentiation at input offset for NREM (red) and various synaptic upscalings in wakefulness (color coded as in panel **A**). Note that information differentiation is independent of the choice of time point in peristimulus intervals. Error bar shows 95 percent confidence interval. Black dash line represents the chance-level accuracy $= \frac{1}{\#\text{input amplitudes}}$.

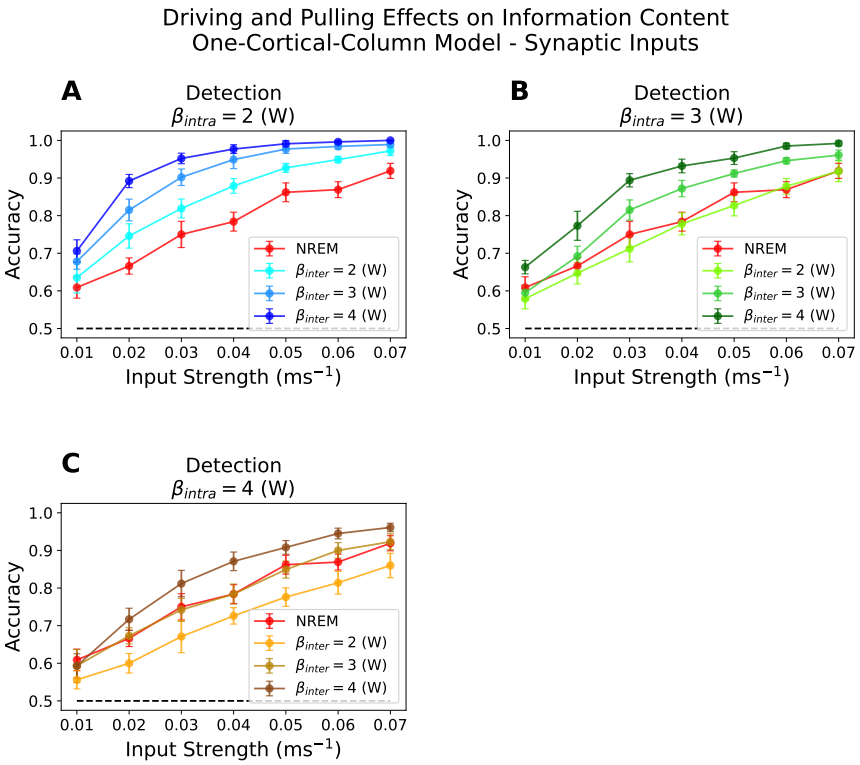

Figure S5.62: Driving and pulling effect due to synaptic upscaling on information detection implementing Generative model at offset compared to another random time point in pristimulus interval in the one-cortical-column model. Results as in Figure 3.5A-C. (**A**). Information detection at input offset for various input amplitudes (Inter-synaptic inputs) in NREM (red) and various synaptic upscalings in wakefulness (color coded). Results as in panel **A**, but for $\beta_{intra} = 3$ (**B**) and $\beta_{intra} = 4$ (**C**). Error bar shows 95 percent confidence interval. Black dash line represents the chance-level accuracy $= \frac{1}{\#\text{input amplitudes}}$.

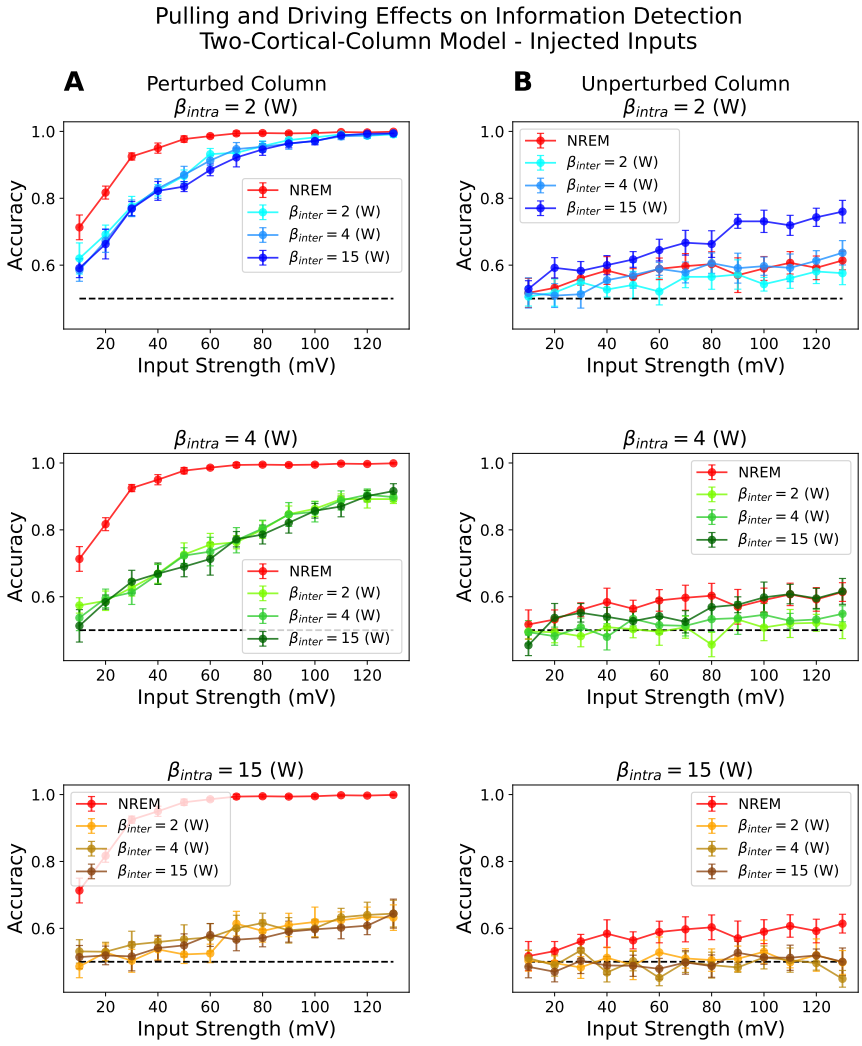

Figure S5.63: Pulling and driving effects due to synaptic upscaling on information detection implementing Generative model at offset compared to another random time point in pristimulus interval in the two-cortical-column model. Results as in Figure 3.9. (**A**). Information detection at input offset in the perturbed column for various input amplitudes (injected inputs) in NREM (red) (next page)

Figure S5.63 *(previous page)*: and various synaptic upscalings in wakefulness when intra-synaptic upscaling is kept constant at $\beta_{intra} = 2$ (*Top*), $\beta_{intra} = 4$ (*Middle*) and $\beta_{intra} = 15$ (*Bottom*). (**B**). As in panel **A**, but for the unperturbed column. Error bar shows 95 percent confidence interval. Black dash line represents the chance-level accuracy $= \frac{1}{\#\text{input amplitudes}}$.

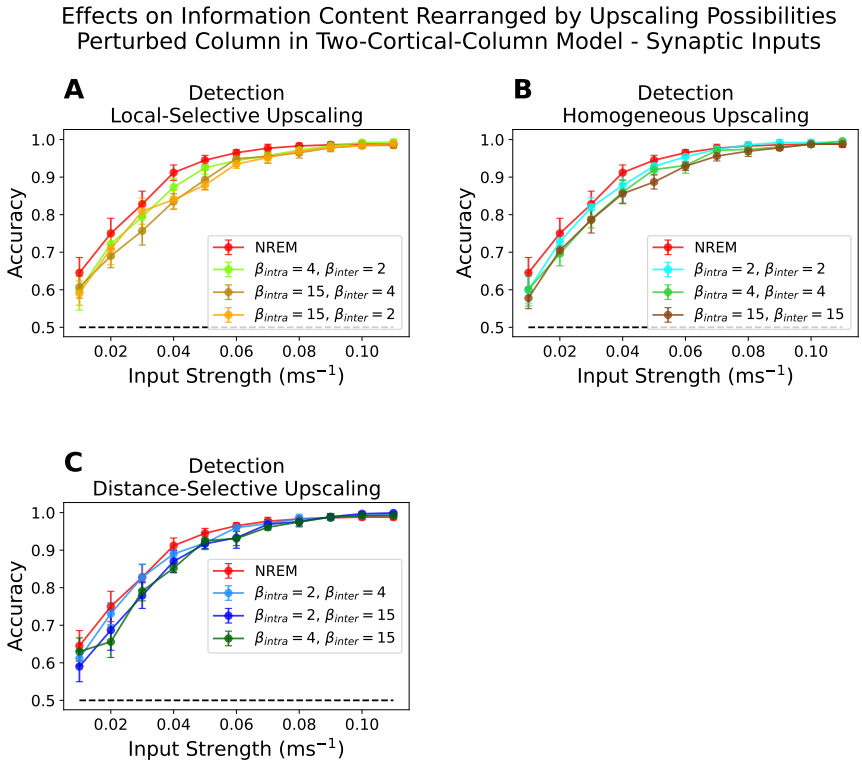

Figure S5.64: Effects of synaptic upscaling on information detection at offset compared to another random time point in pristimulus interval in the perturbed column in the two-cortical-column model rearranged by synaptic upscaling scenarios. Results as in Figure 3.12. (**A**). Information detection at input offset for various input amplitudes in NREM (red) and local-selective synaptic upscaling scenario in wakefulness (color coded). (**B**), (**C**). As in panel **A**, but for homogeneous and distance-selective synaptic upscaling scenarios in wakefulness, respectively. Error bar shows 95 percent confidence interval. Black dash line represents the chance-level accuracy $= \frac{1}{\#\text{input amplitudes}}$.

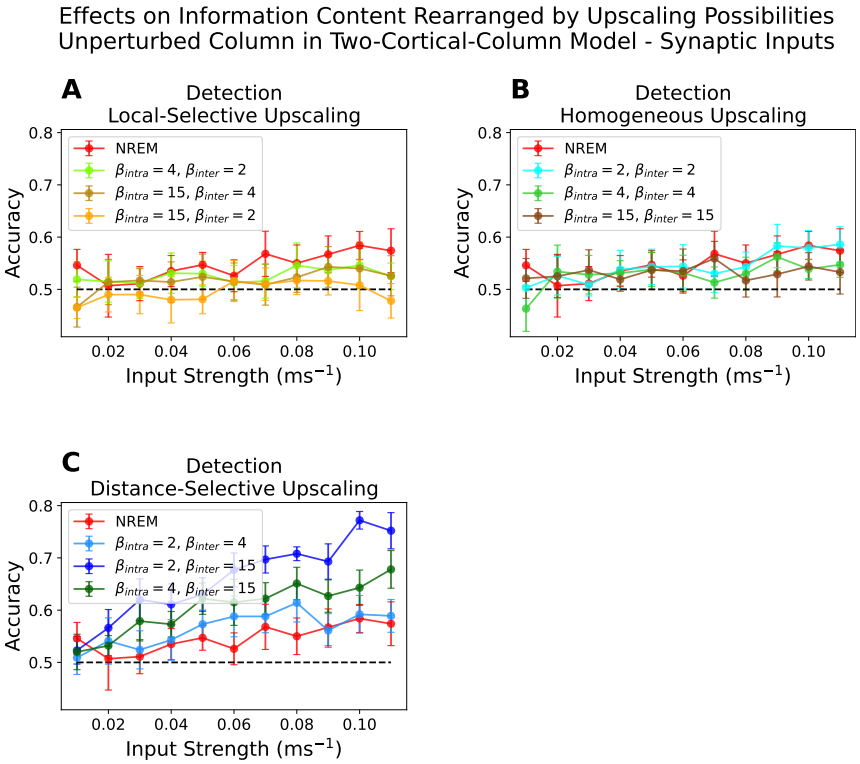

Figure S5.65: Effects of synaptic upscaling on information detection at offset compared to another random time point in pristimulus interval in the unperturbed column in the two-cortical-column model rearranged by synaptic upscaling scenarios. Results as in Figure 3.13. (**A**). Information detection at input offset for various input amplitudes in NREM (red) and local-selective synaptic upscaling scenario in wakefulness (color coded). (**B**), (**C**). As in panel **A**, but for homogeneous and distance-selective synaptic upscaling scenarios in wakefulness, respectively. Error bar shows 95 percent confidence interval. Black dash line represents the chance-level accuracy $= \frac{1}{\#\text{input amplitudes}}$.

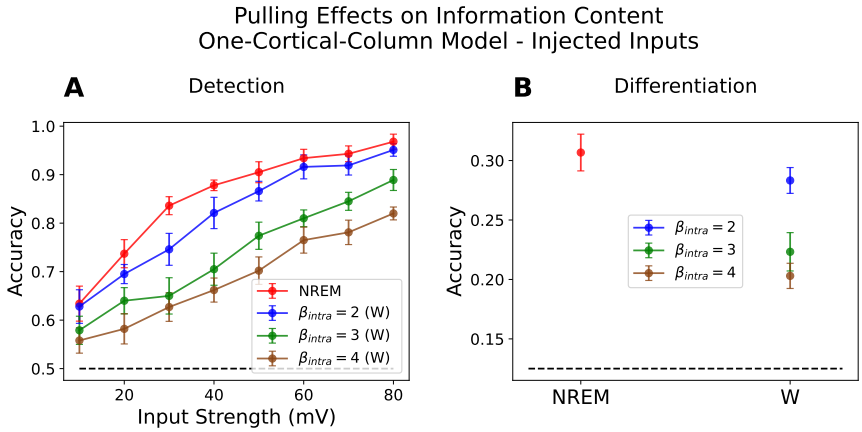

Figure S5.66: Pulling effects of synaptic upscaling on information content implementing Generative model at 20 ms prior offset in the one-cortical-column model. Results as in Figure 3.3. (**A**). Information detection at 20 ms prior offset for various input amplitudes (injected inputs) in NREM (red) and various synaptic upscalings in wakefulness (color coded). (**B**). Information differentiation at input offset for NREM (red) and various synaptic upscalings in wakefulness (color coded as in panel **A**). Error bar shows 95 percent confidence interval. Black dash line represents the chance-level accuracy $= \frac{1}{\#\text{input amplitudes}}$.

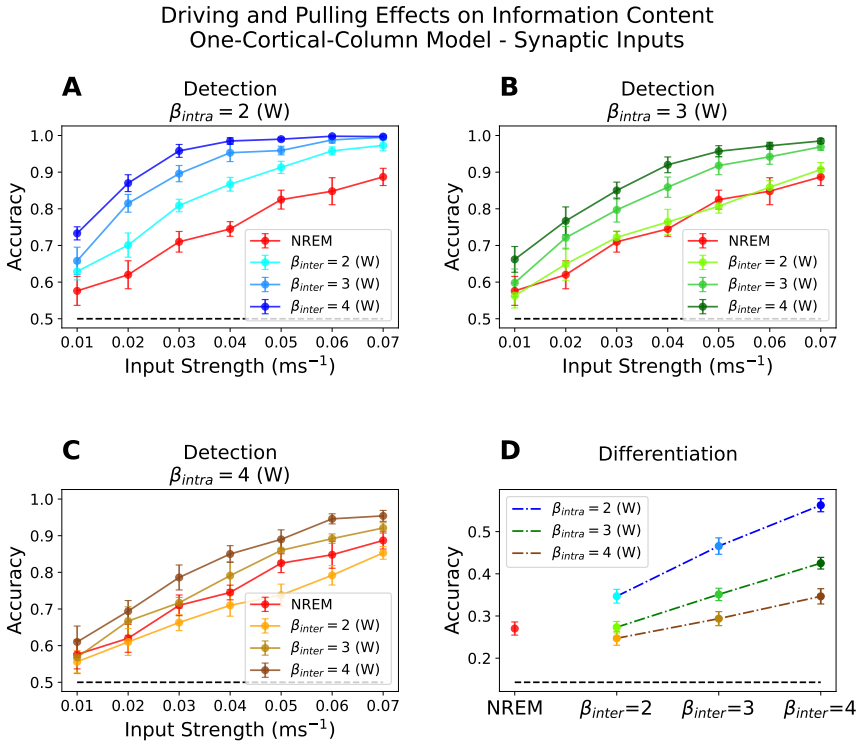

Figure S5.67: Driving and pulling effect due to synaptic upscaling on information content implementing Generative model at 20 ms prior offset in the one-cortical-column model. Results as in Figure 3.5. (**A**). Information detection at 20 ms prior offset for various input amplitudes (Inter-synaptic inputs) in NREM (red) and various synaptic upscalings in wakefulness (color coded). Results as in panel **A**, but for $\beta_{intra} = 3$ (**B**) and $\beta_{intra} = 4$ (**C**). (**D**). Information differentiation at 20 ms prior input offset for NREM (red) and various synaptic upscalings in wakefulness (color coded). Error bar shows 95 percent confidence interval. Black dash line represents the chance-level accuracy $= \frac{1}{\#\text{input amplitudes}}$.

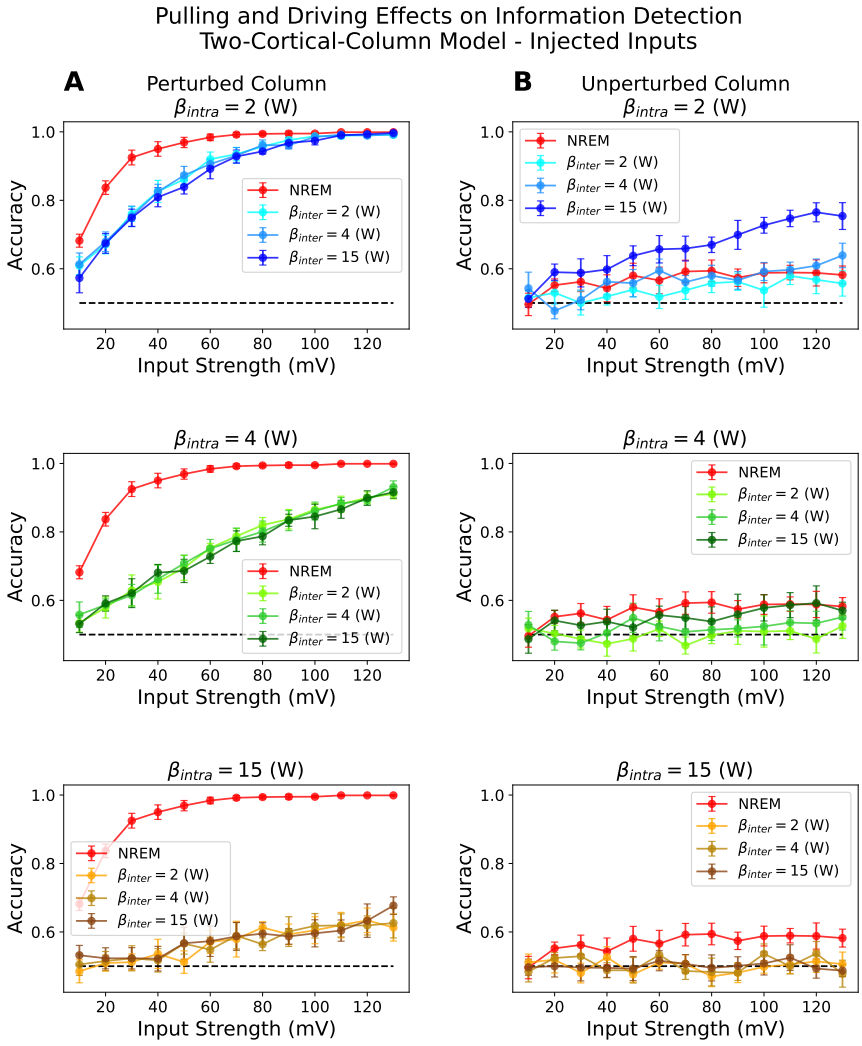

Figure S5.68: Pulling and driving effects due to synaptic upscaling on information detection implementing Generative model at 20 ms prior offset in the two-cortical-column model. Results as in Figure 3.9. (**A**). Information detection at 20 ms prior offset in the perturbed column for various input amplitudes (injected inputs) in NREM (red) and various synaptic upscalings in wakefulness (next page)

Figure S5.68 *(previous page)*: when intra-synaptic upscaling is kept constant at $\beta_{intra} = 2$ (*Top*), $\beta_{intra} = 4$ (*Middle*) and $\beta_{intra} = 15$ (*Bottom*). (**B**). As in panel **A**, but for the unperturbed column. Error bar shows 95 percent confidence interval. Black dash line represents the chance-level accuracy $= \frac{1}{\#\text{input amplitudes}}$.

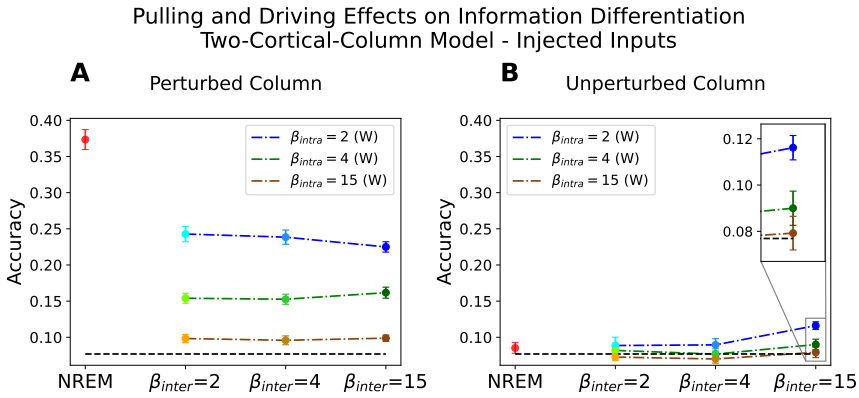

Figure S5.69: Pulling and driving effects due to synaptic upscaling on information differentiation implementing Generative model at 20 ms prior offset in the two-cortical-column model. Results as in Figure 3.10. (**A**). Information differentiation at 20 ms prior offset in the perturbed column for various input amplitudes (injected inputs) in NREM (red) and various synaptic upscalings in wakefulness (color coded). (**B**). As in panel **A**, but for the unperturbed column. Error bar shows 95 percent confidence interval. Black dash line represents the chance-level accuracy $= \frac{1}{\#\text{input amplitudes}}$.

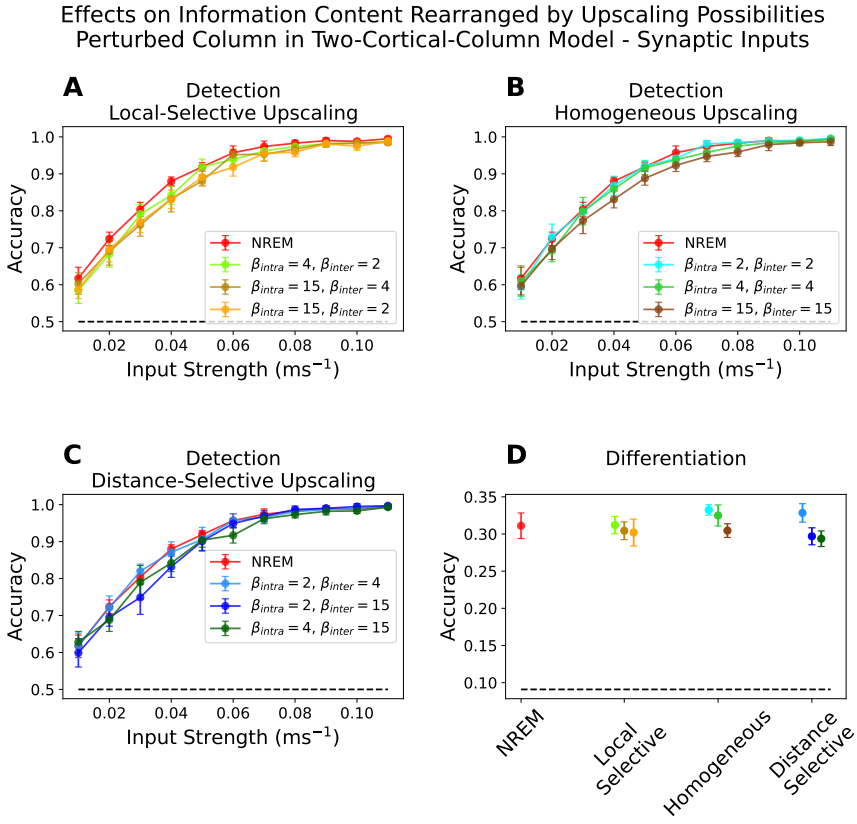

Figure S5.70: Effects of synaptic upscaling on information content implementing Generative model at 20 ms prior offset in the perturbed column in the two-cortical-column model rearranged by synaptic upscaling scenarios. Results as in Figure 3.12. (**A**). Information detection at input offset for various input amplitudes in NREM (red) and local-selective synaptic upscaling scenario in wakefulness (color coded). (**B**), (**C**). As in panel **A**, but for homogeneous and distance-selective synaptic upscaling scenarios in wakefulness, respectively. (**D**) Information differentiation for NREM and three synaptic upscaling scenarios in wakefulness. Error bar shows 95 percent confidence interval. Black dash line represents the chance-level accuracy $= \frac{1}{\#\text{input amplitudes}}$.

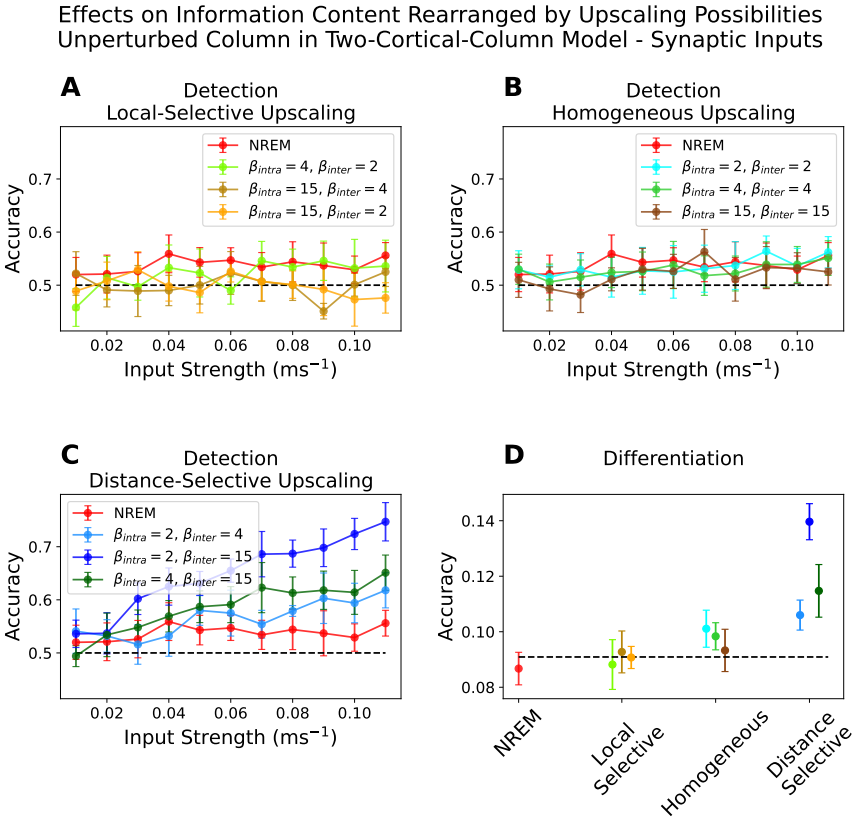

Figure S5.71: Effects of synaptic upscaling on information content implementing Generative model at 20 ms prior offset in the unperturbed column in the two-cortical-column model rearranged by synaptic upscaling scenarios. Results as in Figure 3.13. (**A**). Information detection at input offset for various input amplitudes in NREM (red) and local-selective synaptic upscaling scenario in wakefulness (color coded). (**B**), (**C**). As in panel **A**, but for homogeneous and distance-selective synaptic upscaling scenarios in wakefulness, respectively. (**D**) Information differentiation for NREM and three synaptic upscaling scenarios in wakefulness. Error bar shows 95 percent confidence interval. Black dash line represents the chance-level accuracy $= \frac{1}{\#\text{input amplitudes}}$.

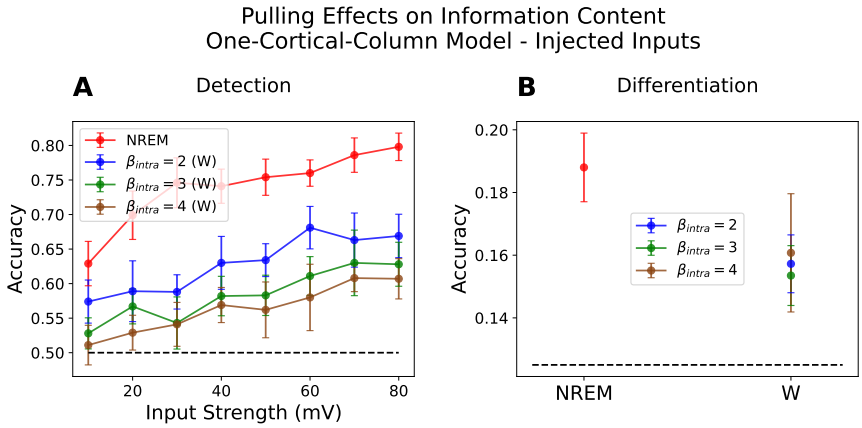

Figure S5.72: Pulling effects of synaptic upscaling on information content implementing Generative model at 20 ms post offset in the one-cortical-column model. Results as in Figure 3.3. (**A**). Information detection at 20 ms post offset for various input amplitudes (injected inputs) in NREM (red) and various synaptic upscalings in wakefulness (color coded). (**B**). Information differentiation at input offset for NREM (red) and various synaptic upscalings in wakefulness (color coded as in panel **A**). Error bar shows 95 percent confidence interval. Black dash line represents the chance-level accuracy $= \frac{1}{\#\text{input amplitudes}}$.

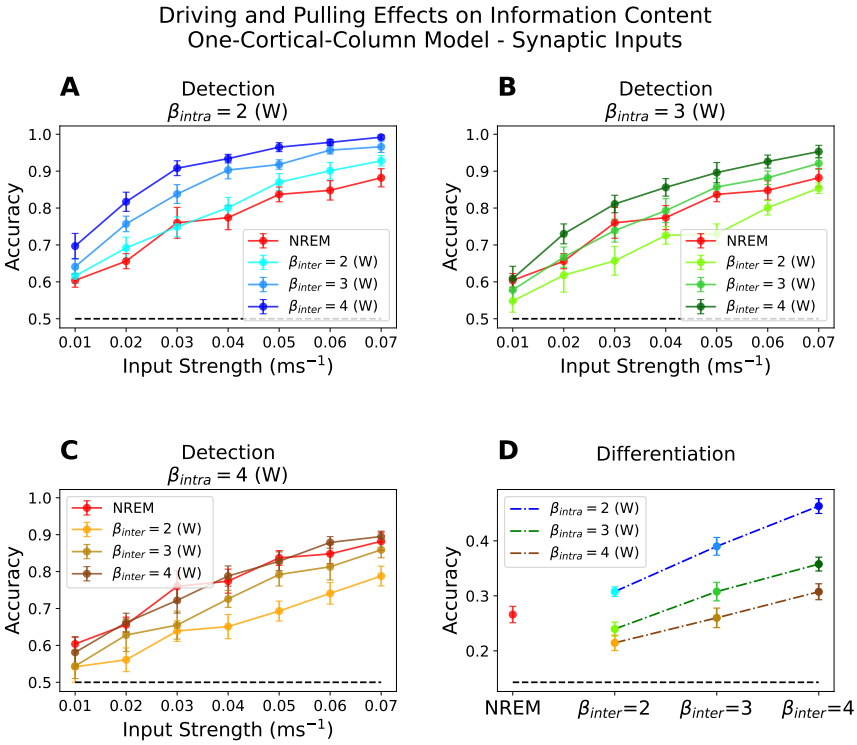

Figure S5.73: Driving and pulling effect due to synaptic upscaling on information content implementing Generative model at 20 ms post offset in the one-cortical-column model. Results as in Figure 3.5. (**A**). Information detection at 20 ms post offset for various input amplitudes (Inter-synaptic inputs) in NREM (red) and various synaptic upscalings in wakefulness (color coded). Results as in panel **A**, but for $\beta_{intra} = 3$ (**B**) and $\beta_{intra} = 4$ (**C**). (**D**). Information differentiation at 20 ms post to input offset for NREM (red) and various synaptic upscalings in wakefulness (color coded). Error bar shows 95 percent confidence interval. Black dash line represents the chance-level accuracy $= \frac{1}{\#\text{input amplitudes}}$.

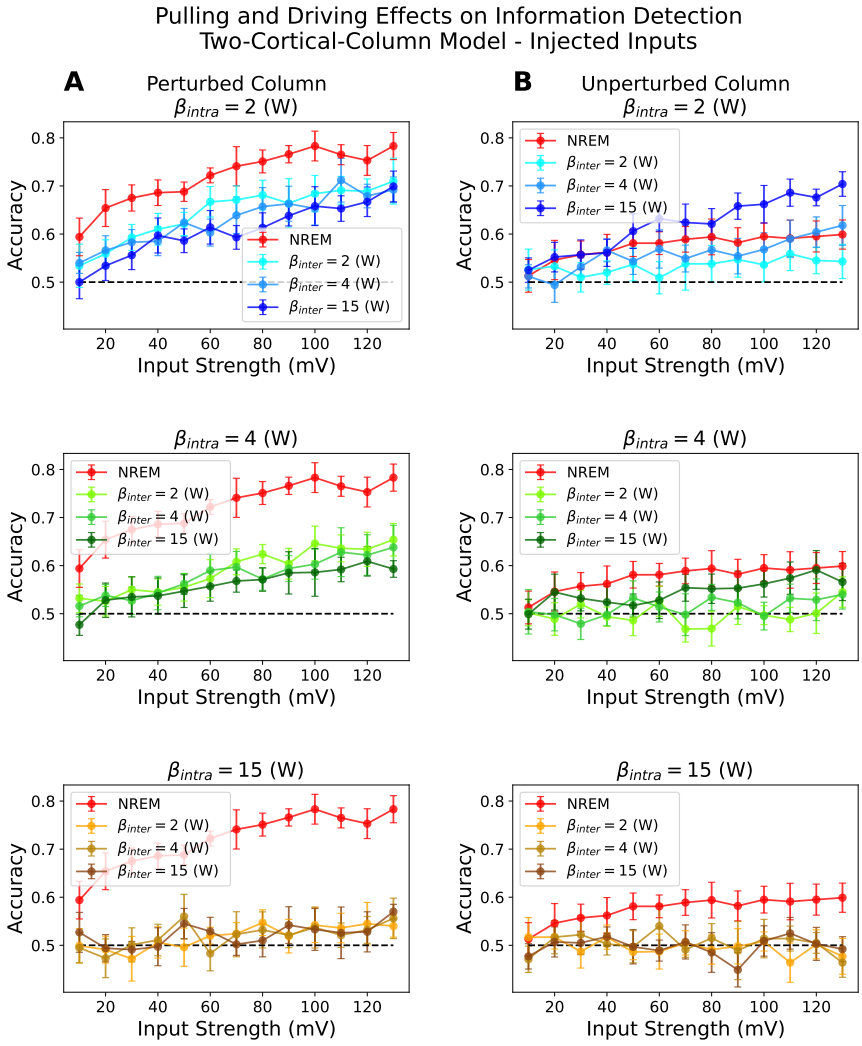

Figure S5.74: Pulling and driving effects due to synaptic upscaling on information detection implementing Generative model at 20 ms post offset in the two-cortical-column model. Results as in Figure 3.9. (**A**). Information detection at 20 ms post offset in the perturbed column for various input amplitudes (injected inputs) in NREM (red) and various synaptic upscalings in wakefulness (next page)

Figure S5.74 *(previous page)*: when intra-synaptic upscaling is kept constant at $\beta_{intra} = 2$ (*Top*), $\beta_{intra} = 4$ (*Middle*) and $\beta_{intra} = 15$ (*Bottom*). (**B**). As in panel **A**, but for the unperturbed column. Error bar shows 95 percent confidence interval. Black dash line represents the chance-level accuracy $= \frac{1}{\#\text{input amplitudes}}$.

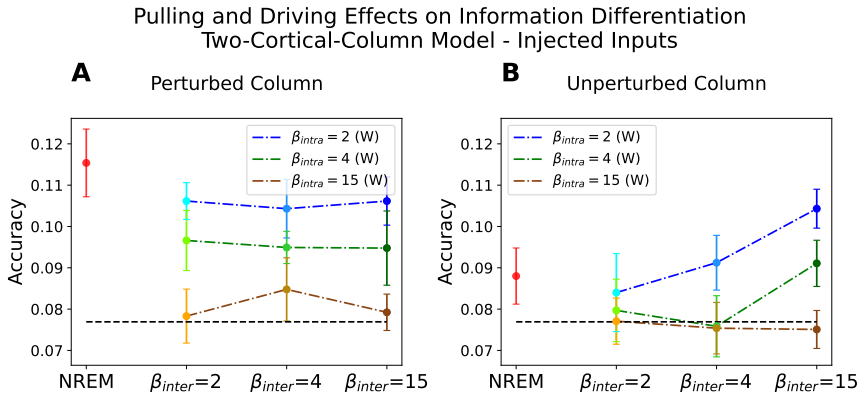

Figure S5.75: Pulling and driving effects due to synaptic upscaling on information differentiation implementing Generative model at 20 ms post offset in the two-cortical-column model. Results as in Figure 3.10. (**A**). Information differentiation at 20 ms post offset in the perturbed column for various input amplitudes (injected inputs) in NREM (red) and various synaptic upscalings in wakefulness (color coded). (**B**). As in panel **A**, but for the unperturbed column. Error bar shows 95 percent confidence interval. Black dash line represents the chance-level accuracy $= \frac{1}{\#\text{input amplitudes}}$.

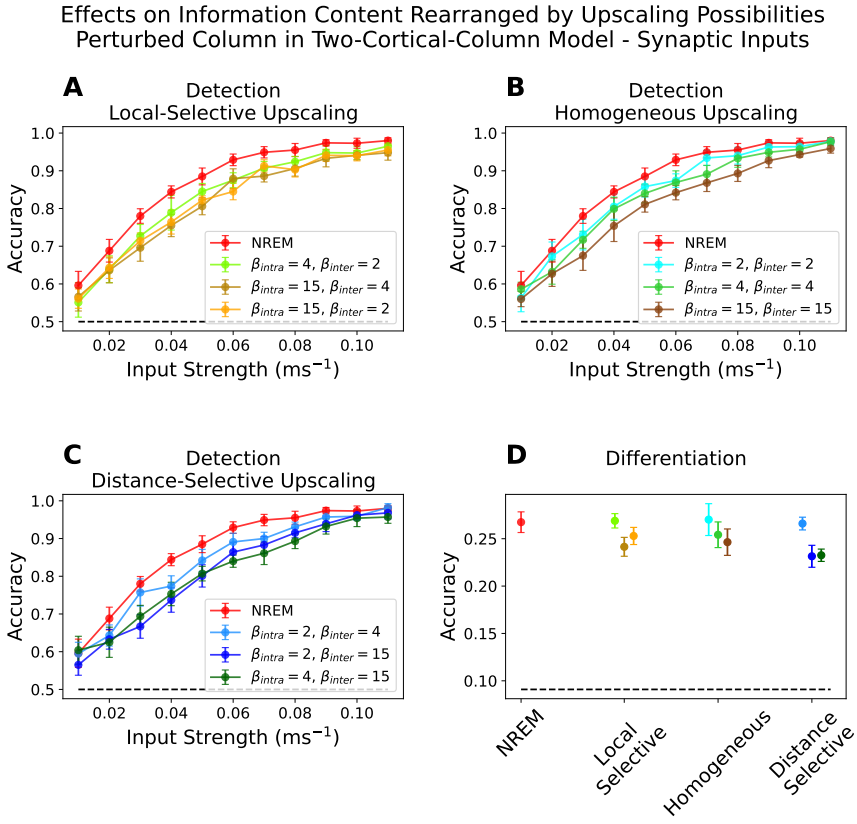

Figure S5.76: Effects of synaptic upscaling on information content implementing Generative model at 20 ms post offset in the perturbed column in the two-cortical-column model rearranged by synaptic upscaling scenarios. Results as in Figure 3.12. (**A**). Information detection at input offset for various input amplitudes in NREM (red) and local-selective synaptic upscaling scenario in wakefulness (color coded). (**B**), (**C**). As in panel **A**, but for homogeneous and distance-selective synaptic upscaling scenarios in wakefulness, respectively. (**D**) Information differentiation for NREM and three synaptic upscaling scenarios in wakefulness. Error bar shows 95 percent confidence interval. Black dash line represents the chance-level accuracy $= \frac{1}{\#\text{input amplitudes}}$.

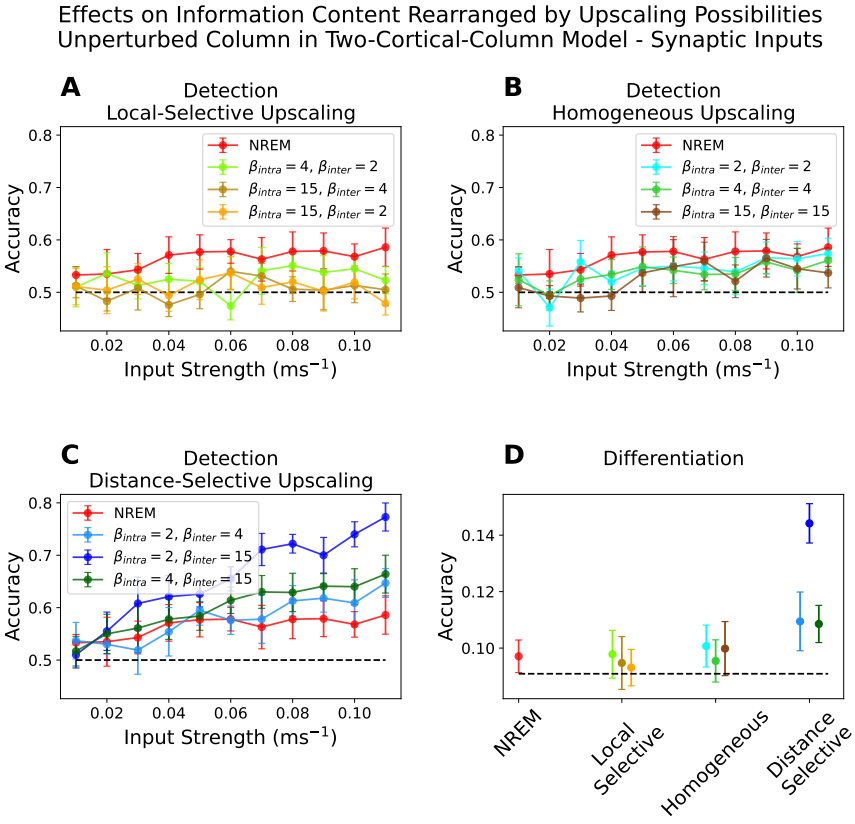

Figure S5.77: Effects of synaptic upscaling on information content implementing Generative model at 20 ms post offset in the unperturbed column in the two-cortical-column model rearranged by synaptic upscaling scenarios. Results as in Figure 3.13. (**A**). Information detection at input offset for various input amplitudes in NREM (red) and local-selective synaptic upscaling scenario in wakefulness (color coded). (**B**), (**C**). As in panel **A**, but for homogeneous and distance-selective synaptic upscaling scenarios in wakefulness, respectively. (**D**) Information differentiation for NREM and three synaptic upscaling scenarios in wakefulness. Error bar shows 95 percent confidence interval. Black dash line represents the chance-level accuracy $= \frac{1}{\#\text{input amplitudes}}$.

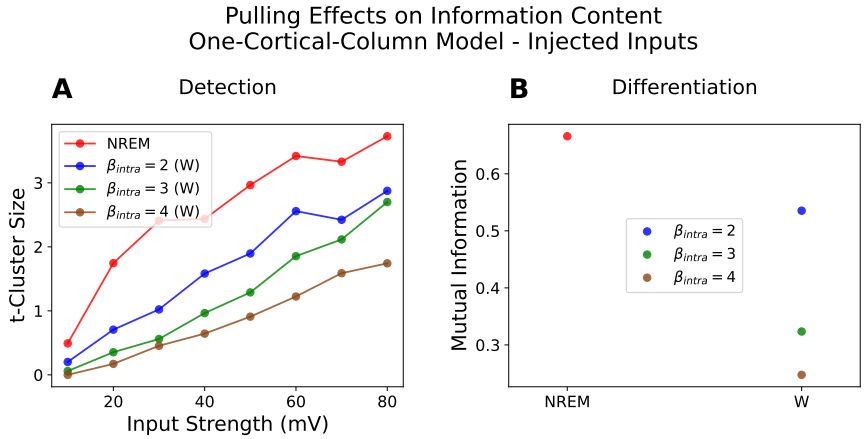

Figure S5.78: Pulling effects of synaptic upscaling on information content implementing significance test and mutual information in the one-cortical-column model. (**A**). t-cluster statistics (Bonferroni correction) when comparing the evoked responses in firing rate signals with spontaneous activities in the peristimulus intervals. Size of t-cluster statistics for various input amplitudes (injected inputs) in NREM (red) and various synaptic upscalings in wakefulness (color coded). Size of t-cluster statistics increases with increasing input amplitude. However, it decreases as synaptic upscaling in wakefulness increases: pulling effect. (**B**). Mutual information at input offset for NREM (red) and various synaptic upscalings in wakefulness (color coded as in panel **A**). Note that t-cluster statistics and mutual information qualitatively reproduce results for information detection and information differentiation, respectively, implementing machine learning techniques (for instance see Figure 3.3).

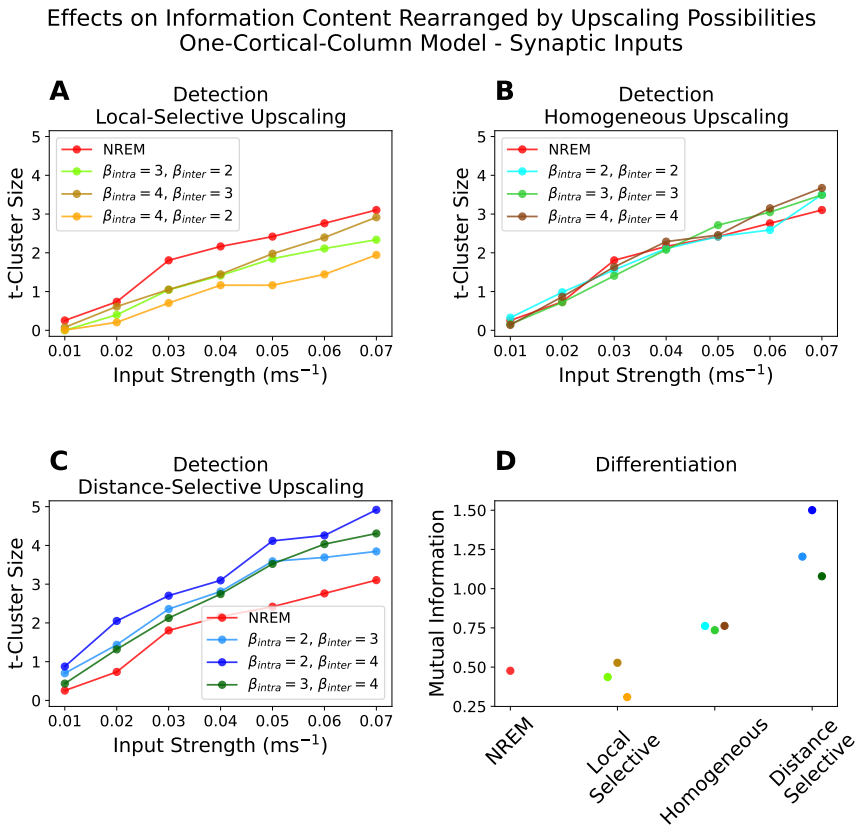

Figure S5.79: Driving and pulling effect due to synaptic upscaling on information content implementing significance test and mutual information in the one-cortical-column model rearranged by synaptic upscaling scenarios. (**A**), (**B**) and (**C**) show the size of t-cluster statistics for local-selective, homogeneous and distance-selective synaptic upscaling scenarios in wakefulness, respectively. (**D**) Mutual information at input offset for NREM (red) and various synaptic upscalings in wakefulness (color coded as in panel **A**, **B** and **C**). Note that t-cluster statistics and mutual information qualitatively reproduce results for information detection and information differentiation, respectively, implementing machine learning techniques (for instance see Figure 3.6).

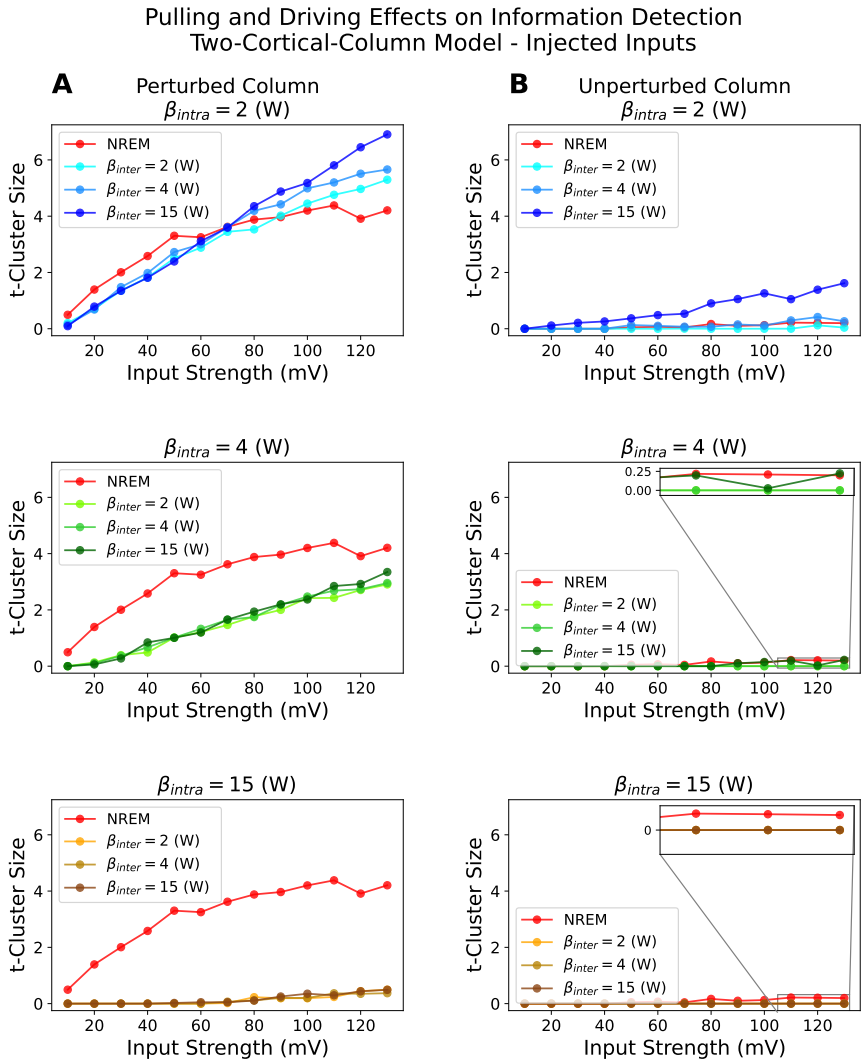

Figure S5.80: Pulling and driving effects due to synaptic upscaling on information detection implementing significance test in the two-cortical-column model. (**A**). Size of t-cluster statistics in the perturbed column for various input amplitudes (injected inputs) in NREM (red) and various synaptic (next page)

Figure S5.80 *(previous page)*: upscalings in wakefulness when intra-synaptic upscaling is kept constant at $\beta_{intra} = 2$ (*Top*), $\beta_{intra} = 4$ (*Middle*) and $\beta_{intra} = 15$ (*Bottom*). (**B**). As in panel **A**, but for the unperturbed column. Note that t-cluster statistics qualitatively reproduce results for information detection, implementing machine learning techniques (for instance see Figure 3.9).

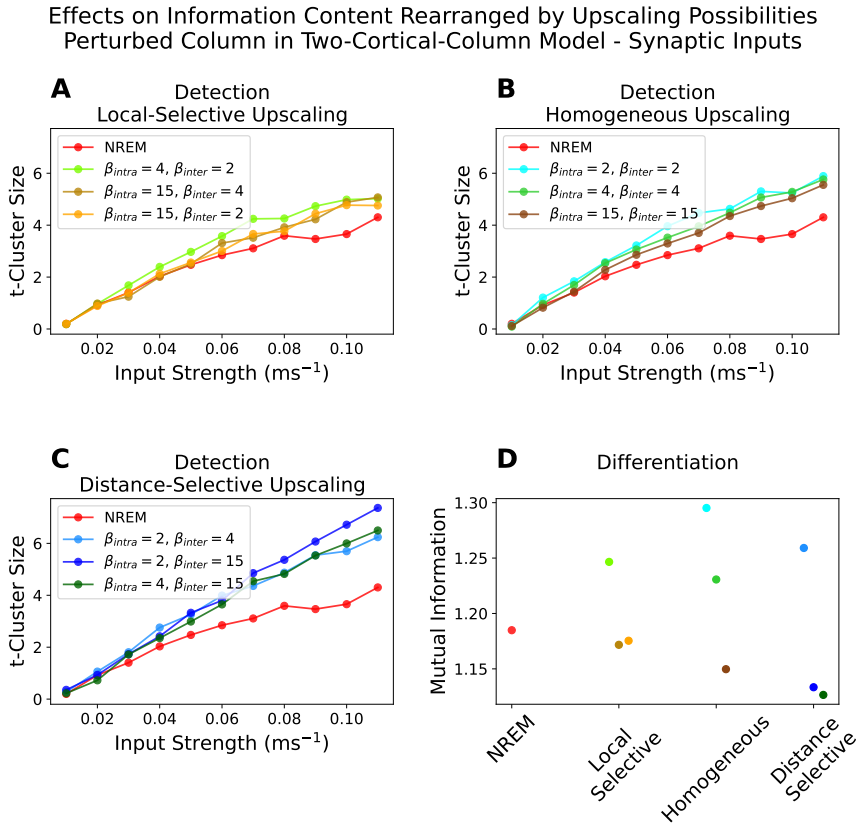

Figure S5.81: Effects of synaptic upscaling on information content implementing significance test and mutual information in the perturbed column in the two-cortical-column model rearranged by synaptic upscaling scenarios. Results correspond to the perturbed column. (**A**). Size of t-cluster statistics for various input amplitudes in NREM (red) and local-selective synaptic upscaling scenarios in wakefulness (color coded). (**B**), (**C**). As in panel **A**, but for homogeneous and distance-selective synaptic upscaling scenarios in wakefulness, respectively. (**D**) Mutual information for NREM and three synaptic upscaling scenarios in wakefulness. Note that t-cluster statistics and mutual information qualitatively reproduce results for information detection and information differentiation, respectively, implementing machine learning techniques (for instance see Figure 3.12).

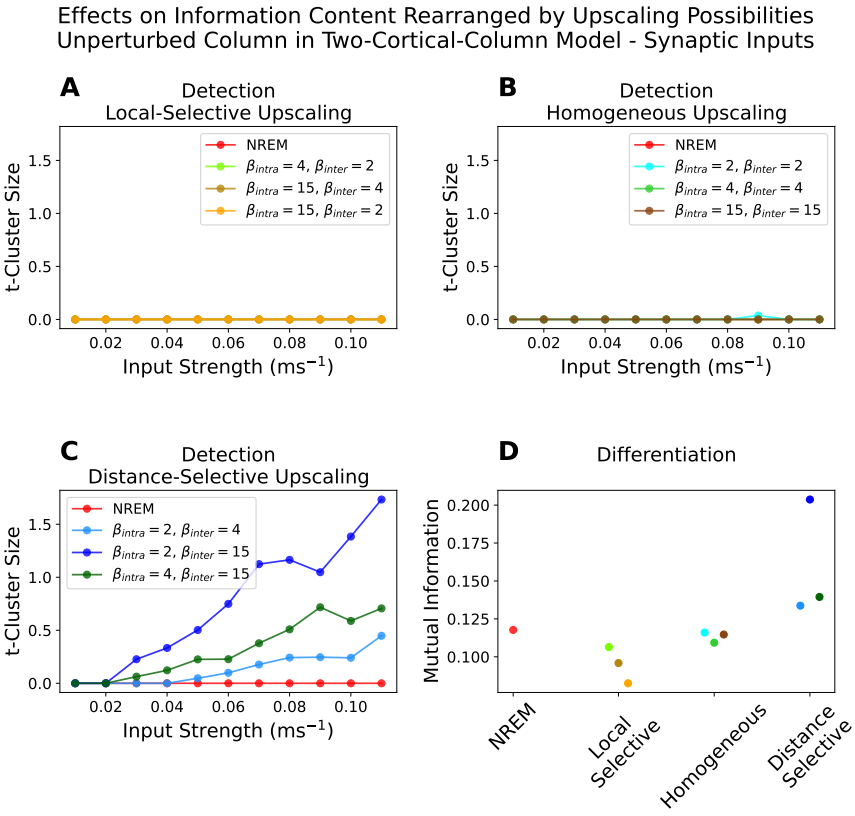

Figure S5.82: Effects of synaptic upscaling on information content implementing significance test and mutual information in the unperturbed column in the two-cortical-column model rearranged by synaptic upscaling scenarios. Results correspond to the perturbed column. (**A**). Size of t-cluster statistics for various input amplitudes in NREM (red) and local-selective synaptic upscaling scenarios in wakefulness (color coded). (**B**), (**C**). As in panel **A**, but for homogeneous and distance-selective synaptic upscaling scenarios in wakefulness, respectively. (**D**) Mutual information for NREM and three synaptic upscaling scenarios in wakefulness. Note that t-cluster statistics and mutual information qualitatively reproduce results for information detection and information differentiation, respectively, implementing machine learning techniques (for instance see Figure 3.13).

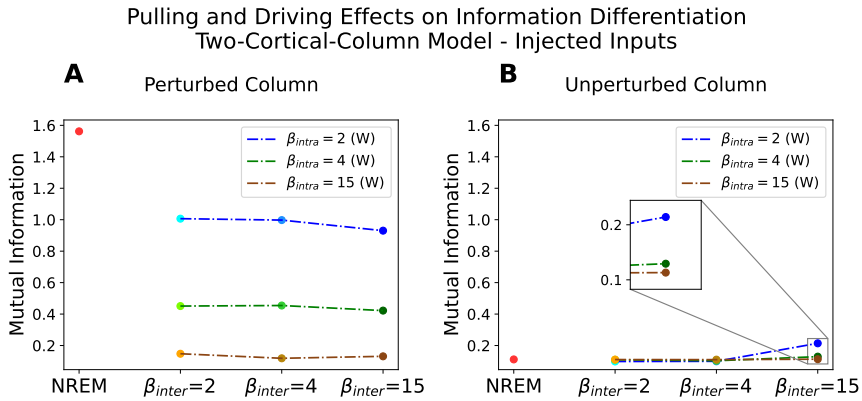

Figure S5.83: Pulling and driving effects due to synaptic upscaling on information differentiation implementing mutual information in the two-cortical-column model. (**A**). Mutual information at input offset in the perturbed column for various input amplitudes (injected inputs) in NREM (red) and various synaptic upscalings in wakefulness (color coded). (**B**). As in panel **A**, but for the unperturbed column. Note that mutual information qualitatively reproduces results for information differentiation, implementing machine learning techniques (for instance see Figure 3.10).

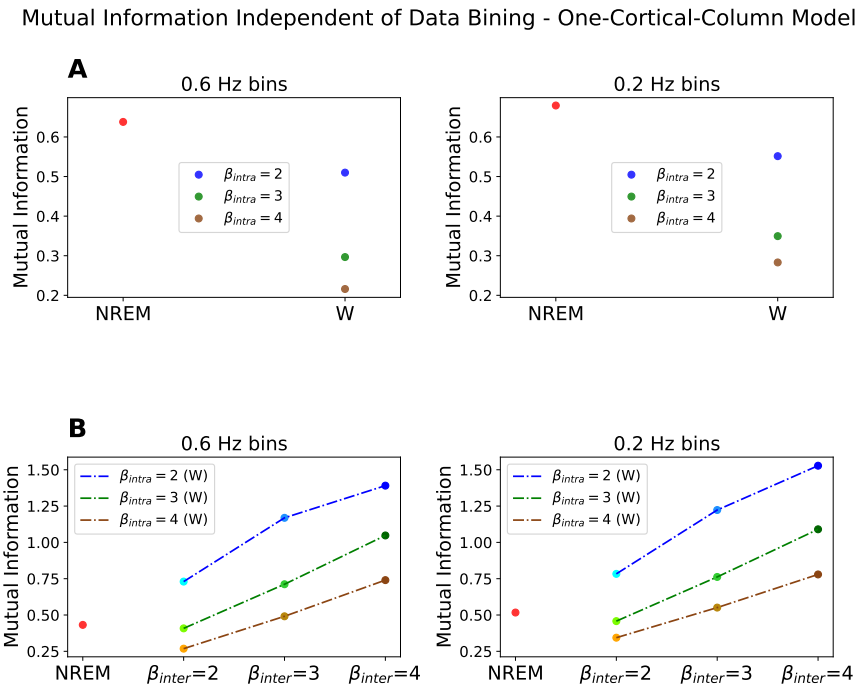

Figure S5.84: Pulling and driving effects on mutual is independent of data binning. (**A**) Mutual information in the one-cortical-column model (injected inputs) when 0.6 Hz and 0.2 Hz bins are used for data discretization. (**B**). Results as in panel **A** but for synaptic inputs. Note that mutual information for different bin number qualitatively reproduces results for information differentiation, implementing machine learning techniques.

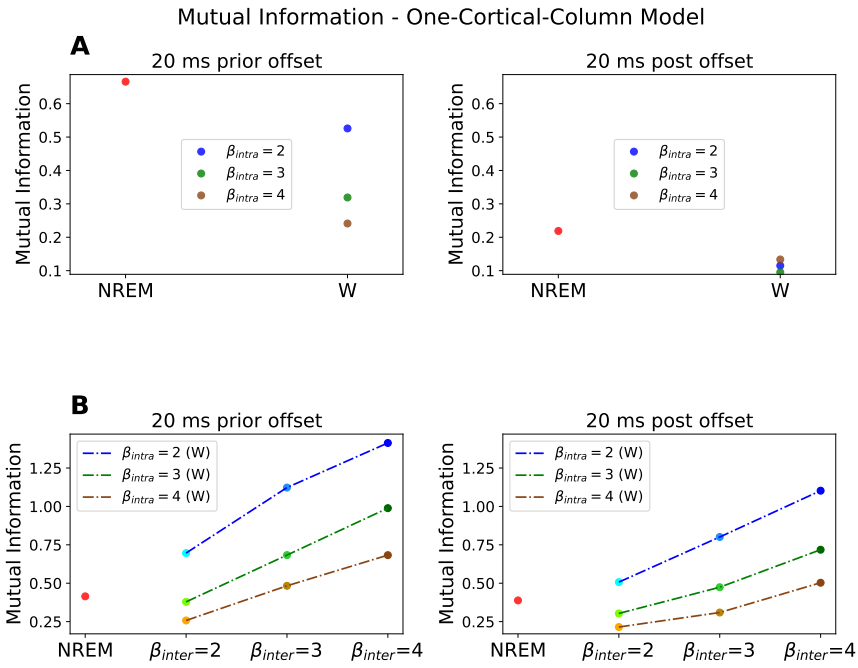

Figure S5.85: Effects of synaptic upscaling on mutual information at 20 ms prior offset and 20 ms post offset in the one-cortical-column model. (**A**). Mutual information at 20 ms prior offset (*left*) and 20 ms post offset (*right*) for various input amplitudes (injected inputs) in NREM (red) and various synaptic upscalings in wakefulness (color coded). (**B**). As in panel **A**, but for synaptic inputs.

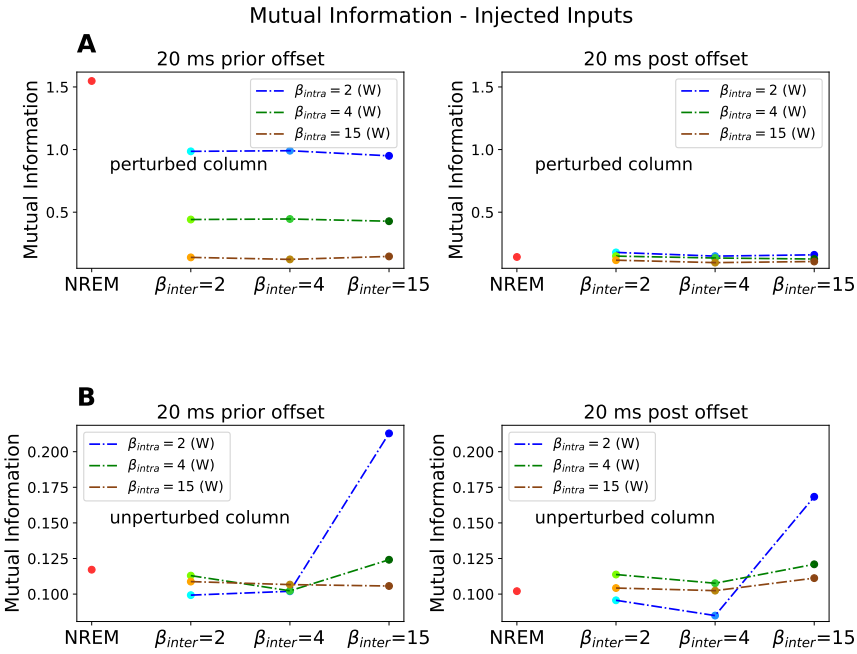

Figure S5.86: Effects of synaptic upscaling on mutual information at 20 ms prior offset and 20 ms post offset to injected inputs in the two-cortical-column model. (**A**). Mutual information at 20 ms prior offset (*left*) and 20 ms post offset (*right*) in the perturbed column for various input amplitudes in NREM (red) and various synaptic upscalings in wakefulness (color coded). (**B**). As in panel **A**, but for the unperturbed column.

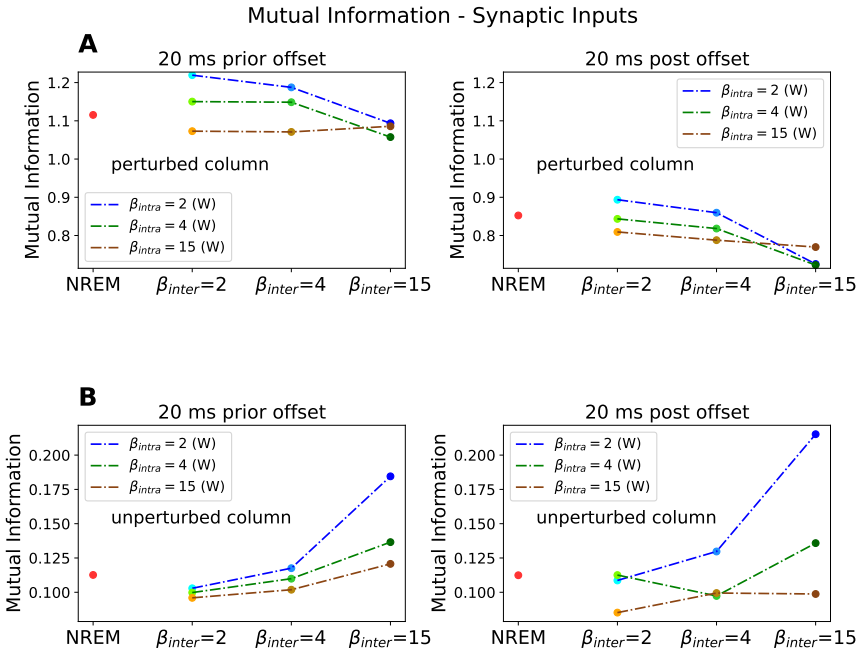

Figure S5.87: Effects of synaptic upscaling on mutual information at 20 ms prior offset and 20 ms post offset to synaptic inputs in the two-cortical-column model. (**A**). Mutual information at 20 ms prior offset (*left*) and 20 ms post offset (*right*) in the perturbed column for various input amplitudes in NREM (red) and various synaptic upscalings in wakefulness (color coded). (**B**). As in panel **A**, but for the unperturbed column.

Appendix A

APPENDIX

This Chapter includes appendix of the study.

A.1 Appendix A: Neural Mass Model Equations

In this section, we provide full model equations for one- and two-cortical-column models. A cortical column is described by the neural mass model of pyramidal and inhibitory populations mutually connected through AMPAergic and GABAergic synapses.

Synapse Dynamics

Assuming that the postsynaptic response of a synapse $s_{kk'}$—given a presynaptic population k' and a postsynaptic population k—is obtained by the convolution of presynaptic firing, $H(t)$, at time t at the synaptic site, and average synaptic response to a single spike is $\alpha_{k'}$, $s_{kk'}(t)$ takes the following form:

$$s_{kk'}(t) = H(t) \circledast \alpha_{k'}(t),$$

$$= \int_0^t H(\tau)\ \alpha_{k'}(t-\tau)\ d\tau,$$

where $\alpha_{k'}(t)$ has an exponential decay time course:

$$\alpha_{k'}(t) = \gamma_{k'}^2\ t\ \exp(-\gamma_{k'} t),$$

Therefore, the first derivative of the $s_{kk'}(t)$ with respect to t taking into account the Leibniz integral rule is as follows:

$$\begin{aligned}
\dot{s}_{kk'}(t) &= \frac{d}{dt}\left[\int_0^t H(\tau)\ \alpha_{k'}(t-\tau)\ d\tau\right], \\
&= H(t)\ \alpha_{k'}(t-t)\ +\ \int_0^t H(\tau)\ \frac{d}{dt}\left[\alpha_{k'}(t-\tau)\right]\ d\tau, \\
&= \int_0^t H(\tau)\ \left[\gamma_{k'}^2\ \exp(-\gamma_{k'}(t-\tau))\right]\ d\tau \\
&\quad - \int_0^t H(\tau)\ \left[\gamma_{k'}^3(t-\tau)\ \exp(-\gamma_{k'}(t-\tau))\right]\ d\tau, \\
&= \int_0^t H(\tau)\ \gamma_{k'}^2\ \exp(-\gamma_{k'}(t-\tau))\ d\tau \\
&\quad -\ \gamma_{k'} \int_0^t H(\tau)\ \gamma_{k'}^2(t-\tau)\ \exp(-\gamma_{k'}(t-\tau))\ d\tau, \\
&= \int_0^t H(\tau)\ \gamma_{k'}^2\ \exp(-\gamma_{k'}(t-\tau))\ d\tau \\
&\quad -\ \gamma_{k'} \int_0^t H(\tau)\ \alpha_{k'}(t-\tau)\ d\tau, \\
&= \int_0^t H(\tau)\ \gamma_{k'}^2\ \exp(-\gamma_{k'}(t-\tau))\ d\tau\ -\ \gamma_{k'}\ s_{kk'}(t).
\end{aligned}$$

In the same way, the second derivative of the $s_{kk'}(t)$ with respect to t is:

$$\begin{aligned}
\ddot{s}_{kk'}(t) &= \gamma_{k'}^2\ H(t)\ +\ \gamma_{k'} \int_0^t\ H(\tau)\ \gamma_{k'}^2(t-\tau)\ \exp(-\gamma_{k'}(t-\tau))\ d\tau \\
&\quad -\ \gamma_{k'}\ \dot{s}_{kk'}(t), \\
&= \gamma_{k'}^2\ H(t)\ -\ \gamma_{k'}\ (\dot{s}_{kk'}(t)\ +\ \gamma_{k'}\ s_{kk'}(t))\ -\ \gamma_{k'}\ \dot{s}_{kk'}(t), \\
&= \gamma_{k'}^2\ H(t)\ -\ \gamma_{k'}^2\ s_{kk'}(t)\ -\ 2\gamma_{k'}\ \dot{s}_{kk'}(t), \\
&= \gamma_{k'}^2\ [H(t)\ -\ s_{kk'}(t)]\ -\ 2\gamma_{k'}\ \dot{s}_{kk'}(t),
\end{aligned}$$

Finally, by substituting the $H(t) = N_{kk'}\ Q_{k'}(V_{k'}) + \phi_k$—which is the presynaptic drive at synapse of population k—the postsynaptic response $s_{kk'}$ takes the form of:

$$\ddot{s}_{kk'} = \gamma_{k'}^2\ (N_{kk'}\ Q_{k'}(V_{k'}) + \phi_k - s_{kk'})\ - 2\gamma_{k'},\ \dot{s}_{kk'}$$

Please note that the noise term ϕ_k is a stochastic Gaussian process with zero autocorrelation time constant. The Gaussian noise is only applied on excitatory synapses.

One-Cortical-Column Model

One-cortical-column model consists of one pyramidal and one inhibitory population (see panel A in Figure 2.1). The model utilizes the mathematical formalism of the Hodgkin-Huxley model to describe the membrane voltage activity in terms of driving synaptic activity. The synaptic activity contains one leak, two synaptic (AMPAergic and GABAergic) currents and one activity-dependent potassium current. In the absence of the Gaussian noise, the system relaxes on the steady state solution. At every time point, the Gaussian noise puts the system out of the steady state solution,

however, the aforementioned synaptic currents drive the system back to the steady state solution. The full model equations for the one-cortical-column model are described by:

$$\begin{aligned}\tau_p \dot{V}_p &= -I_{\mathrm{L}}^p - I_{\mathrm{AMPA}}^p - I_{\mathrm{GABA}}^p - \tau_p C_m^{-1} I_{\mathrm{KNa}},\\ \tau_i \dot{V}_i &= -I_{\mathrm{L}}^i - I_{\mathrm{AMPA}}^i - I_{\mathrm{GABA}}^i,\end{aligned}$$

$$\begin{aligned}\ddot{s}_{pp}^{\text{intra}} &= \gamma_p^2 \left(N_{pp}\, Q_p(V_p) + \phi_p - s_{pp}^{\text{intra}}\right) - 2\gamma_p\, \dot{s}_{pp}^{\text{intra}},\\ \ddot{s}_{pi}^{\text{intra}} &= \gamma_i^2 \left(N_{pi}\, Q_i(V_i) - s_{pi}^{\text{intra}}\right) - 2\gamma_i\, \dot{s}_{pi}^{\text{intra}},\\ \ddot{s}_{ip}^{\text{intra}} &= \gamma_p^2 \left(N_{ip}\, Q_p(V_p) + \phi_i - s_{ip}^{\text{intra}}\right) - 2\gamma_p\, \dot{s}_{ip}^{\text{intra}},\\ \ddot{s}_{ii}^{\text{intra}} &= \gamma_i^2 \left(N_{ii}\, Q_i(V_i) - s_{ii}^{\text{intra}}\right) - 2\gamma_i\, \dot{s}_{ii}^{\text{intra}},\end{aligned}$$

$$\tau_{\mathrm{Na}}\, [\dot{\mathrm{Na}}] = \alpha_{\mathrm{Na}} Q_p(V_p) - \mathrm{Na}_{\mathrm{pump}}([\mathrm{Na}]),$$

with the currents defined by:

$$\begin{aligned}I_{\mathrm{L}}^k &= \bar{g}_{\mathrm{L}}(V_k - E_{\mathrm{L}}^k),\\ I_{\mathrm{AMPA}}^k &= \beta_{intra}\, \bar{g}_{\mathrm{AMPA}} s_{kp}^{\text{intra}} (V_k - E_{\mathrm{AMPA}}),\\ I_{\mathrm{GABA}}^k &= \beta_{\mathrm{GABA}}^k\, \bar{g}_{\mathrm{GABA}} s_{ki}^{\text{intra}} (V_k - E_{\mathrm{GABA}}),\\ I_{\mathrm{KNa}} &= \bar{g}_{\mathrm{KNa}}\, \frac{0.37}{1 + (\frac{38.7}{[\mathrm{Na}]})^{3.5}}\, (V_p - E_{\mathrm{K}}),\ \textit{for}\ k \in \{p,\ i\},\end{aligned}$$

The sodium pump and firing rate functions are given by:

$$\mathrm{Na}_{\mathrm{pump}}([\mathrm{Na}]) = R_{\mathrm{pump}} \left(\frac{[\mathrm{Na}]^3}{[\mathrm{Na}]^3 + 3375} - \frac{[\mathrm{Na}]_{\mathrm{eq}}^3}{[\mathrm{Na}]_{\mathrm{eq}}^3 + 3375} \right),$$

$$Q_k(V_k) = Q_k^{max}\frac{(1+\tanh(C(V_k-\theta_k)/\sigma_k))}{2}, \quad C = \frac{\pi}{2\sqrt{3}}$$

Symbol descriptions and parameter values are provided in Tables 2.1, 2.2 and 2.3.

Two-Cortical-Column Model

Two-cortical-column model consists of two cortical columns each containing one pyramidal and one inhibitory population (see Appendix A.1) that are mutually coupled through AMPAergic connections (see panel B in Figure 2.1). Full model equations for two-cortical-column model are described by:

$$\begin{aligned}
\tau_p \dot{V}_p &= -I_{\mathrm{L}}^p - I_{\mathrm{AMPA}}^p - I_{\mathrm{GABA}}^p - \tau_p C_m^{-1} I_{\mathrm{KNa}}^p, \\
\tau_i \dot{V}_i &= -I_{\mathrm{L}}^i - I_{\mathrm{AMPA}}^i - I_{\mathrm{GABA}}^i,
\end{aligned}$$

$$\begin{aligned}
\tau_{p'} \dot{V}_{p'} &= -I_{\mathrm{L}}^{p'} - I_{\mathrm{AMPA}}^{p'} - I_{\mathrm{GABA}}^{p'} - \tau_{p'} C_m^{-1} I_{\mathrm{KNa}}^{p'}, \\
\tau_{i'} \dot{V}_{i'} &= -I_{\mathrm{L}}^{i'} - I_{\mathrm{AMPA}}^{i'} - I_{\mathrm{GABA}}^{i'},
\end{aligned}$$

$$\begin{aligned}
\ddot{s}_{pp}^{\text{intra}} &= \gamma_p^2 \left(N_{pp}\, Q_p(V_p) + \phi_p - s_{pp}^{\text{intra}}\right) - 2\gamma_p\, \dot{s}_{pp}^{\text{intra}}, \\
\ddot{s}_{pi}^{\text{intra}} &= \gamma_i^2 \left(N_{pi}\, Q_i(V_i) - s_{pi}^{\text{intra}}\right) - 2\gamma_i\, \dot{s}_{pi}^{\text{intra}}, \\
\ddot{s}_{ip}^{\text{intra}} &= \gamma_p^2 \left(N_{ip}\, Q_p(V_p) + \phi_i - s_{ip}^{\text{intra}}\right) - 2\gamma_p\, \dot{s}_{ip}^{\text{intra}}, \\
\ddot{s}_{ii}^{\text{intra}} &= \gamma_i^2 \left(N_{ii}\, Q_i(V_i) - s_{ii}^{\text{intra}}\right) - 2\gamma_i\, \dot{s}_{ii}^{\text{intra}},
\end{aligned}$$

$$\begin{aligned}
\ddot{s}_{p'p'}^{\text{intra}} &= \gamma_{p'}^2 \left(N_{p'p'}\, Q_{p'}(V_{p'}) + \phi_{p'} - s_{p'p'}^{\text{intra}}\right) - 2\gamma_{p'}\, \dot{s}_{p'p'}^{\text{intra}}, \\
\ddot{s}_{p'i'}^{\text{intra}} &= \gamma_{i'}^2 \left(N_{p'i'}\, Q_{i'}(V_{i'}) - s_{p'i'}^{\text{intra}}\right) - 2\gamma_{i'}\, \dot{s}_{p'i'}^{\text{intra}}, \\
\ddot{s}_{i'p'}^{\text{intra}} &= \gamma_{p'}^2 \left(N_{i'p'}\, Q_{p'}(V_{p'}) + \phi_{i'} - s_{i'p'}^{\text{intra}}\right) - 2\gamma_{p'}\, \dot{s}_{i'p'}^{\text{intra}},
\end{aligned}$$

$$\ddot{s}^{\text{intra}}_{i'i'} = \gamma^2_{i'}\ (N_{i'i'}\ Q_{i'}(V_{i'}) - s^{\text{intra}}_{i'i'})\ - 2\gamma_{i'}\ \dot{s}^{\text{intra}}_{i'i'},$$

$$\ddot{s}^{\text{inter}}_{pp'} = \gamma^2_{p'}\ (N_{pp'}\ Q_{p'}(V_{p'}) - s^{\text{inter}}_{pp'})\ - 2\gamma_{p'}\ \dot{s}^{\text{inter}}_{pp'},$$
$$\ddot{s}^{\text{inter}}_{ip'} = \gamma^2_{p'}\ (N_{ip'}\ Q_{p'}(V_{p'}) - s^{\text{inter}}_{ip'})\ - 2\gamma_{p'}\ \dot{s}^{\text{inter}}_{ip'},$$

$$\ddot{s}^{\text{inter}}_{p'p} = \gamma^2_{p}\ (N_{p'p}\ Q_{p}(V_{p}) - s^{\text{inter}}_{p'p})\ - 2\gamma_{p}\ \dot{s}^{\text{inter}}_{p'p},$$
$$\ddot{s}^{\text{inter}}_{i'p} = \gamma^2_{p}\ (N_{i'p}\ Q_{p}(V_{p}) - s^{\text{inter}}_{i'p})\ - 2\gamma_{p}\ \dot{s}^{\text{inter}}_{i'p},$$

$$\tau_{\text{Na}}\ [\dot{\text{Na}}]_p = \alpha_{\text{Na}} Q_p(V_p) - \text{Na}_{\text{pump}}([\text{Na}]_p),$$
$$\tau_{\text{Na}}\ [\dot{\text{Na}}]_{p'} = \alpha_{\text{Na}} Q_{p'}(V_{p'}) - \text{Na}_{\text{pump}}([\text{Na}]_{p'}),$$

where I^h_{KNa} is the sodium-dependent potassium current of either the perturbed pyramidal population ($h = p$) or the unperturbed pyramidal population ($h = p'$). The currents are defined by:

$$I^k_{\text{L}} = \bar{g}_{\text{L}}(V_k - E^k_{\text{L}}),\ \textit{for}\ k \in \{p,\ i,\ p',\ i'\},$$

$$\begin{aligned} I^k_{\text{AMPA}} =\ & \beta_{intra}\ \bar{g}_{\text{AMPA}}\ s^{\text{intra}}_{kp'}\ (V_k - E_{\text{AMPA}}) \\ & +\ \beta_{inter}\ \bar{g}_{\text{AMPA}}\ s^{\text{inter}}_{kp'}\ (V_k - E_{\text{AMPA}}),\ \textit{for}\ k \in \{p,\ i\}, \\ I^k_{\text{GABA}} =\ & \beta^k_{\text{GABA}}\ \bar{g}_{\text{GABA}} s^{\text{intra}}_{ki}(V_k - E_{\text{GABA}}),\ \textit{for}\ k \in \{p,\ i\}, \end{aligned}$$

$$\begin{aligned} I^k_{\text{AMPA}} =\ & \beta_{intra}\ \bar{g}_{\text{AMPA}}\ s^{\text{intra}}_{kp}\ (V_k - E_{\text{AMPA}}) \\ & +\ \beta_{inter}\ \bar{g}_{\text{AMPA}}\ s^{\text{inter}}_{kp}\ (V_k - E_{\text{AMPA}}),\ \textit{for}\ k \in \{p',\ i'\}, \\ I^k_{\text{GABA}} =\ & \beta^k_{\text{GABA}}\ \bar{g}_{\text{GABA}} s^{\text{intra}}_{ki'}(V_k - E_{\text{GABA}}),\ \textit{for}\ k \in \{p',\ i'\}, \end{aligned}$$

$$I^h_{\text{KNa}} = \bar{g}_{\text{KNa}} \frac{0.37}{1 + (\frac{38.7}{[\text{Na}]_h})^{3.5}} (V_h - E_{\text{K}}), \textit{ for } h \in \{p,\ p'\},$$

The sodium pump and firing rate functions are given by:

$$\text{Na}_{\text{pump}}([\text{Na}]_h) = R_{\text{pump}} \left(\frac{[\text{Na}]^3_h}{[\text{Na}]^3_h + 3375} - \frac{[\text{Na}]^3_{\text{eq}}}{[\text{Na}]^3_{\text{eq}} + 3375} \right),$$

$$Q_k(V_k) = Q^{max}_k \frac{(1 + \tanh(C(V_k - \theta_k)/\sigma_k))}{2}, \quad C = \frac{\pi}{2\sqrt{3}}$$

Symbol descriptions and parameter values are provided in Tables 2.1, 2.2, 2.4 and 2.5.

A.2 Appendix B: Dynamical Constrains on β^k_{GABA}

One-Cortical-Column Model

Upscaling the conductance of excitatory synapses by a factor β_{intra} allows us to place the model from NREM sleep dynamics into wakefulness, in agreement with SHY . To counterbalance the overexcitation each population receives due to intra-synaptic upscaling, the average GABAergic conductance on pyramidal and inhibitory population are increased by a factor β^k_{GABA}, $k \in \{p,\ i\}$. To do so, we use the peaks of V_p and V_i values during Up states in NREM sleep as the steady state value of average membrane potential of pyramidal and inhibitory populations in wakefulness. β^k_{GABA} is increased until the value of V_k, ($k \in \{p,\ i\}$), is obtained for various intra-synaptic upscalings in wakefulness.

The steady state solution of the model equations for one-cortical-column (see Appendix A.1) are obtained by setting derivative of all variables to zero:

$$0 = -I^p_{\text{L}} - I^p_{\text{AMPA}} - I^p_{\text{GABA}} - \tau_p C^{-1}_m I^p_{\text{KNa}},$$

$$
\begin{aligned}
0 &= -I^i_{\mathrm{L}} - I^i_{\mathrm{AMPA}} - I^i_{\mathrm{GABA}}, \\
s_{kk'} &= N_{kk'}\, Q_{k'}(V_{k'}), \\
[\mathrm{Na}] &= \sqrt[3]{\frac{\mathrm{A}\cdot 3375}{1-\mathrm{A}}}, \\
\mathrm{A} &= \frac{\alpha_{\mathrm{Na}}}{R_{\mathrm{pump}}} Q_p(V_p) + \frac{[\mathrm{Na}]^3_{\mathrm{eq}}}{[\mathrm{Na}]^3_{\mathrm{eq}} + 3375},
\end{aligned}
$$

Therefore, β^k_{GABA}, $k \in \{p,\ i\}$ are as follows:

$$
\beta^{\,p}_{\mathrm{GABA}} = \frac{-\bar{g}_{\mathrm{L}}(V_p - E^p_{\mathrm{L}}) - \beta_{intra}\ \bar{g}_{\mathrm{AMPA}}\ s^{\mathrm{intra}}_{pp}(V_p - E_{\mathrm{AMPA}})}{\bar{g}_{\mathrm{GABA}}\ s^{\mathrm{intra}}_{pi}(V_p - E_{\mathrm{GABA}})}
$$

$$
+ \frac{-\bar{g}_{\mathrm{KNa}}\ \dfrac{0.37}{1+(\frac{38.7}{[\mathrm{Na}]})^{3.5}}\ (V_p - E_{\mathrm{K}})}{\bar{g}_{\mathrm{GABA}}\ s^{\mathrm{intra}}_{pi}(V_p - E_{\mathrm{GABA}})},
$$

$$
\beta^{\,i}_{\mathrm{GABA}} = \frac{-\bar{g}_{\mathrm{L}}(V_i - E^i_{\mathrm{L}}) - \beta_{intra}\ \bar{g}_{\mathrm{AMPA}} s^{\mathrm{intra}}_{ip}(V_i - E_{\mathrm{AMPA}})}{\bar{g}_{\mathrm{GABA}}\ s^{\mathrm{intra}}_{ii}(V_i - E_{\mathrm{GABA}})},
$$

β^k_{GABA}, $k \in \{p,\ i\}$ in wakefulness for various intra-synaptic upscalings in wakefulness are obtained by substituting corresponding β_{intra} and the peaks of V_p and V_i values during Up states in NREM sleep.

Two-Cortical-Column Model

Inter-cortical column coupling introduces overexcitation to the pyramidal and inhibitory populations in NREM sleep. To keep the steady state

value of V_p and V_i in two-cortical-column model equal to the ones in one-cortical-column model in NREM sleep, β^k_{GABA}, $k \in \{p,\ i,\ p',\ i'\}$, are increased to counterbalance the inter-cortical column coupling. The same procedure is carried out for various synaptic upscalings in wakefulness.

The steady state solution of the model equations for two-cortical-column (see Appendix A.1) is obtained by setting the derivatives of all variables to zero:

$$
\begin{aligned}
0 &= -I_{\text{L}}^{p/p'} - I_{\text{AMPA}}^{p/p'} - I_{\text{GABA}}^{p/p'} - \tau_{p/p'} C_m^{-1} I_{\text{KNa}}^{p/p'},\\
0 &= -I_{\text{L}}^{i/i'} - I_{\text{AMPA}}^{i/i'} - I_{\text{GABA}}^{i/i'},\\
s_{kk'} &= N_{kk'}\, Q_{k'}(V_{k'}),\\
s_{kk'}^{\text{inter}} &= N_{kk'}\, Q_{k'}(V_{k'})\\
[\text{Na}]_{p/p'} &= \sqrt[3]{\frac{\text{A}_{p/p'} \cdot 3375}{1 - \text{A}_{p/p'}}},\\
\text{A}_{p/p'} &= \frac{\alpha_{\text{Na}}}{R_{\text{pump}}} Q_{p/p'}(V_{p/p'}) + \frac{[\text{Na}]_{\text{eq}}^3}{[\text{Na}]_{\text{eq}}^3 + 3375},
\end{aligned}
$$

By taking into account the symmetry between the two cortical columns, we set the steady state value of V_p and V_i equal to $V_{p'}$ and $V_{i'}$, respectively ($V_{p'} = V_p$ and $V_{i'} = V_i$). Therefore, to keep average membrane potential of pyramidal and inhibitory populations in two-cortical-column model equal to the ones in the one-cortical-column model both during NREM sleep and wakefulness, β^k_{GABA}, $k \in \{p,\ i,\ p',\ i'\}$, change as follows:

$$
\beta_{\text{GABA}}^{p/p'} = \frac{-\bar{g}_{\text{L}}(V_p - E_{\text{L}}^p) - \beta_{intra}\ \bar{g}_{\text{AMPA}}\ s_{pp}^{\text{intra}}(V_p - E_{\text{AMPA}})}{\bar{g}_{\text{GABA}}\ s_{pi}^{\text{intra}}(V_p - E_{\text{GABA}})}
$$

$$+\frac{-\beta_{inter}\ \bar{g}_{\text{AMPA}}\ s^{\text{inter}}_{pp'}(V_p - E_{\text{AMPA}})}{\bar{g}_{\text{GABA}}\ s^{\text{intra}}_{pi}(V_p - E_{\text{GABA}})}$$

$$+\frac{-\bar{g}_{\text{KNa}}\ \frac{0.37}{1+(\frac{38.7}{[\text{Na}]})^{3.5}}\ (V_p - E_{\text{K}})}{\bar{g}_{\text{GABA}}\ s^{\text{intra}}_{pi}(V_p - E_{\text{GABA}})},$$

$$\beta^{\ i/i'}_{\text{GABA}} = \frac{-\bar{g}_{\text{L}}(V_i - E^i_{\text{L}}) - \beta_{intra}\ \bar{g}_{\text{AMPA}} s^{\text{intra}}_{ip}(V_i - E_{\text{AMPA}})}{\bar{g}_{\text{GABA}}\ s^{\text{intra}}_{ii}(V_i - E_{\text{GABA}})}$$

$$+\frac{-\beta_{inter}\ \bar{g}_{\text{AMPA}}\ s^{\text{inter}}_{ip'}(V_i - E_{\text{AMPA}})}{\bar{g}_{\text{GABA}}\ s^{\text{intra}}_{ii}(V_i - E_{\text{GABA}})},$$

β^{k}_{GABA}, $k \in \{p,\ i,\ p',\ i'\}$, in NREM sleep in two-cortical-column model are obtained by setting $\beta_{intra} = \beta_{inter} = 1$ and the steady state values of V_p and V_i in NREM sleep in one-cortical-column model.

β^{k}_{GABA}, $k \in \{p,\ i,\ p',\ i'\}$, for various synaptic upscalings in wakefulness in two-cortical-column model are obtained by substituting corresponding β_{intra} and β_{inter} and the peaks of V_p and V_i values during Up states in NREM sleep in one-cortical-column model.

Bibliography

[1] R. E. Brown, R. Basheer, J. T. McKenna, R. E. Strecker, and R. W. McCarley, "Control of sleep and wakefulness," *Physiol. Rev.*, vol. 92, pp. 1087–1187, jul 2012.

[2] M. Massimini, F. Ferrarelli, S. Sarasso, and G. Tononi, "Cortical mechanisms of loss of consciousness: Insight from TMS/EEG studies," *Arch. Ital. Biol.*, vol. 150, no. 2-3, pp. 44–55, 2012.

[3] A. Pigorini, S. Sarasso, P. Proserpio, C. Szymanski, G. Arnulfo, S. Casarotto, M. Fecchio, M. Rosanova, M. Mariotti, G. Lo Russo, J. M. Palva, L. Nobili, and M. Massimini, "Bistability breaks-off deterministic responses to intracortical stimulation during non-REM sleep," *Neuroimage*, vol. 112, pp. 105–113, may 2015.

[4] B. W. Balleine and J. P. O'Doherty, "Human and rodent homologies in action control: Corticostriatal determinants of goal-directed and habitual action," *Neuropsychopharmacology*, vol. 35, pp. 48–69, jan 2010.

[5] J. G. Jenkins and K. M. Dallenbach, "Obliviscence during Sleep and Waking," *Am. J. Psychol.*, vol. 35, p. 605, oct 1924.

[6] R. Stickgold, L. James, and J. A. Hobson, "Visual discrimination learning requires sleep after training," *Nat. Neurosci.*, vol. 3, pp. 1237–1238, dec 2000.

[7] M. P. Walker, T. Brakefield, J. A. Hobson, and R. Stickgold, "Dissociable stages of human memory consolidation and reconsolidation," *Nature*, vol. 425, pp. 616–620, oct 2003.

[8] R. Huber, M. F. Ghilardi, M. Massimini, and G. Tononi, "Local sleep and learning," *Nature*, vol. 430, pp. 78–81, jul 2004.

[9] L. Marshall, H. Helgadóttir, M. Mölle, and J. Born, "Boosting slow oscillations during sleep potentiates memory," *Nature*, vol. 444, pp. 610–613, nov 2006.

[10] J. Tamminen, J. D. Payne, R. Stickgold, E. J. Wamsley, and M. G. Gaskell, "Sleep spindle activity is associated with the integration of new memories and existing knowledge," *J. Neurosci.*, vol. 30, pp. 14356–14360, oct 2010.

[11] S. Diekelmann and J. Born, "The memory function of sleep," *Nat. Rev. Neurosci.*, vol. 11, pp. 114–126, feb 2010.

[12] A. L. Loomis, E. N. Harvey, and G. Hobart, "Potential rhythms of the cerebral cortex during sleep," *Science (80-.).*, vol. 81, pp. 597–598, jun 1935.

[13] A. L. Loomis, E. N. Harvey, and G. Hobart, "Further observations on the potential rhythms of the cerebral cortex during sleep," *Science (80-.).*, vol. 82, pp. 198–200, aug 1935.

[14] F. A. Gibbs, H. Davis, and W. G. Lennox, "The Electro Encephalogram in Epilepsy and in Conditions of Impaired Consciousness," *Am. J. EEG Technol.*, vol. 8, pp. 59–73, jun 1968.

[15] M. H. Kryger, W. C. Dement, and T. Roth, *Principles and practice of sleep medicine*. Elsevier, 2010.

[16] A. L. Loomis, E. N. Harvey, and G. A. Hobart, "Distribution of Disturbance-Patterns in the Human Electroencephalogram, With Special Reference To Sleep," *J. Neurophysiol.*, vol. 1, pp. 413–430, sep 1938.

[17] D. A. McCormick, "Cholinergic and noradrenergic modulation of thalamocortical processing," *Trends Neurosci.*, vol. 12, pp. 215–221, jun 1989.

[18] M. Steriade, D. A. McCormick, and T. J. Sejnowski, "Thalamocortical oscillations in the sleeping and aroused brain," *Science (80-.).*, vol. 262, pp. 679–685, oct 1993.

[19] D. A. McCormick and T. Bal, "Sensory gating mechanisms of the thalamus," *Curr. Opin. Neurobiol.*, vol. 4, pp. 550–556, aug 1994.

[20] M. Steriade, A. Nunez, and F. Amzica, "A novel slow (< 1 Hz) oscillation of neocortical neurons in vivo: Depolarizing and hyperpolarizing components," *J. Neurosci.*, vol. 13, pp. 3252–3265, aug 1993.

[21] F. Amzica and M. Steriade, "The K-complex: Its slow (<1-Hz) rhythmicity and relation to delta waves," *Neurology*, vol. 49, pp. 952–959, oct 1997.

[22] S. S. Cash, E. Halgren, N. Dehghani, A. O. Rossetti, T. Thesen, C. M. Wang, O. Devinsky, R. Kuzniecky, W. Doyle, J. R. Madsen, E. Bromfield, L. Eross, P. Halász, G. Karmos, R. Csercsa, L. Wittner, and I. Ulbert, "The human K-complex represents an isolated cortical down-state," *Science (80-.).*, vol. 324, pp. 1084–1087, may 2009.

[23] S. M. Sherman and R. W. Guillery, "The role of the thalamus in the flow of information to the cortex," *Philos. Trans. R. Soc. B Biol. Sci.*, vol. 357, pp. 1695–1708, dec 2002.

[24] L. M. Fernandez and A. Lüthi, "Sleep spindles: Mechanisms and functions," *Physiol. Rev.*, vol. 100, pp. 805–868, apr 2020.

[25] M. Steriade, D. Contreras, R. C. Dossi, and A. Nunez, "The slow (<1 Hz) oscillation in reticular thalamic and thalamocortical neurons: Scenario of sleep rhythm generation in interacting thalamic and neocortical networks," *J. Neurosci.*, vol. 13, pp. 3284–3299, aug 1993.

[26] M. Steriade, I. Timofeev, and F. Grenier, "Natural waking and sleep states: A view from inside neocortical neurons," *J. Neurophysiol.*, vol. 85, pp. 1969–1985, may 2001.

[27] I. Timofeev and M. Steriade, "Low-frequency rhythms in the thalamus of intact-cortex and decorticated cats," *J. Neurophysiol.*, vol. 76, pp. 4152–4168, dec 1996.

[28] M. V. Sanchez-Vives and D. A. McCormick, "Cellular and network mechanisms of rhytmic recurrent activity in neocortex," *Nat. Neurosci.*, vol. 3, pp. 1027–1034, oct 2000.

[29] V. V. Vyazovskiy, U. Olcese, E. C. Hanlon, Y. Nir, C. Cirelli, and G. Tononi, "Local sleep in awake rats," *Nature*, vol. 472, pp. 443–447, apr 2011.

[30] Y. Nir, R. J. Staba, T. Andrillon, V. V. Vyazovskiy, C. Cirelli, I. Fried, and G. Tononi, "Regional Slow Waves and Spindles in Human Sleep," *Neuron*, vol. 70, no. 1, pp. 153–169, 2011.

[31] M. V. Sanchez-Vives, "Origin and dynamics of cortical slow oscillations," *Curr. Opin. Physiol.*, vol. 15, pp. 217–223, jun 2020.

[32] V. V. Vyazovskiy, U. Olcese, Y. M. Lazimy, U. Faraguna, S. K. Esser, J. C. Williams, C. Cirelli, and G. Tononi, "Cortical Firing and Sleep Homeostasis," *Neuron*, vol. 63, pp. 865–878, sep 2009.

[33] S. Chauvette, S. Crochet, M. Volgushev, and I. Timofeev, "Properties of slow oscillation during slow-wave sleep and anesthesia in cats," *J. Neurosci.*, vol. 31, pp. 14998–15008, oct 2011.

[34] A. Destexhe, S. W. Hughes, M. Rudolph, and V. Crunelli, "Are corticothalamic 'up' states fragments of wakefulness?," *Trends Neurosci.*, vol. 30, pp. 334–342, jul 2007.

[35] D. A. McCormick, Z. Wang, and J. Huguenard, "Neurotransmitter control of neocortical neuronal activity and excitability," *Cereb. Cortex*, vol. 3, no. 5, pp. 387–398, 1993.

[36] A. Compte, M. V. Sanchez-Vives, D. A. McCormick, and X. J. Wang, "Cellular and network mechanisms of slow oscillatory activity (<1 Hz) and wave propagations in a cortical network model," *J. Neurophysiol.*, vol. 89, pp. 2707–2725, may 2003.

[37] G. T. Neske, "The slow oscillation in cortical and thalamic networks: Mechanisms and functions," *Front. Neural Circuits*, vol. 9, no. JAN2016, p. 88, 2016.

[38] G. Moruzzi and H. W. Magoun, "Brain stem reticular formation and activation of the EEG," *Electroencephalogr. Clin. Neurophysiol.*, vol. 1, pp. 455–473, jan 1949.

[39] T. E. Scammell, E. Arrigoni, and J. O. Lipton, "Neural Circuitry of Wakefulness and Sleep," *Neuron*, vol. 93, pp. 747–765, feb 2017.

[40] E. F. Pace-Schott and J. A. Hobson, "The neurobiology of sleep: Genetics, cellular physiology and subcortical networks," *Nat. Rev. Neurosci.*, vol. 3, pp. 591–605, aug 2002.

[41] E. R. Kandel, J. H. Schwartz, T. M. Jessell, S. Siegelbaum, A. J. Hudspeth, S. Mack, *et al.*, *Principles of neural science*, vol. 4. McGraw-hill New York, 2000.

[42] G. Aston-Jones and F. E. Bloom, "Activity of norepinephrine-containing locus coeruleus neurons in behaving rats anticipates fluctuations in the sleep-waking cycle," *J. Neurosci.*, vol. 1, pp. 876–886, aug 1981.

[43] H. A. Baghdoyan and R. Lydic, "The Neurochemistry of Sleep and Wakefulness," in *Basic Neurochem. Princ. Mol. Cell. Med. Neurobiol. Eighth Ed.*, pp. 982–999, Elsevier, 2011.

[44] T. Gallopin, P. Fort, E. Eggermann, B. Cauli, P. H. Luppi, J. Rossier, E. Audinat, M. Mühlethaler, and M. Serafin, "Identification of sleep-promoting neurons in vitro," *Nature*, vol. 404, pp. 992–995, apr 2000.

[45] S. Boucetta, Y. Cissé, L. Mainville, M. Morales, and B. E. Jones, "Discharge profiles across the sleep-waking cycle of identified cholinergic, GABAergic, and glutamatergic neurons in the pontomesencephalic tegmentum of the rat," *J. Neurosci.*, vol. 34, pp. 4708–4727, mar 2014.

[46] R. W. Mccarley and J. A. Hobson, "Neuronal excitability modulation over the sleep cycle: A structural and mathematical model," *Science (80-.).*, vol. 189, pp. 58–60, jul 1975.

[47] J. E. Sherin, P. J. Shiromani, R. W. McCarley, and C. B. Saper, "Activation of ventrolateral preoptic neurons during sleep," *Science (80-.).*, vol. 271, pp. 216–219, jan 1996.

[48] I. Oswald, A. M. Taylor, and M. Treisman, "Discriminative responses to stimulation during human sleep," *Brain*, vol. 83, pp. 440–453, sep 1960.

[49] M. R. Schreck, L. Zhuang, E. Janke, A. H. Moberly, J. P. Bhattarai, J. A. Gottfried, D. W. Wesson, and M. Ma, "State-dependent olfactory processing in freely behaving mice," *Cell Rep.*, vol. 38, p. 110450, mar 2022.

[50] J. Brualla, M. F. Romero, M. Serrano, and J. R. Valdizán, "Auditory event-related potentials to semantic priming during sleep," *Electroencephalogr. Clin. Neurophysiol. - Evoked Potentials*, vol. 108, pp. 283–290, apr 1998.

[51] F. Perrin, L. García-Larrea, F. Mauguière, and H. Bastuji, "A differential brain response to the subject's own name persists during sleep," *Clin. Neurophysiol.*, vol. 110, pp. 2153–2164, dec 1999.

[52] A. Ibáñez, V. López, and C. Cornejo, "ERPs and contextual semantic discrimination: Degrees of congruence in wakefulness and sleep," *Brain Lang.*, vol. 98, pp. 264–275, sep 2006.

[53] S. Kouider, T. Andrillon, L. S. Barbosa, L. Goupil, and T. A. Bekinschtein, "Inducing task-relevant responses to speech in the sleeping brain," *Curr. Biol.*, vol. 24, pp. 2208–2214, sep 2014.

[54] T. Andrillon, A. T. Poulsen, L. K. Hansen, D. L É Ger, and S. Kouider, "Neural markers of responsiveness to the environment in human sleep," *J. Neurosci.*, vol. 36, pp. 6583–6596, jun 2016.

[55] G. Legendre, T. Andrillon, M. Koroma, and S. Kouider, "Sleepers track informative speech in a multitalker environment," *Nat. Hum. Behav.*, vol. 3, pp. 274–283, mar 2019.

[56] M. Koroma, C. Lacaux, T. Andrillon, G. Legendre, D. Léger, and S. Kouider, "Sleepers Selectively Suppress Informative Inputs during Rapid Eye Movements," *Curr. Biol.*, vol. 30, pp. 2411–2417.e3, jun 2020.

[57] B. M. Mazoyer, N. Tzourio, V. Frak, A. Syrota, N. Murayama, O. Levrier, G. Salamon, S. Dehaene, L. Cohen, and J. Mehler, "The cortical representation of speech," *J. Cogn. Neurosci.*, vol. 5, pp. 467–479, oct 1993.

[58] J. Binder, J. A. Frost, T. A. Hammeke, P. S. Bellgowan, J. A. Springer, J. N. Kaufman, and E. T. Possing, "Human temporal lobe activation by speech and nonspeech sounds," *Cereb. Cortex*, vol. 10, pp. 512–528, may 2000.

[59] G. Dehaene-Lambertz, S. Dehaene, and L. Hertz-Pannier, "Functional neuroimaging of speech perception in infants," *Science (80-.).*, vol. 298, pp. 2013–2015, dec 2002.

[60] C. M. Portas, K. Krakow, P. Allen, O. Josephs, J. L. Armony, and C. D. Frith, "Auditory processing across the sleep-wake cycle: Simultaneous EEG and fMRI monitoring in humans," *Neuron*, vol. 28, pp. 991–999, dec 2000.

[61] M. Czisch, T. C. Wetter, C. Kaufmann, T. Pollmächer, F. Holsboer, and D. P. Auer, "Altered processing of acoustic stimuli during sleep: Reduced auditory activation and visual deactivation detected by a combined fMRI/EEG study," *Neuroimage*, vol. 16, pp. 251–258, may 2002.

[62] M. Czisch, R. Wehrle, C. Kaufmann, T. C. Wetter, F. Holsboer, T. Pollmächer, and D. P. Auer, "Functional MRI during sleep: BOLD signal decreases and their electrophysiological correlates," *Eur. J. Neurosci.*, vol. 20, pp. 566–574, jul 2004.

[63] F. Perrin, P. Maquet, P. Peigneux, P. Ruby, C. Degueldre, E. Balteau, G. Del Fiore, G. Moonen, A. Luxen, and S. Laureys, "Neural mechanisms involved in the detection of our first name: A combined

ERPs and PET study," *Neuropsychologia*, vol. 43, no. 1, pp. 12–19, 2005.

[64] M. Wilf, M. Ramot, E. Furman-Haran, A. Arzi, Y. Levkovitz, and R. Malach, "Diminished auditory responses during NREM sleep correlate with the hierarchy of language processing," *PLoS One*, vol. 11, p. e0157143, jun 2016.

[65] E. B. Issa and X. Wang, "Sensory responses during sleep in primate primary and secondary auditory cortex," *J. Neurosci.*, vol. 28, pp. 14467–14480, dec 2008.

[66] Y. Nir, V. V. Vyazovskiy, C. Cirelli, M. I. Banks, and G. Tononi, "Auditory responses and stimulus-specific adaptation in rat auditory cortex are preserved across NREM and REM sleep," *Cereb. Cortex*, vol. 25, pp. 1362–1378, may 2015.

[67] Y. Sela, A. J. Krom, L. Bergman, N. Regev, and Y. Nir, "Sleep differentially affects early and late neuronal responses to sounds in auditory and perirhinal cortices," *J. Neurosci.*, vol. 40, pp. 2895–2905, apr 2020.

[68] H. Hayat, A. Marmelshtein, A. J. Krom, Y. Sela, A. Tankus, I. Strauss, F. Fahoum, I. Fried, and Y. Nir, "Reduced neural feedback signaling despite robust neuron and gamma auditory responses during human sleep," *Nat. Neurosci.*, vol. 25, pp. 935–943, jul 2022.

[69] G. Buzsáki, C. A. Anastassiou, and C. Koch, "The origin of extracellular fields and currents-EEG, ECoG, LFP and spikes," *Nat. Rev. Neurosci.*, vol. 13, pp. 407–420, may 2012.

[70] M. Massimini, F. Ferrarelli, R. Huber, S. K. Esser, H. Singh, and G. Tononi, "Neuroscience: Breakdown of cortical effective connectivity during sleep," *Science (80-.).*, vol. 309, pp. 2228–2232, sep 2005.

[71] G. F. Woodman, "A brief introduction to the use of event-related potentials in studies of perception and attention," *Atten. Percept. Psychophys.*, vol. 72, pp. 2031–2046, nov 2010.

[72] P. A. Davis, "Effects of Acoustic Stimuli on the Waking Human Brain," *J. Neurophysiol.*, vol. 2, pp. 494–499, nov 1939.

[73] H. Davis, P. A. Davis, A. L. Loomis, E. N. Harvey, and G. Hobart, "Electrical Reactions of the Human Brain To Auditory Stimulation During Sleep," *J. Neurophysiol.*, vol. 2, pp. 500–514, nov 1939.

[74] E. D. Weitzman and H. Kremen, "Auditory evoked responses during different stages of sleep in man," *Electroencephalogr. Clin. Neurophysiol.*, vol. 18, pp. 65–70, jan 1965.

[75] B. Van Sweden, J. G. Van Dijk, and J. F. Caekebeke, "Auditory information processing in sleep: Habituationto repetitive stimuli," *Neuropsychobiology*, vol. 30, no. 2-3, pp. 143–147, 1994.

[76] H. Bastuji, L. García-Larrea, C. Franc, and F. Mauguière, "Brain processing of stimulus deviance during slow-wave and paradoxical sleep: A study of human auditory evoked responses using the oddball paradigm," *J. Clin. Neurophysiol.*, vol. 12, pp. 155–167, mar 1995.

[77] W. Ritter, H. G. Vaughan, and L. D. Costa, "Orienting and habituation to auditory stimuli: A study of short terms changes in average evoked responses," *Electroencephalogr. Clin. Neurophysiol.*, vol. 25, pp. 550–556, dec 1968.

[78] D. L. Woods and R. Elmasian, "The habituation of event-related potentials to speech sounds and tones," *Electroencephalogr. Clin. Neurophysiol. Evoked Potentials*, vol. 65, pp. 447–459, nov 1986.

[79] M. Regev, E. Simony, K. Lee, K. M. Tan, J. Chen, and U. Hasson, "Propagation of Information Along the Cortical Hierarchy as a Function of Attention while Reading and Listening to Stories," *Cereb. Cortex*, vol. 29, pp. 4017–4034, sep 2019.

[80] M. A. Just, P. A. Carpenter, T. A. Keller, W. F. Eddy, and K. R. Thulborn, "Brain activation modulated by sentence comprehension," *Science (80-.).*, vol. 274, pp. 114–116, oct 1996.

[81] M. Massimini, F. Ferrarelli, S. K. Esser, B. A. Riedner, R. Huber, M. Murphy, M. J. Peterson, and G. Tononi, "Triggering sleep slow waves by transcranial magnetic stimulation," *Proc. Natl. Acad. Sci. U. S. A.*, vol. 104, pp. 8496–8501, may 2007.

[82] G. M. Shepherd and N. Yamawaki, "Untangling the cortico-thalamo-cortical loop: cellular pieces of a knotty circuit puzzle," *Nat. Rev. Neurosci.*, vol. 22, pp. 389–406, jul 2021.

[83] B. B. Theyel, D. A. Llano, and S. M. Sherman, "The corticothalamocortical circuit drives higher-order cortex in the mouse," *Nat. Neurosci.*, vol. 13, pp. 84–88, jan 2010.

[84] S. M. Sherman, "Thalamus plays a central role in ongoing cortical functioning," *Nat. Neurosci.*, vol. 19, pp. 533–541, apr 2016.

[85] M. M. Halassa and S. M. Sherman, "Thalamocortical Circuit Motifs: A General Framework," *Neuron*, vol. 103, pp. 762–770, sep 2019.

[86] S. M. Sherman, "Interneurons and triadic circuitry of the thalamus," *Trends Neurosci.*, vol. 27, pp. 670–675, nov 2004.

[87] T. T. Dang-Vu, S. M. McKinney, O. M. Buxton, J. M. Solet, and J. M. Ellenbogen, "Spontaneous brain rhythms predict sleep stability in the face of noise," *Curr. Biol.*, vol. 20, pp. R626–7, aug 2010.

[88] Y. Sela, V. V. Vyazovskiy, C. Cirelli, G. Tononi, and Y. Nir, "Responses in rat core auditory cortex are preserved during sleep spindle oscillations," *Sleep*, vol. 39, pp. 1069–1082, may 2016.

[89] T. Andrillon, Y. Nir, R. J. Staba, F. Ferrarelli, C. Cirelli, G. Tononi, and I. Fried, "Sleep spindles in humans: Insights from intracranial EEG and unit recordings," *J. Neurosci.*, vol. 31, pp. 17821–17834, dec 2011.

[90] M. D'Andola, B. Rebollo, A. G. Casali, J. F. Weinert, A. Pigorini, R. Villa, M. Massimini, and M. V. Sanchez-Vives, "Bistability, causality, and complexity in cortical networks: An in vitro perturbational study," *Cereb. Cortex*, vol. 28, pp. 2233–2242, jul 2018.

[91] H. KATTLER, D. â. DIJK, and A. A. BORBÉLY, "Effect of unilateral somatosensory stimulation prior to sleep on the sleep EEG in humans," *J. Sleep Res.*, vol. 3, pp. 159–164, sep 1994.

[92] M. Mukovski, S. Chauvette, I. Timofeev, and M. Volgushev, "Detection of active and silent states in neocortical neurons from the field potential signal during slow-wave sleep," *Cereb. Cortex*, vol. 17, pp. 400–414, feb 2007.

[93] M. Massimini, F. Ferrarelli, M. J. Murphy, R. Huber, B. A. Riedner, S. Casarotto, and G. Tononi, "Cortical reactivity and effective connectivity during REM sleep in humans," *Cogn. Neurosci.*, vol. 1, pp. 176–183, aug 2010.

[94] A. Arena, R. Comolatti, S. Thon, A. G. Casali, and J. F. Storm, "General anesthesia disrupts complex cortical dynamics in response to intracranial electrical stimulation in rats," *eNeuro*, vol. 8, no. 4, 2021.

[95] S. Sarasso, M. Boly, M. Napolitani, O. Gosseries, V. Charland-Verville, S. Casarotto, M. Rosanova, A. G. Casali, J. F. Brichant, P. Boveroux, S. Rex, G. Tononi, S. Laureys, and M. Massimini, "Consciousness and complexity during unresponsiveness induced by propofol, xenon, and ketamine," *Curr. Biol.*, vol. 25, pp. 3099–3105, dec 2015.

[96] L. D. Claar, I. Rembado, J. R. Kuyat, L. C. Marks, S. R. Olsen, and C. Koch, "Cortico-thalamo-cortical interactions modulate electrically evoked eeg responses in mice," *bioRxiv*, feb 2023.

[97] A. A. Borbély, "Two-Process Model of Sleep Regulation," *Encycl. Neurosci.*, vol. 1, no. 3, pp. 4146–4146, 2008.

[98] G. Tononi and C. Cirelli, "Sleep and synaptic homeostasis: A hypothesis," *Brain Res. Bull.*, vol. 62, pp. 143–150, dec 2003.

[99] G. Tononi and C. Cirelli, "Sleep function and synaptic homeostasis," *Sleep Med. Rev.*, vol. 10, pp. 49–62, feb 2006.

[100] G. Tononi and C. Cirelli, "Sleep and the Price of Plasticity: From Synaptic and Cellular Homeostasis to Memory Consolidation and Integration," *Neuron*, vol. 81, pp. 12–34, jan 2014.

[101] G. Tononi and C. Cirelli, "Sleep and synaptic down-selection," *Eur. J. Neurosci.*, vol. 51, pp. 413–421, jan 2020.

[102] G. L. Collingridge, J. T. Isaac, and T. W. Yu, "Receptor trafficking and synaptic plasticity," *Nat. Rev. Neurosci.*, vol. 5, pp. 952–962, dec 2004.

[103] V. V. Vyazovskiy, C. Cirelli, M. Pfister-Genskow, U. Faraguna, and G. Tononi, "Molecular and electrophysiological evidence for net synaptic potentiation in wake and depression in sleep," *Nat. Neurosci.*, vol. 11, pp. 200–208, feb 2008.

[104] C. Cirelli and G. Tononi, "Effects of sleep and waking on the synaptic ultrastructure," *Philos. Trans. R. Soc. B Biol. Sci.*, vol. 375, p. 20190235, may 2020.

[105] F. S. Chance, L. F. Abbott, and A. D. Reyes, "Gain modulation from background synaptic input," *Neuron*, vol. 35, pp. 773–782, aug 2002.

[106] W. Gerstner, A. K. Kreiter, H. Markram, and A. V. Herz, "Neural codes: Firing rates and beyond," *Proc. Natl. Acad. Sci. U. S. A.*, vol. 94, pp. 12740–12741, nov 1997.

[107] A. Borst and F. E. Theunissen, "Information theory and neural coding," *Nat. Neurosci.*, vol. 2, pp. 947–957, nov 1999.

[108] G. Tononi, M. Boly, M. Massimini, and C. Koch, "Integrated information theory: From consciousness to its physical substrate," *Nat. Rev. Neurosci.*, vol. 17, pp. 450–461, jul 2016.

[109] A. Weigenand, M. Schellenberger Costa, H. V. V. Ngo, J. C. Claussen, and T. Martinetz, "Characterization of K-Complexes and Slow Wave Activity in a Neural Mass Model," *PLoS Comput. Biol.*, vol. 10, p. e1003923, nov 2014.

[110] M. S. Costa, J. Born, J. C. Claussen, and T. Martinetz, "Modeling the effect of sleep regulation on a neural mass model," *J. Comput. Neurosci.*, vol. 41, pp. 15–28, aug 2016.

[111] A. L. Hodgkin, A. F. Huxley, and B. Katz, "Measurement of current-voltage relations in the membrane of the giant axon of Loligo," *J. Physiol.*, vol. 116, pp. 424–448, apr 1952.

[112] H. R. Wilson and J. D. Cowan, "Excitatory and Inhibitory Interactions in Localized Populations of Model Neurons," *Biophys. J.*, vol. 12, pp. 1–24, jan 1972.

[113] O. David and K. J. Friston, "A neural mass model for MEG/EEG: Coupling and neuronal dynamics," *Neuroimage*, vol. 20, pp. 1743–1755, nov 2003.

[114] J. M. Budd and Z. F. Kisvárday, "Local lateral connectivity of inhibitory clutch cells in layer 4 of cat visual cortex (area 17)," *Exp. Brain Res.*, vol. 140, pp. 245–250, sep 2001.

[115] P. Buzás, K. Kovács, A. S. Ferecskó, J. M. Budd, U. T. Eysel, and Z. F. Kisvárday, "Model-based analysis of excitatory lateral connections in the visual cortex," *J. Comp. Neurol.*, vol. 499, pp. 861–881, dec 2006.

[116] J. Antolík, "Rapid long-range disynaptic inhibition explains the formation of cortical orientation maps," *Front. Neural Circuits*, vol. 11, p. 21, mar 2017.

[117] S. K. Esser, S. Hill, and G. Tononi, "Breakdown of effective connectivity during slow wave sleep: Investigating the mechanism underlying a cortical gate using large-scale modeling," *J. Neurophysiol.*, vol. 102, pp. 2096–2111, oct 2009.

[118] G. Deco, A. Ponce-Alvarez, P. Hagmann, G. L. Romani, D. Mantini, and M. Corbetta, "How local excitation-inhibition ratio impacts the whole brain dynamics," *J. Neurosci.*, vol. 34, pp. 7886–7898, jun 2014.

[119] B. P. Cohen, C. C. Chow, and S. Vattikuti, "Dynamical modeling of multi-scale variability in neuronal competition," *Commun. Biol.*, vol. 2, p. 319, dec 2019.

[120] J. S. Goldman, L. Kusch, B. H. Yalcinkaya, D. Depannemaecker, T.-A. E. Nghiem, V. Jirsa, and A. Destexhe, "Brain-scale emergence of slow-wave synchrony and highly responsive asynchronous states

based on biologically realistic population models simulated in The Virtual Brain," *bioRxiv*, p. 2020.12.28.424574, 2020.

[121] A. Barbero-Castillo, P. Mateos-Aparicio, L. D. Porta, A. Camassa, L. Perez-Mendez, and M. V. Sanchez-Vives, "Impact of gabaa and gabab inhibition on cortical dynamics and perturbational complexity during synchronous and desynchronized states," *J. Neurosci.*, vol. 41, pp. 5029–5044, jun 2021.

[122] W. Gerstner, W. M. Kistler, R. Naud, and L. Paninski, *Neuronal dynamics: From single neurons to networks and models of cognition*. Cambridge University Press, 2014.

[123] M. San Miguel and R. Toral, "Stochastic Effects in Physical Systems," in *Instab. Nonequilibrium Struct. VI* (E. Tirapegui, J. Martínez, and R. Tiemann, eds.), pp. 35–127, Dordrecht: Springer Netherlands, 2000.

[124] W. J. Freeman and R. Q. Quiroga, *Imaging brain function with EEG: Advanced temporal and spatial analysis of electroencephalographic signals*, vol. 9781461449843. New York, NY: Springer New York, 2013.

[125] P. D. Welch, "The Use of Fast Fourier Transform for the Estimation of Power Spectra: A Method Based on Time Averaging Over Short, Modified Periodograms," *IEEE Trans. Audio Electroacoust.*, vol. 15, pp. 70–73, jun 1967.

[126] J. J. Faraway, "Generalized Linear Models," in *Int. Encycl. Educ. Third Ed.*, pp. 178–183, Elsevier, 2009.

[127] C. M. Bishop and N. M. Nasrabadi, *Pattern recognition and machine learning*, vol. 4. Springer, 2006.

[128] A. J. Dobson and A. G. Barnett, *An introduction to generalized linear models*. CRC press, 2018.

[129] J. Fox, *Applied regression analysis and generalized linear models*. Sage Publications, 2015.

[130] S. P. Boyd and L. Vandenberghe, *Convex optimization*. Cambridge university press, 2004.

[131] M. Kuhn, K. Johnson, *et al.*, *Applied predictive modeling*, vol. 26. Springer, 2013.

[132] E. Maris and R. Oostenveld, "Nonparametric statistical testing of EEG- and MEG-data," *J. Neurosci. Methods*, vol. 164, pp. 177–190, aug 2007.

[133] S. Dehaene, L. Naccache, G. Le Clec'H, E. Koechlin, M. Mueller, G. Dehaene-Lambertz, P. F. Van De Moortele, and D. Le Bihan, "Imaging unconscious semantic priming," *Nature*, vol. 395, pp. 597–600, oct 1998.

[134] P. M. Merikle, D. Smilek, and J. D. Eastwood, "Perception without awareness: Perspectives from cognitive psychology," *Cognition*, vol. 79, pp. 115–134, apr 2001.

[135] S. Dehaene, L. Naccache, L. Cohen, D. L. Bihan, J. F. Mangin, J. B. Poline, and D. Rivière, "Cerebral mechanisms of word masking and unconscious repetition priming," *Nat. Neurosci.*, vol. 4, pp. 752–758, jul 2001.

[136] K. J. Friston, "Functional and effective connectivity in neuroimaging: A synthesis," *Hum. Brain Mapp.*, vol. 2, no. 1-2, pp. 56–78, 1994.

[137] B. M. Jobst, R. Hindriks, H. Laufs, E. Tagliazucchi, G. Hahn, A. Ponce-Alvarez, A. B. Stevner, M. L. Kringelbach, and G. Deco, "Increased Stability and Breakdown of Brain Effective Connectivity during Slow-Wave Sleep: Mechanistic Insights from Whole-Brain Computational Modelling," *Sci. Rep.*, vol. 7, p. 4634, jul 2017.

[138] C. Cirelli and G. Tononi, "Differential expression of plasticity-related genes in waking and sleep and their regulation by the noradrenergic system," *J. Neurosci.*, vol. 20, pp. 9187–9194, dec 2000.

[139] Z. W. Liu, U. Faraguna, C. Cirelli, G. Tononi, and X. B. Gao, "Direct evidence for wake-related increases and sleep-related decreases in synaptic strength in rodent cortex," *J. Neurosci.*, vol. 30, pp. 8671–8675, jun 2010.

[140] C. Cirelli and G. Tononi, "The why and how of sleep-dependent synaptic down-selection," *Semin. Cell Dev. Biol.*, vol. 125, pp. 91–100, may 2022.

[141] S. Hill and G. Tononi, "Modeling sleep and wakefulness in the thalamocortical system," *J. Neurophysiol.*, vol. 93, pp. 1671–1698, mar 2005.

[142] Y. Wei, G. P. Krishnan, M. Komarov, and M. Bazhenov, "Differential roles of sleep spindles and sleep slow oscillations in memory consolidation," *PLoS Comput. Biol.*, vol. 14, p. e1006322, jul 2018.

[143] S. Bensaid, J. Modolo, I. Merlet, F. Wendling, and P. Benquet, "COALIA: A Computational Model of Human EEG for Consciousness Research," *Front. Syst. Neurosci.*, vol. 13, no. November, p. 59, 2019.

[144] M. D. Volo, A. Romagnoni, C. Capone, and A. Destexhe, "Biologically Realistic Mean-Field Models of Conductance-Based Networks

of Spiking Neurons with Adaptation," *Neural Comput.*, vol. 31, pp. 653–680, apr 2019.

[145] S. H. Strogatz, *Nonlinear dynamics and chaos with student solutions manual: With applications to physics, biology, chemistry, and engineering*. CRC press, 2018.

[146] A. G. Casali, O. Gosseries, M. Rosanova, M. Boly, S. Sarasso, K. R. Casali, S. Casarotto, M. A. Bruno, S. Laureys, G. Tononi, and M. Massimini, "A theoretically based index of consciousness independent of sensory processing and behavior," *Sci. Transl. Med.*, vol. 5, p. 198ra105, aug 2013.

[147] S. H. Lee and Y. Dan, "Neuromodulation of Brain States," *Neuron*, vol. 76, pp. 209–222, oct 2012.

[148] J. R. Cho, J. B. Treweek, J. E. Robinson, C. Xiao, L. R. Bremner, A. Greenbaum, and V. Gradinaru, "Dorsal Raphe Dopamine Neurons Modulate Arousal and Promote Wakefulness by Salient Stimuli," *Neuron*, vol. 94, pp. 1205–1219.e8, jun 2017.

[149] H. Hayat, N. Regev, N. Matosevich, A. Sales, E. Paredes-Rodriguez, A. J. Krom, L. Bergman, Y. Li, M. Lavigne, E. J. Kremer, O. Yizhar, A. E. Pickering, and Y. Nir, "Locus coeruleus norepinephrine activity mediates sensory-evoked awakenings from sleep," *Sci. Adv.*, vol. 6, p. eaaz4232, apr 2020.

[150] F. Nadim and D. Bucher, "Neuromodulation of neurons and synapses," *Curr Opin Neurobiol.*, vol. 29, pp. 48–56, dec 2014.

[151] E. Marder and V. Thirumalai, "Cellular, synaptic and network effects of neuromodulation," *Neural Networks*, vol. 15, no. 4-6, pp. 479–493, 2002.

[152] H. Bastuji and L. García-Larrea, "Evoked potentials as a tool for the investigation of human sleep," *Sleep Med. Rev.*, vol. 3, pp. 23–45, mar 1999.

[153] N. Kharas, A. Andrei, S. R. Debes, and V. Dragoi, "Brain state limits propagation of neural signals in laminar cortical circuits," *Proc. Natl. Acad. Sci. U. S. A.*, vol. 119, p. e2104192119, jul 2022.

[154] F. Razi, R. Moreno Bote, and B. Sancristóbal, "Computational modeling of information propagation during the sleep-waking cycle," *Biology (Basel).*, vol. 10, p. 945, sep 2021.

[155] M. R. Joglekar, J. F. Mejias, G. R. Yang, and X. J. Wang, "Inter-areal Balanced Amplification Enhances Signal Propagation in a Large-Scale Circuit Model of the Primate Cortex," *Neuron*, vol. 98, pp. 222–234.e8, apr 2018.

[156] G. Deco, Y. Sanz Perl, P. Vuust, E. Tagliazucchi, H. Kennedy, and M. L. Kringelbach, "Rare long-range cortical connections enhance human information processing," *Curr. Biol.*, vol. 31, pp. 4436–4448.e5, oct 2021.

[157] S. Sur and V. Sinha, "Event-related potential: An overview," *Ind. Psychiatry J.*, vol. 18, p. 70, jan 2009.

[158] S. Makov, O. Sharon, N. Ding, M. Ben-Shachar, Y. Nir, and E. Z. Golumbic, "Sleep disrupts high-level speech parsing despite significant basic auditory processing," *J. Neurosci.*, vol. 37, pp. 7772–7781, aug 2017.

[159] S. G. Horovitz, A. R. Braun, W. S. Carr, D. Picchioni, T. J. Balkin, M. Fukunaga, and J. H. Duyn, "Decoupling of the brain's default mode network during deep sleep," *Proc. Natl. Acad. Sci. U. S. A.*, vol. 106, pp. 11376–11381, jul 2009.

[160] M. A. Koch, D. G. Norris, and M. Hund-Georgiadis, "An investigation of functional and anatomical connectivity using magnetic resonance imaging," *Neuroimage*, vol. 16, pp. 241–250, may 2002.

[161] R. E. Passingham, K. E. Stephan, and R. Kötter, "The anatomical basis of functional localization in the cortex," *Nat. Rev. Neurosci.*, vol. 3, pp. 606–616, aug 2002.

[162] J. S. Damoiseaux, S. A. Rombouts, F. Barkhof, P. Scheltens, C. J. Stam, S. M. Smith, and C. F. Beckmann, "Consistent resting-state networks across healthy subjects," *Proc. Natl. Acad. Sci. U. S. A.*, vol. 103, pp. 13848–13853, sep 2006.

[163] J. L. Vincent, G. H. Patel, M. D. Fox, A. Z. Snyder, J. T. Baker, D. C. Van Essen, J. M. Zempel, L. H. Snyder, M. Corbetta, and M. E. Raichle, "Intrinsic functional architecture in the anaesthetized monkey brain," *Nature*, vol. 447, pp. 83–86, may 2007.

[164] D. Mantini, M. G. Perrucci, C. Del Gratta, G. L. Romani, and M. Corbetta, "Electrophysiological signatures of resting state networks in the human brain," *Proc. Natl. Acad. Sci. U. S. A.*, vol. 104, pp. 13170–13175, aug 2007.

[165] P. Hagmann, L. Cammoun, X. Gigandet, R. Meuli, C. J. Honey, J. Van Wedeen, and O. Sporns, "Mapping the structural core of human cerebral cortex," *PLoS Biol.*, vol. 6, pp. 1479–1493, jul 2008.

[166] E. Rykhlevskaia, G. Gratton, and M. Fabiani, "Combining structural and functional neuroimaging data for studying brain connectivity: A review," *Psychophysiology*, vol. 45, pp. 173–187, mar 2008.

[167] P. Skudlarski, K. Jagannathan, V. D. Calhoun, M. Hampson, B. A. Skudlarska, and G. Pearlson, "Measuring brain connectivity: Diffusion tensor imaging validates resting state temporal correlations," *Neuroimage*, vol. 43, pp. 554–561, nov 2008.

[168] C. J. Honey, O. Sporns, L. Cammoun, X. Gigandet, J. P. Thiran, R. Meuli, and P. Hagmann, "Predicting human resting-state functional connectivity from structural connectivity," *Proc. Natl. Acad. Sci. U. S. A.*, vol. 106, pp. 2035–2040, feb 2009.

[169] M. E. Raichle, A. M. MacLeod, A. Z. Snyder, W. J. Powers, D. A. Gusnard, and G. L. Shulman, "A default mode of brain function," *Proc. Natl. Acad. Sci. U. S. A.*, vol. 98, pp. 676–682, jan 2001.

[170] M. D. Greicius, B. Krasnow, A. L. Reiss, and V. Menon, "Functional connectivity in the resting brain: A network analysis of the default mode hypothesis," *Proc. Natl. Acad. Sci. U. S. A.*, vol. 100, pp. 253–258, jan 2003.

[171] M. E. Raichle, "The Brain's Default Mode Network," *Annu. Rev. Neurosci.*, vol. 38, pp. 433–447, jul 2015.

[172] G. Tononi and M. Massimini, "Why does consciousness fade in early sleep?," *Ann. N. Y. Acad. Sci.*, vol. 1129, pp. 330–334, may 2008.

[173] P. Fries, "A mechanism for cognitive dynamics: Neuronal communication through neuronal coherence," *Trends Cogn. Sci.*, vol. 9, pp. 474–480, oct 2005.

[174] P. Fries, "Rhythms for Cognition: Communication through Coherence," *Neuron*, vol. 88, pp. 220–235, oct 2015.

[175] A. J. Krom, A. Marmelshtein, H. Gelbard-Sagiv, A. Tankus, H. Hayat, D. Hayat, I. Matot, I. Strauss, F. Fahoum, M. Soehle, J. Bostrom, F. Mormann, I. Fried, and Y. Nir, "Anesthesia-induced loss of consciousness disrupts auditory responses beyond primary cortex," *Proc. Natl. Acad. Sci. U. S. A.*, vol. 117, pp. 11770–11780, may 2020.

[176] F. Ferrarelli, M. Massimini, S. Sarasso, A. Casali, B. A. Riedner, G. Angelini, G. Tononi, and R. A. Pearce, "Breakdown in cortical effective connectivity during midazolam-induced loss of consciousness," *Proc. Natl. Acad. Sci. U. S. A.*, vol. 107, pp. 2681–2686, feb 2010.

[177] M. Dasilva, A. Camassa, A. Navarro-Guzman, A. Pazienti, L. Perez-Mendez, G. Zamora-López, M. Mattia, and M. V. Sanchez-Vives, "Modulation of cortical slow oscillations and complexity across anesthesia levels," *Neuroimage*, vol. 224, p. 117415, jan 2021.

[178] M. Isono, Y. Wakabayashi, M. M. Fujiki, T. Kamida, and H. Kobayashi, "Sleep cycle in patients in a state of permanent unconsciousness," *Brain Inj.*, vol. 16, pp. 705–712, aug 2002.

[179] V. Cologan, X. Drouot, S. Parapatics, A. Delorme, G. Gruber, G. Moonen, and S. Laureys, "Sleep in the unresponsive wakefulness syndrome and minimally conscious state," *J. Neurotrauma*, vol. 30, pp. 339–346, mar 2013.

[180] S. Casarotto, A. Comanducci, M. Rosanova, S. Sarasso, M. Fecchio, M. Napolitani, A. Pigorini, A. G. Casali, P. D. Trimarchi, M. Boly, O. Gosseries, O. Bodart, F. Curto, C. Landi, M. Mariotti, G. Devalle, S. Laureys, G. Tononi, and M. Massimini, "Stratification of unresponsive patients by an independently validated index of brain complexity," *Ann. Neurol.*, vol. 80, pp. 718–729, nov 2016.